Earth-Abundant Transition Metal Oxides for Water Oxidation

Dissertation

Zur

Erlangung der naturwissenschaftlichen Doktorwürde
(Dr. sc. nat.)

vorgelegt der

Mathematisch-naturwissenschaftlichen Fakultät

der

Universität Zürich

von

Hongfei Liu

aus

V. R. China

Promotionskomitee

Prof. Dr. Greta R. Patzke (Vorsitz)

Prof. Dr. Roland Sigel

Prof. Dr. Madhavi Krishnan

Zürich, 2015

CONTENTS

Acknowledgements

How time flies! Four years have passed since I started my PhD study at University of Zurich in October 2011. Looking back over this period, I feel I am in debit a lot to my supervisor, colleagues, friends and parents. Without their help and support, I would not finish my PhD project.

Firstly, I would like to give my special thanks to my supervisor: Prof. Dr. Greta R. Patzke. She offered me one of the most interesting projects in the chemistry field and gave me sufficient liberty to explore my interest and implement my ideas during the research process. I will always remember her inspirable and patient discussions which make my research work much smoother. Additionally, I especially appreciate her generous support in materials characterization and workshop training, which allows me to update my knowledge and get in touch with novel materials characterization techniques.

I would like to thank Prof. Dr. Roger Alberto and Prof. Dr. Roland Sigel's suggestions to my research work during my pre-ACI seminar and Prof. Dr. Madhavi Krishnan as my PhD committee member.

I would like to thank my colleagues because they help me a lot in both my work and daily life. Their suggestions made me adapt to the life in Switzerland more easily and their help enabled me to get familiar with the lab equipments very fast and implement my experiments more efficiently. These colleagues are: Prof. Dr. Ying Zhou, Prof. Dr. Lubin Ni, Dr Franziska Conrad, Dr. Pierre Emmanuel Car, Dr. René Moré, Dr Min Sheng, Dr. Roman Kontic, Dr. Georg Geisberger, Roger Jacot, Kim von Allmen, Fabio Evangelisti, Michael Olah, Fangyuan Song, Rafael Müller, Matteo Corce, Robin Güttinger, Karla Lienau, Simona Conti, and Mauro Schilling. Additionally, I would like to give my special thanks to Michael Olah, Rafael Müller and Karla Lienau for the revision of this thesis.

Additionally, special thanks must goes to the people who give me a lot of technique supports to my research work. They are Dr. Ferdinand Wild (Raman, TG and frequent ICP analysis), Dr. Frank Krumeich (high quality HRTEM pictures, ETH), Mr. Peter Wagli (a lot of patience in my SEM training, EMEZ in ETH), Dr. Thomas Fox (solid state NMR analysis, UZH), Dr. Maxim Yulikov and Prof Dr. Gunnar Jeschke (EPR, ETH), Dr. Jorg Patscheider (XPS, EMPA Dübendorf), and Dr. Li Luo (PXRD, ETH).

Swiss National Science Foundation, University of Zurich and China Scholarship Council funded my research work. These organizations are gratefully acknowledged as well. Morevoer, I wish to thank Dr. Jae Kyoung Pak, Nathalie Fichter, and Erni Ramona for their excellent administrative service.

My friends in Switzerland are also acknowledged as they made my life colorful and brought me a lot of happiness. They are Wangqing Kong, Yuzhen Zhang, Linling Wu, Yunjun Shen, Yanfeng Jiang, Liyuan Zhou, Tao Chen, Kun Zhao, Xu Han, Yanhua Jiang, Famin Qiu, Wenjie Sun, Meng Wang, Yuheng Zhang, Rong Yang, Jun Xu, Jingyi Li, Dr. Xiaoyu Sun. Dr. Zongling Chu, Dr. Xiang Fei, Dr. Zhaodong Li, Jing Xie in Irchel campus are also appreciated for their daily help.

Finally, I would like to express my special thanks to my parents Fuxiu Luo and Sitan Liu. Their endless love, support and guidance give me the courage to overcome all the difficulties in my life.

Zurich, 05/2015

Abbreviations

AES	atomic emission spectrometry
BET	Brunauer-Emmett-Teller
CV	Cyclic Voltammetry
DFT	density functional theory
DSC	differential scanning calorimetry
EDXS	energy dispersive X-ray spectra
EPR	electron paramagnetic resonance spectroscopy
EXAFS	extended X-ray absorption fine structure
FT-IR	Fourier transform infrared spectroscopy
HRTEM	high resolution transmission electron microscopy
LED	light emitting diode
ICP	inductively coupled plasma
MAS	magic angle spinning
MS	mass spectroscopy
NMR	nuclear magnetic resonance
OEC	oxygen evolution cluster
PXRD	powder X-ray diffraction
SAED	selected area electron diffraction
SEM	scanning electron microscopy
SQUID	superconducting quantum interference device
TEM	transmission electron microscopy
TG	therogravimetry
UV/Vis	ultra violet / visible
WOC	water oxidation catalyst
XANES	X-ray absorption near edge structure
XPS	X-ray photoelectron spectroscopy

Publications

The following parts of this PhD thesis have been or will be published:

Chapter 2

1. H. Liu, G. R. Patzke. Cobalt-Manganese Spinel Oxides as Visible-Light-Driven Water Oxidation Catalysts. *Ceram. Eng. Sci. Proc.* **2013**, *34*, 75-86.

Chapter 3

2. H. Liu, G. R. Patzke. Visible-light-driven water oxidation with nanoscale Co_3O_4: New optimization strategies. *Chem. Asian J.* **2014**, *9*, 2249-2259.

Chapter 4

3. H. Liu, Y. Zhou, R. Moré, R. Müller, T. Fox, G. R. Patzke. Correlations between Structure, Electronic Properties and Photochemical Water Oxidation: A Case Study on Lithium Cobalt Oxides. *ACS Catal.* **2015**, *5*, 3791-3800.

Chapter 5

4. H. Liu, G. R. Patzke. Metallic band structure induced enhancement of photochemical water oxidation in strongly correlated electronic systems. *Submitted.*

Chapter 6

5. H. Liu, G. R. Patzke. Delithiation induced enhanced water oxidation of $LiCoPO_4$ and $LiMn_2O_4$. *Under correction.*

Chapter 7

6. H. Liu, G. R. Patzke. Interlayer anions tailored photochemical water oxidation of layered cobalt double hydroxides and cobalt hydroxides. *Under correction.*

Chapter 8

7. H. Liu, M. Schilling, M. Yulikov, S. Luber, G. R. Patzke. Homogeneous photochemical water oxidation with cobalt chloride in acidic media. *ACS Catal.* **2015**, *5*, 4994-4999.

1. Introduction

1.1 General introduction

Currently, the worldwide energy supply is mainly based on fossil fuels, such as coal, petroleum and natural gas, which entail environmental pollution and the greenhouse effect. Moreover, these resources are not sustainable so that an intense search for energy alternatives is currently under way. In this context, access to clean and sustainable energy is turning into an urgent and leading theme for the scientific research in 21st century. Sunlight is the most abundant and permanent energy source available for our planet. Earth receives solar energy at a rate of around 120,000 TW (1 TW = 10^{12} W) which significantly exceeds the annual worldwide energy consumption for both current (~15 TW) and estimated future demands.[1] Thus, conversion of rather diffuse sunlight into readily available solar fuels with higher calorific values emerges as one of the most promising strategies for future energy production.

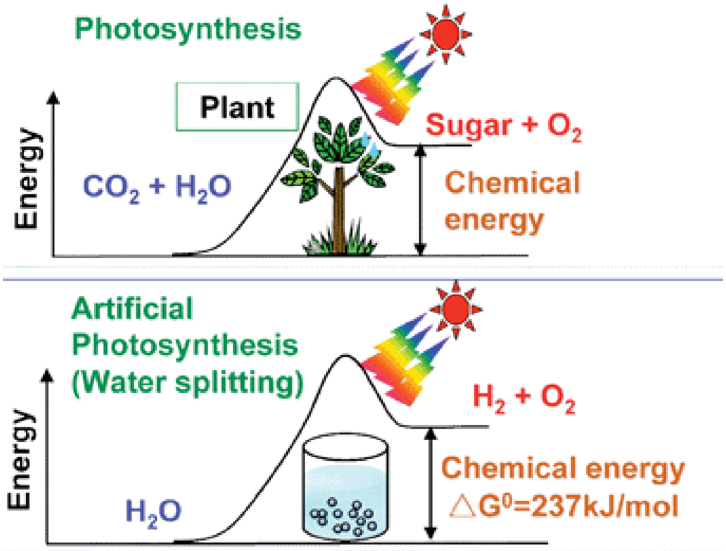

Figure 1.1. Photosynthesis by green plants and artificial photosynthesis for water splitting.[2]

Over billions of years of evolution, nature has gradually developed and optimized its solar energy capture system that can reduce CO_2 to carbohydrates with sunlight as the thermodynamic driving force. This process provides direct inspiration for artificial photosynthesis through water splitting or CO_2 reduction for solar fuels production on a larger scale (Figure 1.1). Among the complex overall process of photosynthesis, photosystem II (PSII) remains in the focus of extensive research activities, because it enables the most thermodynamically demanding and kinetically complex step in biology, namely water oxidation.[3] The same challenges apply for artificial photosynthesis. To improve the solar to fuels conversation efficiency, development of water oxidation catalysts with high activity and stability containing earth-abundant elements is currently an important worldwide scientific trend.

1.2 Water oxidation in PSII

Water oxidation is an uphill reaction which proceeds at a driving potential of at least 1.23 V versus RHE in neutral condition. One oxygen molecule evolution will consume four oxidizing equivalents, entailing the multiple redox properties of catalytic active sites during one reaction cycle. Through persistent effort by molecular biologist, the oxygen evolution core in PSII was identified as a Mn_4O_5Ca cluster which is surrounded by several amino acid ligands (Figure 1.2A). The metal ions in this cluster are interconnected by oxo-bridge with the three Mn and one Ca forming a distorted $CaMn_3O_4$ cubane. The rest one Mn is bound the cubane moiety by additional oxo-bridge.

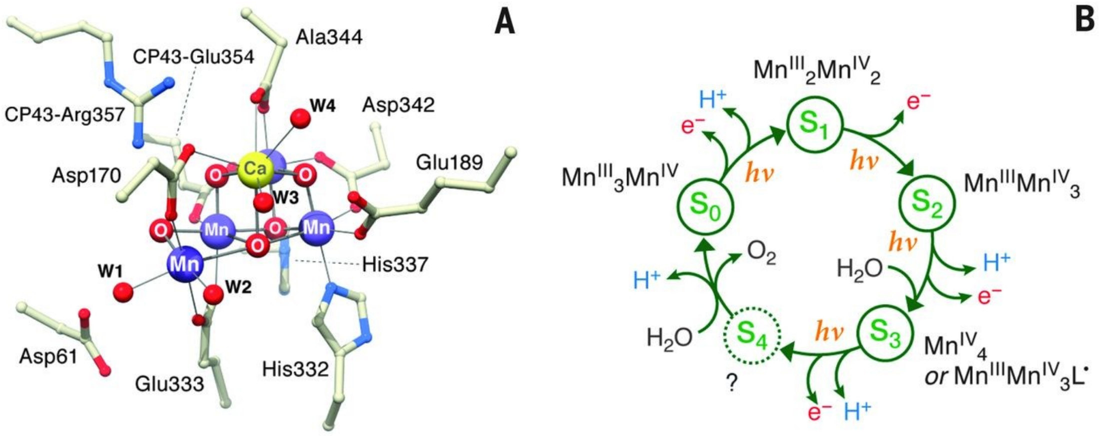

Figure 1.2. The $\{CaMn_4O_5\}$ oxygen evolving complex (OEC) of PSII. (A) Crystallographic structure of $\{CaMn_4O_5\}$. (B) The five intermediate "S" states of the OEC during water oxidation.[2]

The $\{CaMn_4O_5\}$ oxygen evolution cluster (OEC) is known to catalyze the water oxidation through five basic steps known as the Kok cycle (illustrated in Figure 1.2B). During this process, the OEC undergoes five different oxidation states (S_0-S_4) of the four Mn core atoms to store four oxidizing equivalents for the water oxidation. Each cycle is driven by the photo-oxidant of PSII (P680), a multichlorophyll pigment assembly. Even though great progress has been made in the elucidation of PSII mechanisms over the past few decades, all of the precise steps are not yet clarified, e.g. the role of Ca^{2+} ions.[4]

1.3 Artificial water oxidation catalysts

Water oxidation is known to occur on the $\{CaMn_4O_5\}$ OEC with a high oxygen evolution TOF of around 500 s^{1-}.[5] However, construction of direct synthetic replicas of this cluster for practical application is extremely difficult due to its complicated and special structure within a complex bio-matrix. Development of metal containing compounds with analogous motifs and comparable catalytic activity and chemical stability is a more feasible approach for artificial water oxidation.

1.3.1 Water oxidation catalysts types

Artificial water oxidation catalyst (WOC) can be mainly divided into two types (homogenous or heterogeneous) according to their solubility in aqueous conditions. Homogenous catalysts are generally transitional metal-based complexes (e.g. with Ru, Co, Fe, of small molecular size. Heterogeneous catalysts are most often transition metal based oxides with less frequent examples of sulfides and carbides. Polyoxometalates can be considered as a third type of WOCs, because they display molecular sizes between oxides and conventional molecules.

Recently, studies on complexes and polyoxometalate-type WOCs revealed the formation of oxides during water oxidation process,[6-11] which raised intense debates on the real catalytic species and sheds new light on the interface between homogenous and heterogeneous water oxidation, with the polyoxometalate $[Co_4(H_2O)_2(PW_9O_{34})_2]^{10-}$ as a typical example.[12-16] Precipitated oxides (i.e. CoO_x) were frequently assumed to act as real catalysts with the soluble complexes or polyoxometalates just being their precursors. However, direct evidence of water oxidation directly from the oxides rather than from the so-called precursors remains difficult to acquire. Alternatively, the precipitated oxides may be just the byproducts due to the partial decomposition of the soluble WOCs, given that the real catalytic activity of CoO_x is often very low. Further studies are required to clarify this issue.

1.3.2 Techniques for water oxidation tests

Standardized activity evaluation for a given WOC is important for screening newly synthesized for maximum efficiency WOCs. Currently, water oxidation activity is primarily investigated with photochemical or electrochemical techniques.

The photochemical approach generally employs a chromophore (photosensitizer) which produces a single electron oxidant after irradiation in the presence of a proper electron acceptor. Next, the single electron oxidation leads to a charge transfer with the WOC which can further oxidize water after accumulation of sufficient oxidizing equivalents. Earlier studies in the 1980s used $[Fe(bpy)_3]^{2+}$, $[Os(bpy)_3]^{2+}$ and $IrCl_6^{2-}$ as photosensitizers and $[Co(NH_3)_6]_{3+}$ as electron acceptor.[17] However, the most extensively applied protocol these days is based on $[Ru(bpy)_3]^{2+}/S_2O_8^{2-}$ (Figure 1.3) due to several advantages: (a) $[Ru(bpy)_3]^{2+}$ is relatively stable; (b) its oxidation potential is insensitive to the test conditions such as pH, buffer and so on; (c) it can be efficiently quenched by $S_2O_8^{2-}$ on a timescale which is much shorter the water oxidation reactions; (d) $S_2O_8^{2-}$ is transparent for visible light and does not influence the light absorption of $[Ru(bpy)_3]^{2+}$. Recently, platinum-porphyrin was investigated as a photosensitizer for photochemical water oxidation with IrO_2 as WOC, which displayed superior activity compared to $[Ru(bpy)_3]^{2+}$.[18] However, its stability under catalytic conditions needs to be further examined.

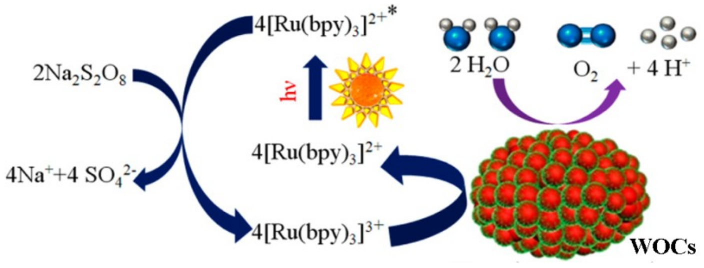

Figure 1.3. Scheme for photochemical water oxidation with the $[Ru(bpy)_3]^{2+}/S_2O_8^{2-}$ protocol.[19]

Electrochemical water oxidation is based on a three electrode setup (counter electrode, reference electrode and working electrode) in an electrochemical workstation, as shown in Figure 1.4. In contrast to the photochemical techniques with energy input from light, electrochemical water oxidation is driven by an external potential applied to the working electrode. For laboratory measurements, homogeneous WOCs are just dissolved in an electrolyte solution, while heterogeneous WOCs have to be attached to the working electrode by dipping, spinning coating or in-situ electrochemical deposition. Electrode preparation for heterogeneous WOCs is a demanding process which requires substantial expertise. The adhesion between working electrode (FTO and glass carbon are generally used) and heterogeneous WOCs can significantly influence the electrochemical water oxidation activities, which renders the quantification of the activity of different WOCs rather difficult.

However, it is noteworthy to mention that water oxidation mechanisms may differ between photochemical and electrochemical conditions. For example, highly electrochemically active α-MnO_2 oxide was found to be inactive under photochemical conditions.[20,21] Moreover, some homogeneous WOCs tested under photochemical conditions may transform into heterogeneous WOCs under electrochemical investigation conditions, with $[Co_4(H_2O)_2(PW_9O_{34})_2]^{10-}$ as a representative example.[12,14] Electrochemical measurements probably exert a stronger influence on the WOCs compared to photochemical process, because the applied potential drives a high-density charge exchange between WOCs and electrode resulting generally in much higher TOF, in contrast to $[Ru(bpy)_3]^{2+}/S_2O_8^{2-}$ which enables less intense charge exchange between the associated $[Ru(bpy)_3]^{2+}$ and WOCs.

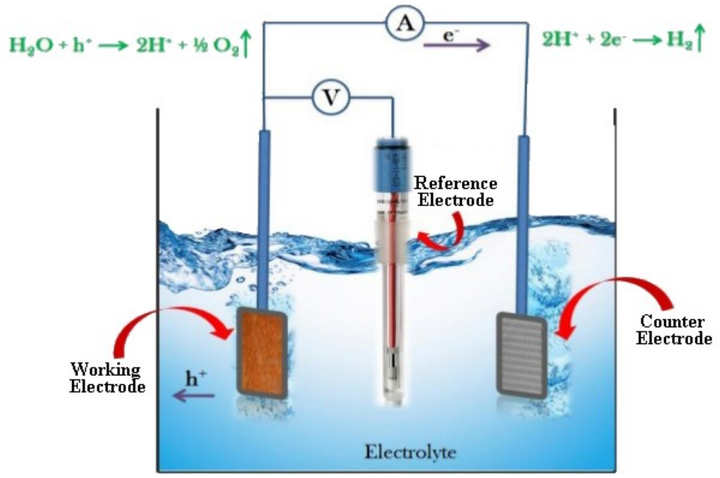

Figure 1.4. Setup for electrochemical water oxidation.

An additional way to assess the catalytic activity is water oxidation assisted by a chemical oxidant. Geneally, a single electron oxidant with sufficiently high potential, such as NaClO, $NaIO_4$, $[Ru(bpy)_3]^{3+}$ and $(NH_4)_2[Ce(NO_3)_6]$, is employed as the chemical driving force for water oxidation.[22] A major disadvantage of this technique is the tendency of the oxidant towards self-decomposition, even in the absence of WOC.

1.3.3. Performance evaluation of WOCs

Turnover number (TON) and turnover frequency (TOF) are the general parameters for assessing the activity of a given catalyst. TON specifies the maximum use that can be made of a catalyst for a special reaction under defined conditions by a number of molecular reactions or reaction cycles occurring at an active site for the given time. TOF quantifies the specific activity of a catalytic center for a special reaction under defined reaction conditions by the number of molecular reactions or catalytic cycles occurring at an active site per time unit. These two parameters are generally more applicable to homogeneous water oxidation because the numbers of active site participating in catalysis is more precisely quantified for homogeneous WOCs compared to heterogeneous WOCs.

Heterogeneous catalysis proceeds exclusively on a biphasic interface so that the catalytically active elements in the bulk of WOCs are not involved in the actual reactions. Quantification of the participating sites in a given reaction remains a challenge for heterogeneous WOCs. The general way to compare the activities between different heterogeneous WOCs is to normalize their total activity to the respective BET surface area. However, morphological factors, such as exposure of specific crystal facets with high reactivity can also significantly influence the catalytic activity, especially for single crystalline WOCs. In this case, normalization the activity to surface area is not a valid standardization method. For heterogeneous electrocatalysts, the total activity can be normalized to the electrochemical active surface area (EASA) for comparison. The general way to determine the electrochemical surface area is through cyclovoltammetric measurements of a reversible redox couple such as $[Fe(CN)_6]^{3-}/^{4-}$ and Fe^{3+}/Fe^{2+} or by ion absorption.[23]

As the definitions of TON and TOF are thus based on certain conditions, the values obtained under considerably different test conditions cannot be directly compared. Plenty of water oxidation test parameters, such as the reactor shape and size, light source, buffer composition and concentration can remarkably influence the resulting TON and TOF values. Additionally, test techniques also change these values to a large extent. For example, the TON values derived from photochemical tests are generally below 500 while they reach orders of magnitude around 10^4 in electrochemical studies.

Stability is another very important parameter that needs to be considered for the practical application of WOCs. Currently, the stability of electrochemical WOCs can be examined by either long-term electrolysis or multiple cycles of CV measurements. A stable catalyst must maintain a constant current density during electrolysis or reproducible CV curves during the CV measurements. Concerning photochemical water oxidation, no consistent evaluation criteria have been agreed on to date. Generally, WOCs are analyzed after the photochemical water oxidation process to check for changes in their structure, composition, valence states or morphology. Recently, stability tests also included recycling of the WOCs for new water oxidation runs.[24] However, this strategy is less suitable for homogeneous WOCs which are more difficult to recover.

1.4 Design strategies for WOCs

Mechanistic understanding of water oxidation reactions is crucial to establish the basic principles for WOC design. However, the underlying complicated four-electron processes remain difficult to elucidate even after more than three decades of preceding studies, especially for heterogeneous WOCs. Therefore, general concepts for the rational design of efficient WOCs still remain to be developed. Currently, many bio-inspired strategies aim to mimic the $\{CaMn_4O_5\}$ cubane OEC of PSII with respect to composition or structure, although its precise working mechanisms remain under investigation. Another major design strategy is inspired by self healing CoPi electrocatalysts which display robust water oxidation activity in neutral conditions and can be easily prepared by electro-deposition of aqueous Co^{2+} in phosphate buffer.[25] The discovery of CoPi-type catalysts triggered widespread interest in amorphous oxides for electrochemical water oxidation.

Nanostructuring is another straightforward strategy for the optimization of solid state WOCs through maximum interfaces with more exposed active sites for the heterogeneous reactions. Other design parameters, such as e_g electron configuration,[26] M-OH bond strength,[27] O p-band energy level,[28] and surface affinity to oxygen species[29] were also introduced for electrochemical water oxidation. However, they are less frequently studied and their influence on water oxidation needs to be further examined.

1.4.1 PSII inspired WOCs

Nearly two decades ago, *Dismukes* and *Ruettinger* reported a cubane $Mn_4O_4L_6$ (L=diphenylphosphinate anion) complex with both compositional and structural similarity to OEC in PSII which released oxygen upon UV irradiation with a quantum efficiency of around 100%.[30-32] These earlier studies suggested the first demonstration of a synthetic PS II OEC mimic capable of forming O-O bonds. Later works on $Mn_4O_4L_6$ embedded in nafion for photo-electrochemical investigation revealed the generation of a photocurrent by applying a potential of 1.0 V (vs. Ag/AgCl) as well as by light illumination. The photocurrent was accompanied by oxygen evolution.[33] Recently, important questions arose on the nature of the water oxidizing species and serious doubts have emerged concerning the actual role of the $Mn_4O_4L_6$ cluster during the catalysis. Indeed, Mn K-edge X-ray absorption spectroscopy and transmission electron microscopy studies applied under catalytic conditions revealed that the $Mn_4O_4L_6$ cluster dissociates into Mn (II) compounds, which are subsequently oxidized to MnIII/IV oxides (birnessite) as responsible species for the water oxidation catalysis.[34] Another interesting tetramer manganese cluster similar to PSII OEC is $[Mn^{IV}{}_4O_5(terpy)_4(H_2O)_2]^{6+}$ which can oxidize water in the presence of strong chemical oxidants such as $(NH_4)_2[Ce(NO_3)_6]$.[35]

$[Co_4(\mu\text{-}O)_4(\mu\text{-}CH_3COO)_4(C_5H_5N)_4]$ is the first reported example of a cobalt cubane complex that can oxidize water to oxygen with $[Ru(bpy)_3]^{2+}$ as photosensitizer and persulfate as sacrificial electron acceptor.[36] However, recent study proposed that the water oxidation activity arises from Co^{2+} impurities rather than from the “Co_4O_4” core itself, given that purified complex samples displayed no activity in both electrochemical and photochemical water oxidation.[37] Recently, our group reported a $[Co^{II}{}_4(hmp)_4(\mu\text{-}OAc)_2(\mu_2\text{-}OAc)_2(H_2O)_2]$ WOC which has a cobalt tetranuclear core as well. The flexible ligand architecture containing monodentate acetate and water molecules allows reversible ligand exchange with water molecules which is likely to provide free sites for the following O-O bond formation.[38]

Hill et al. introduced $[Co_4(H_2O)_2(\alpha\text{-}PW_9O_{34})_2]^{10-}$ as the first cobalt polyoxometalate that can oxidize water under both electrochemical and photochemical conditions. As for the cobalt cubanes, this compound also contains four cobalt cores which are tightly sandwiched by two $\{PW_9O_{34}\}$ ligands. However, the cobalt atoms are arranged in a plane instead of a cubane moiety. [39] Our group reported three sandwich-type POMs with either Co/Bi or Mn/Bi core. The core compositions were found to exert a tremendous influence on the WOC performance, and only Co/Bi-POM exhibits catalytic activity among the series under photochemical water oxidation conditions (with $[Ru(bpy)_3]^{2+}$ as photosensitizer and $S_2O_82^-$ as sacrificial electron acceptor).[40] Recently, *Wang* et al. reported on four $[\{Co_4(OH)_3(PO_4)\}_4(SiW_9O_{34})4]^{32-}$ (X = Si, Ge, P and As) polyoxometalate with a $\{Co_4O_4\}$ cubane core which are capable of oxidizing water in the $[Ru(bpy)_3]^{2+}$/ $S_2O_8{}^{2-}$ system.[41] Laser flash photolysis, dynamic light scattering ^{31}P NMR, UV/Vis absorption, POM extraction, and ICP-MS analysis results collectively confirmed that these four compounds can maintain their structural integrity under the photocatalytic conditions. Additionally, the compounds were successfully recrystallized from solution after photocatalytic tests and they displayed no structural changes. Most recently, the same authors reported on three Ni polyoxometalates which contain either {Ni_3O_3} quasi-cubane or {Ni_4O_4} cubane units and are highly active for photochemical water oxidation.[42] Multiple experiments including dynamic light-scattering, UV/Vis absorption, catalysts aging experiments, tetra-n-heptylammonium nitrate ($THpANO_3$) toluene extraction, and capillary electrophoretic measurements results confirm that these three compounds are dominant active catalysts, with no contribution of Ni^{2+} ions or nickel oxide under the photocatalytic conditions. *Bonchio* et al. recently reported the first manganese polyoxometalate that can photochemically oxidize water even though the activity is quite low. This compound composes of four manganese cores in mixed valence states, mimicking the S_0 state of the PSII OEC.[43]

Dismukes et al. indicated the possible impact of {Co_4O_4} motifs on the water oxidation activity of oxide based WOCs.[44] In a case study, two different $LiCoO_2$ modifications (spinel and layer structures) were investigated for photochemical water oxidation and only the spinel structure containing {Co_4O_4} motif was found to be active in water oxidation.

Kurz et al. studied calcium manganese (III) oxides for water oxidation which have a compositional similarity to the "Mn_4O_5Ca" cluster in PSII. They found that the presence of calcium could greatly improve the performances of these heterogeneous catalyst materials.[45] Recently, they further investigated the effect of interlayer alkaline earth cations on the water oxidation activity of layered manganese oxides, which demonstrated that the oxides (like the OEC) require the presence of calcium in their structures to reach the maximum catalytic activity.[46] In contrast, *Jiao* et al. indicated that alkaline cations do not significantly influence the water oxidation activity of δ-MnO_2 except for stabilizing the layered structure.[47] Until now, the precise influence of inert elements such as Ca, K and Na is still challenging to elucidate. The function of Ca^{2+} in the {$CaMn_4O_5$} OEC of photosystem II is a most prominent example: while its importance is evident, its mechanistic role remains under intense investigation. Recent studies indicate that it does not only play a structural role, but might also serve as a binding site for water molecules during the water oxidation process.[48] Further studies on synthetic OEC mimics pointed to a major influence of redox-inert cations on the redox potential of the active transition metal sites.[49,50]

1.4.2 CoPi related WOCs

In 2008, *Kanan* and *Nocera* discovered an oxygen-evolving catalyst that forms in situ upon anodic polarization of an inert electrode in neutral aqueous phosphate solutions containing Co^{2+}.[25] This catalyst film (so-called CoPi) could split water at low overpotential (onset of catalysis observed at an overpotential = 280 mV with maximum current achieved at = 410 mV or a potential of 1.23 V at pH 7.0). This catalyst display several advantages: (a) composed of earth-abundant materials; (b) works at near neutral pH; (c) can be prepared easily by electrodeposition of soluble cobalt salt on various electrode substrates and geometries; (d) its self healing ability guarantees the sustainable catalytic activity over long-term run; (e) relatively low overpotential. Later studies ascribed its self-healing property to a dynamic equilibrium established between the deposition and oxidation of cobalt ions from solution and the dissolution of film material during water oxidation.[51] Additionally, replacing the phosphate buffer with other proton-accepting buffers such as methylphosphonate and borate buffers results in similar catalysts films with comparable activities to CoPi.[52] Further EPR study of the CoPi film revealed the presence of Co^{4+} after electrocatalytic water oxidation.[53]

The amorphous character of CoPi renders the structural investigations of CoPi catalyst rather difficult. Despite extensive studies in the past a few year, no consensus has reached on its local structure. In 2009, *Dau* et al. conducted the first structural study using extended X-ray absorption fine structure (EXAFS) and near-edge X-ray absorption (XANES) spectroscopy.[54] XANES results showed that the film was mainly composed of Co(III) ions in an octahedral coordination environment consisting of six oxygen atoms. EXAFS data revealed the Co-O distances of 1.89 Å and Co-Co distances of 2.81 Å and 5.62 Å. 1.89 Å of Co-O distances implies that cobalt is octahedrally coordinated by six oxygen atoms and confirms the XANES results. A Co-Co distance of 2.81 Å is indicative of cobalt atoms in a cubane-type geometry with di-μ-oxo bridges. Co-Co distances of 5.62 Å (twice 2.81 Å) would indicate two cubanes sharing a vertex (Figure 1.5b).

In 2010, *Nocera* and coworkers performed further XAS studies of the cobalt catalyst film.[55] XANES spectra of the bulk and surface films were compared to the spectra of Co(II) and Co(III) models. This comparison showed that the average valence of the catalyst under potential is above three. When the potential was removed, edge-energy shifts indicate the release of aqueous Co(II) from the deposited film. Comparison of the XANES spectra between the bulk and surface films revealed a slightly higher average valence state in the bulk films than in the surface films. Results from EXAFS studies show a high correlation between the film structure and the structural motif of CoO(OH), a cobalt-oxide/hydroxide mineral that is able to accommodate a large population of Co(IV) ions, with some significant differences. Most importantly, by comparing the major features found in the EXAFS spectra of surface CoPi, bulk CoPi, and CoO(OH), it was found that the structural motifs of the film more closely resemble edge-sharing CoO_6 octahedra (Figure 1.5b) found in CoO(OH) rather than the vertex-sharing CoO_6 octahedra proposed by *Dau* and coworkers (Figure 1.5b). Recently, pair distribution function (PDF) analysis of X-ray scattering data further indicated that CoPi is most likely composed of edge-sharing CoO_6 octahedra with a domain size of a few nanometers.[56,57]

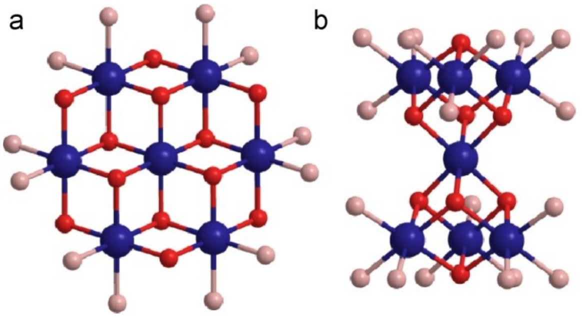

Figure 1.5. Structural models of the CoPi catalyst derived from XAS measurements. Edge-sharing octahedral model proposed by *Nocera* et al. (a), vertex-sharing model for films proposed by *Dau* et al. (b). Cobalt atoms are shown in blue, bridging oxygen atoms in red and terminal oxygen atoms in pink.[55]

The discovery of CoPi has raised wide interest on the development of earth abundant metal oxides for water oxidation, preferably those with an amorphous character. *Berlinguette* et al. developed a photochemical route for the deposition of amorphous oxides from metal organic precursors for electrocatalytic water oxidation.[58] *Dau* and *Driess* prepared an amorphous MnO_x catalyst with both photochemical and electrochemical activity for water oxidation by oxidation of MnO with ceric ammonium nitrate as oxidant.[59] Recently, *Driess* et al. again synthesized amorphous $CoFe_2O_4$ oxides via solvothermal methods which exhibited even higher water oxidation activity than crystalline $CoFe_2O_4$ with a spinel structure.[60] Likewise, *Dutta* and *Suib* reported superior photochemical water oxidation activity of porous amorphous manganese oxides to crystalline manganese oxides with either birnessite or octahedral molecular sieve structures.[61] *Geng* et al. invented an aerosol spray method for fabricating amorphous mixed metal oxides for electrochemical water oxidation. Through this method, the proportion of metal elements can be rather accurately controlled (±5 % range) and the products can be sustainably obtained on a suitable scale for industrial applications.[62]

As the structural analysis of CoPi film supports that it is constituted of stacks of edge-sharing $\{CoO_6\}$ layers, which are similar to cobalt hydroxide, layered double hydroxides and oxyhydroxide, metal hydroxides keep attracting increasing interest as potential water oxidation catalysts. *Dai* et al. investigated Ni−Fe layered double hydroxide electrocatalysts for water oxidation and enhanced their performance by hybrid formation with mildly oxidized multiwalled carbon nanotubes.[63] Exfoliation of layered double hydroxides of Co-Co, Co-Fe and Co-Ni was found to dramatically enhance their electrocatalytic water oxidation activities by *Song* and *Hu*.[64] Recently, they further studied ultrathin cobalt-manganese layered double hydroxide for electrochemical water oxidation which displays a turnover frequency (TOF) more than 20 times higher than that of Co and Mn oxides and hydroxides, and 9 times higher than the well-known noble metal IrO_2 catalyst.[65] Nickel oxyhydroxide was studied for electrochemical water oxidation and a slight incorporation of Fe into the oxide matrix was found to greatly improve the water oxidation activity. Detailed analyses indicate that the enhanced activity is due to both increased conductivity and partial-charge transfer activation effect to Ni by Fe.[66] A follow-up study on $Co_{1-x}Fe_x(OOH)$ indicated a ∼100-fold higher activity for $x \approx 0.6\text{-}0.7$ than for $x = 0$ based on per-metal turnover frequency. Fe incorporation and increased activity correlate with an anodic shift in the nominal $Co^{2+}/^{3+}$ redox wave, indicating strong electronic interactions between the two elements and, likely due to substitutional doping of Co by Fe.[67]

1.4.3 Nanotructured WOCs

Nanoscience and nanotechnology have made great progress over the past few decades by uncovering many superior effects of nanostructured materials. Nanomaterials excel, for example, through their high surface-to-volume ratio which maximizes the active sites for heterogeneous catalysis. Additionally, the quantum confinement to nanometer dimensions can significantly modify the electronic properties of the given materials, thus rendering their reactivity tunable by the particle size.

Recently, Co_3O_4 and CoO were found to split pure water directly into hydrogen and oxygen under visible light irradiation for the first time when their respective particle sizes decreased to several nanometers.[68,69] This is an instructive example of quantum confinement effects on tuning the band gap, charge carrier mobility and catalytic properties. However, the quantum confinement only sets in when the particle size is below its Bohr exciton radius (generally a few nanometers), thereby limiting its effect predominately to quantum dot materials. For the majority of nanocatalysts, the nanoeffect is mainly ascribed to their high surface-to-volume ratio.

Recently, *Frei* et al. reported that the water oxidation activity of Co_3O_4 and MnO_x was notably enhanced through supporting the oxides on mesoporous silica substrates.[70-72] Next, the authors further synthesized efficient Mg-doped mesoporous Co_3O_4-WOCs through leaching of silica from silica-Co_3O_4 nanocomposite precursors. Removal of the Mg dopant further increased the catalyst porosity and enhanced the water oxidation performance.[73] *Vela* et al. studied the microstructure effects of porous silica supports on the photochemical water oxidation activities of Co_3O_4 WOCs and revealed the possible influence of silica substrate morphologies on the accessibility of Co_3O_4 to reactants.[74] *Jiao* et al. further investigated the influence of support materials on the photochemical water oxidation with Co_3O_4 nanoclusters. KIT-6 was found to be a better support than SBA-15, because the 3D porous structure of KIT-6 offers more accessible pores than the 1D channel of SBA-15. Moreover, the authors indicated that the composition of the support does not obviously influence the catalytic activation and thus concluded that the major role of catalyst supports in Co_3O_4-assisted water oxidation is to provide a medium to physically separate Co_3O_4 nanoclusters from aggregation to enable superior photocatalytic activities.[75] In contrast, a recent study described that the surface acidity of substrates can dramatically change the photochemical water oxidation activities of mononuclear cobalt catalysts.[76]

Schmuki et al. prepared highly active porous cobalt oxide nanowire arrays by self-organized electrochemical anodization of Co metal foil and subsequent heat treatment.[77] Likewise, *Qiao* et al. obtained electrocatalysts with ultra high water oxidation activity based on porous Co_3O_4 nanowire/carbon hybrid arrays by a facile carbonization of the metal-organic framework grown on Cu foil.[78] *Suib* et al. prepared mesoporous manganese oxides with excellent activities for both electrochemical and photochemical water oxidation by a micelle templating approach.[79] *Xie* et al. reported on porous Co_3O_4 sheets with atomic dimensions displaying an electrocatalytic current up to 341.7 mA/cm^2 which is roughly 50-times larger than that of the bulk counterpart.[80] Recently, a highly efficient cobalt oxide WOC with particle sizes below 5 nm was prepared by pulsed laser ablation in liquid media,[81] and very small cobalt domains displayed high WOC activity on mesoporous silica surfaces.[82] Moreover, the productive influence of reduced particle sized on the water oxidation activity of Co_3O_4 was illustrated in a systematic study by *Grzelczak* et al.[83]

1.5 Strategy and framework of present thesis

1.5.1 Basic strategy

Development of water oxidation catalysts based on earth-abundant metals is crucial for large-scale water splitting in long-term application perspectives. While homogeneous WOCs are more amenable to spectroscopic, crystallographic, and physicochemical as well as mechanistic characterizations, they are more likely to suffer from stability issues such as ligands oxidation and decomposition. In this thesis, we mainly target the synthesis, characterization and performance evaluation of transition metal (Fe, Co, Mn and Ni) based oxide WOCs. Through correlating water oxidation activity with the structure and electronic properties of the investigated WOCs, we aim to identify the preferable electronic properties for water oxidation. The results are expected to provide generally applicable guidelines for future WOCs design.

1.5.2 Thesis strategy

Figure 1.6 illustrates the architecture of the present thesis. We started with mixed Co/Mn oxides, which contain cubane moieties similar to the OEC in PSII (Chapter 2). The influence of composition and cubane structure on the water oxidation activity was investigated and $\{Co_4O_4\}$ motifs were found to be more active compared to $\{Mn_4O_4\}$. Next, we proceeded to Co_3O_4 as a well-defined model system and examined the possible factors that can optimize its water oxidation activity (Chapter 3). In Chapter 4, we further studied the role of $\{Co_4O_4\}$ motifs in water oxidation by comparing two $LiCoO_2$ modifications: the spinel structure with $\{Co_4O_4\}$ cubane units and the layered structure without such cubanes. Moreover, the influence of the electronic structure on the water oxidation was investigated by delithiation of both structure types. The promoting effects of delithiation and $\{Co_4O_4\}$ cubane motifs on water oxidation were consistently explained by enhanced hole mobility. The productive effect of delithiation on the water oxidation activities was further confirmed for other lithium battery materials, such as $LiCoPO_4$ and $LiMn_2O_4$ (Chapter 5). In Chapter 6, the impact of hole mobility on the water oxidation performance was further verified by a series of perovskite oxides, such as $La_{1-x}Sr_xMO_3$ and $La_{2-x}Sr_xMO_4$ (M= Co, Fe, Mn and Ni) with conveniently tunable hole mobility. The productive influence of delithiation on the water oxidation activity inspired us to study the possibility of tuning the performance of layered cobalt double hydroxides through their interlayer anions (Chapter 7). As mentioned in the introduction, several recently investigated homogeneous Co-WOCs were later found to be precatalysts for in-situ precipitated CoO_x as the true catalyst. The observation of cobalt leaching from our Co/Mn spinel oxide-based and $LiCoO_2$ oxide-based WOCs finally inspired us to explore the water oxidation properties of free Co^{2+} ions (Chapter 8).

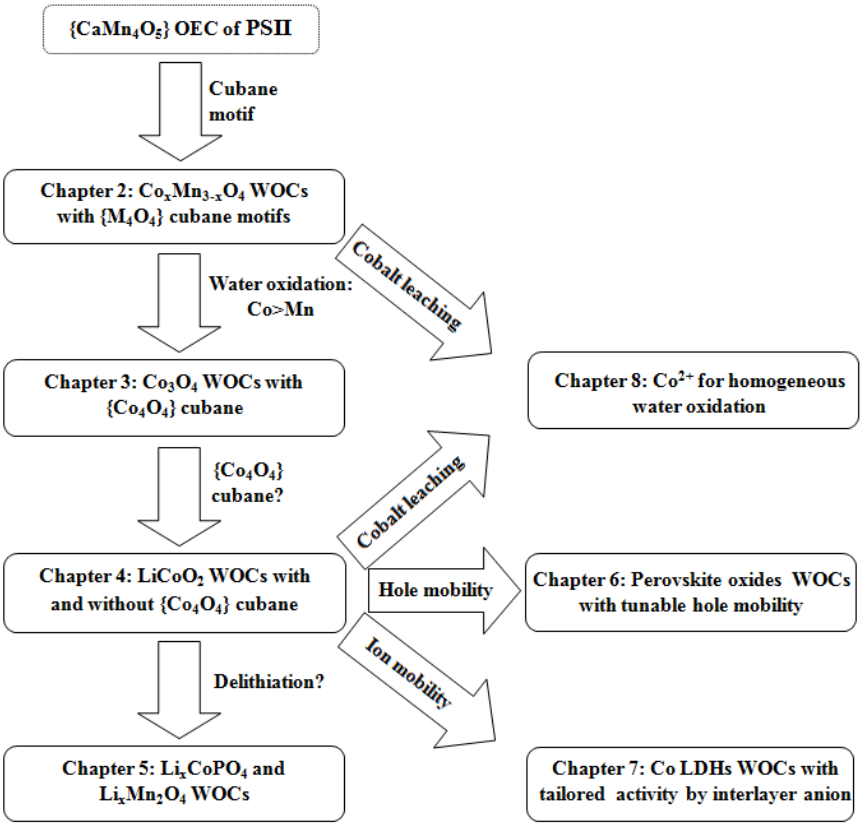

Figure 1.6. Framework scheme of the present thesis.

References

[1] R. E. Blankenship, D. M. Tiede, J. Barber, G. W. Brudvig, G. Fleming, M. Ghirardi, M. R. Guner, W. Junge, D. M. Kramer, A. Melis, T. A. Moore, C. C. Moser, D. G. Nocera, A. J. Nozik, D. R. Ort, W. W. Parson, R. C. Prince, R. T. Sayre. *Science* **2011**, *332*, 805-809.

[2] A. Kudo, Y. Miseki. *Chem. Soc. Rev.* **2009**, *38*, 253-278.

[3] K. N. Ferreira, T. M. Iverson, K. Maghlaoui, J. Barber, S. Iwata. *Science* **2004**, *303*, 1831-1838.

[4] K. Yamaguchi, S. Yamanaka, H. Isobe, T. Saito, K. Kanda, Y. Umena, K. Kawakami, J.-R. Shen, N. Kamiya, M. Okumura, H. Nakamura, M. Shoji, Y. Yoshioka. Int. J. Quantum Chem. **2013**, *113*, 453-473.

[5] N. Cox, D. A. Pantazis, F. Neese, W. Lubitz. *Acc. Chem. Res.* **2013**, *46*, 1588-1596.

[6] M. M. Najafpour, A. N. Moghaddam, H. Dau, I. Zaharieva. *J. Am. Chem. Soc.* **2014**, *136*, 7245-7248.

[7] R. K. Hocking, R. Brimblecombe, L.-Y. Chang, A. Singh, M. H. Cheah, C. Glover, W. H. Casey, L. Spiccia. *Nat. Chem.* **2011**, *3*, 461-466.

[8] N. D. Schley, J. D. Blakemore, N. K. Subbaiyan, C. D. Incarvito, F. D'Souza, R. H. Crabtree, G. W. Brudvig. *J. Am. Chem. Soc.* **2011**, *133*, 10473-10481.

[9] S. Fu, Y. Liu, Y. Ding, X. Du, F. Song, R. Xiang, B. Ma. *Chem. Commun.* **2014**, *50*, 2167-2169.

[10] D. Hong, J. Jung, J. Park, Y. Yamada, T. Suenobu, Y. -M. Lee, W. Nam, S. Fukuzumi, *Energy Environ. Sci.* **2012**, *5*, 7606-7616.

[11] G. Chen, L. Chen, S.-M. Ng, W.-L. Man, T.-C. Lau. *Angew. Chem. Int. Ed.* **2013**, *52*, 1-4.

[12] J. J. Stracke, R. G. Finke. *J. Am. Chem. Soc.* **2011**, *133*, 14872-14875.

[13] M. Natali, S. Berardi, A. Sartorel, M. Bonchio, S. Campagna, F. Scandola. *Chem. Commun.* **2012**, *48*, 8808-8810.

[14] J. W. Vickers, H. Lv, J. M. Sumliner, G. Zhu, Z. Luo, D. G. Musaev, Y. V. Geletii, C. L. Hill. *J. Am. Chem. Soc.* **2013**, *135*, 14440-14118.

[15] R. Schiwon, K. Klingan, H. Dau, C. Limberg. *Chem. Commun.* **2014**, *50*, 100-102.

[16] J. J. Stracke, R. G. Finke. *ACS Catal.* **2014**, *4*, 79-89.

[17] V. Y. Shafirovich, N. K. Khannanov, V. V. Strelets. *Nouv. J. Chim.* **1980**, *4*, 81-87.

[18] H.-C. Chen, D. G. H. Hetterscheid, R. M. Williams, J. I. van der Vlugt, J. N. H. Reek, A. M. Brouwer. *Enery. Environ. Sci.* **2015**, *8*, 975-982.

[19] X. Fei, W. Li, Z. Shao, S. Seeger, D. Zhao, X. Chen. *J. Am. Chem. Soc.* **2014**, *136*, 15781-15786.

[20] D. M. Robinson, Y. B. Go, M. Mui, G. Gardner, Z. Zhang, D. Mastrogiovanni, E. Garfunkel, J. Li, M. Greenblatt, G. C. Dismukes. *J. Am. Chem. Soc.* **2013**, *135*, 3494-3501.

[21] Y. Meng, W. Song, H. Huang, Z. Ren, S.-Y. Chen, S. L. Suib. *J. Am. Chem. Soc.* **2014**, *136*, 11452-11464.

[22] J. L. Fillol, Z. Codolà, I. Garcia-Bosch, L. Gómez, J. J. Pla, M. Costas. *Nat. Chem.* **2011**, *3*, 807-813.

[23] R. F. Savinell, R. L. Zeller Ⅲ, J. A. Adams. *J. Electrochem. Soc.* **1990**, *137*, 489-494.

[24] D. Hong, Y. Yamada, T. Nagatomi, Y. Takai, S. Fukuzumi. *J. Am. Chem. Soc.* **2012**, *134*, 19572-19575.

[25] M. W. Kanan, D. G. Nocera. *Science* **2008**, *321*, 1072-1075.

[26] J. Suntivich, K. J. May, H. A. Gasteiger, J. B. Goodenough, Y. Shao-Horn. *Science* **2011**, *334*, 1383-1385.

[27] R. Subbaraman, D. Tripkovic, K.-C. Chang, D. Strmcnik, P. A. Paulikas, P. Hirunsit, M. Chan, J. Greeley, V. Stamenkovic, N. M. Markovic. *Nat. Mater.* **2012**, *11*, 550-557.

[28] A. Grimaud, K. J. May, C. E. Carlton, Y.-L. Lee, M. Risch, W. T. Hong, J. Zhou, Y. Shao-Horn. *Nat. Commun.* **2013**, *4*, 2439.

[29] J. Rossmeisl, Z. W. Qu, H. Zhu, G. J. Kroes, J. K. Norskov. *J. Electroanal. Chem.* **2007**, 607, 83-89.

[30] W. Ruettinger, C. Campana, G. C. Dismukes. *J. Am. Chem. Soc.* **1997**, *119*, 6670-6671.

[31] W. Ruettinger, M. Yagi, K. Wolf, S. Bemasek, G. C. Dismukes. *J. Am. Chem. Soc.* **2000**, *122*, 10353-10357.

[32] M. Yagi, K. V. Wolf, P. J. Baesjou, S. L. Bernasek, G. C. Dismukes. *Angew. Chem. Int. Ed.* **2001**, *40*, 2925-2928.

[33] R. Brimblecome, G. F. Swiegers, G. C. Dismukes, L. Spiccia. *Angew. Chem. Int. Ed.* **2008**, *47*, 7335-7338.

[34] R. K. Hocking, R. Brimblecome, L. Y. Chang, A. Singh, M. H. Cheah, C. Glover, W. H. Casey, L. Spiccia. *Nat.Chem.* **2011**, *3*, 461-466.

[35] Y. Gao, R. H. Crabtree, G. W. Brudvig. *Inorg. Chem.* **2012**, *51*, 4043-4050.

[36] N. S. McCool, D. M. Robinson, J. E. Sheats, G. C. Disumkes. *J. Am. Chem. Soc.* **2011**, *133*, 11446-11449.

[37] A. M. Ullman, Y. Liu, M. Huynh, D. K. Bediako, H. Wang, B. L. Anderson, D. C. Powers, J. J. Breen, H. D. Abruna, D. G. Nocera. *J. Am. Chem. Soc.* **2014**, *136*, 17681-17688

[38] F. Evangelisti, R. Güttinger, R. Moré, S. Luber, G. R. Patzke. *J. Am. Chem. Soc.* **2013**, *135*, 18734-18737.

[39] Q. S. Yin, J. M. Tan, C. Besson, Y. V. Geletii, D. G. Musaev, A. E. Kuznetsov, Z. Luo, K. I. Hardcastle, C. L. Hill. *Science* **2010**, *328*, 342-345.

[40] F. Evangelisti, P.-E. Car, O. Blacque, G. R. Patzke. *Catal. Sci. Tech.* **2013**, *3*, 3117-3129.

[41] X.-B. Han, Z.-M. Zhang, T. Zhang, Y.-G. Li, W. Lin, W. You, Z.-M. Su, E.-B. Wang. *J. Am. Chem. Soc.* **2014**, *136,* 5359-5366.

[42] X.-B. Han, Y.-G. Li, Z.-M. Zhang, H.-Q. Tan, Y. Lu, E.-B. Wang. *J. Am. Chem. Soc.* **2015**, *137,* 5486-5493.

[43] R. Al-Oweini, A. Sartorel, B. S. Bassil, M. Natali, S. Berardi, F. Scandola, U. Kortz, M. Bonchio. *Angew. Chem. Int. Ed.* **2014**, *53*, 11182-11185.

[44] G. P. Gardner, Y. B. Go, D. M. Robinson, P. F. Smith, J. Hadermann, A. Abakumov, M. Greenblatt, G. C. Dismukes. *Angew. Chem. Int. Ed.* **2012**, *51*, 1616-1619.

[45] M. M. Najafpour, T. Ehrenberg, M. Wiechen, and P. Kurz. *Angew. Chem. Int. Ed.* **2010**, *49*, 2233-2237.

[46] M. Wiechen, I. Zaharieva, H. Dau, P. Kurz. *Chem. Sci.* **2012**, *3*, 2330-2339.

[47] V. B. R. Boppana, S. Yusuf, G. S. Hutchings, F. Jiao. *Adv. Funct. Mater.* **2013**, *23*, 878-884.

[48] F. H. M. Koua, Y. Umena, K. Kawakami, J.-R. Shen. *Proc. Natl. Acad. Sci.USA* **2013**, *110*, 3889-3894.

[49] E. Y. Tsui, T. Agapie. *Proc. Natl. Acad. Sci.USA* **2013**, *110*, 10084-10088.

[50] E. Y. Tsui, R. Tran, J. Yano, T. Agapie. *Nat. Chem.* **2013**, *5*, 293-299.

[51] D. A. Lutterman, Y. Surendranath, D. G. Nocera. *J. Am. Chem. Soc.* **2009**, *131*, 3838-3839.

[52] Y. Surendranath, M. Dincă, D. G. Nocera. *J. Am. Chem. Soc.* **2009**, *131*, 2615-2620.

[53] J. G. McAlpin, Y. Surendranath, M. Dincă, T. A. Stich, S. A. Stoian, W. H. Casey, D. G. Nocera, R. D. Britt . *J. Am. Chem. Soc.* **2010**, *132*, 6882-6883.

[54] M. Risch, V. Khare, I. Zaharieva, L. Gerencser, P. Chernev, H. Dau. *J. Am. Chem. Soc.* **2009**, *131*, 6936-6937.

[55] M. W. Kanan, J. Yano, Y. Surendranath, M. Dincă, V. K. Yachandra, D. G. Nocera. *J. Am. Chem. Soc.* **2010**, *132*, 13692-13701.

[56] C. L. Farrow, D. K. Bediako, Y. Surendranath, D. G. Nocera, S. J. L. Billinge. *J. Am. Chem. Soc.* **2013**, *135*, 6403-6406.

[57] P. Du, O. Kokhan, K. W. Chapman, P. J. Chupas, D. M. Tiede. *J. Am. Chem. Soc.* **2012**, *134*, 11096-11099.

[58] R. D. L. Smith, M. S. Prévot, R. D. Fagan, Z. Zhang, P. A. Sedach, M. K. J. Siu, S. Trudel, C. P. Berlinguette. *Science* **2013**, *340*, 60-63.

[59] A. Indra, P. Menezes, I. Zaharieva, E. Baktash, J. Pfrommer, M. Schwarze, H. Dau, M. Driess. *Angew. Chem. Int. Ed.* **2013**, *52*, 13206-13210.

[60] A. Indra, P. W. Menezes, N. R. Sahraie, A. Bergmann, C. Das, M. Tallarida, D. Schmeiβer, P. Strasser, M. Driess. *J. Am. Chem. Soc.* **2014**, *136*, 17530-17536.

[61] A. Iyer, J. Del-Pilar, C. K. King'ondu, E. Kissel, H. F. Garces, H. Huang, A. M. El-Sawy, P. K. Dutta, S. L. Suib. *J. Phys. Chem. C* **2012**, *116*, 6474-6483.

[62] L. Kuai, J. Geng, C. Chen, E. Kan, Y. Liu, Q. Wang, B. Geng. *Angew. Chem. Int. Ed.* **2014**, *53*, 7547-7551.

[63] M. Gong, Y. Li, H. Wang, Y. Liang, J. Z. Wu, J. Zhou, J. Wang, T. Regier, F. Wei, H. Dai. *J. Am. Chem. Soc.* **2013**, *135*, 8452-8455.

[64] F. Song, X. Hu. *Nat. Commun.* **2014**, *5*, 4477.

[65] F. Song, X. Hu. *J. Am. Chem. Soc.* **2014**, *136*, 16481-16484.

[66] L. Trotochaud, S. L. Young, J. K. Ranney, S. W. Boettcher. *J. Am. Chem. Soc.* **2014**, *136*, 6744-6753.

[67] M. S. Burke, M. G. Kast, L. Trotochaud, A. M. Smith. *J. Am. Chem. Soc.* **2015**, *137*, 3638-3648.

[68] N. Zhang, J. Shi, S. S. Mao, L. Guo. *Chem. Commun.***2014**, *50*, 2002-2004.

[69] L. Liao, Q. Zhang, Z. Su, Z. Zhao, Y. Wang, Y. Li, X. Lu, D. Wei, G. Feng, Q. Yu, X. Cai, J. Zhao, Z. Ren, H. Fang, F. Robles-Hernandez, S. Baldelli, J. Bao. *Nat. Nanotech.* **2014**, *9*, 69-73.

[70] F. Jiao, H. Frei. *Angew. Chem. Int. Ed.* **2009**, *48*, 1841-1844.

[71] C.-C. Yang, T. M. Eggenhuisen, M. Wolters, A. Agiral, H. Frei, P. E. Jongh, K. P. Jong, G. Mul. *ChemCatChem* **2013**, *5*, 550-556.

[72] F. Jiao, H. Frei. *Chem. Commun.* **2010**, *46*, 2920-2922.

[73] J. Rosen, G. S. Hutchings, F. Jiao. *J. Am. Chem. Soc.* **2013**, *135*, 4516-4521.

[74] C.-C. Lin, Y. Guo, J. Vela. *ACS Catal.* **2015**, *5*, 1037-1044.

[75] S. Yusuf, F. Jiao. *ACS Catal.* **2012**, *2*, 2753-2760.

[76] H. S. Ahn, J. Yano, T. D. Tilley. *ACS Catal.* **2015**, *5*, 2573-2576.

[77] C. Y. Lee, K. Lee, P. Schmuki. *Angew. Chem. Int. Ed.* **2013**, *52*, 1-6.

[78] T. Y. Ma, S. Dai, M. Jaroniec, S. Z. Qiao. *J. Am. Chem. Soc.* **2014**, *136*, 13925-13931.

[79] C.-H. Kuo, I. M. Mosa, A. S. Poyraz, S. Biswas, A. M. El-Sawy, W. Song, Z. Luo, S.-Y. Chen, J. F. Rusling, J. He, S. L. Suib. *ACS Catal.* **2015**, *5*, 1693-1699.

[80] Y. Sun, S. Gao, F. Lei, J. Liu, L. Liang, Y. Xie. *Chem. Sci. 2014*, **5**, 3976-3982.

[81] J. D. Blakemore, H. B. Gray, J. R. Winkler, A. M. Müller. *ACS Catal.* **2013**, *3*, 2497-2500.

[82] H. S. Ahn, J. Yano, T. D. Tilley. *Energy Environ. Sci*. **2013**, *6*, 3080-3087.

[83] M. Grzelczak, J. Zhang, J. Pfrommer, J. Hartmann, M. Driess, M. Antonietti, X. Wang. *ACS Catal.* **2013**, *3*, 383-388.

2. Cobalt-Manganese Spinel Oxides as Visible-Light-Driven Water Oxidation Catalysts

2.1 Introduction

One of major innovations in WOC research are inspired by the μ-oxido-{Mn_4Ca} cluster core of nature's photosystem II (PSII) which brought forward a variety of Mn- and Co-based WOCs with structurally related motifs.[1 - 4] Recently, *Robinson* . obtained a high-performance WOC with a cubic {Mn_4O_4} core through delithiation of the spinel oxide $LiMn_2O_4$.[5] *Dismukes* and coworkers reported on $Co_4O_4(OAc)_4(py)_4$ with a related molecular {Co_4O_4} cubane core that efficiently oxidizes water when powered by a standard photochemical oxidation source or via electrochemical oxidation.[6] In 2008, *Nocera* et al. discovered the robust and powerful CoPi-WOC based on {Co_4O_4} units which self-assemble under neutral conditions in the presence of phosphate buffer.[7] To date, there is ample evidence for a strong correlation between WOC efficiency and the presence of PSII-related {M_4O_4} cubane moieties.[8,9]

Manifold studies on such Co- and Mn-containing cubane systems have been conducted under visible-light-driven and electrochemical conditions in order to explore their robustness and abundance for further technological implementation. For example, *Frei* et al. reported that nanostructured Co_3O_4 or Mn-oxide clusters loaded on silica matrices showed significantly enhanced visible-light-driven WOC catalytic activity compared to their pristine microscale counterparts.[10,11] Starting from nanobelt carriers, *Yu* et al. synthesized efficient $Mn_3O_4/CoSe_2$ nanocomposites for electrocatalytic oxygen evolution.[12] Moreover, Co_3O_4 has recently been discovered as an exceptionally promising and versatile photocatalyst type for H_2 generation under visible light illumination.[13,14]

However, the majority of Co- and Mn-WOC studies are still focused on binary WOCs, whereas far less is known about mixed Co/Mn-WOCs and possible catalytic synergisms therein. Recently, we brought forward a novel mixed spinel-type visible-light-driven WOC, namely hitherto elusive Co-Mn-Ga nanoparticles which were obtained from a specially developed microwave-hydrothermal (MW-HT) approach. We found that the incorporation of Co and Mn centers into the Ga spinel matrix via MW-HT techniques led to enhanced WOC activity of Co-Mn-Ga nanospinels in comparison with their Co-Ga and Mn-Ga WOC analogues.[15] The influence of the gallium oxide matrix in these mixed spinels remains to be elucidated, and recent reports on overall water splitting with Ga_2O_3 indicate its active role.[16] Furthermore, *Chen* . reported on room temperature synthesized Co-Mn spinels which were found to exhibit excellent dual electrocatalytic functionalities for both oxygen reduction and evolution.[17] Most recently, Co_2MnO_4-graphene hybrids were reported to exhibit superior electrocatalytic oxygen reduction activity in comparison with Co_3O_4-graphene or $CoMn_2O_4$-graphene, respectively.[18] Although the first steps have been taken towards exploration of Co-Mn-oxide WOCs, these more complex mixed systems still raise plenty of challenging questions, and the correlation between their electro- and photochemical WOC activities remains to be explored.

In the following, we thus present a systematic study of visible-light-driven WOC activities of $Co_xMn_{3-x}O_4$ (x = 0, 1, 2, 3) spinel oxides.

2.2 Experimental

2.2.1 Catalysts preparation

$Co_xMn_{3-x}O_4$ (x = 0, 1, 2, 3) spinel oxides were synthesized via a hydrothermal route. All chemicals were purchased from Sigma Aldrich in AR rate. Co_2MnO_4 was obtained from a representative protocol as follows: 2 mmol cobalt(II) acetate tetrahydrate and 1 mmol manganese(II) acetate tetrahydrate were dissolved into 2.5 mL deionized water, then 0.5 mL 25 wt% $NH_3\cdot H_2O$ was added to the solution which was stirred for 2 h. After aging, the solution was mixed with 7.5 mL ethanol (high purity). Finally, the reaction mixture was transferred to a 15 mL autoclave and kept at 140 ^oC for 20 h. Products were isolated by centrifugation, washed three times with acetone and dried at 80 ^oC in air.

2.2.2 Analytical techniques

X-ray powder diffraction patterns (PXRD patterns) were recorded on a STOE STADI P diffractometer (transmission mode, Ge monochromator) with Mo $K\alpha_1$ radiation, followed by conversion to Cu $K\alpha_1$ radiation patterns with the JADE 5.0 software. Sample morphologies were examined by scanning electron microscopy (SEM) performed on a LEO 1530 (FEG) microscope. A JEOL-6060 electron microscope with a Bruker energy-dispersive X-ray spectrometer (EDXS) was used for approximate elemental analysis. Brunauer-Emmett-Teller (BET) surface area measurements were conducted on a Quadrasorb SI machine in N_2-adsorption mode. Samples were degassed at 150 °C for 24 h under vacuum prior to the measurement. Raman spectra were recorded on a Renishaw Ramascope spectrometer at 514 nm laser excitation. Fourier transformed infrared (FT-IR) spectra were collected on a Bruker Opus spectrometer. UV/Vis spectra were recorded on a Lambda 650 S Perkin Elmer UV-visible spectrometer.

2.2.3 Photocatalytic tests

WOC tests were performed according to standard $[Ru(bpy)_3]^{2+}/S_2O_8^{2-}$ protocols.[15] Firstly, a suspension was prepared by mixing 0.1 mmol oxide photocatalyst, 16.17 mg $[Ru(bpy)_3]Cl_2$ photosensitizer and 25.67 mg NaS_2O_8 in a 20 mL Na_2SiF_6 buffer (20 mmol/L, Na_2SiF_6, pH 6). The suspension was then degassed with helium to remove O_2 in both solution and in the 15 mL head vial. A 300 W Xe lamp (LOT Oriel) in line with a cut-off filter ($\lambda > 400$ nm) was used as visible light source. The light intensity was kept constantly at 200,000 lux through calibration with a photometer. After specific time intervals, 100 μL samples of gas from the head vial were injected into a gas chromatograph (Varian CP-3800, equipped with He as carrier gas and a 3 m × 2 mm column packed with molecular sieve 13X 80-100) by a gas tight microliter syringe (Hamilton 1825 RN).

2.3 Results and discussion

2.3.1 Structure and morphology of $Co_xMn_{3-x}O_4$

PXRD patterns of the $Co_xMn_{3-x}O_4$ ($x = 0, 1, 2, 3$) spinel oxide series are compared in Figure 2.1. Mn_3O_4 and $CoMn_2O_4$ display tetragonal symmetry in line with literature data (JCPDS 16-0154 and 77-0471), whereas Co_2MnO_4 and Co_3O_4 exhibit cubic symmetry (cf. JCPDS 23-1237 and 71-0816). Decreasing symmetry with increasing Mn content can be ascribed to a Jahn-Teller distortion of the MnO_6 octahedra, and the slight shift in peak positions towards higher angles upon comparison of $CoMn_2O_4$ with Mn_3O_4 or Co_3O_4 with Co_2MnO_4, respectively, agrees with preceding studies as well.[19,20] Table 2.1 furthermore demonstrates a decrease of lattice constants for the respective cubic and tetragonal compound pairs upon increasing cobalt content due to the smaller ionic radius of Co^{3+} (0.65 Å) in comparison to Mn^{3+} (0.78Å).

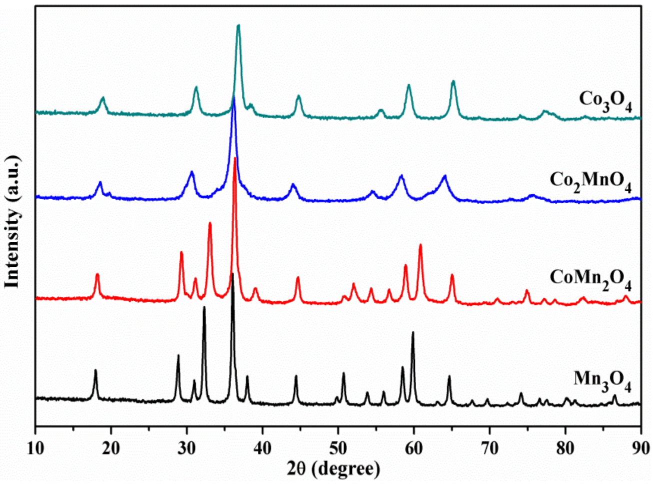

Figure 2.1. PXRD patterns of $Co_xMn_{3-x}O_4$ (x = 0, 1, 2, 3) spinel oxides recorded at room temperature.

Table 2.1. Lattice constants of $Co_xMn_{3-x}O_4$ (x = 0, 1, 2, 3) spinel oxides.

Catalyst	a(Å)	c(Å)
Mn_3O_4	5.761(7)	9.463(6)
$CoMn_2O_4$	5.730(6)	9.238(5)
Co_2MnO_4	5.753(4)	--
Co_3O_4	5.735(5)	--

Figure 2.1 summarizes the Raman spectra of the $Co_xMn_{3-x}O_4$ (x = 0, 1, 2, 3) spinel oxide series. The peaks at 190.7, 470.4, 514.2, 608.5 and 675.2 cm^{-1} agree well with data for Co_3O_4 from preceding reports,[21] which further supports the phase purity observed from the PXRD pattern (Figure 2.1). Likewise, the peaks at 306.1, 358.2 and 645.9 cm^{-1} clearly indicate the formation of phase pure Mn_3O_4.[22] However, Raman peaks of $CoMn_2O_4$ and Co_2MnO_4 are notably weaker and broadened in comparison with the binary compounds (cf. inset in Figure 2.2) which are in line with observations of *Kovandaa* et al. on Mn-doped Co_3O_4.[23] Additionally, the intensity decrease points to a slight distortion of the crystal lattice of the mixed Co-Mn spinels. The most intense peaks of all four spinel oxides are attributed to the M-O vibrations of the MO_6 units. As a result, the main peak of Co_2MnO_4 at 663.8 cm^{-1} is located between the respective peaks of Mn_3O_4 and Co_3O_4, and the broadened peak shape indicates an overlap of MnO_6 and CoO_6 contributions. In contrast, the main peak of $CoMn_2O_4$ at 645.9 cm^{-1} agrees well with that of Mn_3O_4, because the CoO_6 vibration is absent due to the preferential location of Co on the tetrahedral sites.[24] It is well known that 1/3 of the Co or Mn atoms occur as tetrahedrally coordinated M^{2+} cations in the binary Co_3O_4 or Mn_3O_4 spinel oxides, whereas the remaining 2/3 are M^{3+} cations on octahedral sides. As Mn^{2+} is more easily oxidized to Mn^{3+} than Co^{2+} in solution,[25] it has a strong preference for

the octahedral sites of the mixed Co-Mn spinels which is consistent with the observed Raman spectra.

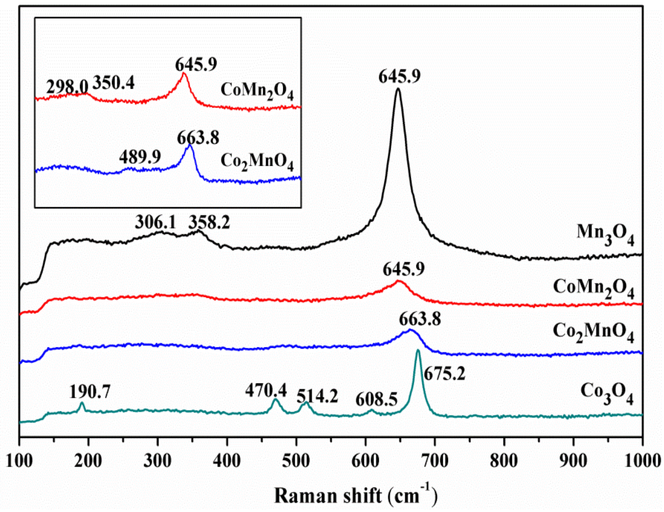

Figure 2.2. Raman spectra of $Co_xMn_{3-x}O_4$ (x = 0, 1, 2, 3) spinel oxides.

FT-IR spectra of $Co_xMn_{3-x}O_4$ (x = 0, 1, 2, 3) spinel oxides are shown in Figure 2.3. All samples have two characteristic strong peaks of spinels in the 500-700 cm^{-1} range in common. Whereas the peak at lower wavenumbers is ascribed to M-O vibrations on the octahedral positions, the according vibrations of the tetrahedral sites appear at higher wavenumbers.[26] Their slight shift towards higher wavenumbers upon increasing Co content (Figure 2.3) furthermore agrees well with previous reports of *Tian* .[27] The typical weak and broadened peaks of the O-H or N-H stretching vibrations around 3300 cm^{-1} are present in the three Co-containing spinels, but they are absent for Mn_3O_4 (Figure 2.3).[28] This indicates a stronger surface interaction of Co-rich spinels with H_2O or NH_3 molecules in comparison with Mn_3O_4. Interestingly, this agrees with our observation that Co_3O_4 nanocrystals slowly transform into $Co(OH)_2$ through reaction with surface adsorbed H_2O upon long-time storage ambient conditions (Figure 2.4). This is most likely due to Co^{2+} leaching from the high surface area sample (Table 2.2) after several months of exposure to sunlight irradiation in combination with air moisture. The triplet peaks located around 1500 cm^{-1} can either be attributed to the C-O stretch vibration of surface-adherent carbonate ions,[29] or to the O-H bending vibration of H_2O molecules. Additional peaks around 1000 cm^{-1} were assigned to O_2^{2-} species (i.e. oxygen molecules adsorbed by surface oxygen vacancies) by *Al-Mashta* .[30]

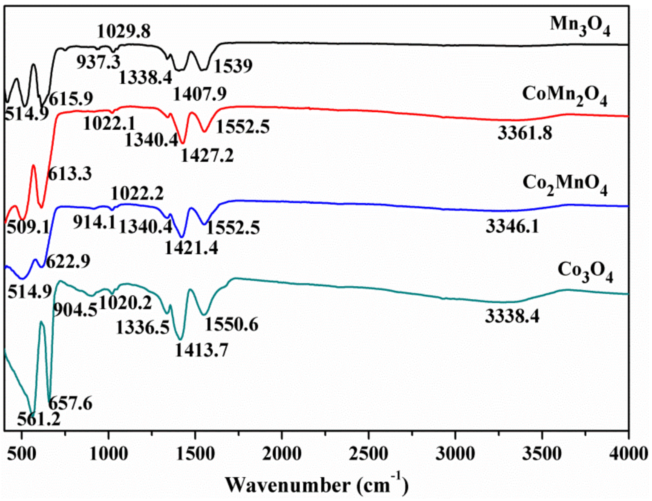

Figure 2.3. FT-IR spectra of $Co_xMn_{3-x}O_4$ (x = 0, 1, 2, 3) spinel oxides.

SEM pictures of the $Co_xMn_{3-x}O_4$ (x = 0, 1, 2, 3) spinel oxides are compared in Figure 2.5, and their particle sizes decrease with increasing Co content. At least two different hypotheses can possibly account for this observation. Firstly, formation of $[Co(NH_3)_6]^{2+}$ and $[Co(NH_3)_6]^{3+}$ in solution may decrease the available pristine Co concentration and thus slow down the growth rate.[31] Furthermore, the growth of Co-rich nanospinels may be impeded through their strong surface absorption affinity towards NH_3, H_2O, ethanol and related polar molecules as outlined in the preceding section on FT-IR spectra (cf. Figure 2.4). Additionally, particle sizes were calculated from PXRD patters (Figure 2.1) using the Scherrer equation as approx. 40 nm, 30 nm, 15 nm and 10 nm for Mn_3O_4, $CoMn_2O_4$, Co_2MnO_4 and Co_3O_4, respectively. These results are quite consistent with the SEM data (Figure 2.5). BET surface analyses (Table 2.2) furthermore confirmed this trend and revealed a clear correlation between particle size and surface area over the entire spinel series.

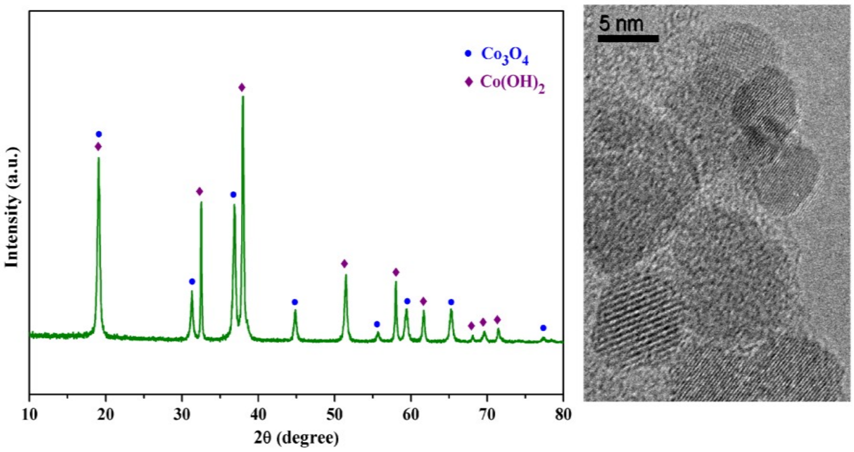

Figure 2.4. PXRD pattern of Co_3O_4 after exposure to ambient conditions for about four months (left) and TEM image of as-synthesized Co_3O_4 nanoparticles (right).

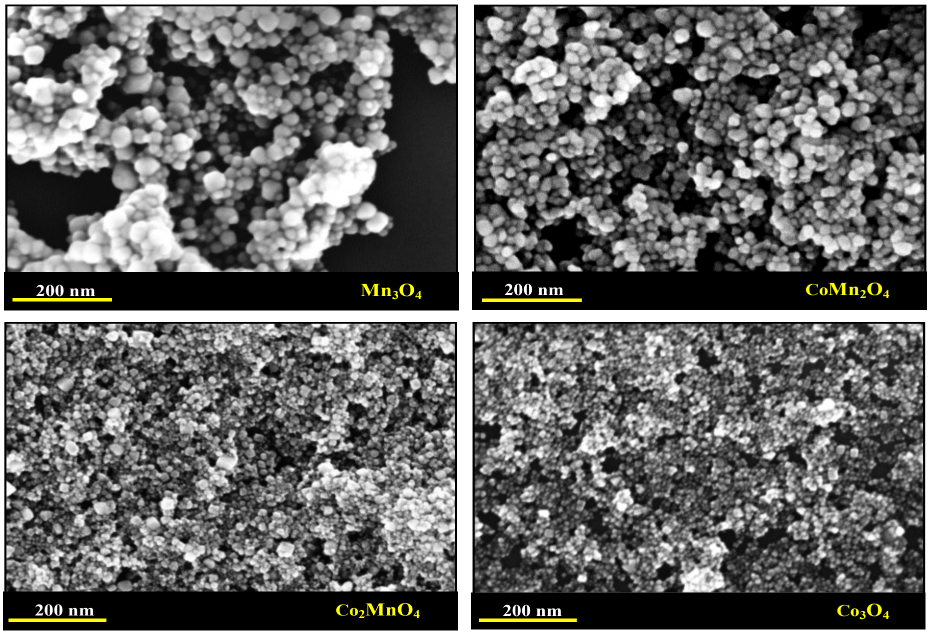

Figure 2.5. Representative SEM images of $Co_xMn_{3-x}O_4$ (x = 0, 1, 2, 3).

Table 2.2. Particle size and BET surface area of the $Co_xMn_{3-x}O_4$ (x = 0, 1, 2, 3) spinel series.

Catalysts	**Average particle size from PXRD (nm)**	**Particle size from SEM (nm)**	**BET (m^2/g)**
Mn_3O_4	40	20-50	41.99
$CoMn_2O_4$	30	20-35	48.05
Co_2MnO_4	15	10-30	86.46
Co_3O_4	10	5-15	100.63

Elemental compositions were confirmed with EDXS techniques, and the observed Co/Mn ratios for $CoMn_2O_4$ and Co_2MnO_4 of 0.54 and 1.94 agree quite well with the precursor compositions. The absence of detectable traces of additional elements further confirms the phase purity of our as-synthesized spinel samples (note that the small peak adjacent to the oxygen signal arises from carbon of the conductive tape on the sample holder).

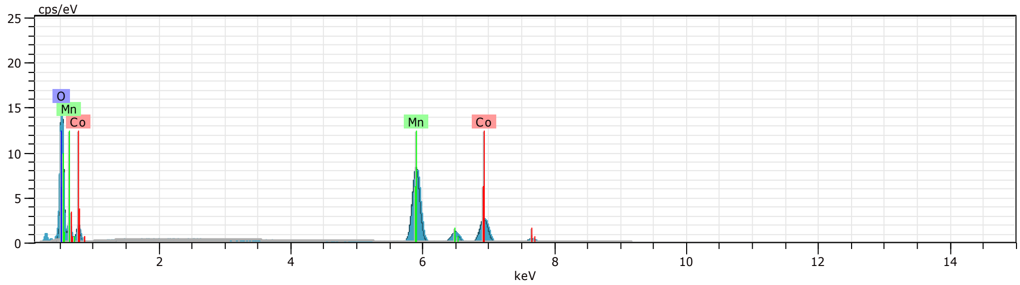

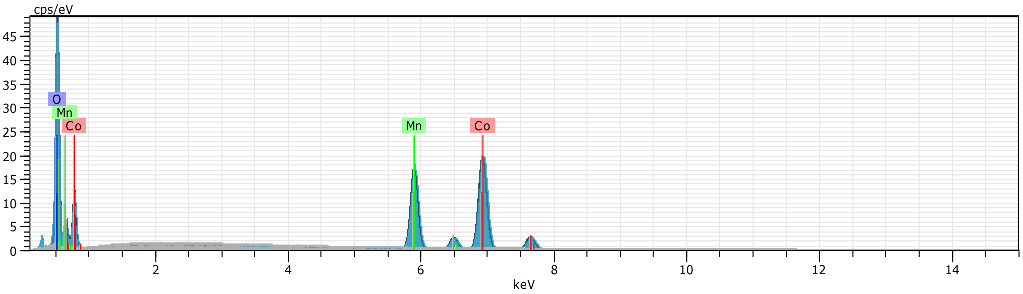

Figure 2.6. Representative EDXS composition analyses of $CoMn_2O_4$ (top) and Co_2MnO_4 (bottom).

2.3.2 Interaction between photosensitizer and $Co_xMn_{3-x}O_4$

The interaction between the spinel WOCs and the $[Ru(bpy)_3]Cl_2$ photosensitizer (PS) was investigated in terms of UV/vis spectroscopy (Figure 2.7). Absorption was recorded in the 350 - 700 nm range for identical WOC concentrations suspended in PS solution. The overlapping peaks in the 400 - 475 nm range arise from the MLCT absorptions of the PS. Generally, the absorption intensities of PS-WOC combinations are stronger than for pristine PS. This can be explained in terms of electron transfer between oxides and PS which may reduce the lifetime of activated $[Ru(bpy)_3]^{2+*}$ and increase the concentration ratio between excited and ground state.

Preceding studies of *Kajiwara* et al. provided first insight into the interaction between $[Ru(bpy)_3]Cl_2$ and various oxides (TiO_2, $SrTiO_3$, ZrO_2, SiO_2) in comparison with methyl viologen. The latter exhibits the fastest quenching rate of $[Ru(bpy)_3]^{2+*}$ among the series due to rapid electron transfer with the activated PS, whilst SiO_2 displayed the lowest performance.[32] These results indicate that faster electron transfer processes lead to a more efficient quenching of the excited PS state. Given that our observed intensity sequence is $Co_3O_4 > Mn_3O_4 > Co_2MnO_4 > CoMn_2O_4$ (Figure 2.6), we propose that the according electron transfer efficiencies follow the same trend.

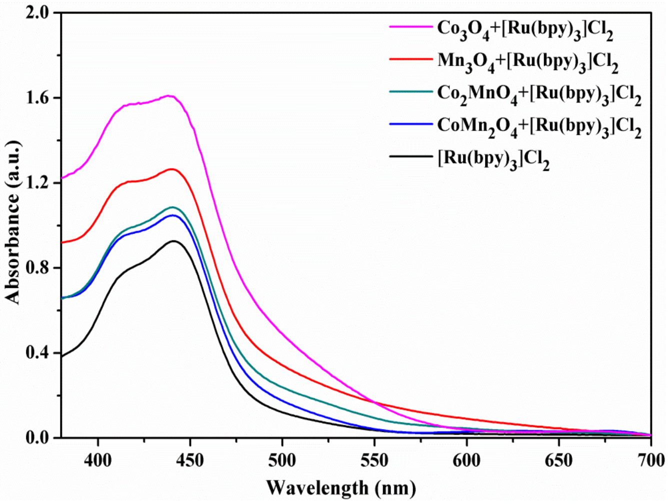

Figure 2.7. UV/Vis spectra of [Ru(bpy)$_3$]Cl_2 (PS) and of various WOC-PS combinations.

2.3.2 Photochemical water oxidation with $Co_xMn_{3-x}O_4$

WOC performance test results are summarized in Figure 2.8 for all four spinel catalysts under identical conditions. Generally, oxygen evolution reaches a maximum after ca. 30 min and then remains constant at this level, i.e. at 9.67, 10.56, 13.04 and 16.58 μmol for Mn_3O_4, $CoMn_2O_4$, Co_2MnO_4 and Co_3O_4, respectively. This performance trend is strongly correlated to the observed BET surface areas and particle sizes (Table 2.2). At first glance, the different WOC activities might thus be primarily explained in terms of increasing number of active surface sites. However, note that this relationship is not proportionally reflected in Figure 2.8: the BET surface area of Co_2MnO_4, for example, is twice as high as that of Mn_3O_4, but the corresponding O_2 evolution ratio is not 2:1, so that oxygen evolution data were normalized to the BET surface area (Table 2.3). However, Co/Mn spinel WOC performance is not solely a function of surface area but a multi-parameter phenomenon encompassing the influence of crystal structure, oxidation states, surface composition, preparative history etc. Interestingly, the high symmetry cubic WOCs Co_2MnO_4 and Co_3O_4 are more active than the tetragonally distorted spinels Mn_3O_4 and $CoMn_2O_4$. Furthermore, the cubane-like units of Mn_3O_4 and $CoMn_2O_4$ are mainly consisting of MnO_6 octahedra, whereas the respective building blocks of Co_2MnO_4 and Co_3O_4 are CoO_6 octahedra (cf. Raman spectra in Figure 2.2). These differences in the key catalytic cubane moieties may partially account for the observed variations in WOC activities. The influence of crystal structure and composition on water oxidation catalysis is also evident from a study on related electrocatalysts: Co_3O_4-graphene composites exhibit higher electrocatalytic activity water oxidation than Co_2MnO_4-graphene and $CoMn_2O_4$-graphene, although their composite morphologies are closely related.[18] Another crucial parameter is the interaction between oxide surface and H_2O molecules which are more pronounced for the Co-rich oxide WOCs (cf. also Figure 2.4). Electron transfer efficiency between spinel oxides and PS does not seem to be the final bottleneck for WOC efficiency, because Mn_3O_4 exhibits lower catalytic activity (Figure 2.8) despite better electron transfer properties than recorded for $CoMn_2O_4$ and Co_2MnO_4 (Figure 2.7).

Table 2.3. Oxygen evolution rate of $Co_xMn_{3-x}O_4$ (x = 0, 1, 2, 3) spinel series.

Catalysts	**Oxygen evolution rate (μmol s^{-1})**	**Oxygen evolution rate normalized to BET surface (μmol s^{-1} g m^{-2})**
Mn_3O_4	5.29×10^{-3}	1.26×10^{-4}
$CoMn_2O_4$	5.76×10^{-3}	1.20×10^{-4}
Co_2MnO_4	7.22×10^{-3}	8.35×10^{-5}
Co_3O_4	9.11×10^{-3}	9.05×10^{-5}

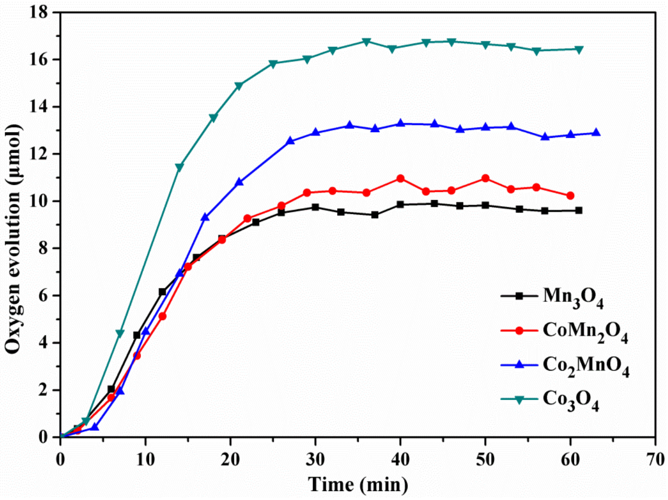

Figure 2.8. Visible-light-driven WOC performance of $Co_xMn_{3-x}O_4$ (x = 0, 1, 2, 3) spinels oxides.

2.4 Conclusions

Phase pure and nanostructured $Co_xMn_{3-x}O_4$ (x = 0, 1, 2, 3) spinel oxides were obtained from acetate precursors via a conventional hydrothermal route, and they were investigated as visible-light-driven water oxidation catalysts. Their water oxidation activity in the presence of $[Ru(bpy)_3]Cl_2$ photosensitizer followed the trend $Co_3O_4 > Co_2MnO_4 > CoMn_2O_4 > Mn_3O_4$. The overall water oxidation performance is a complex interplay of manifold parameters. Under the present experimental conditions, we provide three hypotheses to account for the above catalytic activity order. First, the hydrothermally obtained Co-rich spinel oxides exhibit smaller particle sizes as a favorable prerequisite for water oxidation. Second, structural factors contribute to the oxygen evolution efficiency: the cubic compounds Co_2MnO_4 and Co_3O_4 showed higher WOC activity than the tetragonally distorted Mn-rich spinels $CoMn_2O_4$ and Mn_3O_4. These compositional differences may also affect the efficiency of the crucial cubane-related structural motif which is widely accepted as catalytic center. Finally, higher Co contents promote the interaction of the spinel surface with H_2O which might accelerate the reaction kinetics. All in all, WOC efficiency of Co/Mn-spinels is a challenging multi-parameter problem, and the coordination of structural with surface tuning strategies opens up new perspectives for nanoscale spinel optimization on the way to low-cost WOCs.

References

[1] M. M. Najafpour, T. Ehrenberg, M. Wiechen, and P. Kurz. *Angew. Chem. Int. Ed.* **2010**, *49*, 2233-2237.

[2] R. Brimblecombe, G. F. Swiegers, G. C. Dismukes, L. Spiccia. *Angew. Chem. Int. Ed.* **2008**, *47*, 7335-7338.

[3] J. G. McAlpin, T. A. Stich, C. A. Ohlin, Y. Surendranath, D. G. Nocera, W. H. Casey, R. D. Britt. *J. Am. Chem. Soc.* **2011**, *133*, 15444-15452.

[4] R. Brimblecombe, A. Koo, G. C. Dismukes, G. F. Swiegers, L. Spiccia. *J. Am. Chem. Soc.* **2010**, *132*, 2892-2894.

[5] D. M. Robinson, Y. B. Go, M. Greenblatt, G. C. Dismukes. *J. Am. Chem. Soc.* **2010**, *132*, 11467-11469.

[6] N. S. McCool, D. M. Robinson, J. E. Sheats, G. C. Dismukes. *J. Am. Chem. Soc.* **2011**, *133*, 11446-11449.

[7] M. W. Kanan, D. G. Nocera. *Science* **2008**, *321*, 1072-1075.

[8] G. F. Swiegers, J. K., R. Stranger. *Chem. Sci.* **2011**, *2*, 2254-2262.

[9] G. F. Swiegers, D. R. MacFarlane, D. L. Officer, A. Ballantyne, D. Boskovic, J. Chen, G. C. Dismukes. *Aust. J. Chem.* **2012**, *65*, 577-582.

[10] F. Jiao, H. Frei. *Angew. Chem. Int. Ed.* **2009**, *48*, 1841-1844.

[11] F. Jiao, H. Frei. *Energy Environ. Sci.* **2010**, 3, 1018-1027 .

[12] M.R. Gao, Y.F. Xu, J. Jiang, Y. R. Zheng, S. H. Yu. *J. Am. Chem. Soc.* **2012**, *134*, 2930-2933.

[13] D. Barreca, P. Fornasiero, A. Gasparotto, V. Gombac, C. Maccato, A. Pozza, E. Tondello. *Chem. Vap. Deposition* **2010**, *16*, 296-300.

[14] A. Gasparotto, D. Barreca, D. Bekermann, A. Devi, R. A. Fischer, P. Fornasiero, V. Gombac, O. I. Lebedev, C. Maccato, T. Montini, G. V. Tendeloo, E. Tondello. *J. Am. Chem. Soc.* **2011**, *133*, 19362-19365.

[15] F. Conrad, M. Bauer, D. Sheptyakov, S. Weyeneth, D. Jaeger, K. Hametner, P.-E. Car, J. Patscheider, G. R. Patzke. *RSC Advances,* **2012**, 2, 3076-3082.

[16] X. Wang, Q. Xu, M. Li, S. Shen, X. Wang, Y. Wang, Z. Feng, J. Shi, H. Han, and C. Li. *Angew. Chem. Int. Ed*. **1012**, *51*, 13089-13092.

[17] F. Cheng, J. Shen, B. Peng, Y. Pan, Z. Tao, J. Chen. *Nature Chem.* **2012**, *3*, 78-84.

[18] Y. Liang, H. Wang, J. Zhou, Y. Li, J. Wang, T. Regier, H. Dai. *J. Am. Chem. Soc.* **2012**, *134*, 3517-3523**.**

[19] P. L. Meena, R. Kumar, C.L. Prajapat, K. Sreenivas, V. Gupta. *J. Appl. Phys.*, **2009**, *106*, 024105.

[20] Q. Liang, K.D. Chen, W. H. Hou, Q. J. Yan. *Appl. Catal. A: Gen.* **1998**, *166*, 191-199.

[21] V. G. Hadjievl, M. N. Ilievl, I. V. Vergilov. *J. Phys. C: Solid State Phys.* **1988**, *21*, 199-201.

[22] G. Marban, T.V. Solis, A. B. Fuertes. *Phys. Chem. Chem. Phys.* **2004**, *6*, 453-464.

[23] F. Kovandaa, T. Rojkaa, J. Dobesova, V. Machovic, P. Bezdicka, L. Obalova, K. Jiratova, T. Grugar. *J. Solid State Chem.* **2006**, *179*, 812-823.

[24] H. Bordeneuve, C. Tenailleau, S. Guillemet-Fritsch, R. Smith, E. Suard, A. Rousset. *Solid State Sciences* **2010**, *12*, 379-386.

[25] V. Devadoss, M. Noel, K. Jayaraman, C. A. Basha. *J. Appl. Electrochem.* **2003**, *33*, 319-323.

[26] Q. Liang, K. Chen, W. Hou, Q. Yan. *Appl. Catal. A: Gen.* **1998**, *166*, 191-199.

[27] Z.-Y. Tian, P. H. T. Ngamou, V. Vannier, K. Kohse-Höinghaus, N. Bahlawane. *Appl. Catal. B: Environ.* **2012**, *117-118*, 125-134.

[28] F. Poignant, J. Saussey, J.-C. Lavalley, G. Mabilon. *Catal. Today* **1996**, *29*, 93-97.

[29] J. Jansson*,* A. E. C. Palmqvist, E. Fridell, M. Skoglundh, L. Osterlund, P. Thormahlen, V. Langer. *J. Catal.* **2002***, 211*, 387-397.

[30] F. Al-Mashta, N. Sheppard, V. Lorenzelli, G. Busca. *J. Chem. Soc., Faraday Trans.* **1982**, *78*, 979-989.

[31] M. Wang, L. Zeng, Q. Chen. *Dalton Trans.* **2011**, *40*, 597-601.

[32] T. Kajiwara, K. Hasimoto, T. Kawai, T. Sakata. *J. Phys. Chem.* **1982**, *86*, 4516-4522.

3. Visible-Light-Driven Water Oxidation with Nanoscale Co_3O_4

3.1. Introduction

Whereas spinel-type Co_3O_4 has emerged as a highly promising WOC candidate for large-scale and advanced applications,[1-3] simultaneous performance optimization of the mixed valent spinel matrix along with its surface and morphological features remains a major challenge. In this study, we shed new light on "top down" calcination and "bottom up" hydrothermal strategies to achieve straightforward control over the manifold interdependent design parameters for Co_3O_4-WOCs.

Generally, the complex process of photochemical water oxidation in WOC-photosensitizer systems is influenced by numerous parameters, and their individual impact on the WOC performance remains difficult to assess.[4] To the best of our knowledge, the individual mechanistic steps of the four-electron-transfer process remain to be fully elucidated for oxide-based heterogeneous WOCs. More detailed insight would render targeted optimization of photocatalysts far less empirical and difficult.[5] To date, a wide range of studies illustrates the effect of rather diverse factors, such as crystal structure,[6-9] morphology,[10,11] composition,[12-15] valence state,[16-19] crystallinity,[20, 21] and even the buffer medium[22-26] on water oxidation processes. Nevertheless, each new WOC system still requires an individual re-assignment of these synthetic and operational parameters to acquire optimal oxygen evolution rates.

Spinel-type Co_3O_4-WOCs have emerged as a particularly worthwhile target for in-depth studies and for development of composite materials due to their combination of low-cost production options, high efficiency and structural tunability.[27-29] However, further performance optimization is required to turn them into an economic alternative to noble metal-based WOCs (preferably IrO_2 and RuO_2) for commercial applications.

Generally, the structural flexibility of spinel-type oxides is an asset for the tuning of site occupancies, oxidation states and dopant contents toward higher catalytic activity.[30-35] On the other hand, the comprehensive surface, structural and morphological characterization of a given spinel-based material quickly turns into a demanding task that requires numerous complementary analytical techniques, especially for complex and mixed valent compounds. UV/Vis spectroscopic analyses, for example, impressively demonstrate the divergence of structural characteristics as a function of the applied synthetic parameters in spinel preparation.[36-38]

This challenge is reflected in numerous studies on catalytic performance improvement of Co_3O_4, which currently place special emphasis on morphology and surface area as key tuning parameters.[39-41] In a representative investigation on nanostructured cobalt oxide clusters, *Frei* et al. discovered that water oxidation activity was notably enhanced through supporting on mesoporous silica.[42, 43] *Schmuki* et al. prepared a highly active porous cobalt oxide WOC by self-organized electrochemical anodization of Co metal foil and subsequent heat treatment.[44] Implementing a related strategy toward maximum surface areas, *Feng* et al. synthesized efficient Mg-doped mesoporous Co_3O_4-WOCs through leaching of silica from silica-Co_3O_4 nanocomposite precursors. Removal of the Mg dopant further increased the catalyst porosity and enhanced the water oxidation performance.[45] Moreover, the productive influence of reduced particle sized on the water oxidation activity of Co_3O_4 was illustrated in a systematic study by *Grzelczak* et al.[46] Most recently, a highly efficient cobalt oxide WOC with particle sizes below 5 nm was prepared by pulsed laser ablation in liquid media,[47] and very small cobalt domains displayed high WOC activity on mesoporous silica surfaces.[48] Furthermore, development of Co-based catalysts for electrochemical water oxidation with Co-Pi as the most prominent representative[49] brought forward amorphous features as a complementary design criterion.[50-52]

All in all, the most widely accepted synthetic paradigm for Co_3O_4-WOC development is the straightforward relationship between high catalytic activity and high surface area to maximize the number of accessible catalytic sites. However, the limited insight into the complex overall process of water oxidation calls for the precise investigation and assessment of other significant factors for WOC development. In particular, this entails (a) the effect of synthetic protocols on surface/bulk valence states, defect types/concentrations, structural order and overall morphology/crystallinity and (b) their respective influence on the efficiency of charge transfer between WOCs and photosensitizer as well as on the subsequent oxygen evolution steps.

In the following, we illustrate the key role of the preparative history in the photocatalytic performance of hydrothermally synthesized nanoscale Co_3O_4-WOCs. "Bottom up" chemical treatment or "top down" post-synthetic modification strategies were identified as convenient alternatives to surface maximization for facile Co_3O_4-WOC production.

3.2 Experimental

3.2.1 Synthetic methods

Co_3O_4 nanoparticles were accessed with conventional hydrothermal strategies. All chemicals were purchased from Sigma Aldrich in AR grade. Representative syntheses were conducted as follows: 3 mmol cobalt(II) acetate tetrahydrate were dissolved in 2.5 mL deionized water and 0.5 mL 25 wt% $NH_3{\cdot}H_2O$ was added to the solution which was stirred for 2 h. After ageing for 2 h, 7.5 mL ethanol (high purity) were added to the reaction mixture which was then transferred to a 15 mL autoclave and kept at 140 ^oC for the given reaction time. Products were isolated by centrifugation, washed three times with acetone and dried at 80 ^oC in air. A slightly modified protocol was applied for the synthesis of Co_3O_4_20h_H_2O_2 by replacing 2.5 mL deionized water with a mixture of 2 mL deionized water and 0.5 mL 30 wt% H_2O_2.

3.2.2 Photocatalytic tests

Water oxidation activity was evaluated according to standard $[Ru(bpy)_3]^{2+}/S_2O_8^{2-}$ protocols.[31] First, a suspension was prepared by mixing 24.08 mg (0.1 mM) oxide photocatalyst, 16.17 mg $[Ru(bpy)_3]Cl_2$ photosensitizer and 25.67 mg NaS_2O_8 in 20 mL Na_2SiF_6 buffer (20 mmol/L Na_2SiF_6, pH 6) in a dark cabinet. The suspension was then degassed with helium to remove O_2 in both solution and in the head vial. A 300 W Xe lamp (LOT Oriel) in line with a cut-off filter ($\lambda > 400$ nm) was used as visible light source. The light intensity was kept constant at 200,000 Lux through regular calibration with a photometer. After specific time intervals, 100 μL samples of gas from the head vial were injected into a gas chromatograph (Varian CP-3800, equipped with He as carrier gas and a 3 m × 2 mm column packed with molecular sieve 13X 80-100) by a gas tight microliter syringe (Hamilton 1825 RN).

3.2.3 Post-synthetic treatment

Calcination was performed in a muffle furnace under ambient conditions. Samples were heated at a rate of 8 K/min to 350 ^oC and held for 20 h, followed by slow cooling to room temperature. Calcination under oxygen atmosphere was performed in a NETZSCH TG equipped with a 10 mL corundum crucible. The oxygen flux was adjusted to 50 mL/min. Samples were heated to 300 ^oC at a rate of 50 K/min and held for 20 min, followed by equilibration to room temperature. Reduction in argon atmosphere was performed with an analogous protocol (TG with Ar flux of 50 mL/min). Samples were heated to 400 ^{o}C at a rate of 15 K/min and then slowly cooled to room temperature.

3.2.4 Analytical techniques

Powder X-ray diffraction patterns (PXRD patterns) were recorded on a STOE STADI P diffractometer (transmission mode, Ge monochromator) with Co $K_{\alpha1}$ radiation. Rietveld refinement was performed with the GSAS software package vs. ICSD-28158 as ideal spinel model data set for Co_3O_4. Scale factor, zero point, cell parameters, isotropic thermal factors, atomic displacement, site occupancies and background were refined stepwise. Sample morphologies were examined by scanning electron microscopy (SEM, LEO 1530 (FEG)) and high resolution transmission electron microscopy (HRTEM, FEI Tecnai F30 FEG (300 kV)). Brunauer-Emmett-Teller (BET) surface area measurements were conducted on a Quadrasorb SI machine in N_2-adsorption mode. Samples were degassed at 150 °C for 24 h under vacuum prior to the measurements. Raman spectra were recorded on a Renishaw Ramascope spectrometer at 514 nm laser excitation. UV/Vis spectra were recorded on a Lambda 650 S Perkin Elmer UV-visible spectrometer. XPS spectra were measured on a PHI Quantum 2000 microprobe spectrometer from Physical Electronics Inc. The measurements were taken with a monochromatic Al K_{α} source without any preceding sputter cleaning or other procedures that might alter the surface of the crystals. The C 1s peak at 284.6 eV was set as a reference for all XPS peak positions. Spectra were fitted with the XPSPEAK software package. EPR spectra were recorded at ambient temperature with a Bruker Elexsys 500 spectrometer equipped with a Super-High-Q resonator ER 4122 SHQ. At a frequency of about 9.875 GHz five scans with a magnetic field range from 0.2 to 900.2 mT were accumulated with 8192 data points each (time constant 5.12 ms, conversion time 20.48 ms), microwave attenuation of 15 dB (6.36 mW), and a field modulation amplitude of 0.5 mT at 100 kHz modulation frequency. A spectrum acquired under the same conditions on an empty sample tube was subtracted and the spectra were baseline-corrected with a second order polynomial function. To obtain the relative spin count, the spectra were integrated twice, with another second-order polynomial baseline correction after the first integration. In addition, identical amounts (13.3 mg) of samples were used for the EPR tests to ensure a proper comparison of spin counts between different samples. Luminescence decay dynamics were measured at room temperature on a LP920 spectrometer from Edinburgh Instruments Ltd. Samples were prepared as follows: 5 mg WOC was dispersed in 10 mL 0.5 mM

$[Ru(bpy)_3]Cl_2$ solution and the resulting suspension was sonicated in an ultrasound bath for 5 min and kept in the dark for 1 h to establish adsorption equilibrium. Next, the suspensions were centrifuged at 5000 rpm for 5 min to obtain stable supernatants for transient luminescence experiments without oxygen degassing to simulate actual water oxidation conditions. The excitation wavelength was fixed to the most intense absorption of $[Ru(bpy)_3]Cl_2$ at 465 nm.

3.3 Results and discussion

3.3.1. Straightforward WOC tuning strategies

Nanoscale Co_3O_4 water oxidation catalysts (WOCs) were obtained by hydrothermal treatment of $Co(OAc)_2{\cdot}4H_2O$ precursors in ethanol-water media. Visible-light-driven water oxidation activity was evaluated with a standard protocol using $[Ru(bpy)_3]^{2+}$ as photosensitizer and $S_2O_8^{2-}$ as electron acceptor (for synthetic and catalytic details cf. Experimental and Figures 3.1-3.2). All PXRD patterns of Co_3O_4-WOCs are in good agreement with literature data (JCPDS 71-0816), thus confirming the formation of phase pure cubic spinels (Figure 3.3, cf. also analytical section below). BET surface and WOC activities of Co_3O_4 samples obtained after different hydrothermal treatment times (Co_3O_4_20h, Co_3O_4_35h and Co_3O_4_50h) are compared in Figure 3.1. As expected, BET surface areas decreased with prolonged hydrothermal treatment and the relatively large surface of Co_3O_4_20h, for example, was reduced from ca. 100 to 64 m^2/g upon extending the hydrothermal treatment interval to 50 h. Counterintuitively, prolonged hydrothermal treatment times led to increased catalytic activity, so that reduction of the surface area by approx. one third of the original value went hand in hand with a 1.7-fold enhanced oxygen evolution rate for Co_3O_4_50 h (Figure 3.1).

Table 3.1. Comparison of BET surface, particle size and turnover frequency (TOF) for Co_3O_4-WOCs.

WOC	**Surface area/ $m^2\,g^{-1}$**	**Particle size/nm**	**TOF (O_2)/ µmol $s^{-1}\,g\,m^{-2}$**
Co_3O_4_20h	100	~5-15	3.5×10^{-3}
Co_3O_4_35h	69	~10-25	7.4×10^{-3}
Co_3O_4_50h	64	~20-50	9.6×10^{-3}
Co_3O_4_20h_H_2O_2	74	~10-30	1.0×10^{-2}
Co_3O_4_20h_calc	25	up to 200	2.1×10^{-2}

SEM investigations (Figure 3.2) showed that the particle size of Co_3O_4-WOCs significantly increased with hydrothermal treatment time, in line with their continuously decreasing BET surface areas. The productive effect of extended hydrothermal treatment is even more evident from normalized O_2 evolution rates (cf. turnover frequency (TOF) values in Table 3.1). Although extending the reaction time from 20 h to 35 h led to an approx. 30% reduction of surface area, the TOF of Co_3O_4_35h is twice as high as observed for Co_3O_4_20h (Table 3.1). An additional 15 h treatment interval did not significantly affect the surface area, but further increased the TOF of Co_3O_4_50 h by ca. 20% in comparison with Co_3O_4_35h.

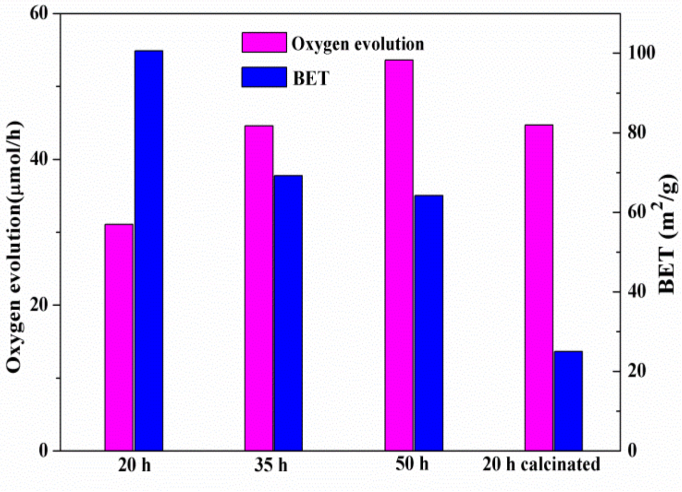

Figure 3.1. Oxygen evolution rate (pink columns) vs. BET surface (blue columns) of Co_3O_4 WOCs after different (hydro)thermal treatment intervals.

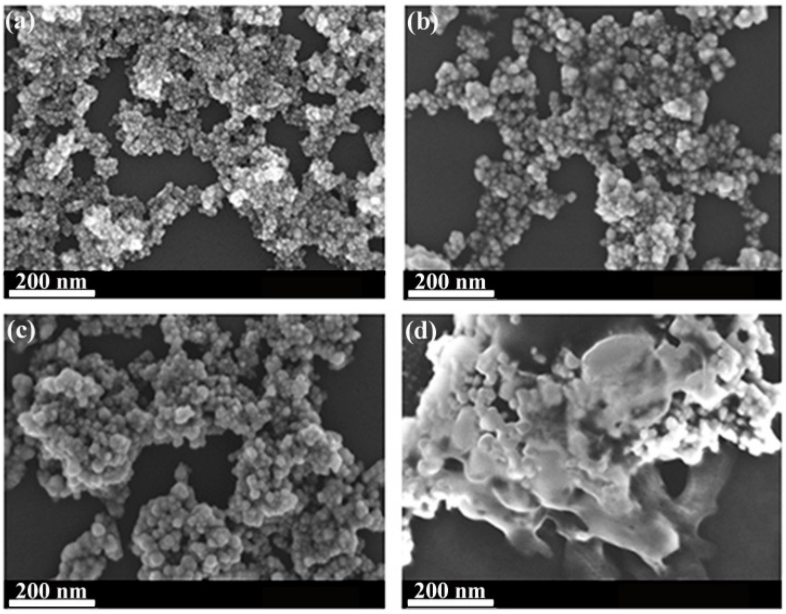

Figure 3.2. Representative SEM images of Co_3O_4-WOCs after different (hydro)-thermal treatment programs: (a) Co_3O_4_20h, (b) Co_3O_4_35h, (c) Co_3O_4_50h, (d) Co_3O_4_20h_cal.

The most drastic improvement of catalytic activity is achieved through thermal post-synthetic treatment of Co_3O_4_20h: calcination for 20 h in air at 350 °C reduced the BET surface to a quarter (25 m^2g^{-1}) of the initial 100 m^2g^{-1}, whereas the TOF of sample Co_3O_4_20h_cal underwent a six-fold increase (Table 3.1).

Next, we examined the influence of surface modifications on the Co_3O_4-WOC performance by subsequent treatment of Co_3O_4_20h_cal at 300 °C in pure O_2 atmosphere for 20 min in order to reduce the possible influence of surface-associated defects, amorphous layers and related effects. Figure S3.2 shows that the effect of short oxidative post-synthetic annealing on the WOC performance is almost negligible. Next, Co_3O_4_20h_H_2O_2 (discussed in the following section) was treated in Ar atmosphere under mild reductive conditions, and a slight weight loss pointing to oxygen release was observed in the thermogravimetric curve above 300 °C (Figure S3.5). As can be seen in Figure S3.6, water oxidation activity after post-synthetic treatment in Ar was reduced by a factor of ca. 1/3 compared to the untreated sample (Figures S3.6). This underscores the efficiency of subsequent bulk annealing in air as a convenient "top down" optimization approach.

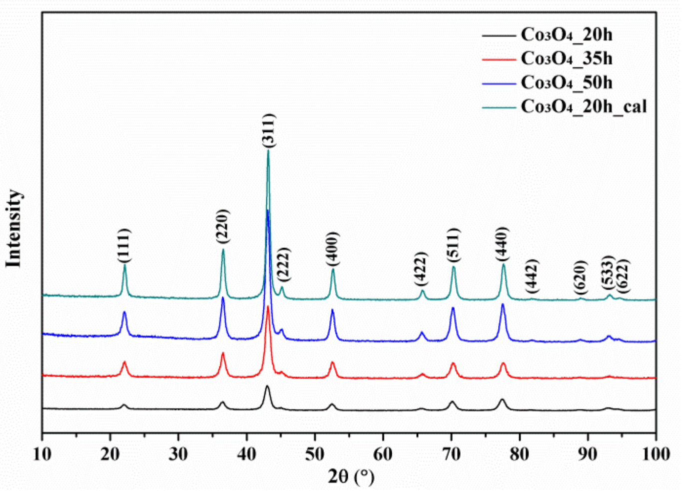

Figure 3.3. PXRD patterns of Co_3O_4-WOCs after different (hydro)thermal treatments.

In the following step, the influence of "bottom up" chemical oxidation during hydrothermal treatment on the water oxidation activity of Co_3O_4-WOCs was investigated. Addition of H_2O_2 to the applied hydrothermal protocol (details cf. Experimental) affords phase pure spinel samples (Figure 3.4). Compared to short oxidative post-synthetic annealing in O_2 atmosphere (Figure S3.2), the presence of H_2O_2 during hydrothermal synthesis notably enhanced the O_2 evolution rate (cf. Figure 3.5 and normalized O_2 evolution rates in Table 3.1). The TOF of Co_3O_4_20h_H_2O_2 is 2.8 times as high as that of Co_3O_4_20h despite identical hydrothermal synthesis times. However, extension of hydrothermal treatment to 50 h in the presence of H_2O_2 did not lead to further improvement of WOC performance (cf. Figure S3.3).

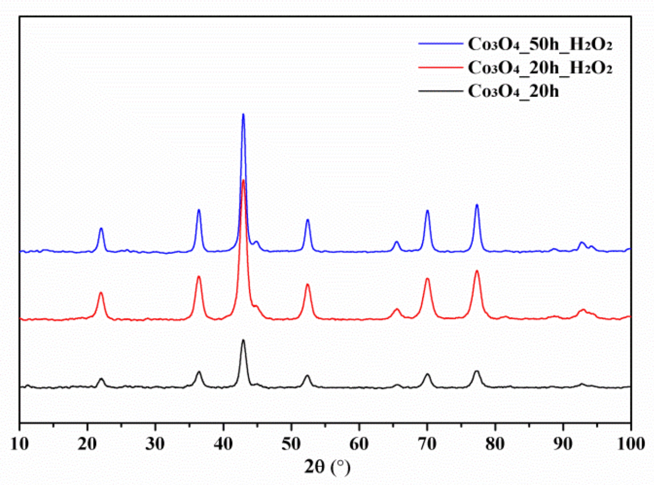

Figure 3.4. PXRD patterns of Co_3O_4-WOCs synthesized hydrothermally in the presence or absence of H_2O_2.

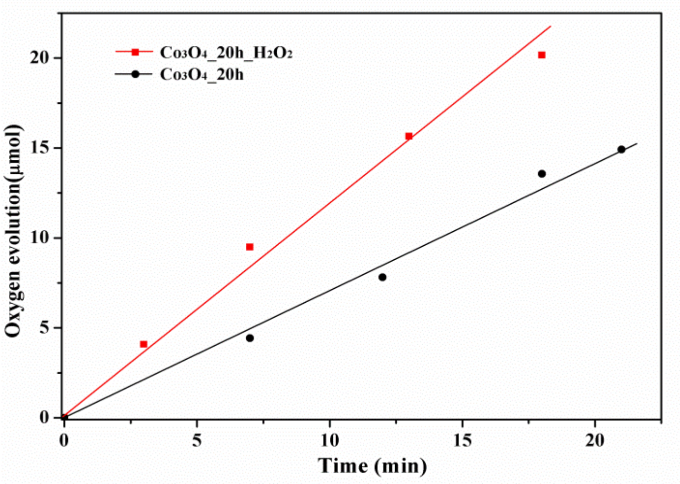

Figure 3.5. Water oxidation activity of Co_3O_4-WOCs hydrothermally synthesized in the presence or absence of H_2O_2.

3.3.2. Characterization and structure-activity relationships of Co_3O_4 WOCs

TEM images of Co_3O_4 WOCs synthesized in the presence or absence of H_2O_2 are compared in Figure 3.6. Both samples clearly display the (110) or (220) lattice planes of Co_3O_4, and the respective SAED images are well in line with PXRD patterns. The presence of H_2O_2 leads to a size increase of the cubic Co_3O_4 particles from 5-15 nm (Co_3O_4_20h, Figure 3.6a) to 10~30 nm (Co_3O_4_20h_H_2O_2, Figure 3.6b), in line with the observed reduction of BET surface area by ca. 25% (Table 3.1). HRTEM investigations of pristine Co_3O_4_20h and Co_3O_4_20h_H_2O_2 (cf. Figure S3.10) did not point to significant amounts of amorphous phases, so that the lower crystallinity of Co_3O_4_20h is probably due to growth defects, such as vacancies or dislocations of cobalt ions. This hypothesis agrees well with Raman and UV/Vis spectroscopic investigations (cf. Figures 3.8-3.9 and discussion below).

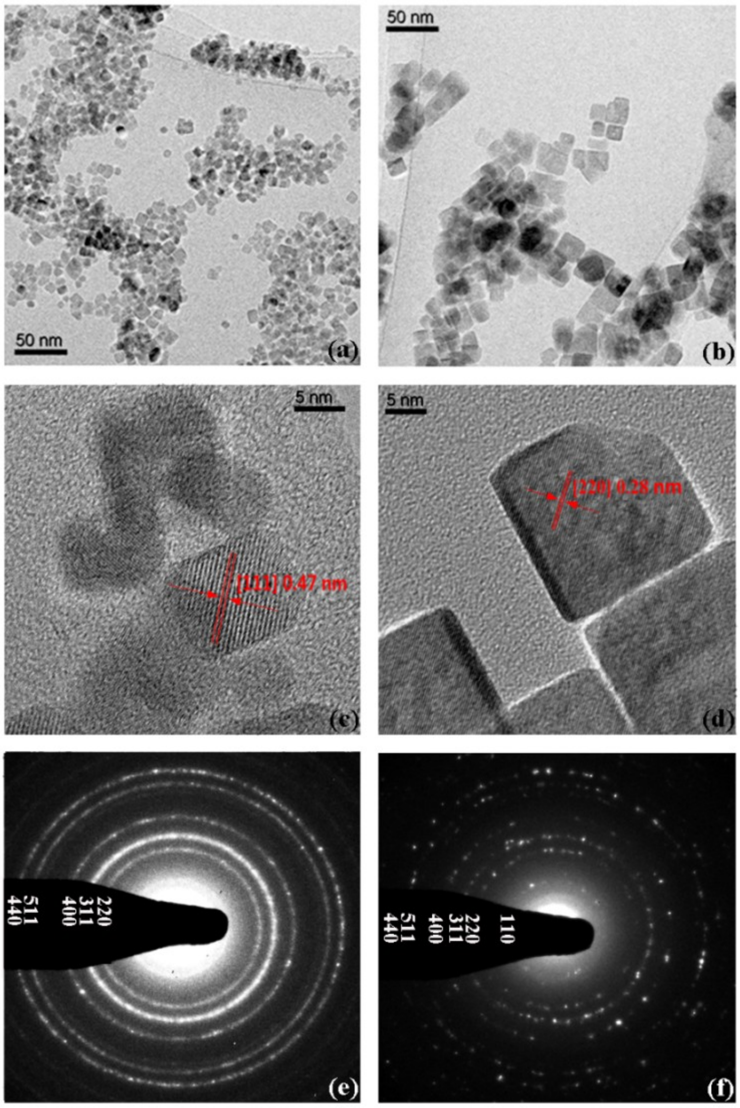

Figure 3.6. Representative HRTEM images and SEAD patterns of Co_3O_4_20h (left column) and Co_3O_4_20h_H_2O_2 (right column).

Generally, as-synthesized Co_3O_4 samples cover a wide spectrum of structural arrangements between two end members, i.e. the ideal $[Co^{II}]_{8a}[Co^{III}_2]_{16d}[O_4]_{32e}$ spinel structure with Co^{2+} occupying one-eighth of the available tetrahedral sites and Co^{3+} located at half of the octahedral positions on the one hand, and the fully inverted $[Co^{III}]_{8a}[Co^{III}Co^{II}]_{16d}[O_4]_{32e}$

arrangement on the other hand.[30] Moreover, dislocation of Co^{2+} or Co^{3+} from the original tetrahedral (8a) or octahedral (16d) positions to other available tetrahedral (8b, 48f) and octahedral (16c) interstitial sites has been frequently observed.[53, 54] Rietveld refinement trends among PXRD patterns vs. ideal spinel model data for Co_3O_4 (ICSD-28158) show that an increase of the peak intensity in combination with sharper profiles (Figure 3.7 and Figure S3.11) goes hand in hand with decreasing lattice constants (Table 3.2). The trend towards smaller lattice constants after extended hydrothermal or post-synthetic thermal treatment points to a complex interplay of various structural changes, such as redistribution of Co^{2+}/Co^{3+} ions over different sites and decreasing numbers of cobalt and oxygen vacancies (Table 3.2). Comparison of Co_3O_4_20h_cal and Co_3O_4_20h reveals an increase of the (111)/(440) peak ratios after calcination, which points to a higher occupancy of the tetrahedral 8a site. Furthermore, the presence of ions on interstitial sites and redox processes may alter the lattice constants as well due to the different effective ionic radii of Co^{2+} and Co^{3+}.[55]

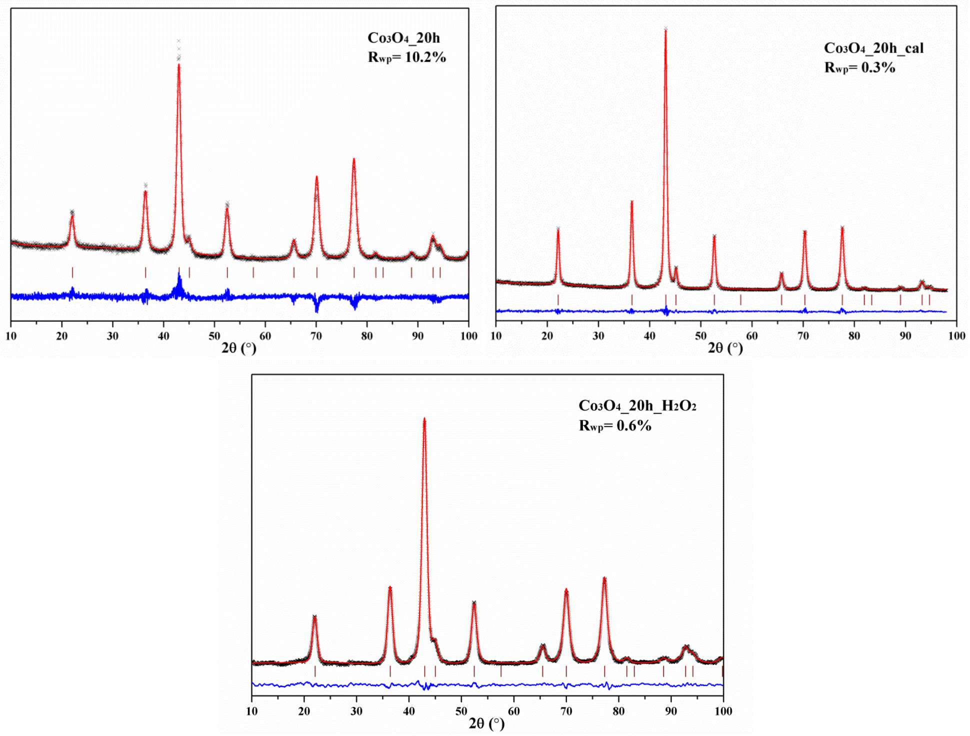

Figure 3.7. Rietveld refinement for samples Co_3O_4_20h, Co_3O_4_20h_cal and Co_3O_4_20h_H_2O_2.

Whereas Rietveld refinement of PXRD patterns recorded on samples Co_3O_4_20h_cal and Co_3O_4_20h_H_2O_2 led to agreeable fitting results, the R_{wp} value for Co_3O_4_20h was notably higher, thus pointing to major deviations from the ideal spinel model. Samples which were subjected to chemical oxidation or post-synthetic thermal treatment show a clear trend toward higher Co site occupancies (Table 3.2). Unfortunately, neither X-ray or neutron diffraction methods permit a distintion between Co^{2+} and Co^{3+} due to their similar scattering factors, which renders the calculation of Co^{2+}/Co^{3+} ratios from Co-O bond lengths rather inaccurate.[56] Consequently, elucidating the interplay between local crystallinity, bulk defects and particle size requires a spectrum of complementary analytical methods.

Table 3.2. Comparison of Rietveld refinement results for different Co_3O_4-WOCs vs. Co_3O_4 reference with ideal spinel structure (ICSD-28518).

WOC	**8a(Co) occ.**	**16d (Co) occ.**	**32e (O) occ.**	**a/Å**
Co_3O_4_20h	0.77(4)	0.78(7)	0.89(3)	8.137(6)
Co_3O_4_35h	0.87(5)	0.94(2)	1.00(4)	8.088(4)
Co_3O_4_50h	0.91(4)	0.96(7)	1.00(5)	8.061(2)
Co_3O_4_20h_ H_2O_2	0.95(1)	0.98(3)	0.99(1)	8.054(4)
Co_3O_4_20h_cal	0.96(2)	1.00(6)	1.00(3)	7.918(1)
Co_3O_4 (ICSD-28518)	1.00	1.00	1.00	8.084

The influence of H_2O_2 treatment on the bulk crystallinity of Co_3O_4 WOC samples was further analyzed with Raman spectroscopy (Figure 3.8). The bands around 195 cm^{-1}, 480 cm^{-1}, 520 cm^{-1}, 618 cm^{-1} and 690 cm^{-1} agree well with the reported F_{2g}, E_g, $2F_{2g}$, $3F_{2g}$ and A_{1g} phonon modes of Co_3O_4,[57] respectively, thus providing complementary evidence of phase purity in addition to PXRD data. Interestingly, the A_{1g} peak around 690 cm^{-1} (inset of Figure 3.8) exhibited a sharper profile for samples synthesized in the presence of H_2O_2. This is in line with the disappearance of the A_{1g} shoulder after thermal treatment in the spectrum of Co_3O_4_20h_cal compared to pristine Co_3O_4_20h (Figure S3.1). Reduced Co_3O_4_20h_H_2O_2_Ar displayed obvious broadening of the A_{1g} peak (inset of Figure 3.8). The observed correlation between enhanced crystallinity and smaller Raman peak width agrees with recent studies on disordered Co-Mn spinel oxide.[58]

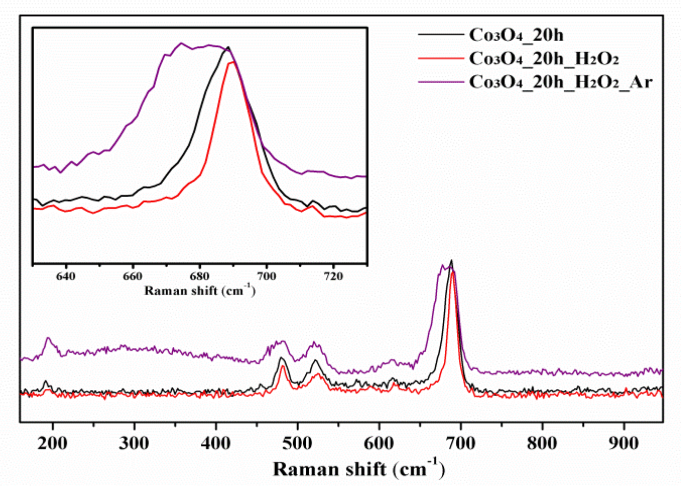

Figure 3.8. Raman spectra comparing the influence of H_2O_2 and post-synthetic treatment on Co_3O_4 WOCs.

UV/Vis spectra of spinel-type Co_3O_4 often vary widely as a function of the preparative parameters and the resulting changes in oxidation states and site occupancies.[59-61] Co_3O_4 samples containing a considerable amount of defects or lattice distortions have been reported to display different absorption characteristics due to a reduction of orbital degeneracy.[62] Recently, *Yang* et al. reported on disordered spinel-type $Co_{1.28}Mn_{1.71}O_4$ as hydrogen evolution photocatalyst which showed a flat absorption band across the whole visible light range, whereas crystalline $CoMn_2O_4$ displayed higher resolution of the individual absorption peaks.[58]

In line with these trends, UV/Vis spectra for the Co_3O_4_20h WOC series (Figure 3.9) display three main peaks in the range from 250 to 800 nm. The peak around 250～325 nm in the UV region arises from O→Co^{2+} charge transfer, and the remaining peaks located in the regions around 350-500 nm and 580-750 nm are attributed to d-d transitions of Co^{3+} in octahedral and Co^{2+} in tetrahedral sites, respectively.[63 - 65] The absorption band of tetrahedrally coordinated Co^{2+} in Co_3O_4_20h is more intense than that of octahedrally coordinated Co^{3+} ions, and there is no clear separation between these two peaks due to various intermediate shoulders (Figure 3.9, black curve). The presence of H_2O_2 during hydrothermal synthesis leads to a more intense Co^{3+} absorption for Co_3O_4_20h_H_2O_2, which is comparable to the Co^{2+} absorption peak (Figure 3.9, red curve). In contrast, reductive post-synthetic treatment of Co_3O_3_20h_H_2O_2_Ar results in a single broad absorption band across the entire visible light range, which does not permit further differentiations between the cobalt valence states, along with a reduced absorption intensity that requires further investigation.

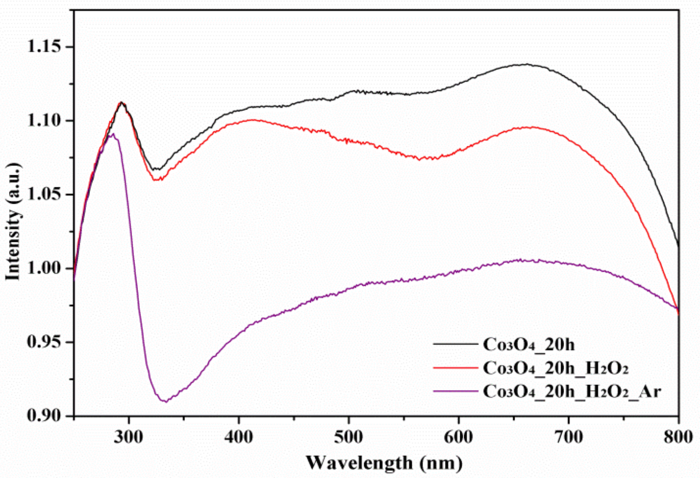

Figure 3.9. UV/Vis spectra comparing the influence of H_2O_2 and post-synthetic treatment on Co_3O_4 WOCs.

Co valence states of Co_3O_4_20h and Co_3O_4_20h_H_2O_2 were compared with X-ray photoelectron emission spectroscopy (XPS), and Co 2p and Co 3p spectra are shown in Figures 3.10 and S3.12. The main peaks at 780 eV and 796 eV arise from the Co $2p_{3/2}$ and Co $2p_{1/2}$ states, respectively, and their corresponding shake up peaks appear at 779.5 eV and 786.5 eV.[66] Generally, paramagnetic Co^{2+} exhibits more intense satellite peaks than Co^{3+}.[67] However, Co 2p spectra of samples synthesized in the presence or absence of H_2O_2 do not display significant differences (cf. Figure S3.12). In contrast, Co 3p spectra of Co_3O_4_20h_H_2O_2 exhibit a significant broadening and peak shift toward higher bonding energy compared to Co_3O_4_20h. Two peaks around 62.5 eV and 59.5 eV in the fitted Co 3p spectra can be assigned to Co^{3+} and Co^{2+}, respectively, and the results clearly demonstrate that the presence of H_2O_2 during hydrothermal synthesis led to a higher Co^{3+}/Co^{2+} ratio in Co_3O_4_20h_H_2O_2 particles (Figure 3.10). This observation agrees with the above-mentioned decreasing intensity of the $O \rightarrow Co^{2+}$ absorption (cf. Figure 3.9 above) and with the EPR signal of samples treated with H_2O_2 (cf. Figure 3.11 below). Given that Co 3p detection is more sensitive toward bulk methods, whereas Co 2p is more responsive to surface analyses,[66] the Co valence distribution of the WOC samples might exhibit a gradient from surface to bulk, probably after exposure to atmospheric moisture and oxygen. However, its quantification would require a detailed analytical study in its own right.

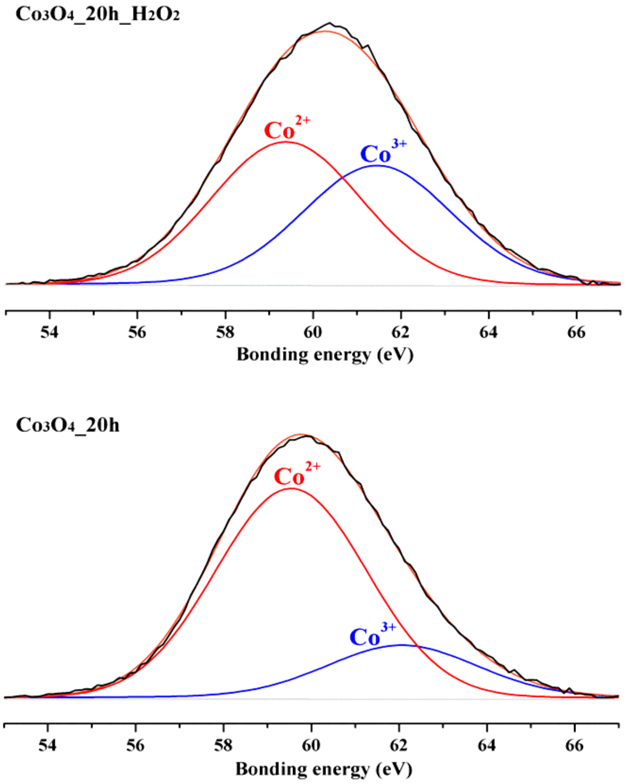

Figure 3.10. Co 3p spectra of Co_3O_4_20h_H_2O_2 (top) and Co_3O_4_20h (bottom).

Electron paramagnetic resonance (EPR) was furthermore employed to investigate the bulk electronic properties (Figure 3.11), and all samples have a characteristic symmetric peak in common that points to the presence of unpaired electrons which were further quantified through integration of the peak areas (Table S3.1). Generally, the unpaired electrons are assigned to 3d t_g orbitals of Co^{2+} ions which preferably occupy tetrahedral sites in the ideal Co_3O_4 spinel lattice, whereas Co^{3+} ions with fully paired electronic configurations are located on the octahedral sites (Co^{2+}: LS $t_{2g}^6e_g^1$, S=1/2 and Co^{3+}: LS: $t_{2g}^6e_g^0$, S=0). Therefore, the EPR signal intensity of a regular Co_3O_4 spinel sample without defects or inversion should be directly proportional to the number of Co^{2+} centers. However, the EPR results for the Co_3O_4 WOC series differ considerably from this ideal scenario of a more or less constant Co^{2+} content around 1/3 (Figure 3.11 and Table S3.1), so that the observed signals should not be solely interpreted on the basis of Co^{2+} concentrations. A recent study on the magnetic properties of nanostructured Co_3O_4 revealed the presence of high spin Co^{3+} (HS Co^{3+}: $t_{2g}^3e_g^3$, S=6/2) in tetrahedral sites due to a lower energy difference between t_g and e_g orbitals for tetrahedral compared to octahedral sites.[54] The presence of HS Co^{3+} centers contributing six unpaired electrons per Co center is a plausible explanation for the considerable variation of unpaired electron numbers among the WOC series. Interestingly, sample Co_3O_4_20h_cal contains a slightly higher amount of unpaired electrons after thermal treatment than pristine Co_3O_4_20h. Co_3O_4_20h_cal probably underwent further oxidation of Co^{2+} to Co^{3+} during post-synthetic calcination in air, and the presence of newly formed paramagnetic HS Co^{3+} centers in tetrahedral environments agrees with the observed higher occupancy of the tetrahedral 8a site. The broader EPR linewidth of Co_3O_4_20h_cal compared to nanoscale Co_3O_4_20h may arise from a stronger interaction between paramagnetic centers due to the redistribution of Co^{2+} from interstitial to regular lattice sites, as suggested by the higher occupancy of the 8a and 16d sites after calcination (Table 3.2).

In contrast, samples Co_3O_4_50h and Co_3O_4_20h_H_2O_2 underwent prolonged oxidation under autogeneous pressure or direct contact with a chemical oxidant under homogeneous solution conditions, so that the newly formed Co^{3+} ions are located on the octahedral 16d positions of the ideal spinel model as expected, where they do not contribute to the paramagnetic signal.

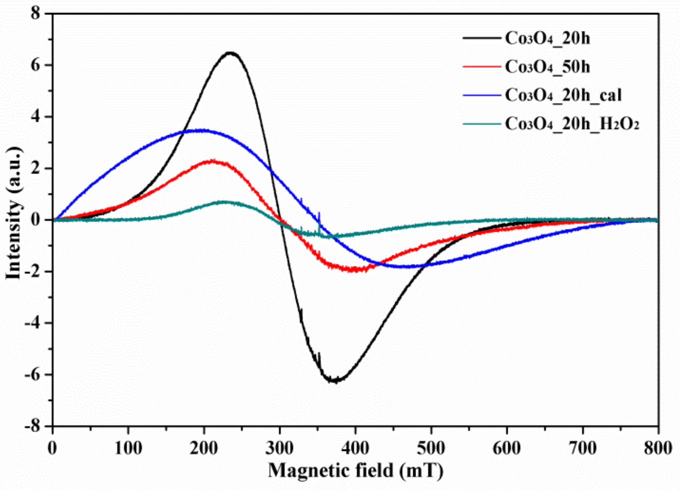

Figure 3.11. EPR spectra of Co_3O_4 WOCs synthesized in the presence and absence of H_2O_2.

The influence of charge transfer efficiency between excited $[Ru(bpy)_3]^{2+}$ photosensitizer (PS) and Co_3O_4-based WOCs is another crucial step of the water oxidation process, which is probably linked to crystallinity or surface oxidation states as a function of the preparative history. Transient spectroscopic analysis of the quenching process of the excited $[Ru(bpy)_3]^{2+}$ has been established as a useful approach to quantify the charge transfer efficiency.[68] Here, we investigated the luminescence decay dynamics of excited $[Ru(bpy)_3]^{2+}$ in the presence of different Co_3O_4-WOCs. Table 3.3 shows that all of the investigated Co_3O_4-WOC samples did not display any significant differences in the lifetime of the excited photosensitizer (derived from fitting the curves in Figure S3.14 to the exponential decay equation $R(t) = Ae^{(-t/\tau)}$, τ = lifetime).

Table 3.3. Transient luminescence decay of excited photosensitizer (PS) in the presence of Co_3O_4 WOCs.

Sample	**Luminescence lifetime/ns**
Co_3O_4_20h + Ru PS	5.7
Co_3O_4_35h + Ru PS	5.9
Co_3O_4_50h + Ru PS	5.8
Co_3O_4_20h_cal + Ru PS	5.7
Ru PS	387.3

All lifetimes fluctuate around 6 ns, i.e. they are significantly below the value for the pristine PS (387 ns) and also lower than the shortest values reported for anatase.[68] This indicates that the different surface areas and oxidation states arising from the individual preparative pathways of the Co_3O_4-WOC samples do not influence the initial steps of the photocatalytic cycle, so that surface adsorption or any diffusion controlled interaction between PS and oxide catalyst do not account for the observed major differences in oxygen evolution rates. Recovery of $[Ru(bpy)_3]^{2+}$ through direct hole injection into Co_3O_4 particles has recently been determined as a longer process (470 nm),[69, 70] but further investigations on the precise influence of Co_3O_4-WOC properties on charge transfer mechanisms and efficiency are required.

3.3.4 Trends for Co_3O_4-WOCs optimization

The above results illustrate that targeted design of spinel-type Co_3O_4-WOCs is a complex multi-parameter process with at least three main factors, namely morphology, crystallinity and valence states. They can be further differentiated into detailed characteristics, such as particle size/surface area, interstitials/defects and degree of inversion/site occupancies. As a consequence, detailed structure-activity relationships for as-synthesized cobalt oxides or species formed from precatalysts[71-73] would require extensive surface and bulk analyses, thus rendering comprehensive "WOC design" rather complicated In the following, we thus analyze and discuss our data in light of practical guidelines for Co_3O_4-WOC production.

Most recently, high surface area has been widely emphasized as a major prerequisite for high performance WOCs.[44, 45] In parallel, Co-based electrocatalysts, especially the Co-Pi systems, were deliberately designed as amorphous materials to improve their robustness and self-healing properties.[49] Furthermore, the productive effect of amorphous features on photocatalytic activity has been in the focus of manifold recent studies.[21, 50-52, 58] The complex interplay of crystallinity and activity is currently controversially studied for a wide variety of processes. For example, *Larcher* et al. investigated Co_3O_4-mediated H_2O_2 decomposition and reported on a superior activity of pristine and defect-rich nanoscale Co_3O_4 compared to samples calcinated at 400 °C.[30]

We here demonstrate an alternative strategy to enhance the WOC activity with straightforward chemical and thermal tuning methods aiming for higher crystallinity at the expense of BET surface area. Whereas the BET surface area among the sample series Co_3O_4_20h, Co_3O_4_50h and Co_3O_4_20h_calc is reduced from 100 over 65 to 25 m^2g^{-1}, the according TOF values increase by factors of 2.7 and 6, respectively, in a counterintuitive manner. Likewise, the presence of H_2O_2 as a chemical oxidant during hydrothermal processing reduces the BET surface area by 25%, whereas the WOC activity of Co_3O_4_20h_H_2O_2 is 2.8-fold higher compared to Co_3O_4_20h. PXRD patterns of all Co_3O_4-WOCs show a clear trend towards more intense and sharper reflections for highly active catalyst samples, along with decreasing lattice constants and improved Rietveld fitting results vs. Co_3O_4_20h. This clearly identifies crystallinity as an important parameter for efficient photocatalytic Co_3O_4-WOC tailoring. Raman spectra further support the link between high crystallinity and enhanced WOC activity, which is particularly evident from the smaller A_{1g} peak width after thermal and oxidative treatment.

Given that the above-mentioned treatment routes strongly influence the complex interplay of crystallinity, structural order and valence states in the Co_3O_4 WOCs, various spectroscopic methods were applied to compare valence states and crystallinity. The productive influence of H_2O_2-assisted hydrothermal synthesis indicates that enhanced Co^{3+}/Co^{2+} ratios in combination with higher crystallinity notably improve the photocatalytic O_2 yields. Interestingly, short oxidative treatment in O_2 atmosphere did not exert a significant productive effect on the catalytic performance, thereby underscoring the importance of a "bottom up" chemical oxidant for higher bulk WOC crystallinity. Comparison of Co^{2+} and Co^{3+} UV/Vis absorption bands for pristine and H_2O_2-oxidized Co_3O_4 samples provide further evidence for improved WOC performance through higher Co^{3+} contents. Vice versa, reductive post-synthetic treatment under Ar atmosphere led to a loss of WOC activity in combination with a broadband UV/Vis absorption indicating structural disorder.[38] XPS data for Co_3O_4_20h and Co_3O_4_20h_H_2O_2 show significantly higher Co^{3+} contents on the surface of the more active chemically oxidized sample, which correspond to the complementary bulk EPR analyses.

Generally, obtaining the ideal 1:2 ratio of Co^{2+}/Co^{3+} in Co_3O_4 through oxidation of Co(II)-precursors in ambient atmosphere can be difficult. However, establishing the precise correlations between crystallinity and site occupancies, quantitative Co^{2+}/Co^{3+} ratios and possible redox gradients or defects in remains a challenging analytical task that would require a combination of high resolution neutron diffraction, solid state NMR and other advanced techniques. This applies especially for the complete differentation between bulk and surface effects of post-synthetic calcination on the catalytic activity of Co_3O_4_20h_cal WOC. The above-mentioned PXRD refinement trend towards smaller lattice constants and better correlation with the regular Co_3O_4 model in comparison with pristine Co_3O_4_20h shows that the "top down" optimization strategy works analogous to the "bottom up" chemical oxidation, namely through "healing" the disordered structure of the pristine hydrothermal material with respect to higher crystallinity and occupancy of regular lattice sites.

The hydrothermal "bottom up" approach is based on maintaining the nanoscale features of the Co_3O_4 WOCs through use of H_2O_2 as a soluble chemical oxidant which promotes homogeneous incorporation of Co^{3+} into the growing nanocrystals. However, nanoscale WOCs with high surface areas are often bound to lose this initial advantage through adsorption, ripening, agglomeration and related adverse processes under long-term operational conditions.[74] Indeed, post-catalytic HRTEM investigations (Figure S3.10) point to a link between loss of WOC activity and formation of an amorphous surface layer on the Co_3O_4_20h_H_2O_2 nanoparticle surface, which is in sharp contrast to the observed productive effect of such coatings on Co-containing electrochemical WOCs.[50-52, 75]

Therefore, we propose an alternative "top down" approach through post-synthetic tuning under ambient atmosphere. Carefully adjusted thermal treatment anticipates coarsening processes in a controlled manner, while considerably improving the catalytic activity through enhanced crystallinity and reduction of defects and interstitial cations. The detrimental influence of defects on the demanding four-electron-transfer process of water oxidation has been illustrated by numerous previous photochemical studies.[22, 76] Bulk WOC defects are likely to act as hole traps, thereby reducing the overall water oxidation efficiency through quenching of charge carriers. Therefore, strategies toward catalytic robustness through self-healing amorphous features, such as in Co-Pi electrocatalysts, cannot be directly transferred upon photocatalyst development, because the latter do not operate with an applied potential to accelerate carrier transfer. This underscores the pivotal role of crystallinity in photocatalyst synthesis so that maximization of BET surface area can not be the sole paradigm for WOC optimization. Related trends have recently emerged for the crucial role of the bulk material in Co-based electrocatalysts.[77] Interestingly, efficient oxide-based WOCs, such as a recently reported new amorphous manganese oxide (AMO) type,[21] might in fact consist of highly ordered domains beyond the resolution of PXRD methods, which are indicated by very sharp peaks in Raman spectra as a superior local structure probe.

3.4 Conclusions

The influence of different preparative histories on the resulting photocatalytic water oxidation activity was investigated for a series of hydrothermally synthesized spinel-type Co_3O_4-WOCs. The complex interplay of morphology/surface area, crystallinity and cobalt valence states was analyzed with a wide range of analytical methods (including PXRD, Raman, UV/Vis, XPS and EPR techniques). We present a counterintuitive trend for WOC activity vs. BET surface area: the most active WOCs displayed significantly reduced surface areas. Crystallinity and oxidation states were identified as more influential parameters than surface area maximization to improve the performance of Co_3O_4-WOCs.

Although cobalt oxide is a benchmark heterogeneous WOC, full control over its complex interplay of numerous interdependent synthetic, structural and surface-related performance parameters would request extensive analytical characterizations to fully assess the influence of a given synthetic protocol on the catalytic performance. This renders setup and implementation of comprehensive design guidelines for Co_3O_4-WOCs challenging.

We therefore compare two straightforward and efficient optimization strategies, namely a "bottom up" approach via H_2O_2 as a chemical oxidant under hydrothermal conditions vs. a "top down" approach based on post-synthetic thermal treatment. The latter controlled ageing strategy notably enhances the WOC activity despite a drastic loss of BET surface area in favor of higher crystallinity and robustness. This opens up alternatives to demanding nanoparticles fabrication on the way to technological implementations of artificial photosynthesis.

References

[1] A. Harriman, I. J. Pickering, J. M. Thomas. *J. Chem. Soc, Faraday Trans. 1* **1988**, *84*, 2795-2806.

[2] S. Yusuf, F. Jiao. *ACS Catalysis* **2012**, *2*, 2753-2760.

[3] J. W. Ko, W. -H. Ryu, I.-D. Kim, C. B. Park. *Chem. Commun*. **2013**, *49*, 9725-9727.

[4] G. J. Kavarnos, N. J. Turro. *Chem. Rev.* **1986**, *86*, 401-449.

[5] J. Ungelenk, C. Feldmann. *Appl. Catal. B* **2012**, *127*, 11-17.

[6] G. P. Gardner, Y. B. Go, D. M. Robinson, P. F. Smith, J. Hadermann, A. Abakumov, M. Greenblatt, G. C. Dismukes. *Angew. Chem. Int. Ed.* **2012**, *51*, 1616-1619.

[7] D. M. Robinson, Y. B. Go, M. Mui, G. Gardner, Z. Zhang, D. Mastrogiovanni, E. Garfunkel, J. Li, M. Greenblatt, G. C. Dismukes. *J. Am. Chem. Soc.* **2013**, *135*, 3494-3501.

[8] G. F. Swiegers, J. K. Clegg, R. Stranger. *Chem. Sci.* **2011**, *2*, 2254-2262.

[9] G. F. Swiegers, D. R. MacFarlane, D. L. Officer, A. Ballantyne, D. Boskovic, J. Chen, G. C. Dismukes, G. P. Gardner, R. K. Hocking, P. F. Smith, L. Spiccia, P. Wagner, G. G. Wallace, B. Winther-Jensen, O. Winther-Jensen. *Aust. J. Chem.* **2012**, *65*, 577-582.

[10] Y.-F. Li, Z.-P. Liu. *J. Am. Chem. Soc.* **2011**, *133*, 15743-15752.

[11] R. Li, F. Zhang, D. Wang, J. Yang, M. Li, J. Zhu, X. Zhou, H. Han, C. Li. *Nat. Comm.* **2013**, *4*, 1432.

[12] M. M. Najafpour, T. Ehrenberg, M. Wiechen, P. Kurz. *Angew. Chem. Int. Ed.* **2010**, *49*, 2233-2237.

[13] M. Wiechen, I. Zaharieva, H. Dau, P. Kurz. *Chem. Sci.* **2012**, *3*, 2330-2339.

[14] M. Risch, K. Klingan, F. Ringleb, P. Chernev, I. Zaharieva, A. Fischer, H. Dau. *ChemSusChem* **2012**, *5*, 542-549.

[15] V. B. R. Boppana, S. Yusuf, G. S. Hutchings, F. Jiao. *Adv. Funct. Mater.* **2013**, *23*, 878-884.

[16] Y. Yamada, K. Yano, D. Hong, S. Fukuzumi. *Phys. Chem. Chem. Phys.* **2012**, *14*, 5753-5760.

[17] J. G. McAlpin, Y. Surendranath, M. Dinca, T. A. Stich, S. A. Stoian, W. H. Casey, D. G. Nocera, R. D. Britt. *J. Am. Chem. Soc.* **2010**, *132*, 6882-6883.

[18] Y. Gorlin, B. Lassalle-Kaiser, J. D. Benck, S. Gul, S. M. Webb, V. K. Yachandra, J. Yano, T. F. Jaramillo. *J. Am. Chem. Soc.* **2013**, *135*, 8525-8534.

[19] F. Jiao, H. Frei. *Chem. Commun.* **2010**, *46*, 2920-2922.

[20] S. S. K. Ma, T. Hisatomi, K. Maeda, Y. Moriya, K. Domen. *J. Am. Chem. Soc.* **2012**, *134*, 19993-19996.

[21] A. Iyer, J. Del-Pilar, C. K. King'ondu, E. Kissel, H. F. Garces, H. Huang, A. M. El-Sawy, P. K. Dutta, S. L. Suib. *J. Phys. Chem. C* **2012**, *116*, 6474-6483.

[22] T. Takashima, K. Hashimoto, R. Nakamura. *J. Am. Chem. Soc.* **2012**, *134*, 18153-18156.

[23] J. B. Gerken, J. G. McAlpin, J. Y. C. Chen, M. L. Rigsby, W. H. Casey, R. D. Britt, S. S. Stahl. *J. Am. Chem. Soc.* **2011**, *133*, 14431-14442.

[24] T. Takashima, K. Hashimoto, R. Nakamura. *J. Am. Chem. Soc.* **2012**, *134*, 1519-1527.

[25] F. Evangelisti, R. Güttinger, R. Moré, S. Luber, G. R. Patzke. *J. Am. Chem. Soc.* **2013**, *135*, 18734-18737.

[26] G. Chen, L. Chen, S. M. Ng, W.-L. Man, T.-C. Lau. *Angew. Chem. Int. Ed.* **2013**, *52*, 1-4.

[27] J. Zhang, M. Grzelczak, Y. Huo, K. Maeda, K. Domen, X. Fu, M. Antonietti, X. Wang. *Chem. Sci*. **2012**, *3*, 443-446.

[28] L. Xi, P. D. Tran, S. Y. Chiam, P. S. Bassi, W. F. Mak, H. K. Mulmudi, S. K. Batabyal, J. Barber, J. S. C. Loo, L. H. Wong. *J. Phys. Chem. C* **2012**, *116*, 13884-13889.

[29] S. C. Petitto, E. M. Marsh, G. A. Carson, M. A. Langell. *J. Mol. Catal. A* **2008**, *281*, 49-58.

[30] M. Casas-Cabanas, G. Binotto, D. Larcher, A. Lecup, V. Giordani, J.-M. Tarascon. *Chem. Mater.* **2009**, *21*, 1939-1947.

[31] F. Conrad, M. Bauer, D. Sheptyakov, S. Weyeneth, D. Jaeger, K. Hametner, P.-E. Car, J. Patscheider, G. R. Patzke. *RSC Advances* **2012**, *2*, 3076-3082.

[32] F. Cheng, J. Shen, B. Peng, Y. Pan, Z. Tao, J. Chen. *Nat. Chem.* **2011**, *3*, 79-84.

[33] M. Douin, L. Guerlou-Demourgues, M. Ménétrier, E. Bekaert, L. Goubault, P. Bernard, C. Delmas. *Chem. Mater.* **2008**, *20*, 6880-6888.

[34] F. Tronel, L. Guerlou-Demourgues, M. Ménétrier, L. Croguennec, L. Goubault, P. Bernard, C. Delmas. *Chem. Mater.* **2006**, *18*, 5840-5851.

[35] Y. Liang, H. Wang, J. Zhou, Y. Li, J. Wang, T. Regier, H. Dai. *J. Am. Chem. Soc.* **2012**, *134*, 3517-3523.

[36] T. Warang, N. Patel, R. Fernandes, N. Bazzanella, A. Miotello. *Appl. Catal. B-Environ.* **2013**, *132-133*, 204-211.

[37] S. Esposito, M. Turco, G. Ramis, G. Bagnasco, P. Pernice, C. Pagliuca, M. Bevilacqua, A. Aronne. *J. Solid State Chem.* **2007**, *180*, 3341-3350.

[38] M. Taguchi, T. Nakane, K. Hashi, S. Ohki, T. Shimizu, Y. Sakka, A. Matsushita, H. Abe, T. Funazukuri, T. Naka. *Dalton. Trans*. **2013**, *42*, 7167-7176.

[39] X. W. Xie, Y. Li, Z. Q. Liu, M. Haruta, W. J. Shen. *Nature* **2009**, *458*, 746-749.

[40] Y. Sun, P. Lv, J.-Y. Yang, L. He, J.-C. Nie, X. Liu, Y. Li. *Chem. Commun.* **2011**, *47*, 11279-11281.

[41] L. Hu, Q. Peng, Y. Li. *J. Am. Chem. Soc.* **2008***, 130,* 16136-16137.

[42] F. Jiao, H. Frei. *Angew. Chem. Int. Ed.* **2009**, *48*, 1841-1844.

[43] C.-C. Yang, T. M. Eggenhuisen, M. Wolters, A. Agiral, H. Frei, P. E. Jongh, K. P. Jong, G. Mul. *ChemCatChem* **2013**, *5*, 550-556.

[44] C. Y. Lee, K. Lee, P. Schmuki. *Angew. Chem. Int. Ed.* **2013**, *52*, 1-6.

[45] J. Rosen, G. S. Hutchings, F. Jiao. *J. Am. Chem. Soc.* **2013**, *135*, 4516-4521.

[46] M. Grzelczak, J. Zhang, J. Pfrommer, J. Hartmann, M. Driess, M. Antonietti, X. Wang. *ACS Catal.* **2013**, *3*, 383-388.

[47] J. D. Blakemore, H. B. Gray, J. R. Winkler, A. M. Müller. *ACS Catal.* **2013**, *3*, 2497-2500.

[48] H. S. Ahn, J. Yano, T. D. Tilley. *Energy Environ. Sci*. **2013**, *6*, 3080-3087.

[49] M. W. Kanan, D. G. Nocera. *Science*, **2008**, *321*, 1072-1075.

[50] K. J. May, C. E. Carlton, K. A. Stoerzinger, M. Risch, J. Suntivich, Y.-L. Lee, A. Grimaud, Y. Shao-Horn. *J. Phys. Chem. Lett.* **2012**, *3*, 3264-3270.

[51] M. Risch, A. Grimaud, K. J. May, K. A. Stoerzinger, T. J. Chen, A. N. Mansour, Y. Shao-Horn. *J. Phys. Chem. C*. **2013**, *117*, 8628-8635.

[52] S. W. Lee, C. Carlton, M. Risch, Y. Surendranath, S. Chen, S. Furutsuki, A. Yamada, D. G. Nocera, Y. Shao-Horn. *J. Am. Chem. Soc.* **2012**, *134*, 16959-16962.

[53] R. Stoyanova, E. Zhecheva , S. Angelov. *Mater. Chem. Phys.* **1990**, *26*, 239-244.

[54] P. Sahoo, H. Djieutedjeu, P. F. P. Poudeu. *J. Mater. Chem. A* **2013**, *1*, 15022-15030.

[55] E. G. Babakhani, J. Towfighi, L. Shirazi, A. Nakhaeipour. *J. Mater. Sci. Technol.* **2012**, *28*, 177-183.

[56] H. Bordeneuve, C. Tenailleau, S. Guillemet-Fritsch, R. Smith, E. Suard, A. Rousset. *Solid State Sci*ence **2012**, *12*, 379-386.

[57] F. Kovanda, T. Rojka, J. Dobešová, V. Machovič, P. Bezdička, L. Obalová, K. Jirátová, T. Grygar. *J. Solid State Chem.* **2006**, *179*, 812-823.

[58] Z. P. Chen, J. Xing, H. B. Jiang, H. G. Yang. *Chem. Eur. J.* **2013**, 19, 4123-4127.

[59] A. F. Osorio, A. Vázquez-Olmos, R. Sato-Berru, R. Escudero. *Rev. Adv. Mater. Sci.* **2009**, *22*, 60-66.

[60] J. Taghavimoghaddam, G. P. Knowles. *Top Catal.* **2012**, *55*, 571-579.

[61] G. Wang, X. Shen, J. Horvat, B. Wang, H. Liu, D. Waxler, J. Yao. *J. Phys. Chem. C* **2009**, *113*, 4357-4361.

[62] T. S. Kabre, Co_3O_4 Thin Films: Sol-Gel Synthesis, Electrocatalytic Properties & Photoelectrochemistry, *Master Thesis*, Ohio State University, **2011**.

[63] J. Taghavimoghaddam, G. P. Knowles, A. L. Chaffee. *Top Catal.* **2012**, *55*, 571-579.

[64] A. A. Verberckmoes, B. M. Weckhuysen, R. A. Schoonheydt. *Microporous and Mesoporous Mater.* **1998**, *22*, 165-178.

[65] S. Takada, M. Fujii, S. Kohiki. *Nano Lett.* **2001**, *1*, 379-382.

[66] L. Dahéron, R. Dedryvère, H. Martinez, M. Ménétrier, C. Denage, C. Delmas, D. Gonbeau. *Chem. Mater.* **2008**, *20*, 583-590.

[67] N. Fischer, M. Minnermann, M. Baeumer, E. Van Steen, M. Claeys. *Catal. Lett.* **2012**, *142*, 830-837.

[68] T. Kajlwara, K. Hasimoto, T. Kawai, T. Sakata. *J. Phys. Chem.* **1982**, *86*, 4516-4522.

[69] A. Agiral, H. S. Soo, H. Frei. *Chem. Mater.* **2013**, *25*, 2264-2273.

[70] M. De Respinis, *Master Thesis*, Department of Physics, Technical University of Denmark, Sept. **2011**.

[71] S. Fu, Y. Liu, Y. Ding, X. Du, F. Song, R. Xiang, B. Ma. *Chem. Commun*. **2014**, *50*, 2167-2169.

[72] M. Risch, D. Shevchenko, M. F. Anderlund, S. Styring, J. Heidkamp, K. M. Lange, A. Thapper, I. Zaharieva. *Int. J. Hydrogen Energy* **2012**, *37*, 8878-8888.

[73] J. J. Stracke, R. G. Finke. *J. Am. Chem. Soc.* **2011**, *133*, 14872-14875.

[74] L. Liao, Q. Zhang, Z. Su, Z. Zhao, Y. Wang, Y. Li, X. Lu, D. Wei, G. Feng, Q. Yu, X. Cai, J. Zhao, Z. Ren, H. Fang, F. Robles-Hernandez, S. Baldelli, J. Bao. *Nature Nanotechnol*. **2014**, *9*, 69.

[75] R. D. L. Smith, M. S. Prévot, R. D. Fagan, Z. Zhang, P. A. Sedach, M. K. J. Siu, S. Trudel, C. P. Berlinguette. *Science* **2013**, *340*, 60-63.

[76] F. Zhang, A. Yamakata, K. Maeda, Y. Moriya, T. Takata, T. Kubota, S. Oishi, K. Domen. *J. Am. Chem. Soc.* **2012**, *134*, 8348-8351.

[77] K. Klingan, F. Ringleb, I. Zaharieva, J. Heidkamp, P. Chernev, D. Gonzalez-Flores, M. Risch, A. Fischer, H. Dau. *ChemSusChem* **2014**, *7*, 1301-1310.

Appendix

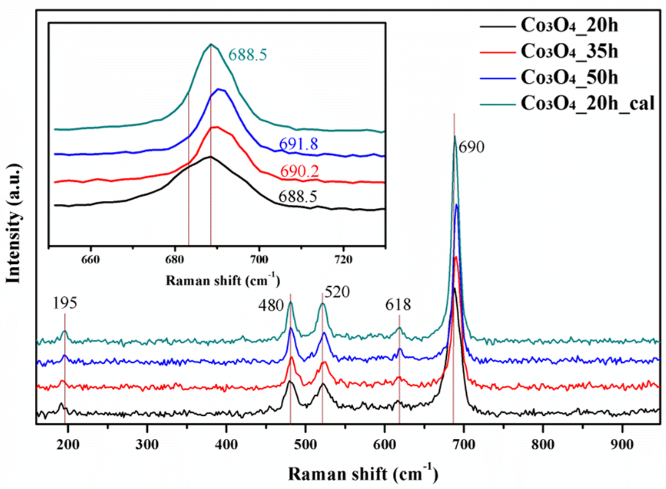

Figure S3.1. Raman spectra of Co_3O_4 WOCs after different synthetic treatments.

The influence of hydrothermal treatment on the local crystallinity of Co_3O_4 WOCs was studied with Raman spectroscopy (Figure S.3.1).[1] The F_{2g} peaks, which are attributed to the vibrations of the tetrahedral $\{CoO_4\}$ sites, are slightly shifted towards higher wavenumbers upon longer hydrothermal treatment. Likewise, the A_{1g} peaks associated with the Co-O stretching vibration of the octahedral $\{CoO_6\}$ sites undergo a shift to higher wavenumbers together with a reduction of peak width after extended reaction times (Figure S.3.1, inset). Generally, Raman peak broadening in Co_3O_4 samples point to symmetry distortions and deviations from ideal spinel structure (i.e. Co^{2+} occupying the $\{CoO_4\}$ positions and Co^{3+} located on the $\{CoO_6\}$ sites) which often arise from synthetic pathways with sluggish diffusion kinetics or from other preparative issues.[2] Sharpening of the A_{1g} peaks with the reaction time may thus point to a reduction of dislocations and defects through hydrothermal treatment.

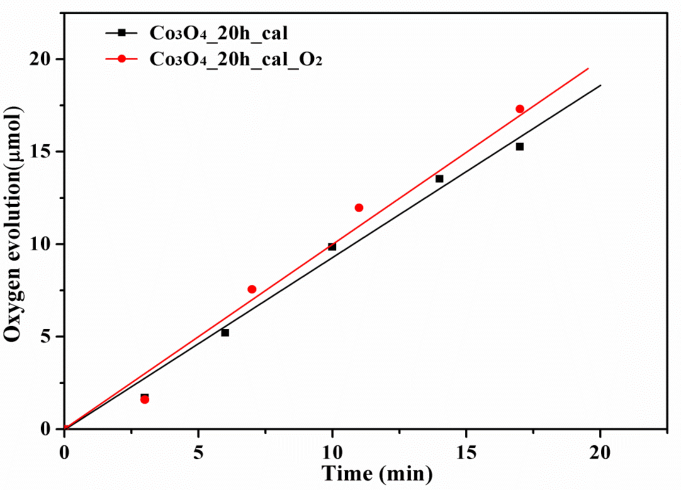

Figure S3.2. Catalytic activity of Co_3O_4 WOCs before and after post-synthetic treatment in oxygen atmosphere.

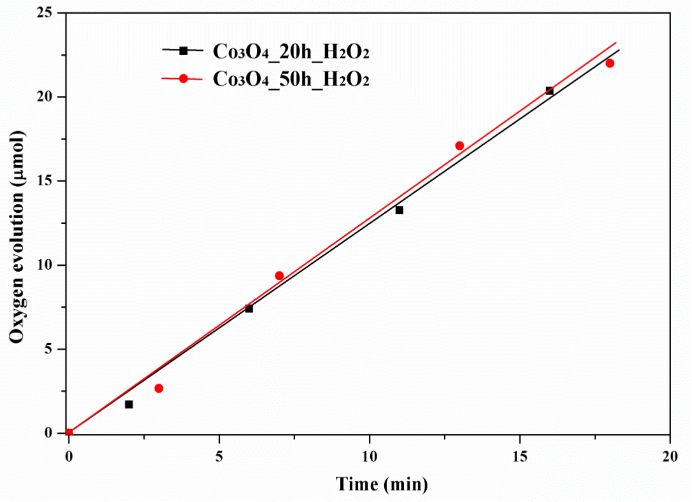

Figure S3.3. Water oxidation performance of Co_3O_4_20h_H_2O_2 and Co_3O_4_50h_H_2O_2.

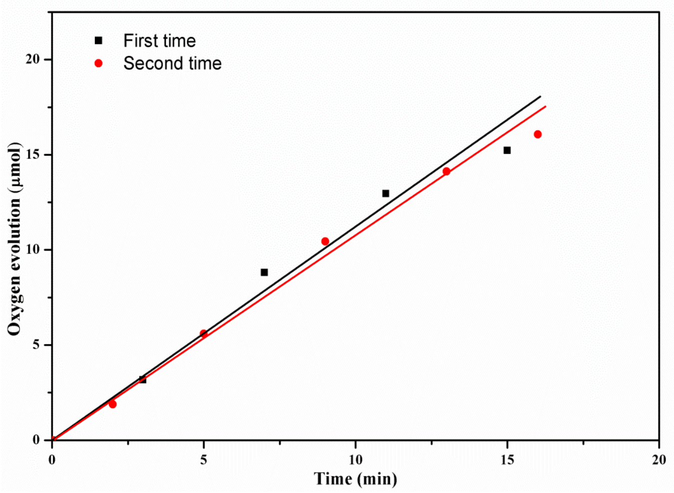

Figure S3.4. Reproducible WOC activity of Co_3O_4_20h_cal.

Co_3O_4_20h_cal was repeatedly synthesized and the different batches were tested for water oxidation activity. The final catalytic test results do not show significant differences between the individual batches, thus indicating that the influence of random operational errors can safely be ruled out.

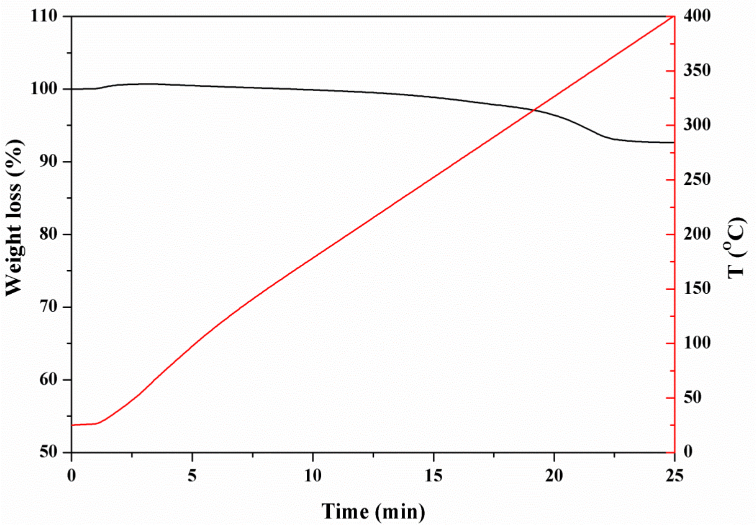

Figure S3.5. Thermogravimetric curve of Co_3O_4_20h_H_2O_2 during thermal post-synthetic treatment in argon atmosphere.

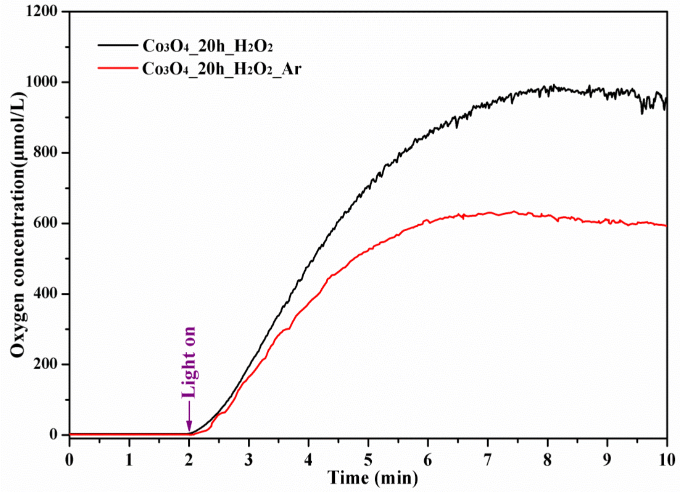

Figure S3.6. Water oxidation activity of Co_3O_4_20h_H_2O_2 before and after reduction.

Water oxidation tests were performed as follows: 10 mg catalyst, 8 mg $[Ru(bpy)_3]Cl_2$ as photosensitizer and 50 mg $Na_2S_2O_8$ as sacrificial electron acceptor were dispersed in 8 mL potassium phosphate buffer (pH 7) by ultrasound treatment. The suspension was transferred to a 10 mL gastight vial and degassed wit He to remove the dissolved oxygen contents. A 470 nm LED with 5500 Lux intensity was used as light source, and oxygen evolution was monitored with a calibrated Clark electrode. The light was switched on two minutes after data collection was started.

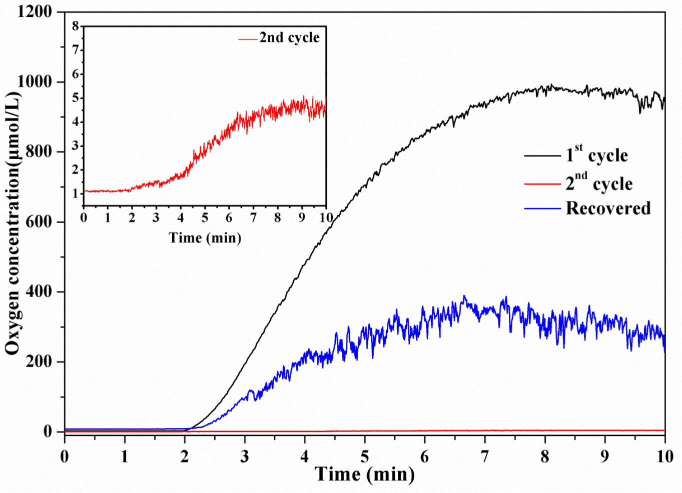

Figure S3.7. Recycling runs of Co_3O_4_20h_H_2O_2 WOC.

The first cycle was run by dispersing 10 mg catalyst, 8 mg $[Ru(bpy)_3]Cl_2$ as photosensitizer and 50 mg $Na_2S_2O_8$ as sacrificial electron acceptor in 8 mL potassium phosphate buffer (pH 7) by ultrasound treatment. The second cycle was initiated by only introducing 50 mg fresh $Na_2S_2O_8$ into the suspension after the first cycle. The recovered cycle was run by separating the WOC from the suspension after the second cycle and proceeding with water oxidation tests as in the first cycle. An obvious decrease of water oxidation performance was observed for the second cycle. This is mainly due to the decomposition of the photosensitizer, as indicated by the intensity decrease of the characteristic absorption band around 470 nm (Figure S.3.7). However, the recovered catalyst displayed loss of water oxidation activity even after addition of fresh PS, probably due to the formation of an amorphous layer on the catalyst surface (Figure S.3.10c).

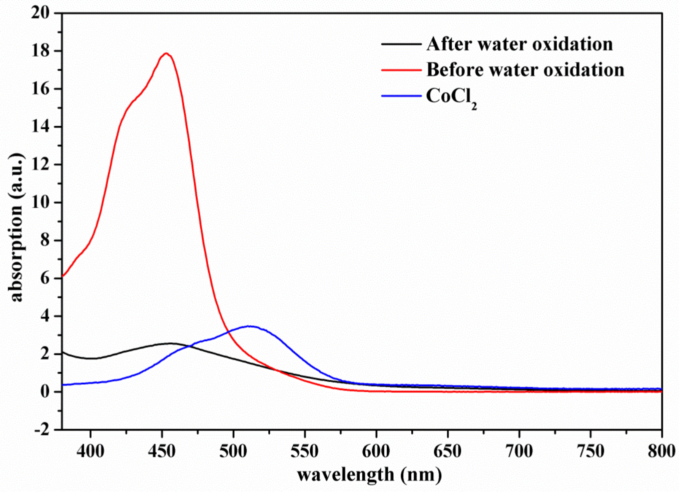

Figure S3.8. UV/Vis spectra of the centrifuged solution before and after the second cycle (cf. Figure S.3.7).

Notable intensity decrease of the absorption band in the range of 400-500 nm indicates that the $[Ru(bpy)_3]Cl_2$ photosensitizer underwent decomposition during the water oxidation process. Reference spectra for $CoCl_2$ do not point to significant amounts of free Co^{2+} ions.[2]

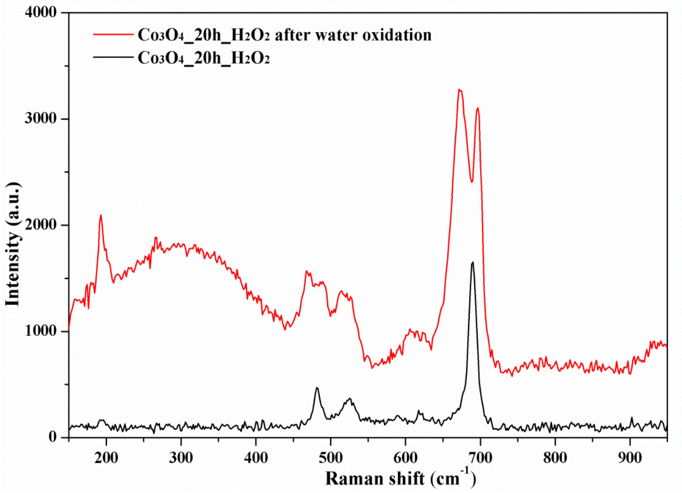

Figure S3.9. Raman spectra of Co_3O_4_20h_H_2O_2 before and after water oxidation.

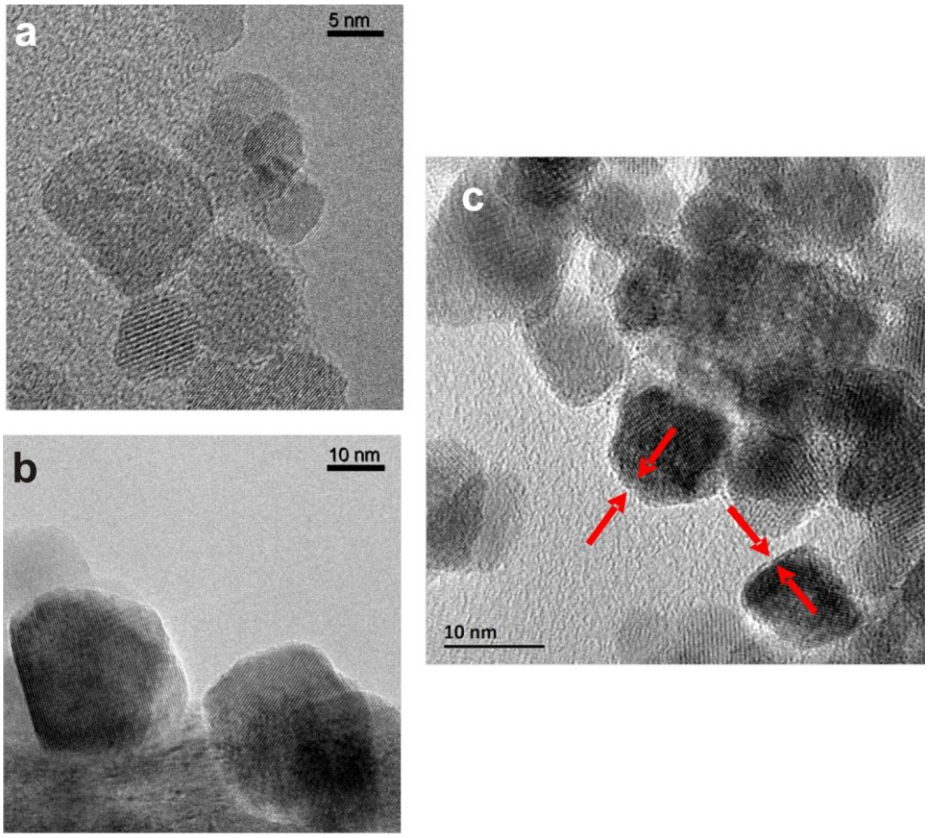

Figure S3.10. TEM images of (a) Co_3O_4_20h and Co_3O_4_20h_H_2O_2 (b) before and (c) after water oxidation.

No visible amorphous layer can be detected on the surface of pristine particles (the blurred particle without lattice stripes is out of focus). However, an amorphous layer appears to be formed during the water oxidation process, which is in accordance with recent results on Co-contanining perovskites or $LiCoPO_4$ oxides.[4-6] The presence of an amorphous layer can account for the broadening and splitting of Raman peaks after the catalytic process (Figure S.3.9).

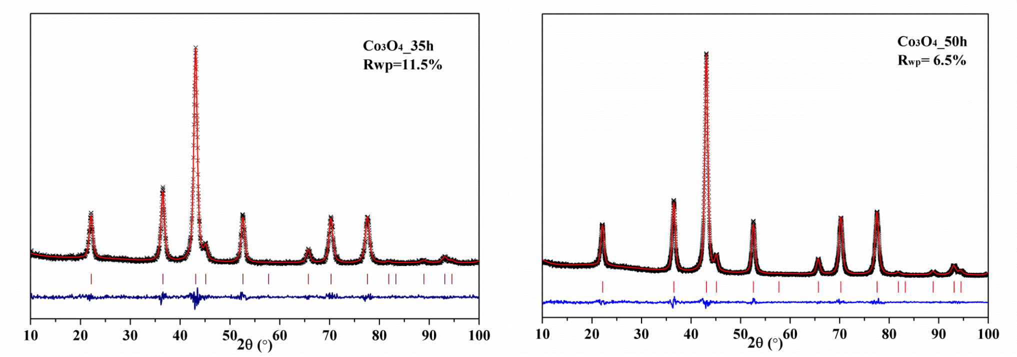

Figure S3.11. Rietveld refinements for samples Co_3O_4_35h and Co_3O_4_50h.

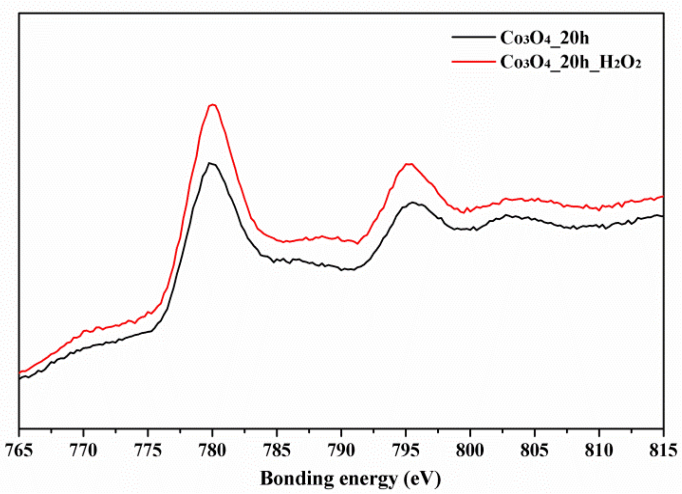

Figure S3.12. Co 2p XPS spectra of Co_3O_4_20h and Co_3O_4_20h_H_2O_2.

Table S3.1. Comparison of unpaired electron contents for different Co_3O_4 WOCs (integration of EPR spectra, cf. Figure 4.3.11).

WOCs	**Intensity / a.u.**
Co_3O_4_20h	17.5
Co_3O_4_50h	8.5
Co_3O_4_20h_cal	19.9
Co_3O_4_20h_H_2O_2	1.5

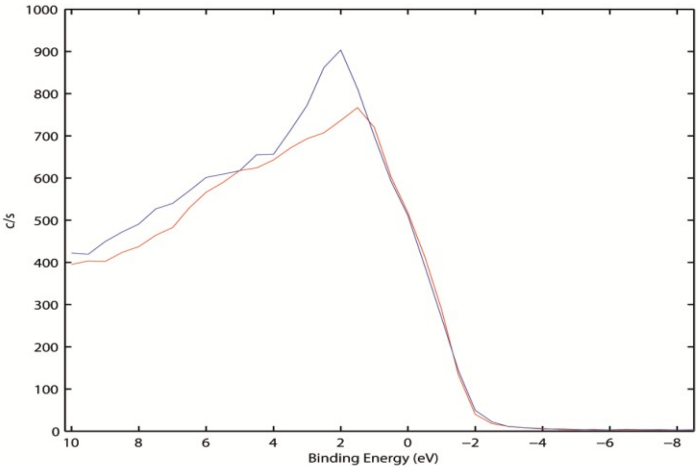

Figure S3.13. Valence band spectra of Co_3O_4_20h (red) and Co_3O_4_20h_H_2O_2 (blue).

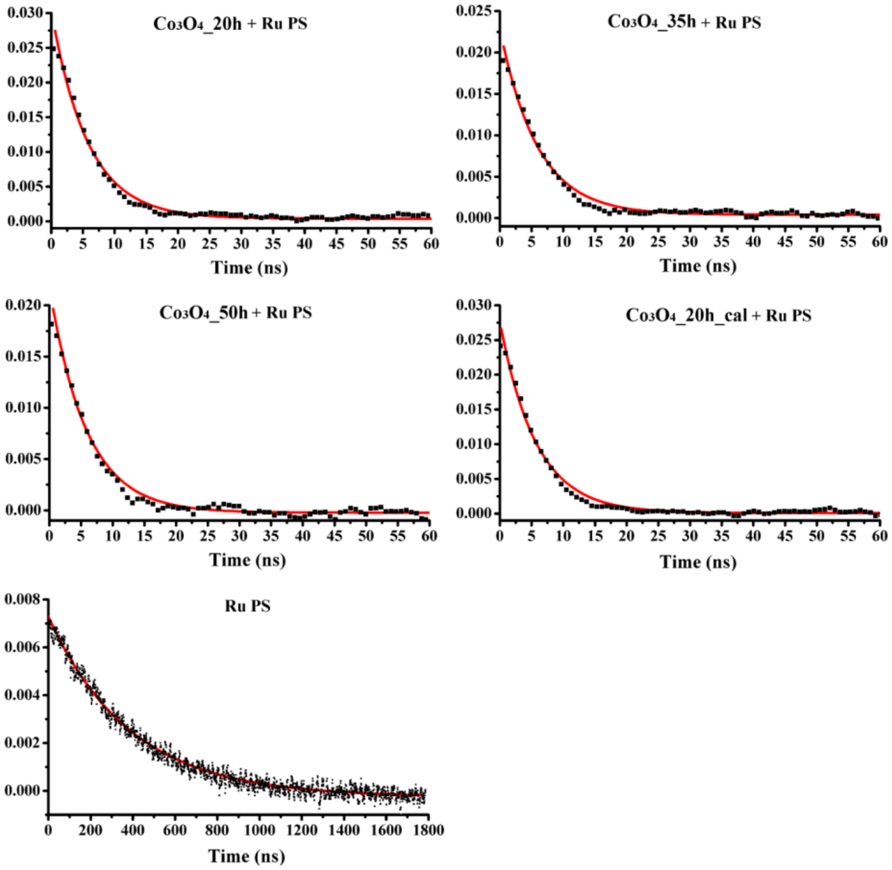

Figure S3.14. Fitted curves for luminescence lifetime measurements.

The lifetime was derived from fitting of curves in Figure S.14 to exponential decay $R(t)=Ae^{(-t/\tau)}$, where τ is the lifetime, R(t) is the fluorescence intensity, t is the time and A is a fitting constant.

References

[1] F. Kovandaa, T. Rojkaa, J. Dobesova, V. Machovic, P. Bezdicka, L. Obalova, K. Jiratova, T. Grugar. *J. Solid State Chem.* **2006**, *179*, 812-823.

[2] H. Liu, G. R. Patzke. *Nanostructured Materials and Nanotechnology VII* **2013**, *34*, 75-86.

[3] G. Gouadec, P. Colomban. *Prog. Cryst. Growth Charact. Mater.* **2007**, *53*, 1-56.

[4] K. J. May, C. E. Carlton, K. A. Stoerzinger, M. Risch, J. Suntivich, Y. -L. Lee, A. Grimaud, Y. Shao-Horn. *J. Phys. Chem. Lett.* **2012**, *3*, 3264-3270.

[5] M. Risch, A. Grimaud, K. J. May, K. A. Stoerzinger, T. J. Chen, A. N. Mansour, Y. Shao-Horn. *J. Phys. Chem. C.* **2013**, *117*, 8628-8635.

[6] S. W. Lee, C. Carlton, M. Risch, Y. Surendranath, S. Chen, S. Furutsuki, A. Yamada, D. G. Nocera, Y. Shao-Horn. *J. Am. Chem. Soc.* **2012**, *134*, 16959-16962.

4. Correlation between Structure, Electronic Properties and Water Oxidation Activities: $LiCoO_2$

4.1 Introduction

In search of general WOC design concepts, cuboidal $\{M_4O_4\}$ motifs (M = Co, Mn) inspired by the $\{CaMn_4O_5\}$ oxygen evolving cluster (OEC) in photosystem II[1-3] were established as an effective design paradigm[4-6] for both molecular,[7-14] oxide[15-24] and polyoxometalate[25-28] based WOCs. Nevertheless, the precise impact of $\{M_4O_4\}$ cubane motifs on the oxygen evolution performance remains under extensive debate,[29] with the amorphous Co-Pi electrocatalysts[30] as a typical example. The absence of long-range order renders structure-activity relations among amorphous Co-Pi type WOCs rather difficult to clarify,[31-34] so that the precise mechanistic role of the proposed $\{Co_4O_4\}$ building blocks remains under investigation.[35-37]

While the water oxidation active oxides such as Co_3O_4, $LiCoO_2$ and λ-MnO_2[15,16] share $\{M_4O_4\}$ as a common construction motif, other oxide-based materials without cubane units (e.g. $Co(OH)_2$, Co-Fe hydroxides and oxyhydroxides) are capable of oxidizing water as well.[38-40] Moreover, a latest study ascribed the water oxidation activity of the well studied $\{Co^{III}{}_4O_4\}$-based $Co_4O_4(OAc)_4(py)_4$ cubane to Co^{2+} impurities instead of assumed $\{Co_4O_4\}$ cubanes.[41] This calls for further investigations on structure-activity correlations.

$LiCoO_2$ has been widely applied and investigated as a battery material, whereas its full potential for photocatalytic water oxidation is just about to be explored.[16] Recently, the structural differences between layered $LiCoO_2$ (*h*igh *t*emperature modification, HT-$LiCoO_2$) and spinel $LiCoO_2$ (*l*ow *t*emperature modification, LT-$LiCoO_2$) were linked to their different properties as cathode materials and WOCs, respectively. The layered arrangement of $\{CoO_6\}$ units in HT-$LiCoO_2$ allows for reversible Li^+ extraction/reintercalation and electronic structure transformations without changing the basic 2D structural framework. LT-$LiCoO_2$ is based on the same oxygen sublattice, albeit with mixed Co/Li (0.25/0.75 and vice versa) occupancies on alternating {111} planes, resulting in $\{Co_4O_4\}$ motifs (marked in yellow in Figure 4.2) related to the cuboidal OEC in photosystem II. While the battery material HT-$LiCoO_2$ is nearly inactive for water oxidation, the electrochemically less relevant LT form displays considerably higher water oxidation activity, which was assigned to its catalytically active $\{Co_4O_4\}$-moieties.[16]

Most recently, the influence of delithiation on the electrochemical water oxidation activity of $LiCoO_2$ oxides was investigated in two parallel studies.[42,43] However, different conclusions were reached in these works. Whereas one study emphasized the beneficial role of delithiation for oxygen evolution, the second investigation indicated that it was detrimental for water oxidation. A further related study[44] even revealed the formation of amorphous layers or phase transition on the surface of $LiCoO_2$ together with in situ delithiation during electrochemical water oxidation, which renders the overall assessment of the water oxidation activity of this material even more complex.

Therefore, the precise impact of delithiation on the water oxidation activity of $LiCoO_2$ materials needs to be further clarified. In the following, we newly investigate photochemical water oxidation with pristine and chemically delithiated $LiCoO_2$ modifications in detail. The standard $[Ru(bpy)_3]Cl_2/Na_2S_2O_8$ protocol was selected to evaluate the water oxidation activity of $LiCoO_2$, because it was reported to leave the surface structure of WOCs intact during water oxidation.[45] A wide range of analytical techniques (including FT-IR, UV/Vis, Raman, ^{7}Li-NMR, XPS spectroscopy and magnetic susceptibility measurements) was applied to assess the impact of delithiation and $\{Co_4O_4\}$ moieties on the water oxidation performance. The tolerance of both LT- and HT-structural frameworks towards delithiation allowed us to differentiate between the influences of structural and electronic properties on water oxidation. A direct correlation between structure, electronic properties and water oxidation activity was successfully established. Bio-inspired architectures ($\{Co_4O_4\}$ moieties) and tuning of the electronic properties via delithiation both work in the same direction towards optimization of charge carrier transport properties for improved water oxidation performance (Figure 4.1).

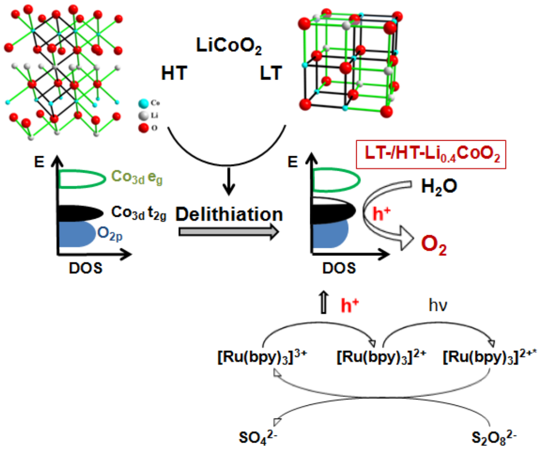

Figure 4.1. Optimization strategies for photochemical water oxidation with $LiCoO_2$ modifications by targeting their electronic properties.

4.2 Experimental

4.2.1 Samples preparations

$LiCoO_2$ nanoparticles were synthesized via a conventional sol-gel method as follows: 10 mmol Li_2CO_3, 20 mmol $Co(NO_3)_2 \cdot 6H_2O$, 40 mmol citric acid and 60 mmol urea were dissolved in 300 mL deionized water. The as-prepared solution was stirred and condensed at 80 °C into a gel which was further decomposed at 170 °C over 4 h into a foam-like precursor. Both LT-$LiCoO_2$ and HT-$LiCoO_2$ were obtained from calcination of the above precursor at 400 ^oC and 700 ^oC for 5 h, respectively. Lithium extraction of as-synthesized $LiCoO_2$-LT and $LiCoO_2$-HT in a bromine-acetonitrile solution (4 mL Br_2 and 10 mL acetonitrile) for 7 d afforded LT- and HT-$Li_{0.4}CoO_2$ as products.

4.2.2 Photocatalytic tests

WOC tests were performed according to well established $[Ru(bpy)_3]^{2+}/S_2O_8^{2-}$ protocols. First, a suspension was prepared by mixing 10 mg water oxidation catalyst, 8 mg $[Ru(bpy)_3]Cl_2$ photosensitizer and 50 mg $Na_2S_2O_8$ in 8 mL phosphate buffer (0.1 M, pH 7, 10 mL vial) in a dark cabinet. Next, the suspension was degassed with helium to remove O_2 in both solution and the head vial. A LED lamp with 470 nm wavelength and 5000 Lux output was used as visible light source. Oxygen production was monitored with a calibrated Clark electrode (Unisense, stirring sensitivity: < 2%, response time (90%): < 10 s) online in solution or by gas chromatography (Agilent 7820A packed with a 3 m × 2 mm molecular sieve 13X 80-100 column). 100 µL gas from the headspace were injected into a gas chromatograph using a gastight microliter syringe (Hamilton 1825 RN) during intervals of several minutes. Helium was chosen as carrier gas to increase the detection sensitivity of O_2 relative to N_2. Gases were detected with a thermal conductivity detector (Varian) operated at 200 °C. Contamination of the headspace by air was constantly monitored through the N_2 peak on GC chromatograms. Calibration was performed by injection of known quantities of pure oxygen diluted in an equivalent vial containing volume and concentration of buffered solution as used for the measurements.

4.2.3 Characterizations

Powder X-ray diffraction patterns (PXRD patterns) were recorded on a XPERT-PRO diffractometer (reflection mode, step size: 0.04°/step, 15 s/step) with $CuK_{\alpha1}$ radiation or on a STOE STADI P diffractometer (transmission mode, step size: 2.09°/step, 35 s/step) with

$CoK_{\alpha1}$ or $CuK_{\alpha1}$ radiation. Brunauer-Emmett-Teller (BET) surface area measurements were conducted on a Quadrasorb SI machine in N_2-adsorption mode. Samples were degassed at 150 °C for 15 h under vacuum prior to the measurements. Raman spectra were recorded on a Renishaw Ramascope spectrometer at 514 nm laser excitation. UV/Vis diffuse reflectance absorption spectra were recorded on a Lambda 650 S Perkin Elmer UV-visible spectrometer in. XPS spectra were measured on an Axis Ultra DLD spectrometer (Kratos, UK) with a 0.1 eV energy resolution. Measurements were performed with a monochromatic Al K_α source without any preceding sputter cleaning or other procedures that might alter the surface of the crystals. The C 1s peak at 284.6 eV was set as a reference for all XPS peak positions. The O 1s peaks were fitted with the XPSPEAK 4.1 software. Magnetic susceptibility measurements were conducted on a 7 T Quantum Design MPMS SQUID at a magnetic field of 1.0 T in the temperature range 5-300 K in both heating and cooling modes. Solid-state ^{7}Li NMR spectra were recorded on Bruker DRX-500 spectrometer modified for solid-state measurements with MAS sample spinning up to 15 kHz (4 mm rotors) and high power 9.5 Hz decoupling. The NMR frequency was 194.41 MHz for ^{7}Li (I=3/2, QM=0.045). The composition of lithium cobalt oxides was analyzed with ICP-AES on an Optima 5300DV spectrometer with a 0.008 nm resolution. Samples were completely dissolved in nitric acid and diluted to concentration within the detection range of the spectrometer. The lithium content of $Li_{1-x}CoO_2$ after different delithiation times was determined by ICP-AES (Mikroanalytisches Labor Pascher, Remagen, Germany).

TG-DSC: TG-DSC data were collected on a NETZSCH TG equipped with a reference corundum crucible. Oxygen and nitrogen protection flux were adjusted to 30 mL/min. Samples were heated to 900 °C at a rate of 15 K/min.

XPS spectra for LT-$Li_{0.4}CoO_2$ before and after water oxidation: XPS spectra were measured on a PHI Quantum 2000 microprobe spectrometer from Physical Electronics Inc. The measurements were taken with a monochromatic Al K_α source without any preceding sputter cleaning or other procedures that might alter the surface of the crystals. The C 1s peak at 284.8 eV was set as a reference for all XPS peak positions.

PXRD patterns: Powder X-ray diffraction patterns for LT-$Li_{0.4}CoO_2$ before and after water oxidation were recorded on a on a STOE STADI P diffractometer (reflection mode, step size: 0.5°/step, 100 s/step) with $CuK_{\alpha1}$ radiation. Powder X-ray diffraction patterns for LT-$Li_{1-x}CoO_2$ and LT-$Li_{0.4}CoO_2$ were recorded on STOE STADI P diffractometer (reflection mode, step size: 0.5°/step, 100 s/step) with Co $K_{\alpha1}$ radiation and were converted to Cu $K_{\alpha1}$ radiation mode by Jade 5.0.

EIS: Electrochemical impedance spectra were collected on a ZAHNER Zennium electrochemical workstation in the range of 10^{-3} to 3×10^{6} Hz. Prior to the impedance measurements, samples were prepared as follows: 15 mg lithium cobalt oxide were dispersed in 2 mL water by sonication. One drop of the above solution was transferred to a glass with two coated gold electrodes. The drop was evenly spread on a 6 x 8 mm space between the two gold electrodes which were dried at 80 ^{o}C in air for 1 d.

^{18}O labeling experiments: 10 mg WOC, 8 mg Ru-PS and 10 mg $Na_2S_2O_8$ were dispersed in 5 mg H_2O with 10 % ^{18}O by sonication. The pH was adjusted to 7 by adding appropriate amounts of KH_2PO_4 and KH_2PO_4. The suspension was transferred to a 10 mL vial and closed with a rubber cap having an aluminum shell. The oxygen in the suspension and headspace was removed by helium flow for 15 min. Photochemical water oxidation was conducted on a 470 nm LED with 5000 Lux. After 30 min of irradiation, 50 µL sample from headspace was injected into a GC-MS instrument for oxygen detection.

X-ray absorption (XAS) experiments: Cobalt K-edge X-ray absorption spectroscopy was performed at the ESRF Swiss Norwegian Beamline BM01B in transmission mode. CoO, Co_3O_4 and $LiCoO_2$ were used as reference samples for cobalt valence determination. Cobalt metal foil was used as calibration standard for all experiments. Energy calibration, background removal and Fourier transformation of XAS spectra were performed with the Athena software and EXAFS fits were performed with the Artemis software.[46]

CV measurements: A rotating disc electrode setup (Metrohm) with an Ag/AgCl reference electrode and a GC-rod counter electrode was used. The sweep rate was set to 0.1 V s^{-1} and the measurements were performed in 0.1 M phosphate buffer at pH 7. Prior to normalization of the data, results from cyclic voltammetry show highly increased water oxidation activity for the delithiated oxides. To exclude any influences of increased surface areas, currents were normalized to the BET surface of the oxide particles (cf. Table S4.2). The increased activity of the delithiated oxides in comparison with their non-delithiated analogues remains significant.

4.3 Results and discussion

4.3.1 Synthesis and structure

Samples of LT- and HT-$LiCoO_2$ were synthesized via a standard citrate sol-gel route.[47] TG-DSC analyses (Figure S4.1) indicate the onset of LT-$LiCoO_2$ formation around 400 °C, followed by an exothermic phase transition to HT-$LiCoO_2$ in the range of 550-800 °C with no further weight loss. Transformation of LT- into HT-$LiCoO_2$ is evident from the appearance of the additional (0 0 6) and (0 1 8) peaks (Figure 4.3) in the powder X-ray diffraction (PXRD) patterns.[47] Raman spectroscopy (Figure S4.2) permits a better differentiation between spinel-type LT-$LiCoO_2$ (*Fd3m*, four active bands around 605, 590, 484, and 449 cm^{-1}) and the layered HT form (*R-3m*, two active bands at 597 and 487 cm^{-1}.[48]

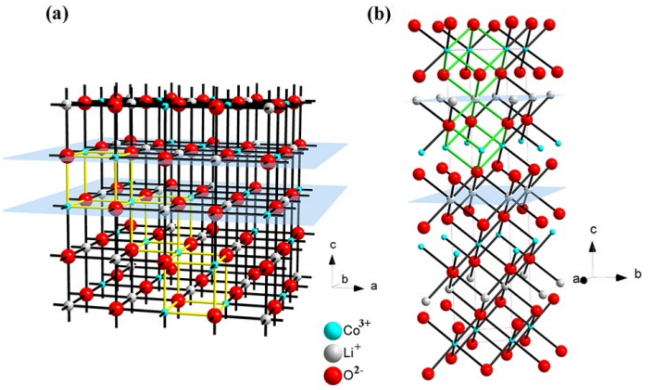

Figure 4.2. Structural models of (a) spinel-type LT-$LiCoO_2$ (yellow pattern: 3D Co-O-Co network composed of {Co_4O_4} cubane motifs) and (b) layered HT-$LiCoO_2$ (green pattern: 2D Co-O-Co layers separated by Li^+).

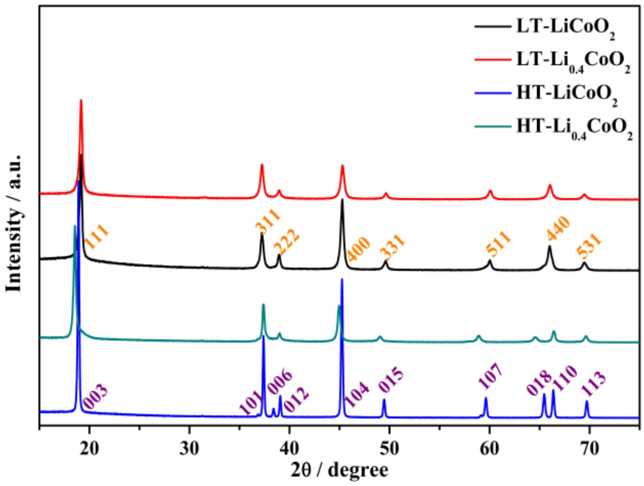

Figure 4.3. PXRD patterns of $LiCoO_2$ samples before and after delithiation.

Both fully lithiated starting materials were converted into LT-/HT-$Li_{0.4}CoO_2$, respectively, through chemical delithiation in a bromine-acetonitrile solution. Regardless of the treatment time (7 d were selected as the standard procedure for all WOCs discussed below), the degree of delithiation remained constant around $Li_{0.4}CoO_2$ for HT- and LT-phases (Table S4.6), which is in line with the reported lithium contents of 0.49 with bromine as oxidant and the degree of delithiation as a function of oxidation potential.[49]

Both HT- and LT-$Li_{0.4}CoO_2$ maintained their basic structural motifs after delithiation while exhibiting the expected lattice constant changes.[50] LT-$Li_{0.4}CoO_2$ undergoes contraction along *b* and *c* whereas HT-$Li_{0.4}CoO_2$ displays shortened *a* and *b* axes along with an expansion along *c* axe due to decreasing electrostatic attraction between the $\{CoO_6\}$ layers (Table S4.1). The slightly asymmetric peak profile of HT-$Li_{0.4}CoO_2$, in particular of the (003) reflection (Figure S4.5), may indicate the onset of sliding of the oxygen layers as observed for deeper delithiated Li_xCoO_2 phases ($x < 0.35$).[51] The HT form underwent peak broadening during delithiation which is ascribed to an increase in lattice strain, given that particle sizes and BET surface areas remain within the same order of magnitude for both modifications (Figures S3-S4 and Table S4.1).

4.3.2 Photochemical water oxidation performance

The photochemical water oxidation activity of pristine and delithiated LT/HT-$LiCoO_2$ was evaluated according to a standard protocol with $[Ru(bpy)_3]^{2+}$ as photosensitizer and $S_2O_8^{2-}$ as sacrificial electron acceptor. A 470 nm LED with an intensity of 5000 Lux was used as light source. Oxygen evolution was monitored by gas chromatography (GC) of the head space and by Clark electrode techniques in solution, respectively. To guarantee the comparability of the WOC activities between the four title compounds, the test conditions (e.g. pH, light intensity, buffer, stirring speed, degassing and ultrasonic dispersing times) for photocatalytic measurements were fixed and selected according to our previous studies.

In line with previous reports,[16] both Clark electrode (Figure 4.4) and GC (Figure 4.5) based results consistently indicate that spinel-type LT-$LiCoO_2$ is more active than layered HT-$LiCoO_2$ which produces only low quantities of oxygen.

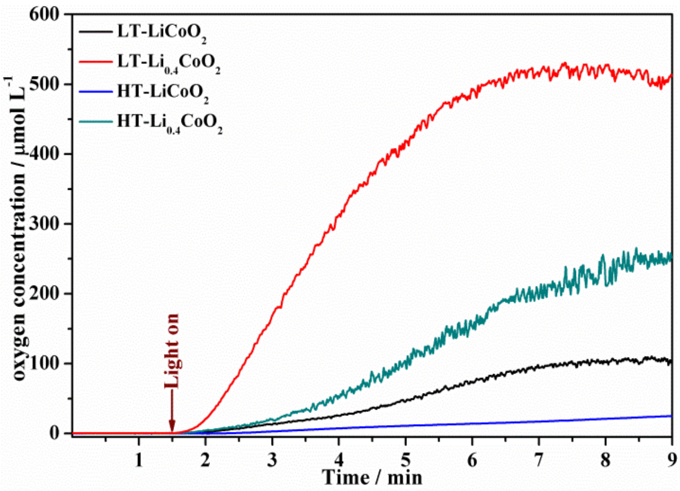

Figure 4.4. Oxygen evolution in solution for $LiCoO_2$ samples before and after delithiation (Clark electrode monitoring in solution; 10 mg WOC, 1.33 mM $[Ru(bpy)_3]Cl_2$, 26.25 mM $Na_2S_2O_8$, 8 mL pH 7 phosphate buffer in 0.1 M, 470 nm LED (5000 Lux intensity)).

Most importantly, the water oxidation activities of both compounds were notably enhanced after delithiation: LT-$Li_{0.4}CoO_2$ and HT-$Li_{0.4}CoO_2$ display 5- and 10-fold higher oxygen evolution in solution under equilibrium conditions (525 µmol/L and 250 µmol/L, respectively, cf. Figure 4.4) than the pristine spinel and layered oxides. Commercial Co_3O_4 nanoparticles were also investigated under the same conditions as reference sample. LT-$Li_{0.4}CoO_2$ produced an even slightly higher oxygen concentration after equilibrium was reached (Figure S4.9). As numerous previous studies revealed the significant influence of BET surface area on the water oxidation performance,[52-57] GC-based activities were furthermore normalized to BET surfaces. As shown in Figure 4.5, the productive effect of delithiation on the water oxidation activity remains significant after normalization: LT (2.1 raised to 10.9 µmol m^{-2}) and HT (1.0 to 9.8 µmol m^{-2}). Therefore, the remarkably enhanced water oxidation performance of both modifications cannot be solely explained with surface effects. These results are in line with our recent study on Co_3O_4 which indicates that surface area is not necessarily the most influential factor in water oxidation.[58] TOF values based on BET surface and oxygen evolution rate were compared to those of Co_3O_4 WOCs reported in our previous study (Table S4.1). The maximum TOF value of 9×10^{-3} µmol s^{-1} m^{-2} for LT-$Li_{0.4}CoO_2$ is 2.5 times higher than the TOF for nanocrystalline Co_3O_4 under identical measurement conditions.

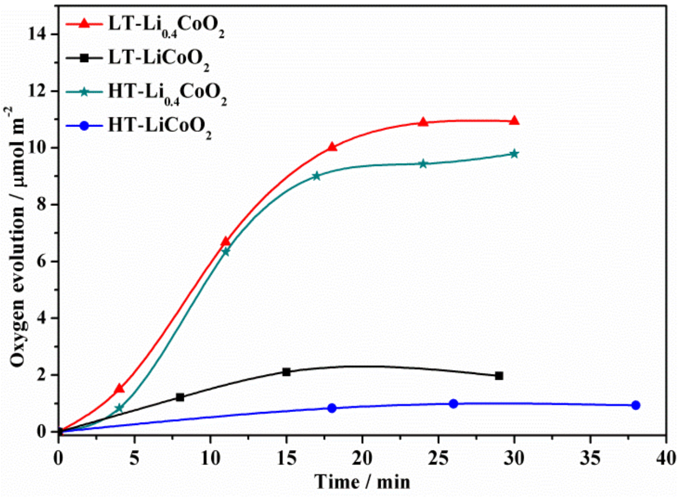

Figure 4.5. Oxygen evolution in solution for $LiCoO_2$ samples before and after delithiation normalized to BET surface area (GC detection in headspace; 10 mg WOC, 1.33 mM $[Ru(bpy)_3]Cl_2$, 26.25 mM $Na_2S_2O_8$, 8 mL pH 7 phosphate buffer, 470 nm LED (5000 Lux intensity)).

Cyclic voltammetry was further conducted to investigate the electrochemical water oxidation with the four lithium cobalt oxide compounds (Figure S4.9). In line with the photochemical results, the delithiated LT/HT-$Li_{0.4}CoO_2$ materials displayed higher activities than their pristine LT/HT-$LiCoO_2$ counterparts. However, the productive effect of delithiation on the electrochemical water oxidation performance is not as significant as on the photochemical process. These observations are well in line with ref. 45.

Generally, the electrochemical process differs considerably from photochemical conditions with respect to the accumulation of much higher charge densities on the electrode surfaces which leads to higher quantities of evolved oxygen. This is likely to exert a much more drastic impact on the catalyst properties than milder photochemical conditions. As for ref. 45, HRTEM investigations on the title catalysts indeed revealed the formation of an amorphous layer on the particle surface after electrochemical water oxidation while their surface was retained during the photochemical process. The stronger influence of electrochemical water oxidation on the nature of the catalyst compared to photochemical protocols has also been reported for prominent polynuclear cluster WOCs. Recent studies, for example, indicate that $[Co_4(H_2O)_2(\alpha\text{-}PW_9O_{34})_2]^{10-}$ operates as a homogeneous catalyst under photochemical conditions, while it is transformed into heterogeneous CoO_x catalysts in electrochemical setups.[59,60]

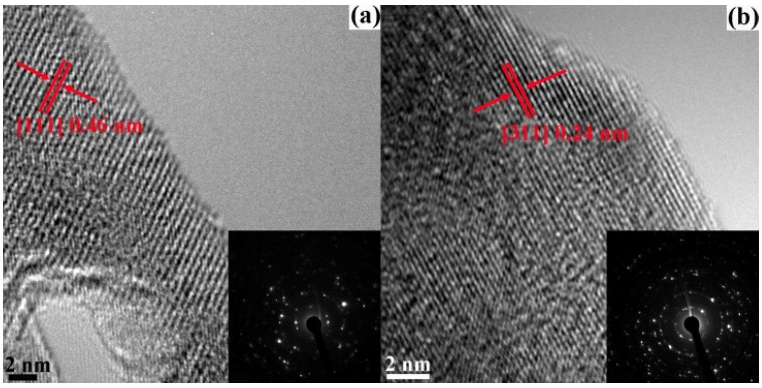

Figure 4.6. HR-TEM pictures of LT-$Li_{0.4}CoO_2$ before (a) and after (b) water oxidation (inset: SAED patterns, scale bar = 2 nm).

The essential catalytic role of delithiated LT-/HT-$Li_{0.4}CoO_2$ WOCs was verified by excluding the leached Co^{2+} as a significant contribution to of total water oxidation activity. As shown in Figure S4.11, nearly 1000-fold higher Co^{2+} concentration than the leached Co^{2+} from lithium cobalt oxides (Table S4.2) is required to obtain the comparable oxygen evolution amount to LT-$Li_{0.4}CoO_2$. Major structural changes during water oxidation were excluded through comparison of PXRD patterns of LT-$Li_{0.4}CoO_2$ before and after water oxidation (Figure S4.17). Co 2p, Co 3p and valence band spectra further confirm that LT-$Li_{0.4}CoO_2$ underwent no significant surface changes (Figure S4.18) during photochemical water oxidation. UV/Vis (Figure S4.19) and FT-IR spectra (Figure S4.20) of LT-$Li_{0.4}CoO_2$ indicate that the metallic properties (discussed below) were retained after water oxidation. In contrast, PXRD patterns of HT-$Li_{0.4}CoO_2$ displayed a broadening of the (003) reflection (Figure S4.22) after water oxidation, which points to an adjustment of the interlayer distance, probably through uptake of water or other species. The morphology of LT-$Li_{0.4}CoO_2$ before and after water oxidation was examined by HR-TEM (Figure 4.6). Different from electrochemical studies,[44, 61, 62] no amorphous layers were present on the edge of the particles after photochemical water oxidation. The lattice distances determined from HR-TEM images correspond well to the PXRD patterns, thereby excluding phase transitions after water oxidation. ^{18}O-labeling experiments identify water as the exclusive oxygen source, because the ratios between $^{16}O^{16}O$, $^{16}O^{18}O$ and $^{18}O^{18}O$ can fit well with theoretical values for the experimentally used 10 % ^{18}O containing water (Figures S4.54 – S4.57).

A previous study indicated that LT-$LiCoO_2$ is stable under photochemical conditions after a single water oxidation run.[16] Here, we further investigated the long term stability of all catalysts through five continuous water oxidation runs. Interestingly, the recovered LT-$LiCoO_2$, LT-$Li_{0.4}CoO_2$ and HT-$LiCoO_2$ even displayed increased water oxidation activity in the second run (Table S4.3). ICP-AES analyses of the supernatant solutions after the first run revealed minor lithium leaching (Table S4.2), which explains their improved water oxidation activity. In contrast, recovered HT-$Li_{0.4}CoO_2$ shows only ca. 50% catalytic activity in the second run (Figure S4.24) which is probably due to the above-mentioned structural adjustment ((003) peak broadening of PXRD pattern, Figure S4.22) after the first water oxidation cycle that outweighs the influence of delithiation. Further water oxidation runs led to decreased activity of all four WOCs (Figure S4.25-S4.27, Table S4.3). Nevertheless, LT-$Li_{0.4}CoO_2$ still displays the highest performance after five cycles. HR-TEM pictures (Figure S4.28) of LT-$Li_{0.4}CoO_2$ confirm the absence of amorphous layers even after the fifth run. PXRD (Figure S4.29-S4.32) and SAED patterns (Figure S4.28) as well as EXAFS spectra (Figure S4.35) ensured that the structure frameworks of the catalysts were retained after photochemical water oxidation. However, the observed significant reflection broadening of the PXRD patterns (Figure S4.31 and S4.32) implies decreasing crystallinity, which might be associated with an increase of lattice defects due to cobalt leaching (Table S4.2). These factors may explain the decrease in water oxidation activity after the second run.

In summary, delithiation significantly improved the water oxidation performance for both $LiCoO_2$ modifications, especially for HT-$LiCoO_2$ which underwent a transition from a nearly inactive material to an active water oxidation catalyst. This profound influence is not only exerted on photochemical water oxidation, but it is also evident from a significant transformation of the electronic structure. In the following, we investigate the influence of delithiation on the electronic properties in detail.

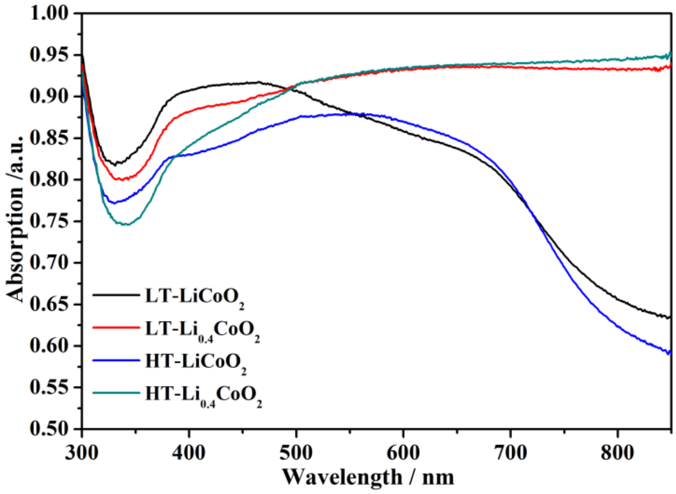

Figure 4.7. UV/Vis spectra of LT-$LiCoO_2$, HT-$LiCoO_2$, LT-$Li_{0.4}CoO_2$ and HT-$Li_{0.4}CoO_2$.

Regardless of their structural differences, both LT-$LiCoO_2$ and HT-$LiCoO_2$ display similar absorption properties in the visible light range with broad absorption edges around 700 to 750 nm. They are transformed into strong absorption bands extending beyond 850 nm (Figures 4.7 and S4.47) upon delithiation, implying significantly decreased band gaps (consistently determined from Tauc plots for $LiCoO_2$ as either direct or indirect semiconductor, cf. Figure S4.36). Furthermore, the disappearance of all characteristic FT-IR bands (Co-O and Li-O vibration modes) below ca. 600 cm^{-1} for LT-/HT-$Li_{0.4}CoO_2$ (Figures 4.8 and S4.46) along with the remarkably low transmission in the 700-1000 cm^{-1} range points to strong IR reflection by free electrons and to an emerging metallic character.[51] The formation of highly mobile holes in the Co 3d t_{2g} band upon delithiation is likely to reduce the characteristic wavelength-dependent absorption through oscillation to any incident frequency. Electrochemical impedance studies (Figure S4.38) revealed remarkable resistance decrease after delithiation, which further verifies the insulator (or semiconductor) to metal transition.

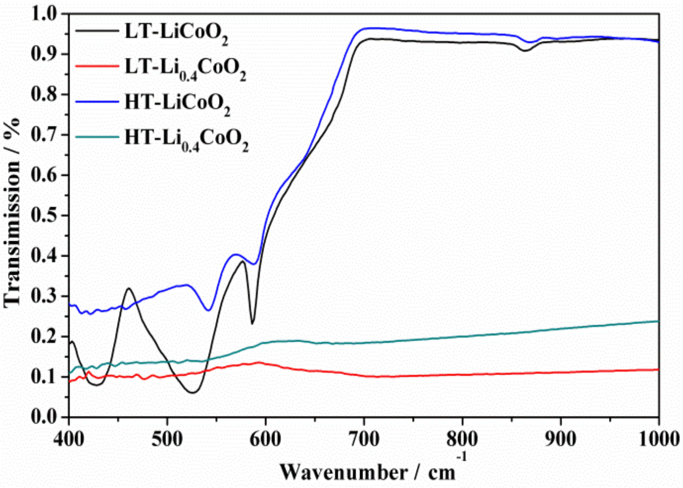

Figure 4.8. FT-IR spectra of LT-/HT-$LiCoO_2$ and LT-/HT-$Li_{0.4}CoO_2$.

Magnetic susceptibility measurements in combination with ^{7}Li NMR spectroscopy provided deeper insight into the positive effect of enhanced charge carrier mobility on the WOC activity of LT- and HT-$Li_{0.4}CoO_2$. The temperature-dependent magnetic susceptibilities of pristine and delithiated lithium cobalt oxides were recorded in heating and cooling mode, respectively, over the temperature range 5~300 K (Figure 4.9: minor hysteresis loop due to residual oxygen after evacuation (Figure S4.37)).[63] All samples exhibited paramagnetic behavior above 100 K, and straightforward Curie-Weiss fits afforded Curie constants (in emu K Oe^{-1} mol^{-1}) and effective magnetic moments (μ_{eff}, equal to charge carriers per cobalt atom) of 0.095 (0.33 μ_B) for both LT- and HT-$LiCoO_2$, compared to 0.315 (0.88 μ_B) and 0.236 (0.70 μ_B) for LT- and HT-$Li_{0.4}CoO_2$, respectively (cf. inset in Figure 4.9).

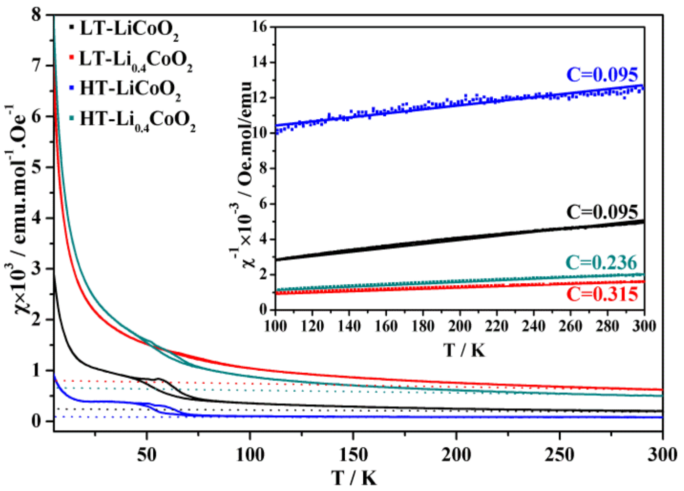

Figure 4.9. Temperature-dependent magnetic susceptibility of LT-/HT-$LiCoO_2$ and LT-/HT-$Li_{0.4}CoO_2$ in the 5-300 K range.

The slight deviation from the expected zero magnetic moment for pristine LT-/HT-$LiCoO_2$ is ascribed to defects or minor lithium nonstoichiometries which give rise to cobalt valence fluctuations. In contrast, the notably higher magnetic moments of the delithiated phases indicate the presence of significant amounts of paramagnetic LS Co^{4+} (LS: $t_{2g}^5e_g^0$, S=1/2) centers accompanied by an increasing fraction of electron vacancies (holes) in the valence band compared to the fully occupied 3d t_{2g} states of LT-/HT-$LiCoO_2$. Previous studies linked the temperature-independent susceptibility (indicated by dotted lines) to the presence of metallic Pauli-paramagnetism arising from itinerant charge carriers.[64,65] This effect is indeed far more pronounced for LT-/HT-$Li_{0.4}CoO_2$ than for fully lithiated LT-/HT-$LiCoO_2$. Most importantly, temperature-independent susceptibility and water oxidation activity display the same trend, implying a possible correlation between them.

^7Li magic-angle-spinning (MAS) NMR spectra for LT-/HT-$LiCoO_2$ display the expected main peaks at 0 ppm for Li^+ in a diamagnetic environment of LS Co^{3+} centers with symmetrically positioned sidebands (Figure 4.10).[63] Delithiation induces a split of the main peak into two peaks located at ca. 0 and 70 ppm for both LT- and HT-$Li_{0.4}CoO_2$, indicating the presence of two different lithium sites surrounded by diamagnetic and paramagnetic centers, respectively. The most intense peak underwent a Knight shift around 70 ppm arising from the presence of free electrons, thus providing evidence for the delocalization of t_{2g} holes,[63] in line with the temperature independent susceptibility data. HT-$Li_{0.4}CoO_2$

displays a considerable line broadening compared to the delithiated LT-spinel type which corresponds well with the presence of a shoulder for (003) reflection after delithiation (PXRD pattern, Figure 4.3), pointing to a higher degree of disorder in packing of the Co-O layers (*ab* planes in Figure 4.2) upon delithiation as well as intense lattice strains.

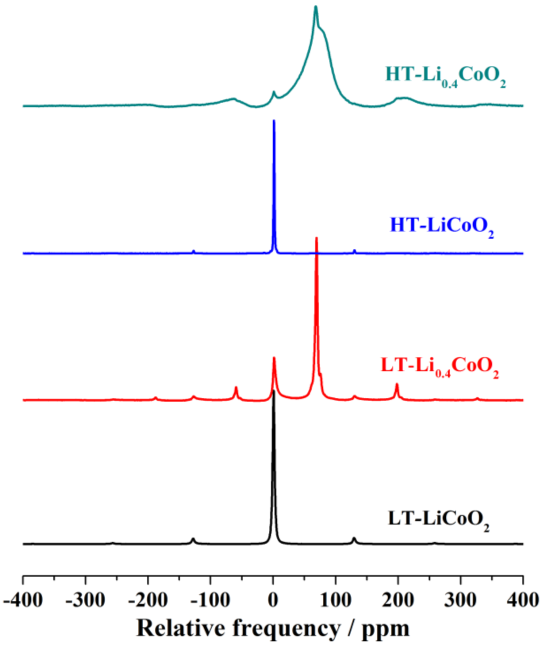

Figure 4.10. ^{7}Li-NMR MAS spectra of LT-/HT-$LiCoO_2$ and LT-/HT-$Li_{0.4}CoO_2$.

The oxidative effect of chemical delithiation is evident from the characteristic Co $2p_{3/2}$ and Co $2p_{1/2}$ XPS peaks located around 779 and 795 eV, respectively, as well as from their MLCT satellites at ca. 10 eV higher binding energies (Figure 4.11).[66] The broadening of the Co 2p peaks toward higher binding energy in combination with decreasing areas of the satellite peaks around 789 eV (grey areas in Figure 4.11) confirm the presence of Co^{4+} in LT-/HT-$Li_{0.4}CoO_2$. O 1s XPS spectra of all compounds (Figure 4.12) are constituted of three components around 529, 531 and 533 eV, respectively. Whereas the highest and lowest energy peaks can be well ascribed to surface absorbed oxygen molecular and lattice oxygen species, respectively, the assignment of the peak around 531 eV, which displays lower intensity after delithiation, is less straightforward and was controversially discussed in previous studies.

The decreased fraction of lattice oxygen species at around 529 eV together with an increased contribution from the middle peak most likely point to the partial oxidation of O^{2-} ions for overall charge compensation via Co t_{2g} hole delocalization after delithiation, resulting in stronger covalence of Co-O bonds and increased binding energy of lattice oxygen.[67-69] This hypothesis is further supported by the stronger dispersion and overlap of the Co 3d - minor Co 2p (0~2 eV) and O 2p (3 ~ 8 eV) valence band (Figure 4.13) as well as by the observed decrease in Co-O bond lengths (Table 4.1) after delithiation. Moreover, the onset shift of the valence band edges towards lower bond energies (i.e. closer to the e_g conduction band) for LT-/HT-$Li_{0.4}CoO_2$ is well in line with band gap narrowing determined from UV/Vis spectra (Figure S4.36).

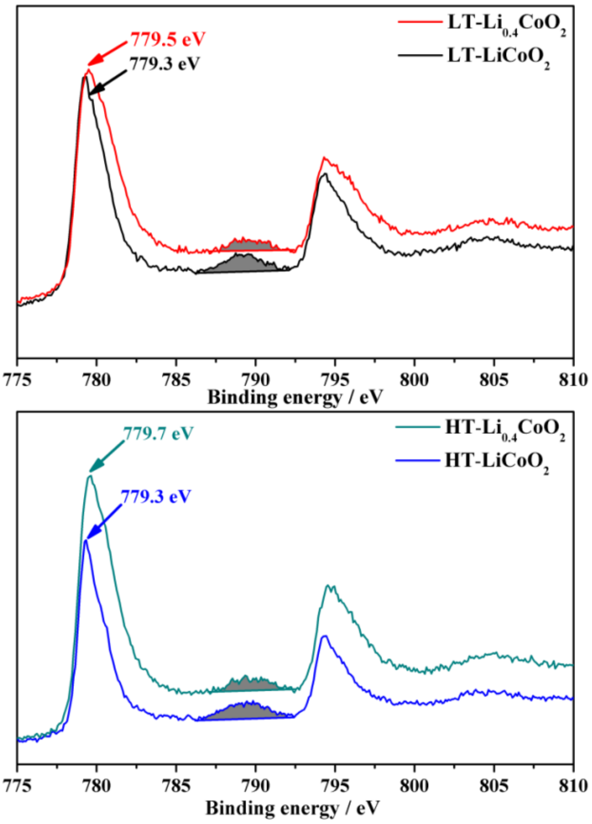

Figure 4.11. Co 2p XPS spectra of LT-/HT-$LiCoO_2$ and LT-/HT-$Li_{0.4}CoO_2$.

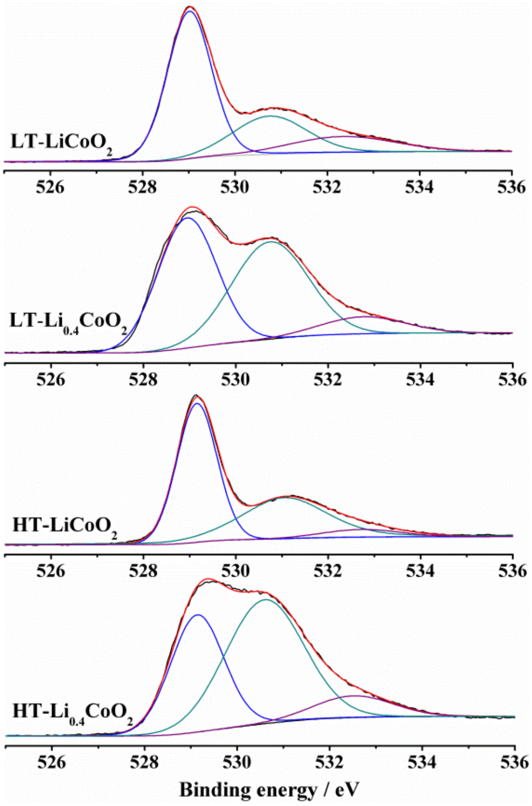

Figure 4.12. O_{1s} XPS spectra of LT-/HT-LiCoO$_2$ and LT-/ HT-Li$_{0.4}$CoO$_2$.

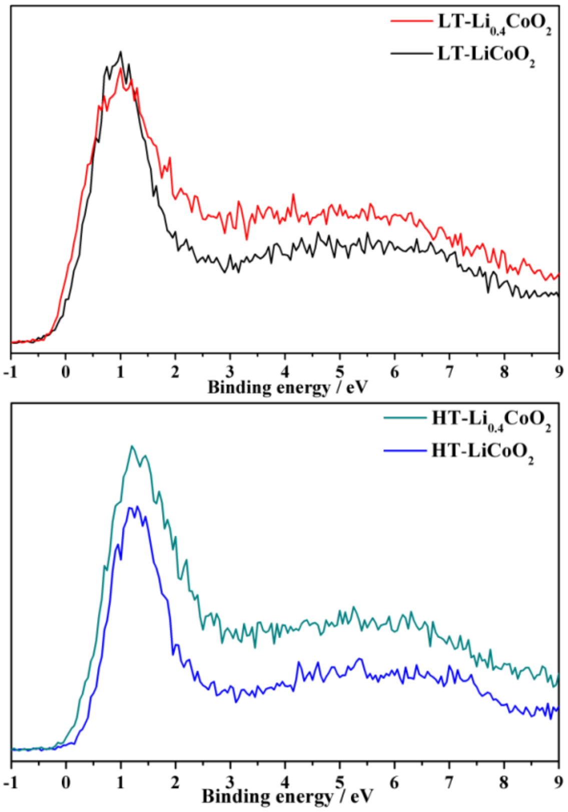

Figure 4.13. Valence band spectra of LT-/HT-LiCoO$_2$ and LT-/HT-Li$_{0.4}$CoO$_2$.

Table 4.1. Correlation between structure, delithiation, electronic properties and water oxidation performance of fully lithiated and delithiated $LiCoO_2$ WOCs.

WOC	Co-O network/ $\{Co_4O_4\}$	Co-O distance [Å]	Co-O hybrid.	μ_B	X_c* [emu/ (mol Oe)]	Resistance [kΩ (AC)]	Resistivity[71] [Ω/cm]	O_2 (abs.) [μmol]	O_2 (BET)# [μmol m^{-2}]
LT-$LiCoO_2$	3D/yes	1.9271(12)	weak	0.33	0.200	7	/	0.48	2.1
LT-$Li_{0.4}CoO_2$	3D/yes	1.8934(17)	strong	0.88	0.625	0.04	/	4.57	10.9
HT-$LiCoO_2$	2D/no	1.9159(7)	weak	0.33	0.084	700	5 (*ab* plane) 4000 (⊥ *ab* plane)	0.15	1.0
HT-$Li_{0.4}CoO_2$	2D/no	1.8697(17)	strong	0.70	0.514	30	0.009 (*ab* plane of $Li_{0.5}CoO_2$)	1.79	9.8

* X_c= temperature-independent susceptibility; # normalized to absolute surface area [BET × sample mass]

4.3.3 Correlation between structure, electronic properties and water oxidation activity

The corresponding effects of delithiation on water oxidation activity as well as on a wide range of spectroscopic characteristics imply a strong correlation between catalytic performance and electronic properties. Both temperature independent susceptibility and photochemical water oxidation activity display the same trend: LT-$Li_{0.4}CoO_2$ > HT-$Li_{0.4}CoO_2$ > LT-$LiCoO_2$ > HT-$LiCoO_2$. This suggests that itinerant charges, especially the mobile holes involved in water oxidation, could be the major driving force for the activity improvement. Enhanced hole mobility after delithiation is furthermore evident from multiple characterizations: (a) pronounced metallic character (cf. UV/Vis-, FT-IR-, ^{7}Li-NMR spectra), (b) formation of Co^{4+} centers which give rise to higher hole concentrations in the valence band (reflected in higher magnetic moments) and (c) enhanced hybridization of Co 3d and O 2p bands (cf. valence band and O 1s XPS spectra) resulting in improved Co 3d t_{2g} hole mobility. These electronic properties transition upon delithiation were further complemented with DFT calculations (Figures S4.40 and S4.41).

The remarkably higher carrier mobility is furthermore illustrated by a sharp decrease of AC resistance upon delithiation (from 7 to 0.04 kΩ for LT-forms and from 700 to 30 kΩ for HT-forms, Table 4.1). Due to the anisotropic conductivity of the HT structure, polycrystal-based measurements lead to significantly overestimated resistance for HT-$LiCoO_2$ and HT-$Li_{0.4}CoO_2$. A more balanced comparison between LT and HT forms would require anisotropic conductivity measurements on single crystalline samples.[70,71]

The conductivity properties (anisotropic or isotropic) of the two $LiCoO_2$ modifications can be directly correlated to the presence or absence of $\{Co_4O_4\}$ units. As the conductivity is arising from electron transport through Co 3d - O 2p covalent interaction, the presence of $\{Co_4O_4\}$ in LT-$LiCoO_2$ and LT-$Li_{0.4}CoO_2$ extends the Co-O-Co bonds into a 3D network (yellow traces in Figure 4.2) and facilitates hole transfer in all directions, while the absence of $\{Co_4O_4\}$ units in HT-$LiCoO_2$ and HT-$Li_{0.4}CoO_2$ limits the hole transfer in a single 2D Co-O-Co layer (*ab* planes in Figure 4.2). This explains the higher water oxidation activity (before normalization) for LT-$LiCoO_2$ and LT-$Li_{0.4}CoO_2$ compared to HT-$LiCoO_2$ and HT-$Li_{0.4}CoO_2$, respectively. Analogously, a most recent study on $LiCoO_2$ for electrochemical water oxidation and oxygen reduction also revealed the impact of charge transfer processes on the catalytic activity.[72]

The water oxidation activity of a given catalyst such as perovskite and lithium battery materials was claimed to be strongly influenced by their surface states. However, recent studies also showed that the activities of two representative materials may still vary, even if they form virtually identical Co-Pi layers on their surface under electrochemical water oxidation conditions. Consequently, the overall water oxidation performance was not solely determined by these Co-Pi layers but also partially arose from the bulk substrate.[44] Furthermore, a recent investigation of perovskite materials for electrochemical water oxidation revealed the influence of substrates and bulk conductivity on water oxidation as well.[73]

The mechanisms of O-O bond formation are currently in the focus of manifold studies,[74-77] while less emphasis was placed on relationships between electronic properties and dye-sensitized charge transfer processes. The complex and heterogeneous hole scavenging steps between oxide WOCs and $[Ru(bpy)_3]^{3+}$ (cf. Figure 4.1) are currently under mechanistic and kinetic investigation.[78-80] As four hole transport steps are required for the formation of an O_2 molecule, the efficiency of hole transfer across the WOC and the heterogeneous interface is very likely to be a crucial step. Acceleration of water oxidation kinetics by WOCs with increased Co-O bond covalence was ascribed to a stronger affinity between cobalt sites and surface absorbed oxygen species (such as hydroxyl groups).[43] However, further investigations are necessary whether this increased affinity also facilitates the interface hole transfer between WOCs and incoming oxygen species.

The present results demonstrate that the absence of a 3D conducting network in HT-$LiCoO_2$ can be overcompensated through delithiation with significantly enhanced covalent character of Co-O bonds. The major correlations between structure, electronic properties and water oxidation activity can be summarized as follows: (1) delithiation of both $LiCoO_2$

modifications leads to increased hole concentration together with more covalent and shorter Co-O bonds; (2) the presence of $\{Co_4O_4\}$ motifs expands Co-O-Co pathways into a 3D charge carrier transportation network with isotropic conductivity; (3) chemical delithiation further strengthens this role of $\{Co_4O_4\}$ motifs; (4) the improvement of water oxidation activity caused by both delithiation and $\{Co_4O_4\}$ motifs can be consistently explained by enhanced hole mobility. Noteworthy the role of hole mobility was further confirmed by our current study on a related material systems whose photochemical water oxidation activities can be flexibly tailored by their tunable hole mobility.

4.4 Conclusions

The HT- and LT-forms of $LiCoO_2$ featuring 3D bio-mimetic $\{Co_4O_4\}$ cubane motifs and 2D layer structures, respectively, were selected as models to study the correlation between structure, electronic properties and dye-sensitized photocatalytic water oxidation. Chemical delithiation of both forms results in significantly improved water oxidation activity compared to the fully lithiated parent compounds. This performance enhancement goes hand in hand with a significant transition of the electronic properties towards metallic behavior upon delithiation. Characterization of the electronic structure with a wide spectrum of analytical techniques indicates that hole mobility is most likely to be the major driving force behind the enhanced water oxidation activity. Cuboidal $\{Co_4O_4\}$ motifs were identified as the basic building blocks of 3D Co-O-Co charge transport networks for enhanced hole transfer efficiency. Their networking role is further reinforced through stronger covalent character of the Co-O bonds after delithiation. These results pave the way to new optimization strategies for water oxidation catalysts through combined control over structural and electronic properties.

References

[1] R. Pokhrel, G. W. Brudvig. *Phys. Chem. Chem. Phys*. **2014**, *16*, 11812-11821.

[2] N. Cox, D. A. Pantazis, F. Neese, W. Lubitz. *Acc. Chem. Res*. 2013, *46*, 1588-1596.

[3] H. Dau, I. Zaharieva, M. Haumann. *Curr. Opin. Chem. Biol.* 2012, *16*, 3-10.

[4] E. Y. Tsui, T. Agapie. *Proc. Natl. Acad. Sci. USA* **2013**, *110*, 10084-10088.

[5] S. Mukherjee, J. A. Stull, J. Yano, T. C. Stamatatos, K. Pringouri, T. A. Stich, K. A. Abboud, R. D. Britt, V. K. Yachandra, G. Christou. *Proc. Natl. Acad. Sci. USA* 2012, *109*, 2257-2262.

[6] D. Shevchenko, M. F. Anderlund, S. Styring, H. Dau, I. Zaharieva, A. Thapper. *Phys. Chem. Chem. Phys*. 2014, *16*, 11965-11975.

[7] N. S. McCool, D. M. Robinson, J. E. Sheats, G. C. Dismukes. *J. Am. Chem. Soc.* **2011**, *133*, 11446-11449.

[8] B. Zhang, F. Li, F. Yu, X. Wang, X. Zhou, H. Li, Y. Jiang, L. Sun. *ACS Catal.* 2014, *4*, 804-809.

[9] S. Berardi, G. L. Ganga, M. Natali, I. Bazzan, F. Puntoriero, A. Sartorel, F. Scandola, S. Campagna, M. Bonchio. *J. Am. Chem. Soc.* 2012, *134,* 11104-11107.

[10] P. F. Smith, C. Kaplan, J. E. Sheats, D. M. Robinson, N. S. McCool, N. Mezle, G. C. Dismukes. *Inorg. Chem.* 2014, *53*, 2113-2121.

[11] Z. Xu, F. Li, H. Li, B. Zhang, F. Yu, L. Sun. *ChemSusChem* 2014, *7*, 2453-2456.

[12] G. L. Ganga, V. M. Nardo, M. Cordaro, M. Natali, S. Vitale, A. Licciardello, F. Nastasi, S. Campagna. *Dalton Trans.* 2014, *43*, 14926-14930.

[13] F. Evangelisti, R. Güttinger, R. Moré, S. Luber, G. R. Patzke *J. Am. Chem. Soc.* 2013, *135,* 18734-18737.

[14] Y. Gao, R. H. Crabtree, G. W. Brudvig. *Inorg. Chem.* 2012, *51*, 4043-4050.

[15] D. M. Robinson, Y. B. Go, M. Greenblatt, G. C. Dismukes. *J. Am. Chem. Soc.* **2010**, *132*, 11467-11469.

[16] G. P. Gardner, Y. B. Go, D. M. Robinson, P. F. Smith, J. Hadermann, A. Abakumov, M. Greenblatt, G. C. Dismukes. *Angew. Chem. Int. Ed.* 2012, *51*, 1616-1619.

[17] A. Iyer, J. Del-Pilar, C. K. King'ondu, E. Kissel, H. F. Garces, H. Huang, A. M. El-Sawy, P. K. Dutta, S. L. Suib. *J. Phys. Chem. C* 2012, *116*, 6474-6483.

[18] M. M. Najafpour, T. Ehrenberg, M. Wiechen, P. Kurz. *Angew. Chem. Int. Ed.* 2010, *49*, 2233-2237.

[19] M. M. Najafpour, T. Ehrenberg, M. Wiechen, P. Kurz. *Angew. Chem. Int. Ed.* 2010, *49*, 2233-2237.

[20] M. Wiechen, I. Zaharieva, H. Dau, P. Kurz. *Chem. Sci.* 2012, *3*, 2330-2339.

[21] K. Jin, J. Park, J. Lee, K. Yang, G. K. Pardhan, U. Sim, D. Jeong, H. L. Jang, S. Park, D. Kim, N.-E. Sung, S. H. Kim, S. Han, K. T. Nan. *J. Am. Chem. Soc.* **2014**, *136*, 7435-7443.

[22] V. B. R. Boppana, S. Yusuf, G. S. Hutchings, F. Jiao. *Adv. Funct. Mater.* **2013**, *23*, 878-884.

[23] D. Hong, Y. Yamada, A. Nomura, S. Fukuzumi. *Phys. Chem. Chem. Phys.* **2013**, *15*, 19125-19128.

[24] R. K. Hocking, R. Brimblecombe, L.-Y. Chang, A. Singh, M. H. Cheah, C. Glover, W. H. Casey, L. Spiccia. *Nat. Chem.* **2011**, *3*, 461-466.

[25] X.-B. Han, Z.-M. Zhang, T. Zhang, Y.-G. Li, W. Lin, W. You, Z.-M. Su, E.-B. Wang. *J. Am. Chem. Soc.* **2014**, *136,* 5359-5366.

[26] Q. S. Yin, J. M. Tan, C. Besson, Y. V. Geletii, D. G. Musaev, A. E. Kuznetsov, Z. Luo, K. I. Hardcastle, C. L. Hill. *Science* **2010**, *328*, 342-345.

[27] H. Lv, J. Song, Y. V. Geletii, J. W. Vickers, J. M. Sumliner, D. G. Musaev, P. Kögerler, P. F. Zhuk, J. Bacsa, G. Zhu, C. L. Hill. *J. Am. Chem. Soc.* **2014**, *136*, 9268-9271.

[28] R. Al-Oweini, A. Sartorel, B. S. Bassil, M. Natali, S. Berardi, F. Scandola, U. Kortz, M. Bonchio. *Angew. Chem. Int. Ed.* **2014***, 53*, 11182-11185.

[29] G. F. Swiegers, J. K. Clegg, R. Stranger.*Chem. Sci.* **2011**, *2*, 2254-2262.

[30] M. W. Kanan, D. G. Nocera. *Science* **2008**, *321*, 1072-1075.

[31] R. D. L. Smith, M. S. Prévot, R. D. Fagan, Z. Zhang, P. A. Sedach, M. K. J. Siu, S. Trudel, C. P. Berlinguette. *Science* **2013**, *340*, 60-63.

[32] M. Rish, K. Klingan, F. Rigleb, P. Chernev, I. Zaharieva, A. Fischer, H. Dau. *ChemSusChem* **2012**, *5*, 542-549.

[33] A. Indra, P. Menezes, I. Zaharieva, E. Baktash, J. Pfrommer, M. Schwarze, H. Dau, M. Driess. *Angew. Chem. Int. Ed.* **2013**, *52*, 13206-13210.

[34] L. Kuai, J. Geng, C. Chen, E. Kan, Y. Liu, Q. Wang, B. Geng. *Angew. Chem. Int. Ed.* **2014**, 53, 7547-7551.

[35] M. Risch, V. Khare, L. Zaharieva, L. Gerencser, H. Dau. *J. Am. Chem. Soc.* **2009**, *131,* 6936-6937.

[36] M. W. Kanan, J. Yano, Y. Surendranath, M. Dincă, V. K. Yachandra, D. G. Nocera. *J. Am. Chem. Soc.* **2010**, *132,* 13692-13701.

[37] J. B. Gerken, J. G. McAlpin, J. Y. C. Chen, M. L. Rigsby, W. H. Casey, R. D. Britt, S. S. Stahl. *J. Am. Chem. Soc.* **2011**, *133,* 14431-14442.

[38] T. Zidki, L. Zhang, V. Shafirovich, S. V. Lymar. *J. Am. Chem. Soc.* **2012**, *134,* 14275-14278.

[39] S. J. Kim, Y. Lee, D. K. Lee, J. W. Lee, J. K. Kang. *J. Mater. Chem. A* **2014**, *2*, 4136-4139.

[40] R. Subbraman, D. Tripkovic, K.-C. Chang, D. Strmcnik, A. P. Paulikas, P. Hirunsit, M. Chan, J. Greeley, V. Stamenkovic, N. M. Markovic. *Nat. Mater.* **2012**, *11*, 550-557.

[41] A. M. Ullman, Y. Liu, M. Huynh, D. K. Bediako, H. Wang, B. L. Anderson, D. C. Powers, J. J. Breen, H. D. Abruna, D. G. Nocera. *J. Am. Chem. Soc.* **2014**, *136*, 17681-17688

[42] T. Maiyalagan, K. A. Jarvis, T. Soosairaj, P. J. Ferreira, A. Manthiram. *Nat. Commun.* **2014**, *5*, 3949.

[43] Z. Lu, H. Wang, D. Kong, Y. Yan, P.-C. Hsu, G. Zheng, H. Yao, Z. Liang, X. Sun, Y. Cui. *Nat. Commun.* **2014**, *5*, 4345.

[44] S. W. Lee, C. Carlton, M. Risch, Y. Surendranath, S. Chen, A. Furutsuki, A. Yamada, D. G. Nocera, Y. Shao-Horn. *J. Am. Chem. Soc.* **2012**, *134*, 16959-16962.

[45] A. Indra, P. W. Menezes, N. R. Sahraie, A. Bergmann, C. Das, M. Tallarida, D. Schmeiβer, P. Strasser, M. Driess. *J. Am. Chem. Soc.* **2014**, *136*, 17530-17536.

[46] B. Ravel, M. Newville. *J. Synchrotron Rad.* **2005***, 12*, 537-541.

[47] H. Porthault, R. Baddour-Hadjeanc, F. L. Cras, C. Bourbon, S. Franger. *Vib. Spectrosc.* **2012**, *62*, 152-158.

[48] W. Huang, R. Frech. *Solid State Ionics* **1996**, *86-88*, 395-400.

[49] M. Valkeapää, Y. Katsumata, I. Asako, T. Motohashi, T. S. Chan, R. S. Liu, J. M. Chen, H. Yamauchi, M. Karppinen. *J. Solid State Chem.* **2007**, *180*, 1608-1615.

[50] F. Nobili, S. Dsoke, M. Minicucci, F. Croce, R. Marassi. *J. Phys. Chem. B* **2006**, *110*, 11310-11313.

[51] R. V. Chebiam, F. Prado, A. Manthiram. *Chem. Mater.* **2001**, *13,* 2951-2957.

[52] F. Jiao, H. Frei. *Angew. Chem. Int. Ed.* **2009**, *48*, 1841-1844.

[53] C.-C. Yang, T. M. Eggenhuisen, M. Wolters, A. Agiral, H. Frei, P. E. Jongh, K. P. Jong, G. Mul. *ChemCatChem* **2013**, *5*, 550-556.

[54] J. Rosen, G. S. Hutchings, F. Jiao. *J. Am. Chem. Soc.* **2013**, *135*, 4516-4521.

[55] M. Grzelczak, J. Zhang, J. Pfrommer, J. Hartmann, M. Driess, M. Antonietti, X. Wang. *ACS Catal.* **2013**, *3*, 383-388.

[56] J. D. Blakemore, H. B. Gray, J. R. Winkler, A. M. Müller. *ACS Catal.* **2013**, *3*, 2497-2500.

[57] H. S. Ahn, J. Yano, T. D. Tilley. *Energy Environ. Sci*. **2013**, *6*, 3080-3087.

[58] H. Liu, G. R. Patzke. *Chem. Asian J.* **2014**, *9*, 2249-2259.

[59] J. W. Vickers, H. Lv, J. M. Sumliner, G. Zhu, Z. Luo, D. G. Musaev, Y. V. Geletii, C. L. Hill. *J. Am. Chem. Soc.* **2013**, *135*, 14110-14118.

[60] J. J. Stracke, R. G. Finke. *J. Am. Chem. Soc.* **2011**, 133, 14872-14875.

[61] K. J. May, C. E. Carlton, K. A. Stoerzinger, M. Risch, J. Suntivich, Y.-L. Lee, A. Grimaud, Y. Shao-Horn. *J. Phys. Chem. Lett.* **2012**, *3*, 3264-3270.

[62] A. Grimaud, K. J. May, C. E. Carlton, Y.-L. Lee, M. Risch, W. T. Hong, J. Zhou, Y. Shao-Horn. *Nat. Commun*. **2013**, *4*, 2439.

[63] S. Levasseur, M. Ménétrier, Y. Shao-Horn, L. Gautier, A. Audemer, G. Demazeau, A. Largeteau, C. Delmas. *Chem. Mater.* **2003**,*15,* 348-354.

[64] T. Motohashi, T. Ono, Y. Katsumata, R. Kanno, M. Karppinen, H. Yamauchi. *J. Appl. Phys.* **2008**, *103*, 07C902.

[65] T. Motohashi, Y. Katsumata, T. Ono, R. Kanno, M. Karppinen, H. Yamauchi. *Chem. Mater.* **2007**, *19*, 5063-5066.

[66] A. T. Appapillai, A. N. Mansour, J. Cho, Y. Shao-Horn. *Chem. Mater.* **2007**, *19*, 5748-5757.

[67] W.-S. Yoon, K.-B. Kim, M.-G. Kim, M.-K. Lee, H.-J. Shin, J.-M. Lee, C.-H. Yo. *J. Phys. Chem. B* **2002**, *106*, 2526-2532.

[68] M. K. Aydinol, A. F. Kohan, G. Ceder, K. Cho, J. Joannopoulos. *Phys. Rev. B: Condens. Mater.* **1997**, *56*, 1354-1365.

[69] V. R. Galakhov, M. Neumann, D. G. Kellerman. *Appl. Phys A* **2009**, *94*, 497-500.

[70] Y. Takahashi, N. Kijima, K. Tokiwa, T. Watanabe, J. Akimoto. *J. Phys.: Condens. Matter.* **2007**, *19*, 436202.

[71] Y. Takahashi, Y. Gotoh, J. Akimoto, S. Mizuta, K. Tokiwa, T. Watanabe. *J. Solid State Chem.* **2002**, *164*, 1-4.

[72] B. Han, D. Qian, M. Risch, H. Chen, M. Chi, Y. S. Meng, Y. Shao-Horn. *J. Phys. Chem. Lett.* **2015**, *6*, 1357-1362.

[73] K. A. Stoerzinger, W. S. Choi, H. Jeen, H. N. Lee, Y. Shao-Horn. *J. Phys. Chem. Lett.* **2015**, *6*, 487-492.

[74] M. Hatakeyama, H. Nakata, M. Wakabayashi, S. Yokojima, S. Nakamur. *J. Phys. Chem. A* **2012**, *116*, 7089-7097.

[75] G. Mattioli, P. Giannozzi, A. A. Bonapasta, L. Guidoni. *J. Am. Chem. Soc.* **2013**, *135*, 15353-15363.

[76] M. Zhang, M. de Respinis, H. Frei. *Nat. Chem.* **2014**, *6*, 362-367.

[77] X. Li, P. E. M. Siegbahn. *J. Am. Chem. Soc.* **2013**, *135*, 13804-13813.

[78] X. Xiang, J. Fielden, W. E. Rodriguez-Cordoba, Z. Huang, N. Zhang, Z. Luo, D. G. Musaev, T. Lian, C. L. Hill. *J. Phys. Chem. C* **2013**, *117*, 918-926.

[79] H. S. Soo, A. Agiral, A. Bachmeier, H. Frei. *J. Am. Chem. Soc.* **2012**, *134*, 17104-17116.

[80] A. Agiral, H. S. Soo, H. Frei. *Chem. Mater.* **2013**, *25*, 2264-2273.

Appendix

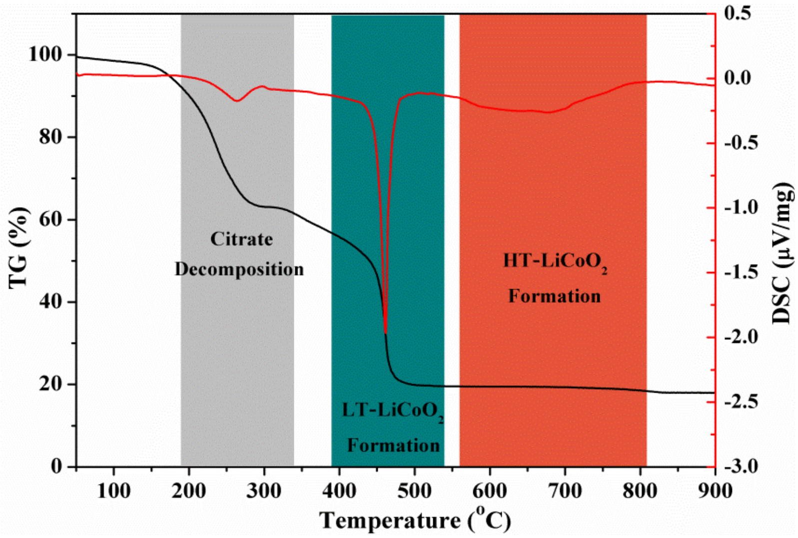

Figure S4.1. TG-DSC measurements monitoring the conversion of gel precursors into $LiCoO_2$ oxides.

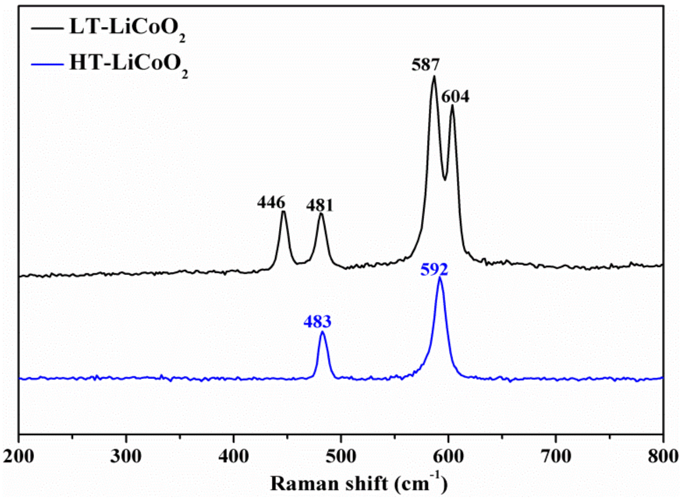

Figure S4.2. Raman spectra of LT-/HT-$LiCoO_2$ (recorded with a 514 nm laser probe).

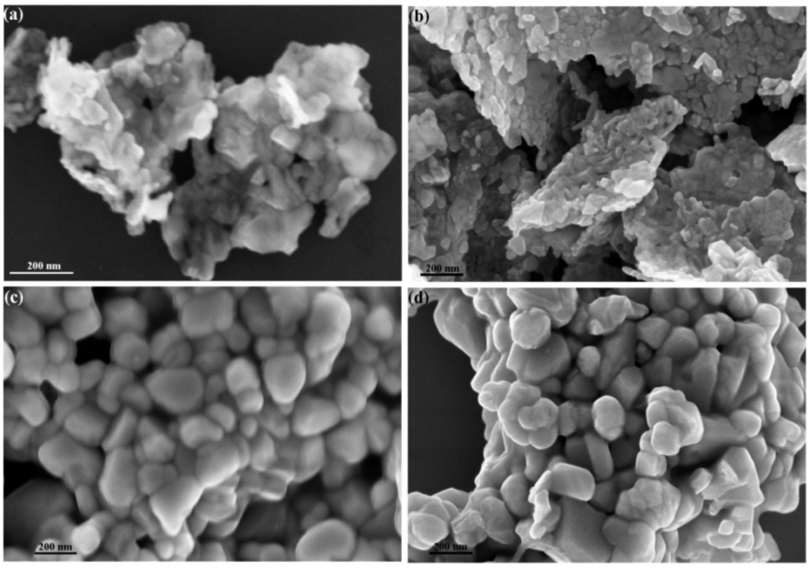

Figure S4.3. Representative SEM images of lithium cobalt oxides: (a) LT-$LiCoO_2$, (b) LT-$Li_{0.4}CoO_2$, (c) HT-$LiCoO_2$ and (d) HT-$Li_{0.4}CoO_2$.

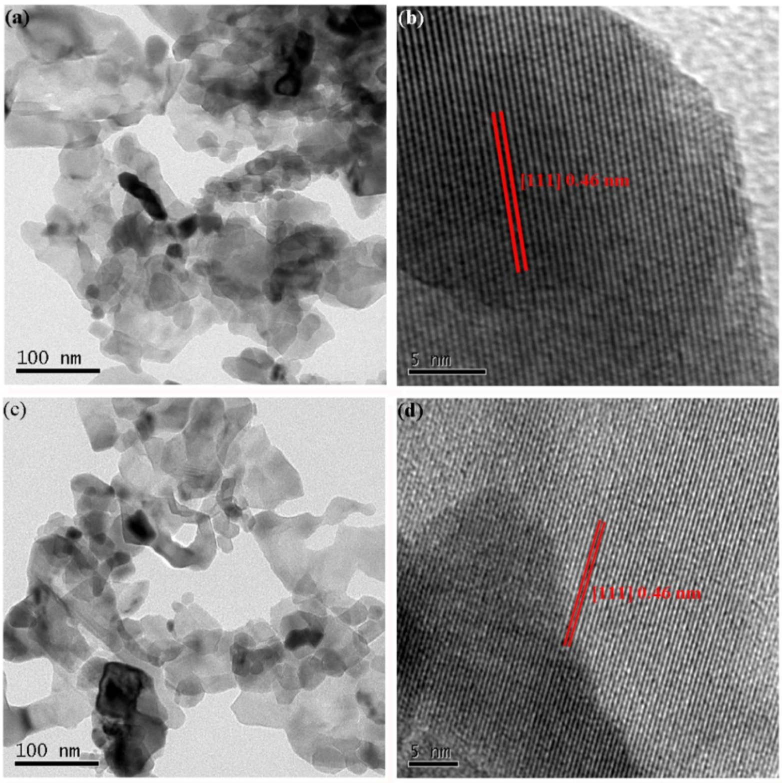

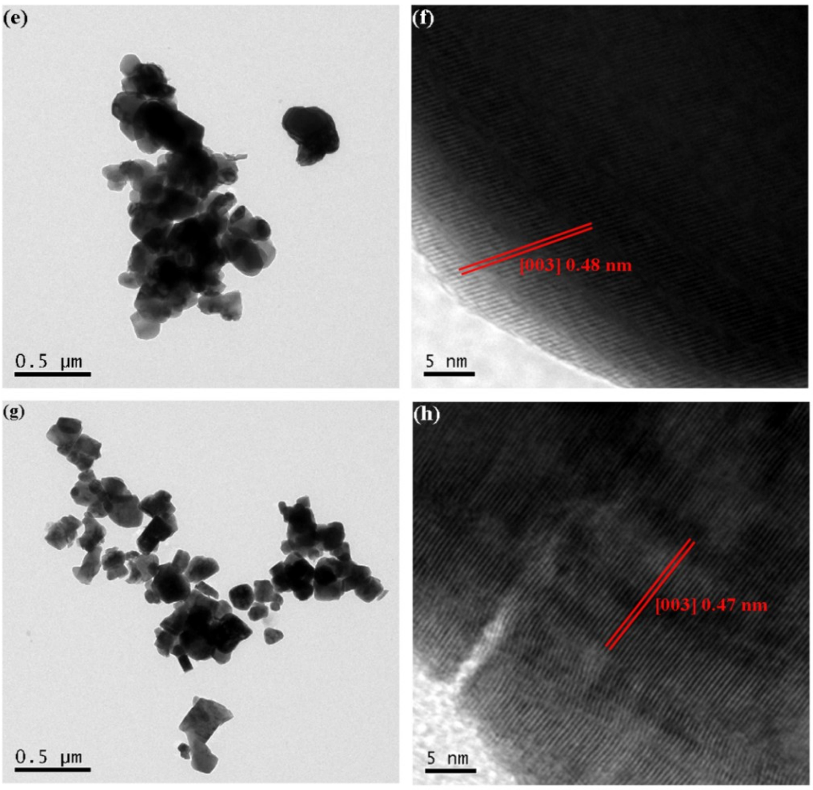

Figure S4.4. Representative TEM images of lithium cobalt oxides: (a, b) LT-$LiCoO_2$, (c, d) LT-$Li_{0.4}CoO_2$, (e, f) HT-$LiCoO_2$ and (g, h) HT-$Li_{0.4}CoO_2$.

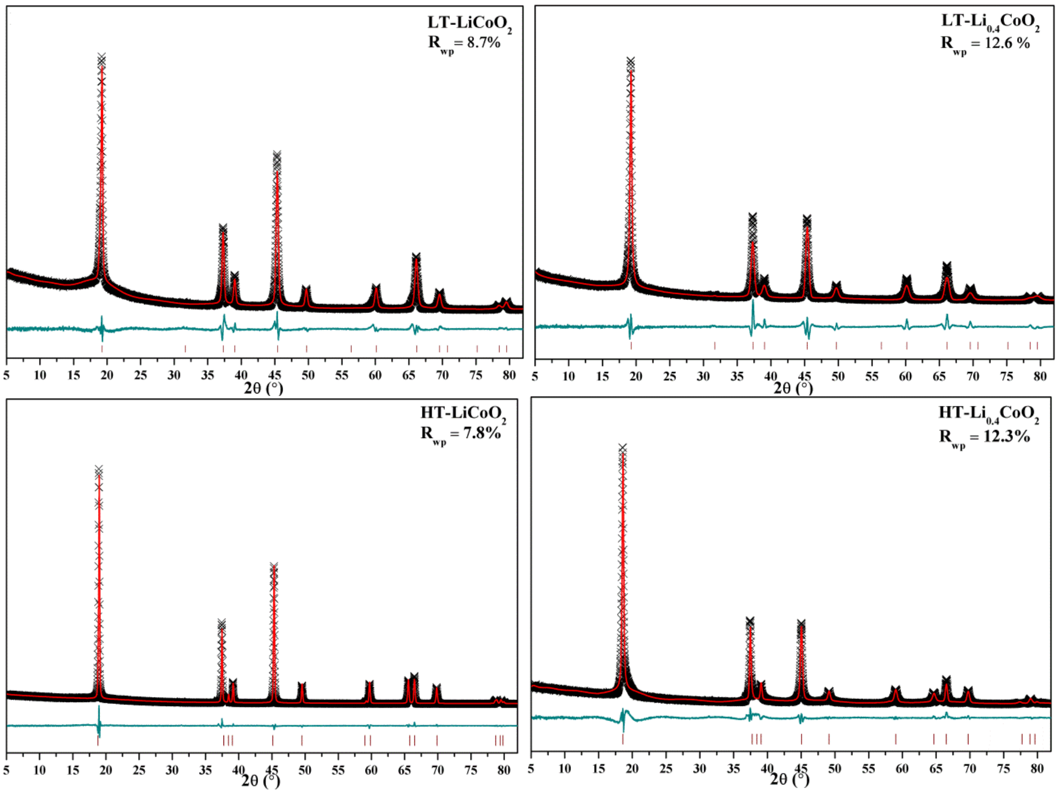

Figure S4.5. Rietveld refinement of PXRD patterns of lithium cobalt oxides (── Calculated; ── Difference; × Observed; │ Brag reflection position).

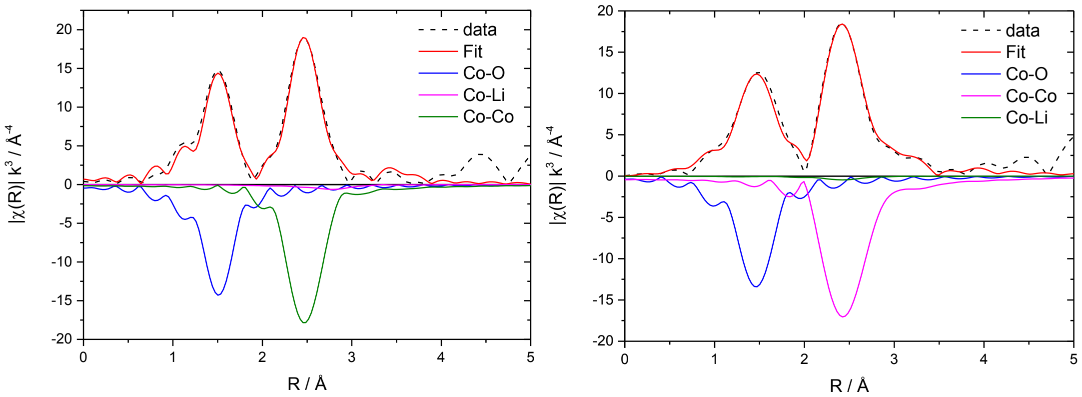

Figure S4.6. Fourier transformed EXAFS regions for LT-$Li_{0.4}CoO_2$ (left) and HT-$Li_{0.4}CoO_2$ (right). Negative signals represent the major scattering paths of Co-Co and Co-O.

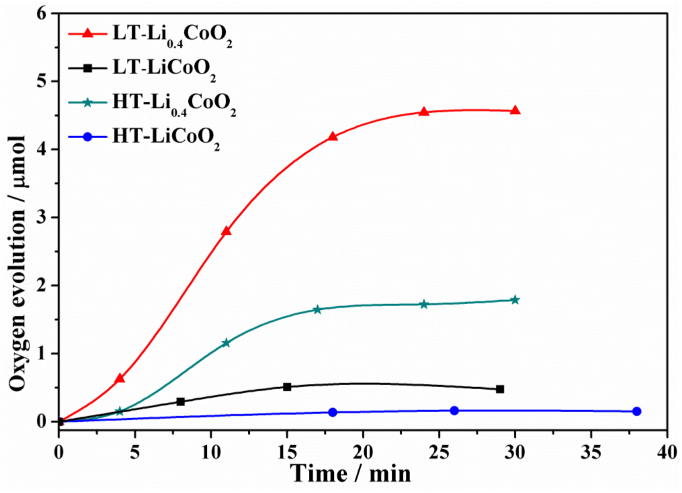

Figure S4.7. Quantification of oxygen evolution activity of pristine and delithiated lithium cobalt oxides (gas chromatography data).

The total amount of oxygen evolved by LT-$Li_{0.4}CoO_2$ and HT-$Li_{0.4}CoO_2$ determined by GC (4.5 µmol and 1.7 µmol), respectively, is more or less consistent with the oxygen quantities calculated from Clark electrode data (LT-$Li_{0.4}CoO_2$: 520 µmol/L× 0.008 L= 4.16 µmol; HT-$Li_{0.4}CoO_2$: 240 µmol/L× 0.008 L= 1.92 µmol). Taking into account the oxygen distribution between solution and headspace, separate monitoring of both sections by the different techniques may not afford completely identical results.

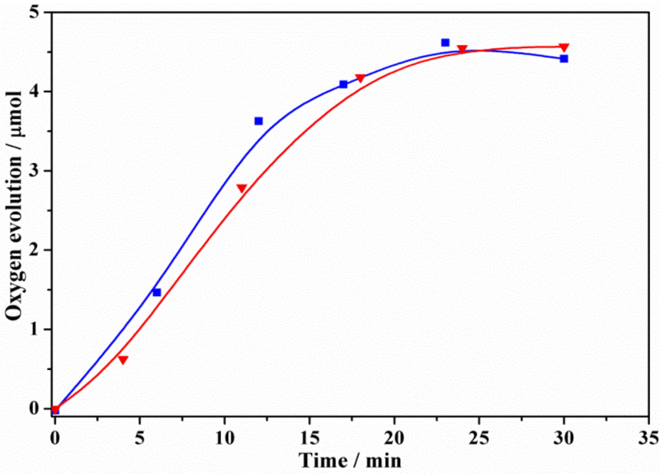

Figure S4.8. Reproducible GC measurement runs of oxygen evolution with LT-$Li_{0.4}CoO_2$.

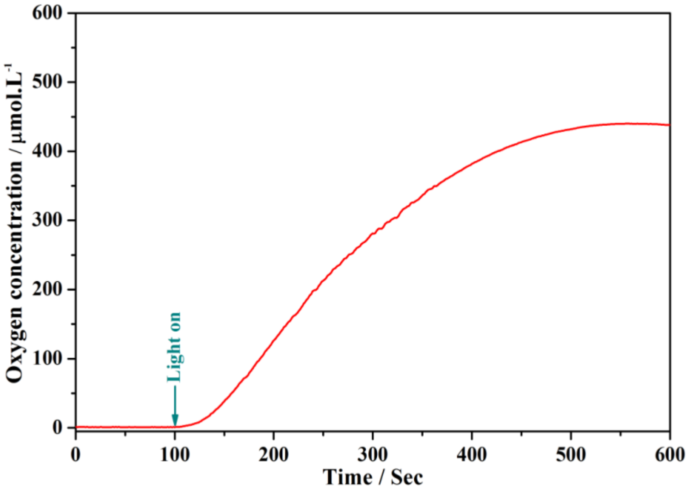

Figure S4.9. Water oxidation with commercial Co_3O_4 (Clark electrode measurements).

Table S4.1. Lattice parameters, BET surface areas and TOF values of lithium cobalt oxides.

Sample	**lattice constants (Å)**	**BET (m^2/g)**	**TOF ($\mu mol \cdot s^{-1} \cdot m^{-2}$)**
LT-$LiCoO_2$	a = 7.9876(4)	24	0.0023
LT-$Li_{0.4}CoO_2$	a = 7.9792(1)	42	0.0092
HT-$LiCoO_2$	a = 2.8108(2), c = 14.0285(2)	16	0.00063
HT-$Li_{0.4}CoO_2$	a = 2.8092(1), c = 14.2915(1)	18	0.0089
Co_3O_4[1]*	a = 8.137(6)	100	0.0035
Co_3O_4[2]	/	34	0.15
Co_3O_4[3]	/	~125	~0.027

* WOC activity measurements were conducted under the same conditions as applied for lithium cobalt oxides in the present study. Generally TOF values between different studies are difficult to compare directly due to variations in the analytic setup and in the reaction conditions and component concentrations.

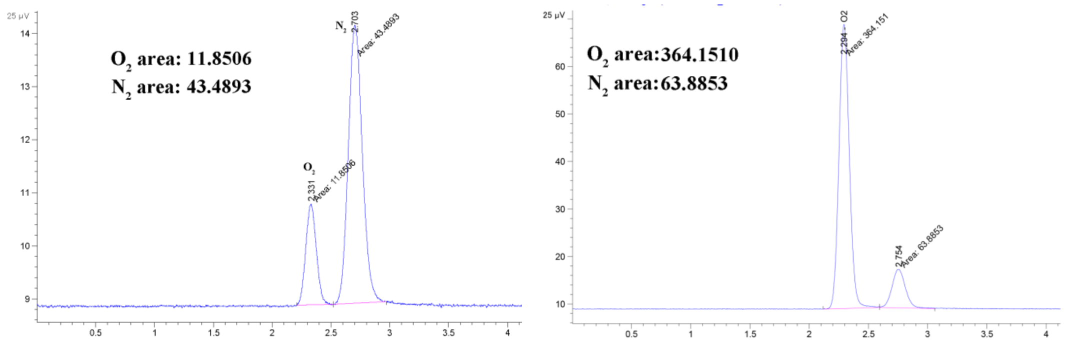

Figure S4.10. Confirmation of oxygen evolution with gas chromatography (left: before water oxidation test, right: after water oxidation test).

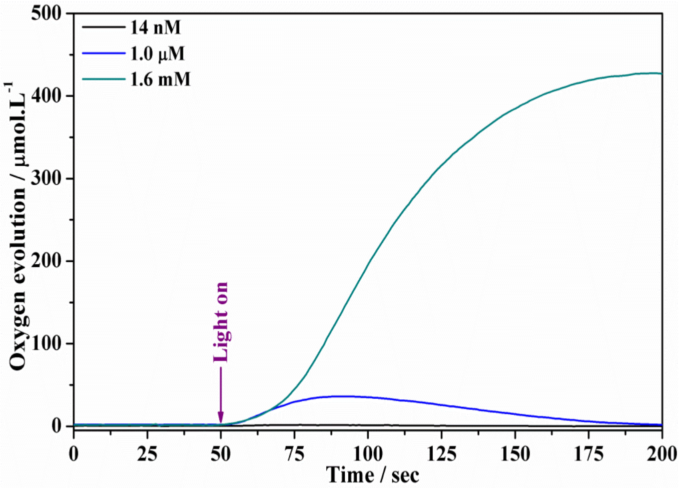

Figure S4.11. Photochemical water oxidation with different concentrations of $Co(NO_3)_2$ (Clark electrode monitoring in solution; 1.33 mM $[Ru(bpy)_3]Cl_2$, 26.25 mM $Na_2S_2O_8$, 8 mL 0.1 M phosphate buffer (pH 7), 470 nm LED (5000 Lux intensity)).

To obtain oxygen evolution which is comparable to LT-$Li_{0.4}CoO_2$ the Co^{2+} concentration (1.6 mmol/L) is three orders of magnitude higher than the cobalt quantities leached from lithium cobalt oxides (Table S4.2).

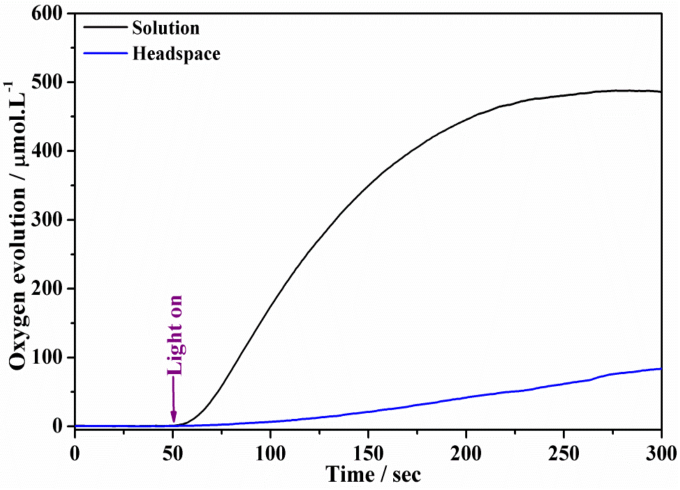

Figure S4.12. Both solution and headspace oxygen monitoring by Clark electrode for photochemical water oxidation with LT-Li$_{0.4}$CoO$_2$ (10 mg WOC, 1.33 mM [Ru(bpy)$_3$]Cl$_2$, 26.25 mM Na$_2$S$_2$O$_8$, 8 mL 0.1 M phosphate buffer (pH 7), 470 nm LED (5000 Lux intensity)).

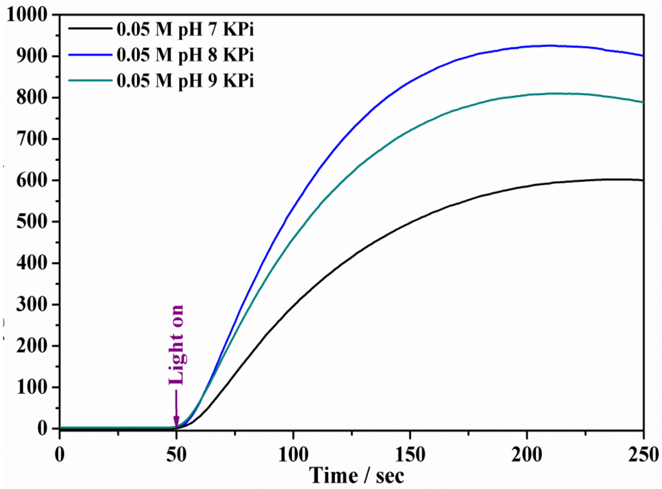

Figure S4.13. Influence of pH on the water oxidation activity of LT-Li$_{0.4}$CoO$_2$ (Clark electrode monitoring in solution (5 mg WOC, 1.33 mM [Ru(bpy)$_3$]Cl$_2$, 5.25 mM Na$_2$S$_2$O$_8$, 8 mL 0.05 M phosphate buffer (pH 7), 470 nm LED (5000 Lux intensity)).

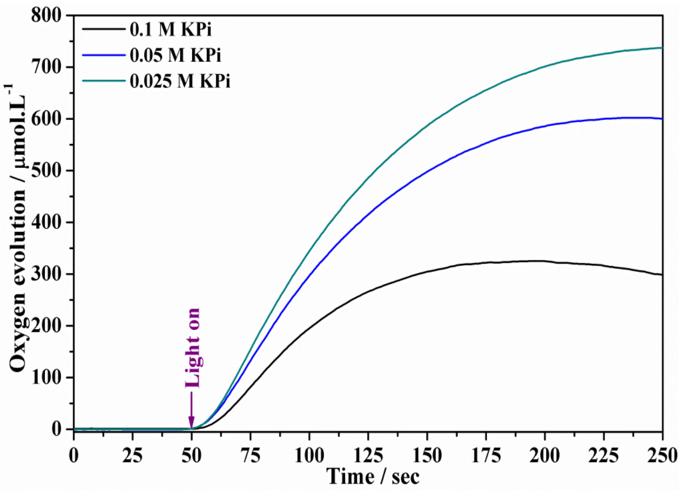

Figure S4.14. Influence of buffer concentration on the water oxidation activity of LT-$Li_{0.4}CoO_2$ (Clark electrode monitoring in solution; 5 mg WOC, 1.33 mM $[Ru(bpy)_3]Cl_2$, 5.25 mM $Na_2S_2O_8$, 8 mL phosphate buffer (pH 7), 470 nm LED (5000 Lux intensity)).

Figures S4.13 and S4.14 illustrate the influence of pH values and buffer concentrations on the water oxidation activity, respectively. Increasing the pH value from 7 to 8 led to enhanced water oxidation activity, probably due to accelerated water oxidation reaction kinetics. However, further increase of pH to 9 led to decreased activities, which indicates the emergence of another adverse factor (namely the stability of photosensitizer). This complex topic was already studied in its own right in our group and is under preparation for publication. Accordingly, WOC activity as a function of buffer concentration entails a competitive process between buffer capacity and photosensitizer decomposition (higher concentrations accelerate photosensitizer decomposition).

(a)

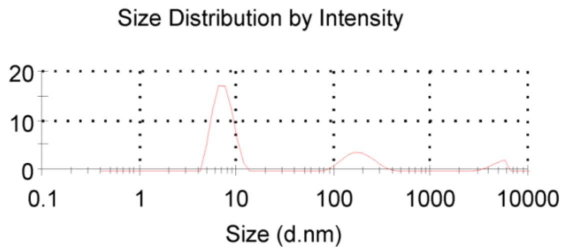

(b)

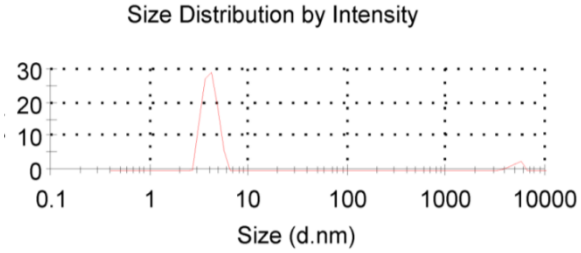

(c)

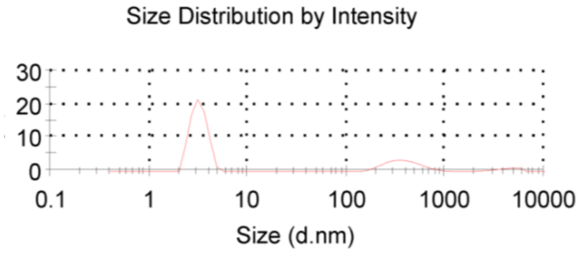

(d)

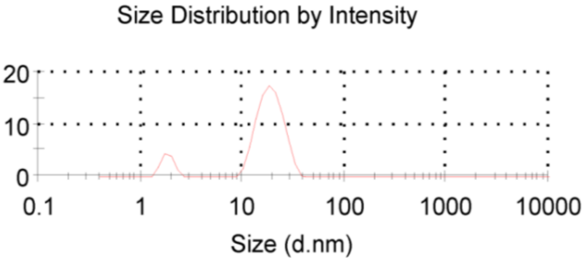

(e)

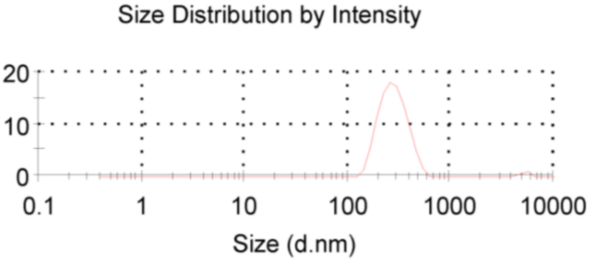

Figure S4.15. DLS measurements of supernatant solutions after water oxidation (top to bottom): (a) distilled water as reference; (b) supernatant of LT-$Li_{0.4}CoO_2$ after water oxidation; (c) supernatant of HT-$Li_{0.4}CoO_2$ after water oxidation; (d) aqueous solution of $Co(NO_3)_2$ after water oxidation; (e) solution of $Co(NO_3)_2$ in phosphate buffer (0.1 M, pH 7) after water oxidation.

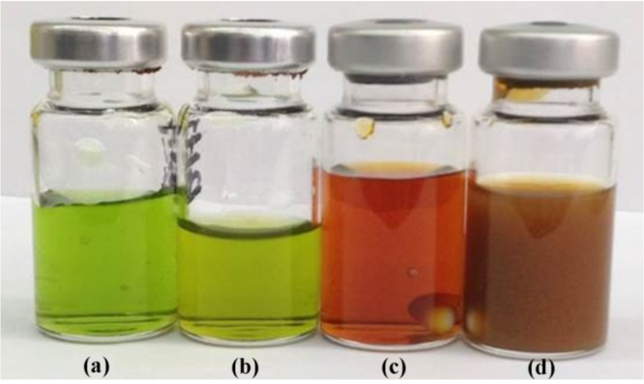

Figure S4.16. Photographs of solutions after water oxidation (left to right): (a) supernatant of LT-$Li_{0.4}CoO_2$ after water oxidation; (b) supernatant of HT-$Li_{0.4}CoO_2$ after water oxidation; (c) aqueous solution of $Co(NO_3)_2$ after water oxidation; (d) solution of $Co(NO_3)_2$ after water oxidation in potassium phosphate buffer (0.1 M, pH 7).

The green color of the supernatant solution shown in Figure S4.16 indeed indicates the presence of $[Ru(bpy)_3]^{3+}$. The decomposition of $[Ru(bpy)_3]^{2+}$ is confirmed by the formation of CO (observed by gas chromatography analyses). However, this phenomenon is not limited to the investigated set of lithium cobalt oxides, but represents a general issue associated with both hetero- and homogeneous water oxidation catalysts.

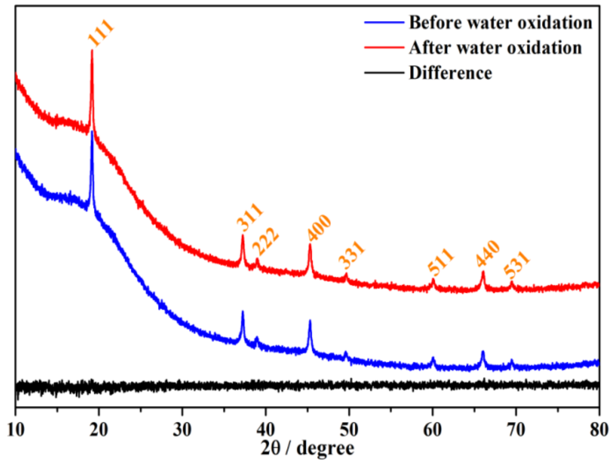

Figure S4.17. PXRD patterns of LT-$Li_{0.4}CoO_2$ before and after water oxidation (recorded on a STOE STADI P diffractrometer with Cu K_α radiation, the strong background is due to fluorescence).

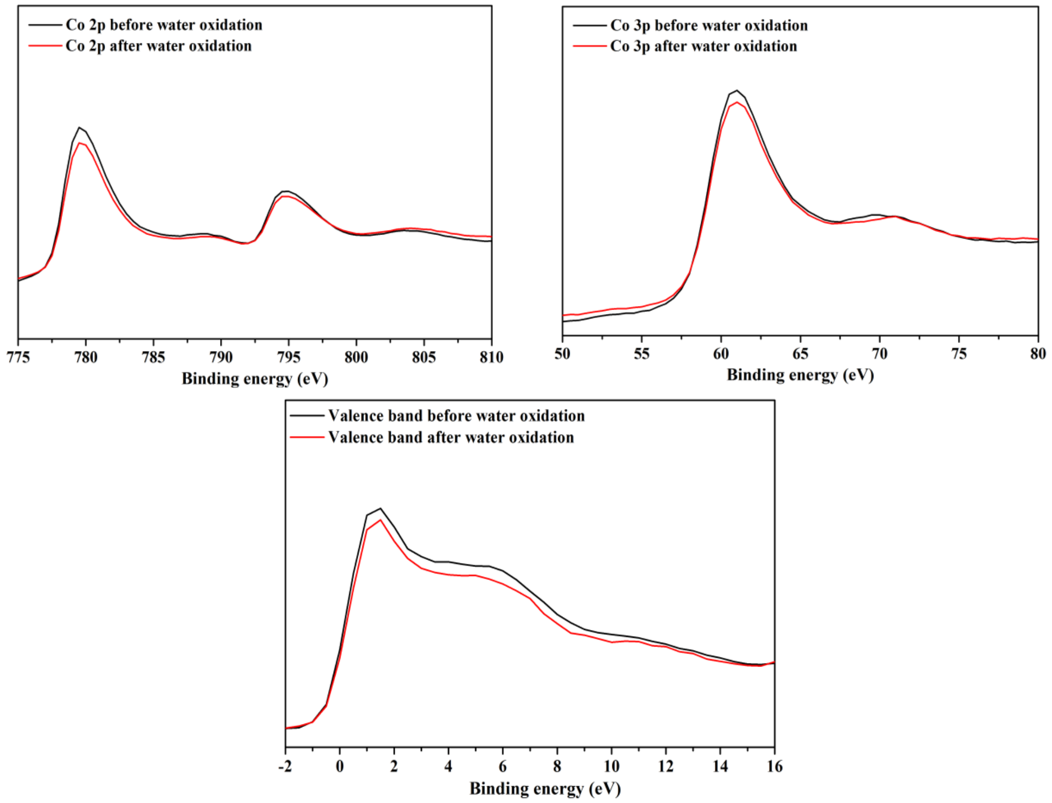

Figure S4.18. XPS spectra of LT-$Li_{0.4}CoO_2$ before and after water oxidation.

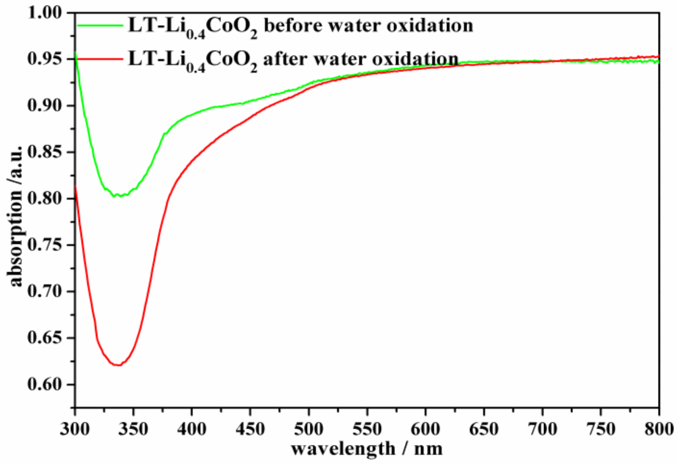

Figure S4.19. UV/Vis spectra of LT-Li$_{0.4}$CoO$_2$ before and after water oxidation. The absorption difference in the range of 300-500 nm is probably arising from cobalt leaching.

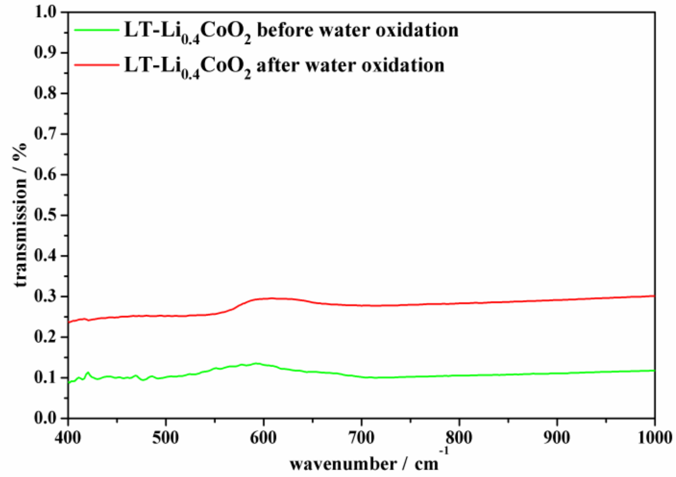

Figure S4.20. FT-IR spectra of LT-Li$_{0.4}$CoO$_2$ before and after water xidation.

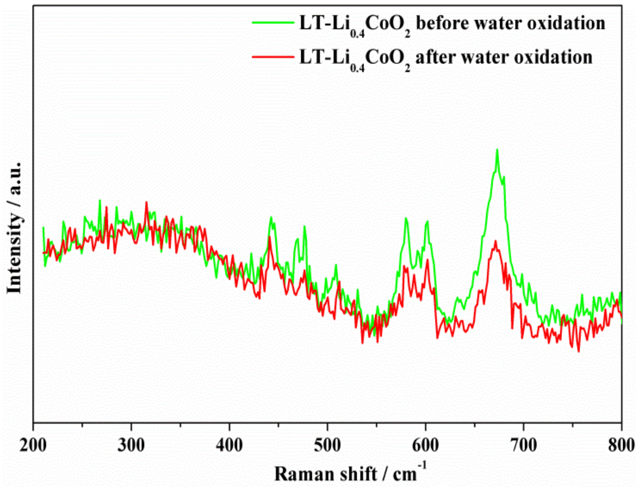

Figure S4.21. Raman spectra of LT-Li$_{0.4}$CoO$_2$ before and after water oxidation.

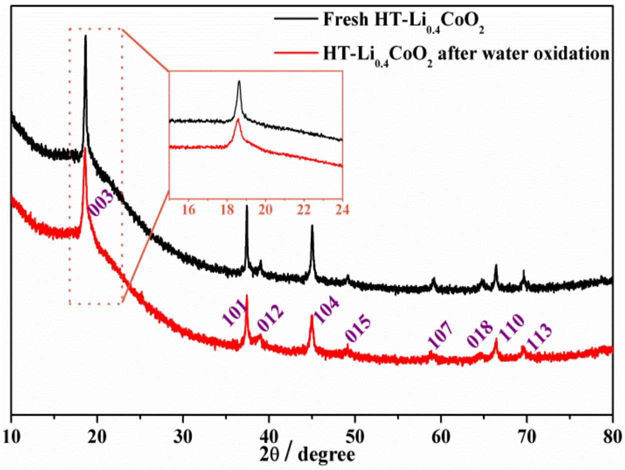

Figure S4.22. PXRD patterns of HT-Li$_{0.4}$CoO$_2$ before and after water oxidation (no amorphous layer was formed after water oxidation, cf. HRTEM images in Figures 6 and S24).

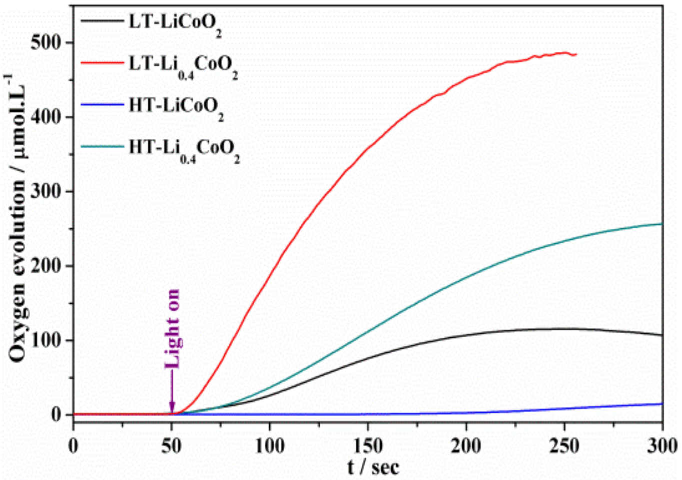

Figure S4.23. First cycle of HT/LT-LiCoO$_2$ and HT/LT-Li$_{0.4}$CoO$_2$ for water oxidation.

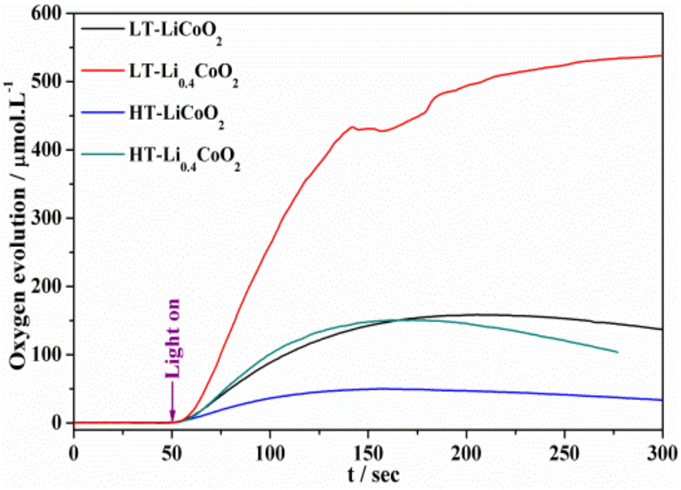

Figure S4.24. Second cycle of HT/LT-LiCoO$_2$ and HT/LT-Li$_{0.4}$CoO$_2$ for water oxidation.

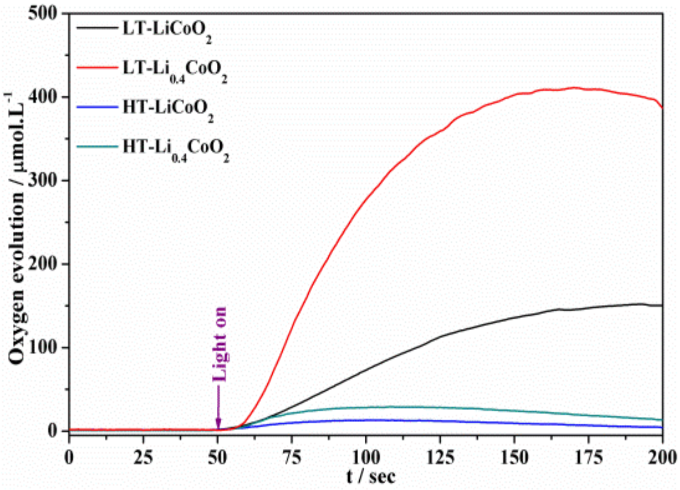

Figure S4.25. Third cycle of HT/LT-LiCoO$_2$ and HT/LT-Li$_{0.4}$CoO$_2$ for water oxidation.

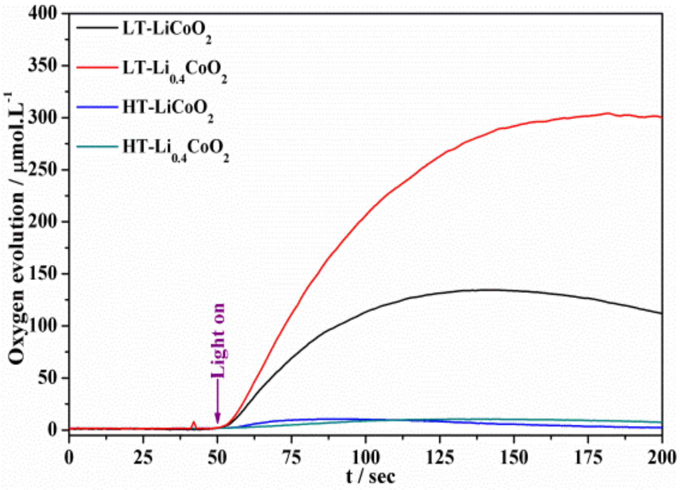

Figure S4.26. Fourth cycle of HT/LT-LiCoO$_2$ and HT/LT-Li$_{0.4}$CoO$_2$ for water oxidation.

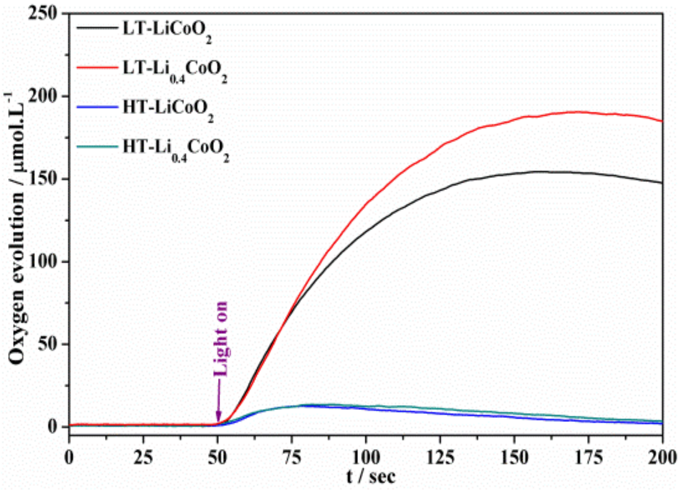

Figure S4.27. Fifth cycle of HT/LT-LiCoO$_2$ and HT/LT-Li$_{0.4}$CoO$_2$ for water oxidation.

Table S4.2. Concentration of Li^+ and Co^{2+} in solution after water oxidation.

WOC	**Li^+ (mmol/L)**	**Co^{2+} (μmol/L)**
LT-$LiCoO_2$	1.04	11.4
LT-$Li_{0.4}CoO_2$	0.65	1.4
HT-$LiCoO_2$	1.25	2.3
HT-$Li_{0.4}CoO_2$	0.78	0.8

Table S4.3. Water oxidation activity of the catalyst series over different cycles.

WOCs	**1st cycle (%) μmol/L**	**2nd cycle (%) μmol/L**	**3rd cycle (%) μmol/L**	**4th cycle (%) μmol/L**	**5th cycle (%) μmol/L**
LT-$LiCoO_2$	(100) 116	(138) 160	(132) 153	(117) 136	(132) 154
LT-$Li_{0.4}CoO_2$	(100) 487	(110) 537	(84) 410	(62) 305	(39) 190
HT-$LiCoO_2$	(100) 14	(357) 50	(93) 13	(93) 13	(100) 14
HT-$Li_{0.4}CoO_2$	(100) 256	(59) 150	(11) 28	(4) 10	(6) 14.5

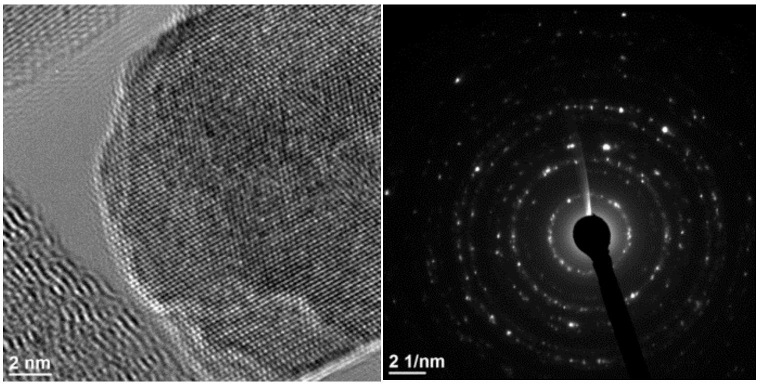

Figure S4.28. HRTEM and SAED patterns of LT-$Li_{0.4}CoO_2$ before and after the 5th water oxidation cycle (left: HRTEM, right: SAED pattern).

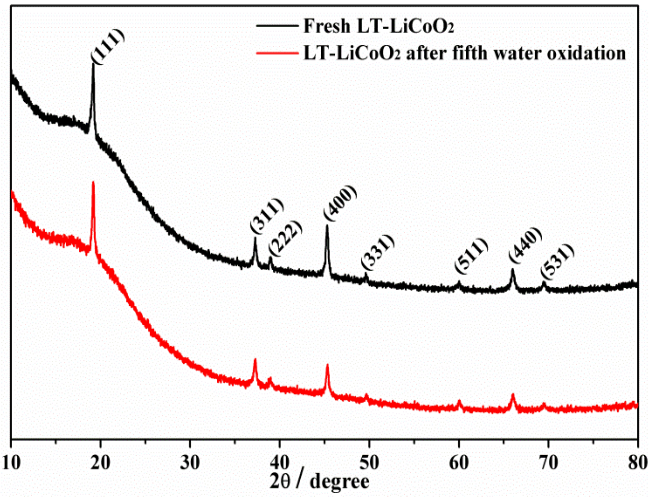

Figure S4.29. PXRD patterns of LT-$LiCoO_2$ before and after water oxidation cycles.

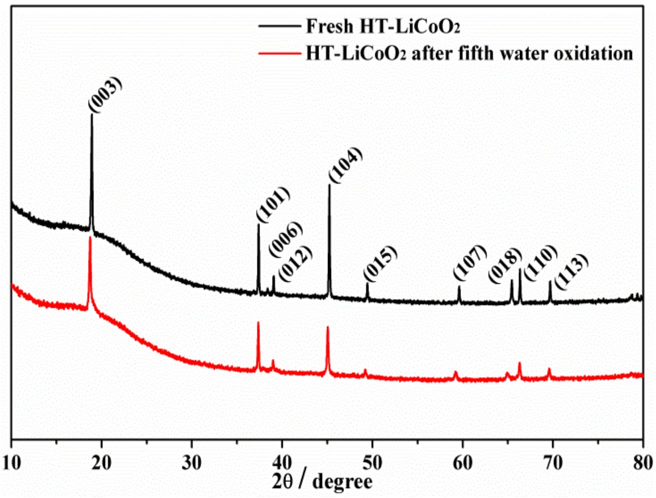

Figure S4.30. PXRD patterns of HT-$LiCoO_2$ before and after water oxidation cycles.

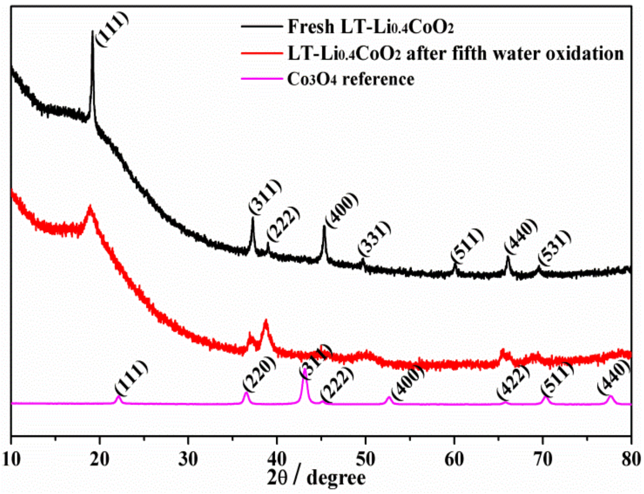

Figure S4.31. PXRD patterns of LT-$Li_{0.4}CoO_2$ before and after water oxidation cycles.

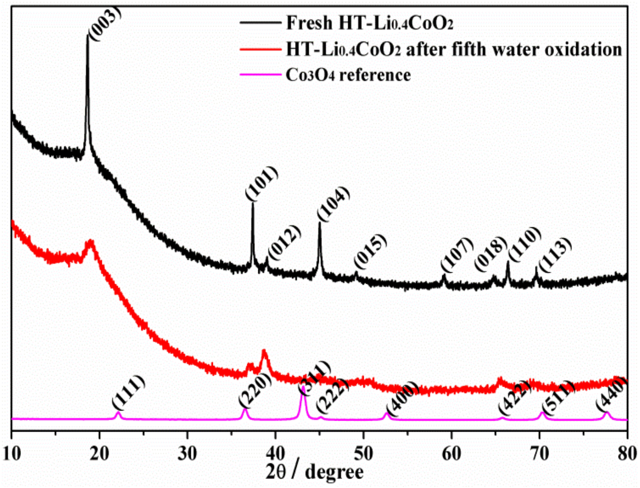

Figure S4.32. PXRD patterns of HT-$Li_{0.4}CoO_2$ before and after water oxidation cycles.

Although reflections are broader and weaker after the fifth cycle, the overall diffraction pattern is still far from corresponding to representative Co_3O_4 data.

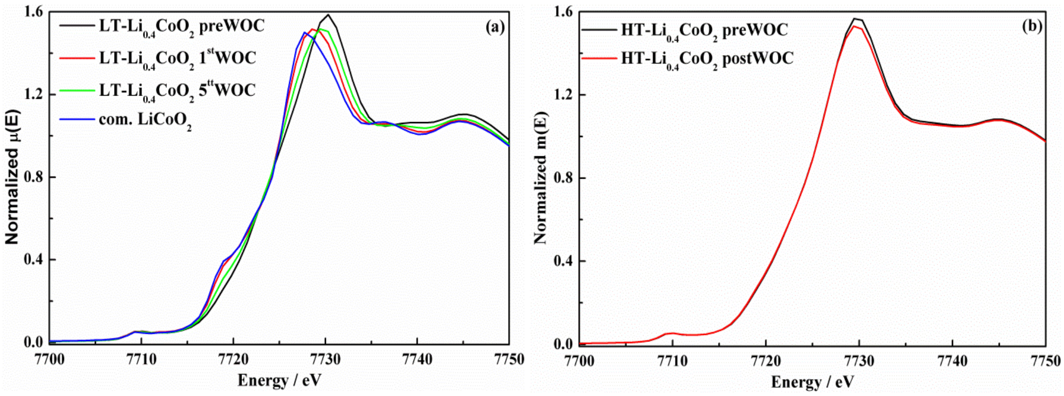

Figure S4.33. *Ex-situ* XANES Co K-edge spectra of LT-$Li_{0.4}CoO_2$ (a) and HT-$Li_{0.4}CoO_2$ (b).

Table S4.4. Results from XANES analysis

Sample	Edge/eV	White line / eV	Edge width / eV	Mean valence
LT-$Li_{0.4}CoO_2$ pre WOC	7727.73	7730.22	2.49	3.6±0.1
LT-$Li_{0.4}CoO_2$ 1st WOC	7725.54	7728.74	3.20	3.2±0.1
LT-$Li_{0.4}CoO_2$ 5th WOC	7725.63	7729.73	4.09	3.2±0.1
HT-$Li_{0.4}CoO_2$ pre WOC	7726.56	7729.80	3.24	3.4±0.1
HT-$Li_{0.4}CoO_2$ post WOC	7726.40	7729.70	3.29	3.4±0.1

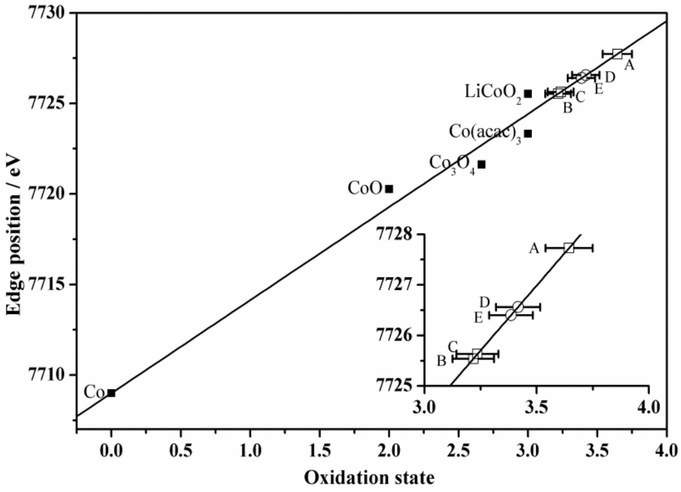

Figure S4.34. Cobalt valence state calibration curve for Co K-edge spectra. (A: LT-$Li_{0.4}CoO_2$ pre -WOC, B: LT-$Li_{0.4}CoO_2$ 1st WOC cycle, C: LT-$Li_{0.4}CoO_2$ 5th WOC cycle, D: HT-$Li_{0.4}CoO_2$ pre-WOC, E: HT-$Li_{0.4}CoO_2$ post-WOC).

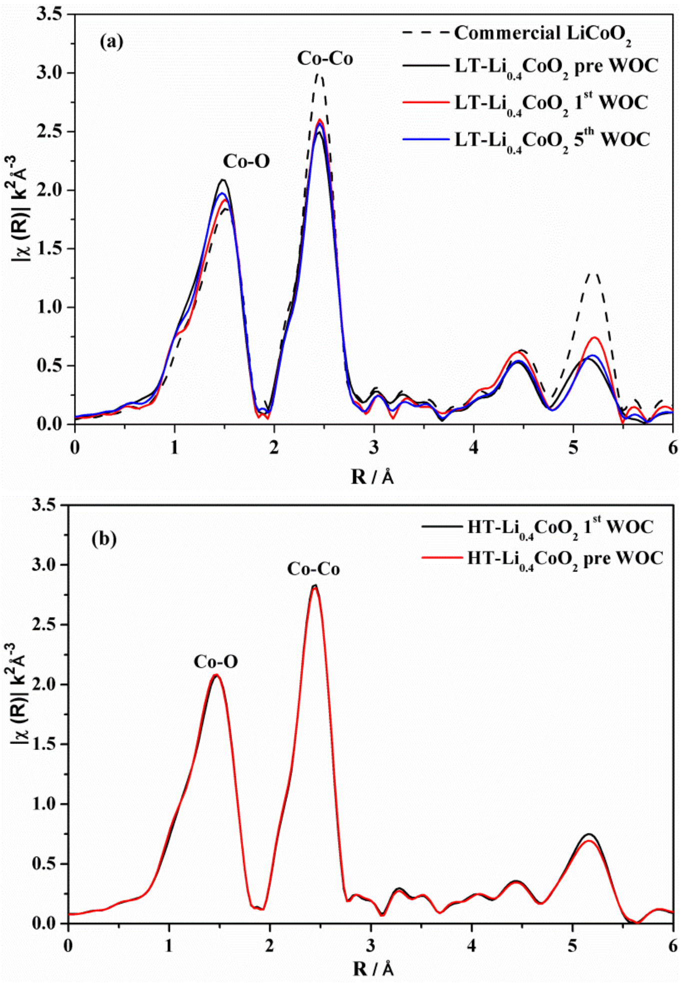

Figure S4.35. Fourier transformed EXAFS regions of pre- and post-catalytic (a) LT-$Li_{0.4}CoO_2$ and (b) HT-$Li_{0.4}CoO_2$.

Table S4.5. Results from EXAFS fitting.

Sample	R-factor	r_{Co-O} / Å	σ^2_{Co-O} / Å^2	r_{Co-Co} / Å	σ^2_{Co-Co} / Å^2	r_{Co-Li} / Å	σ^2_{Co-Li} / Å^2
LT-$Li_{0.4}CoO_2$ pre	2.1 %	1.895±0.006	$(1\pm0.9)\cdot10^{-3}$	2.833±0.007	$(3.1\pm0.7)\cdot10^{-3}$	3.22±0.01	$(5\pm1)\cdot10^{-3}$
LT-$Li_{0.4}CoO_2$ 1st	1.4 %	1.909±0.006	$(2\pm1)\cdot10^{-3}$	2.828±0.005	$(1.5\pm0.5)\cdot10^{-3}$	3.22±0.01	$(18\pm7)\cdot10^{-3}$
LT-$Li_{0.4}CoO_2$ 5th	2.1 %	1.898±0.005	$(1.2\pm0.6)\cdot10^{-3}$	2.835±0.004	$(3.6\pm0.6)\cdot10^{-3}$	3.23±0.01	$(11\pm2)\cdot10^{-3}$

LT-$Li_{0.4}CoO_2$ underwent a cobalt reduction from +3.6 to +3.2 after water oxidation, while HT-$Li_{0.4}CoO_2$ was relatively stable (Figure S4.29). To maintain charge balance, the reduction of cobalt was probably compensated by proton insertion.[5] EXAFS (Figure S4.31) fitting indicates that the basic Co-O framework was maintained for both LT-$Li_{0.4}CoO_2$ and HT-$Li_{0.4}CoO_2$ after water oxidation, which is consistent with the PXRD results and HRTEM images. In addition to lattice defects resulting from cobalt leaching, the broadening of diffraction peaks for LT-$Li_{0.4}CoO_2$ is mainly ascribed to lattice strain caused by Co reduction. In contrast, diffraction peak broadening of post-catalytic HT-$Li_{0.4}CoO_2$ is probably due an intrastructural layer adjustment (e.g. by cation or water uptake). As the observed broadening of PXRD peaks goes hand in hand with lower water oxidation activity, the above factors can well account for the long-term stability issues associated with the delithiated WOCs.

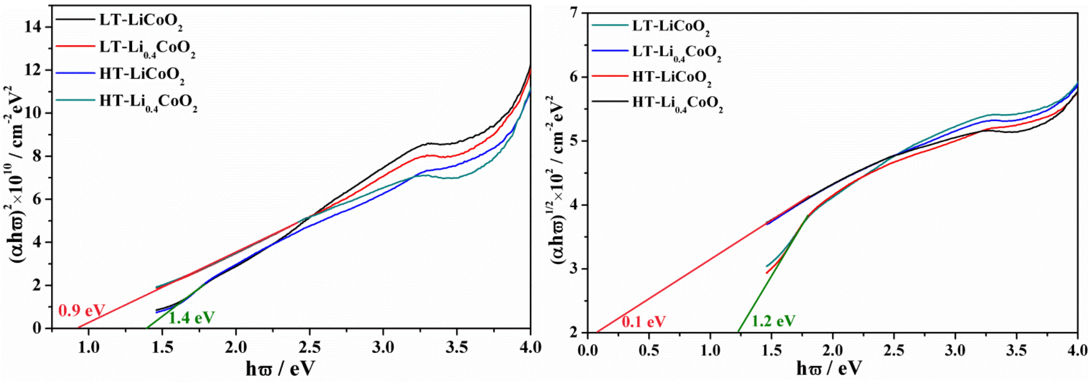

Figure S4.36. Band gap determination from UV/vis spectra for fully lithiated and delithiated lithium cobalt oxide (left: direct band gap, n=1/2; right: indirect band gap, n=2).[4]

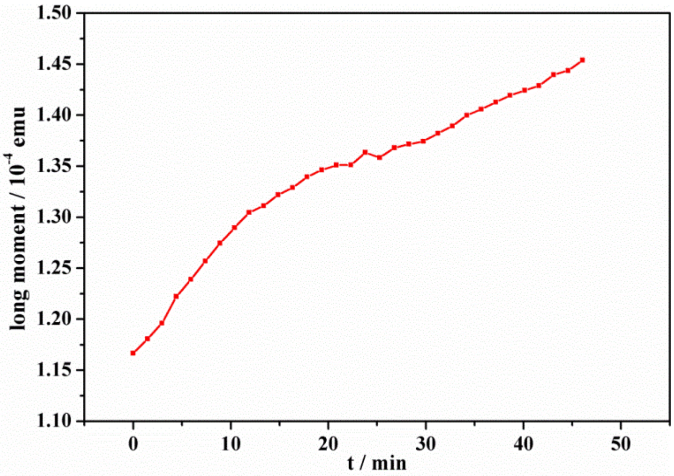

Figure S4.37. Time dependent magnetic susceptibility measurement of LT-$LiCoO_2$ at 65 K.

The time-dependent increase of magnetic moments at 65 K indicates that the abnormal hysteresis loop observed during magnetic measurements (cf. Figure 4.9 in the main text) is due to remnant oxygen rather than to any possible electronic phase transition, because paramagnetic oxygen was subjected to liquefaction around this temperature.

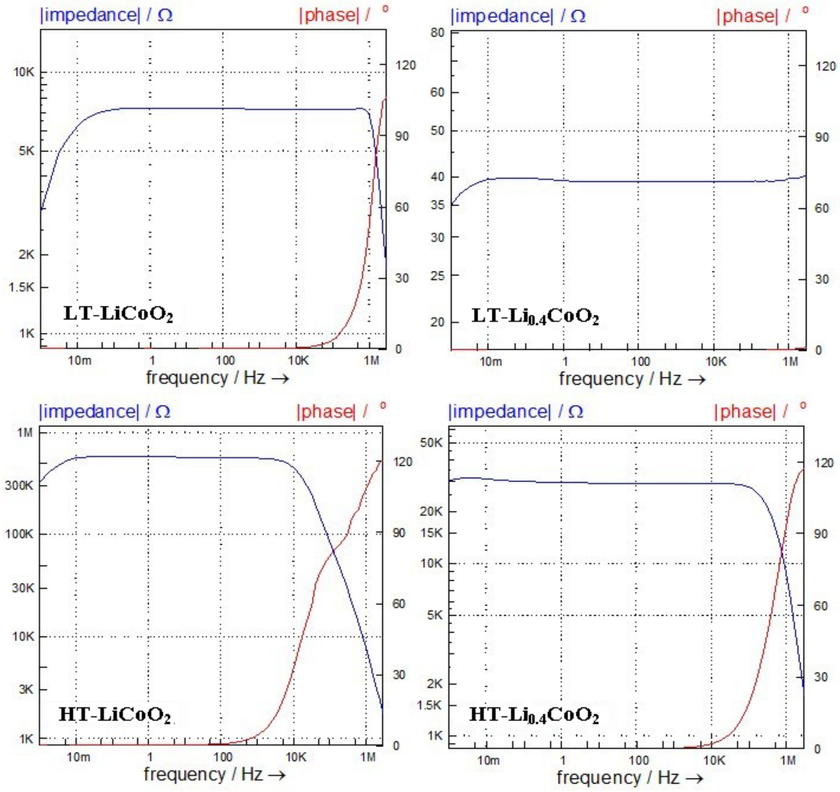

Figure S4.38. Electrochemical impedance spectra of pristine and delithiated lithium cobalt oxides.

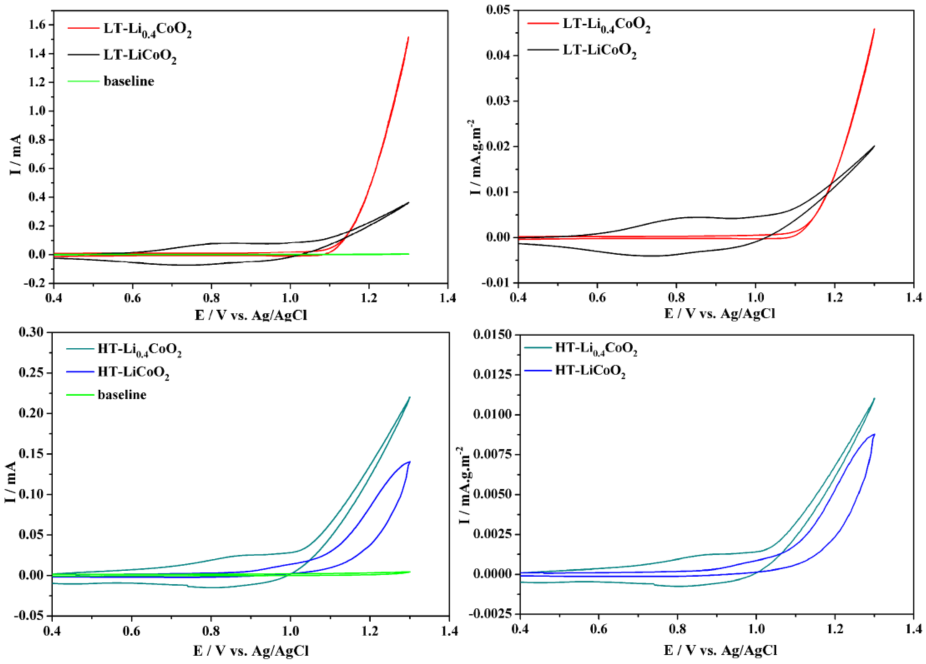

Figure S4.39. Cyclic voltammograms of fully lithiated and delithiated lithium cobalt oxides (left: before normalization; right: normalized to BET surface area).

In line with the photochemical results, the delithiated LT/HT-$Li_{0.4}CoO_2$ materials displayed higher activities than their pristine LT/HT-$LiCoO_2$ counterparts. However, the productive effect of delithiation on the electrochemical water oxidation performance is not as significant as on the photochemical process. These observations are well in line with ref. 5 (Figure 4. vs. Figure 4.5 therein), indicating a different rate-determine step of water oxidation between electrochemical and photochemical process.

DFT calculations on pristine and delithiated lithium cobalt oxides

In order to assign the observed changes in the electronic and optical properties of $LiCoO_2$ oxides after delithiation, we calculated their energy band structures with first-principles density functional theory (DFT). Delithiation of the parent structure was modeled on a 2×2×1 supercell for HT-$LiCoO_2$ and HT-$Li_{1-x}CoO_2$, because no sufficient structural information was available to construct ideal structures for LT-$LiCoO_2$ and LT-$Li_{1-x}CoO_2$ with appropriate modeling of the disordered Li/Co distribution.

Computational details: All calculations were performed at the GGA-PW91 level implemented in the CASTEP package. The plane wave of norm conserving pseudopotential was used to describe the electron-ion interaction. The lattice parameters and the ionic position of the 2×2×1 supercell are fully relaxed, with the convergence thresholds 2×10^5 eV/atom for energy, 2×10^6 eV/atom for SCF tolerance, 0.05 eV/Å for force, and 0.002 Å for displacement. The cutoff energy was set to 600 eV, and a Monkhorst-Pack scheme 3×3×1 *k*-points mesh was used. The convergence of the total energy was assessed via test calculations from proceeding from lower to higher precision. For the calculation of the density of states (DOS), a larger 5×5×2 *k*-points mesh with a separation of 0.01/Å was applied. The scissors operator was selected to be 0.6 eV for plotting the DOS, based on the discrepancy of the predicted band gap and the experimental value determined for bulk $LiCoO_2$.

Electronic structures of HT-$Li_{1-x}CoO_2$ ($0 < x < 1$): The predicted optical band of 2.106 for bulk $LiCoO_2$ corresponds well with the experimental value of 2.1 eV. Both DOS and PDOS became more delocalized with a decrement of x from 1 to 0.083. In particular, the bandwidth of the Co d states undergoes broadening upon delithiation, leading to the formation of continuous band structures, i.e. metallic properties, with increasing values for x.

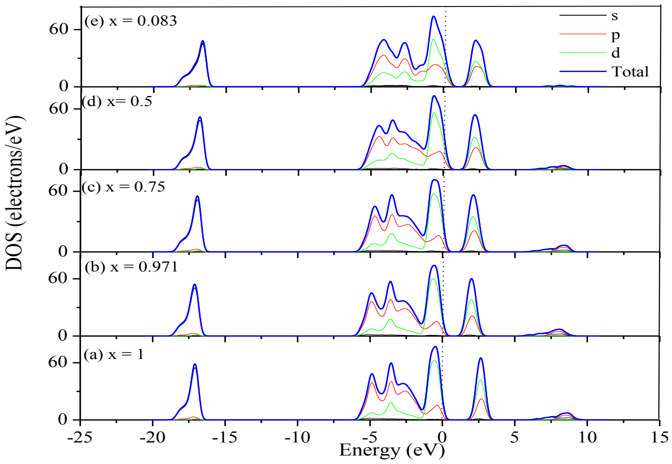

Figure S4.40. DOS and PDOS of HT-Li_xCoO_2 (0<x<1) from DFT calculations: (a) x=1, (b) x= 0.971, (c) x=0.75, (d) x=0.5, (e) x= 0.083.

In line with experimental observations, the following general band structure changes are proposed:

1. Hole introduction into valence band through oxidation of Co^{3+} to Co^{4+} (XPS, magnetic measurements, ^{7}Li NMR)

2. Band gap narrowing after delithiation (UV/vis and valence band spectra)

3. Stronger hybridization of Co 3d and O 2p states (O 1s and valence band XPS spectra)

4. Enhanced mobility of holes (FT-IR, Raman and impedance spectra)

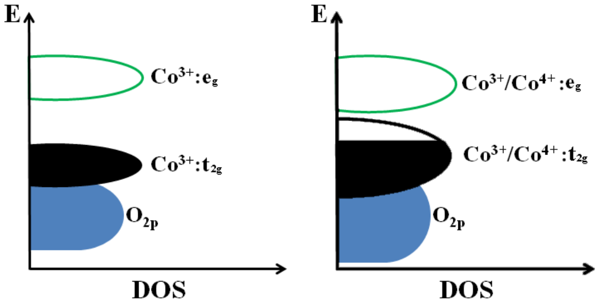

Figure S4.41. Schematic representation of band structure alterations for $LiCoO_2$ upon delithiation.

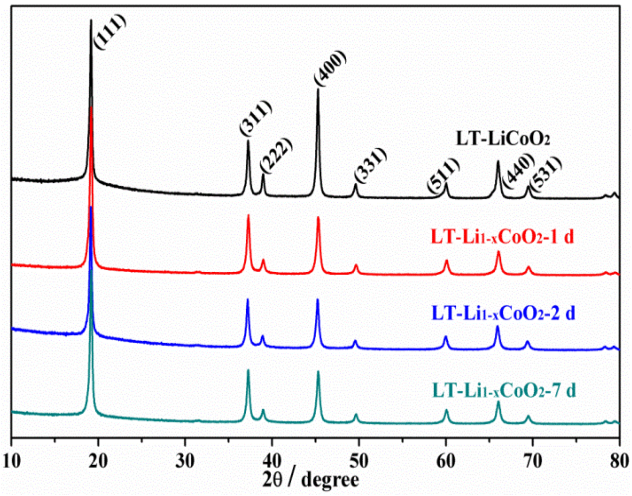

Figure S4.42. PXRD patterns of LT-$Li_{1-x}CoO_2$ obtained after different delithiation times.

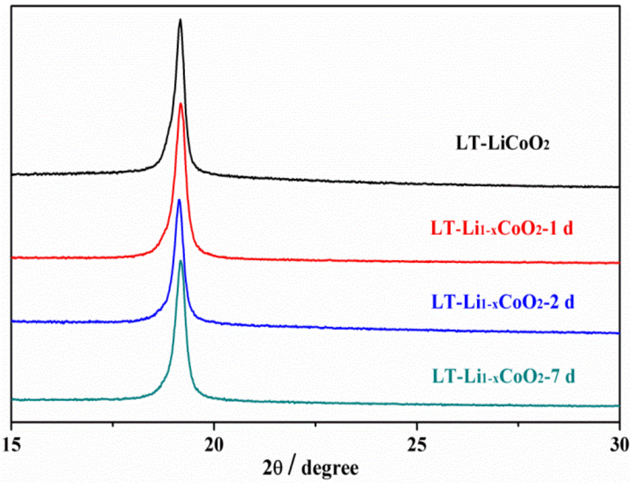

Figure S4.43. (111) peak position of LT-$Li_{1-x}CoO_2$ XRD pattens after different delithiation times.

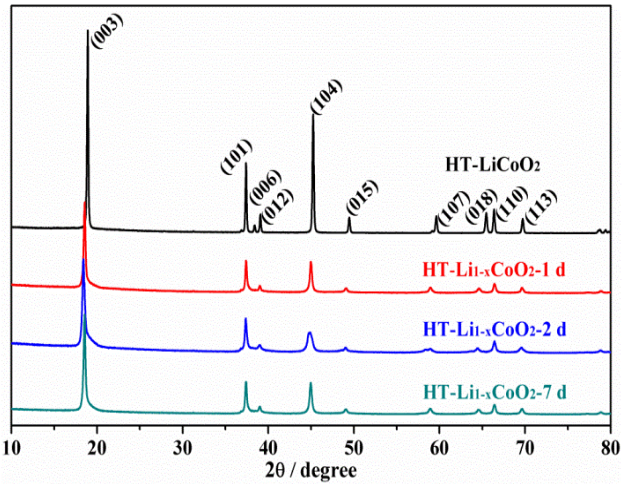

Figure S4.44. PXRD patterns of HT-$Li_{1-x}CoO_2$ samples obtained after different delithiation times.

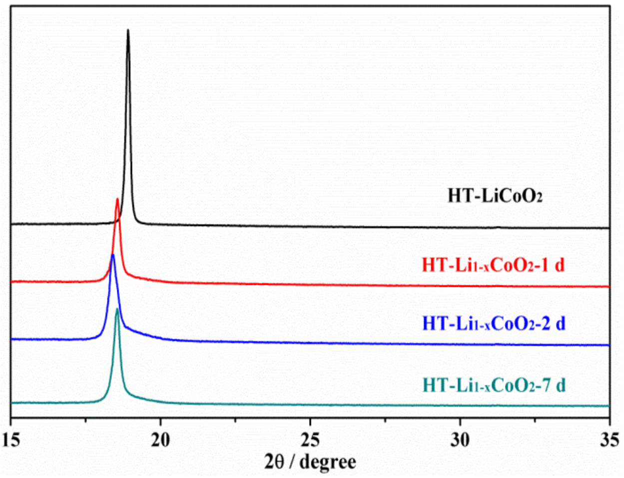

Figure S4.45. (003) peak position of HT-$Li_{1-x}CoO_2$ after different delithiation times.

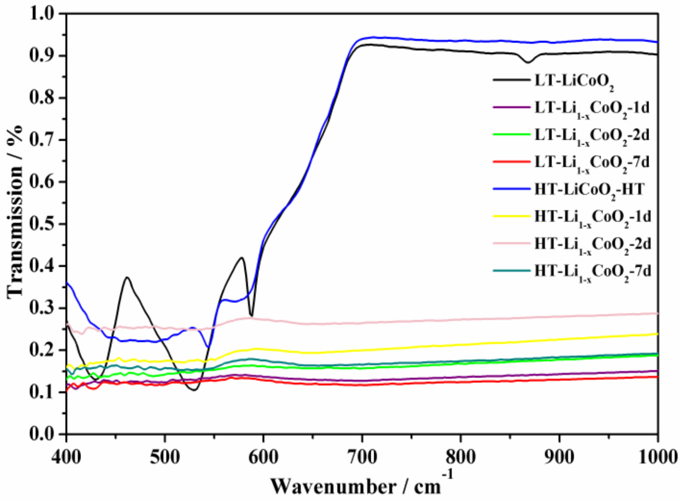

Figure S4.46. FT-IR spectra of LT/HT-$Li_{1-x}CoO_2$ samples obtained after different delithiation times.

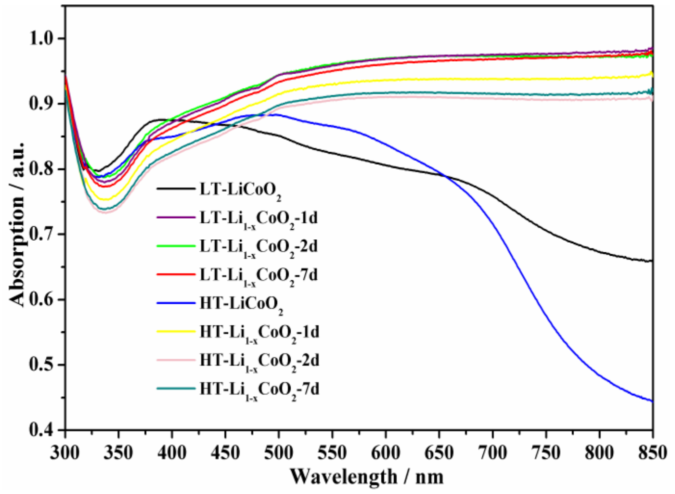

Figure S4.47. UV/vis spectra of LT/HT-$Li_{1-x}CoO_2$ samples obtained after different delithiation times.

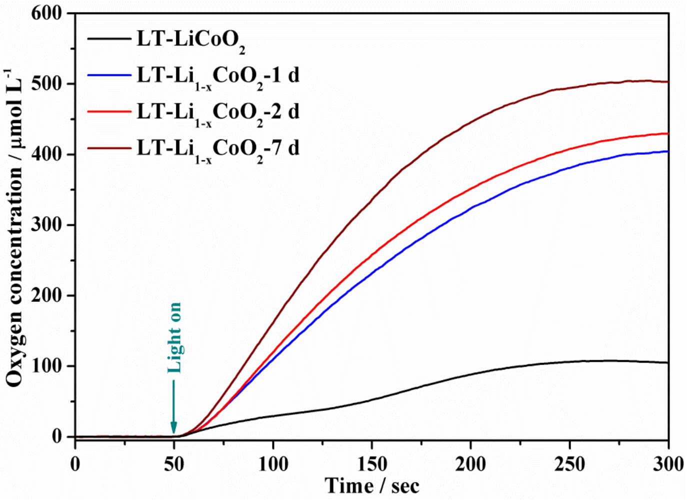

Figure S4.48. Water oxidation activity of LT-$Li_{1-x}CoO_2$WOCs obtained after different delithiation times.

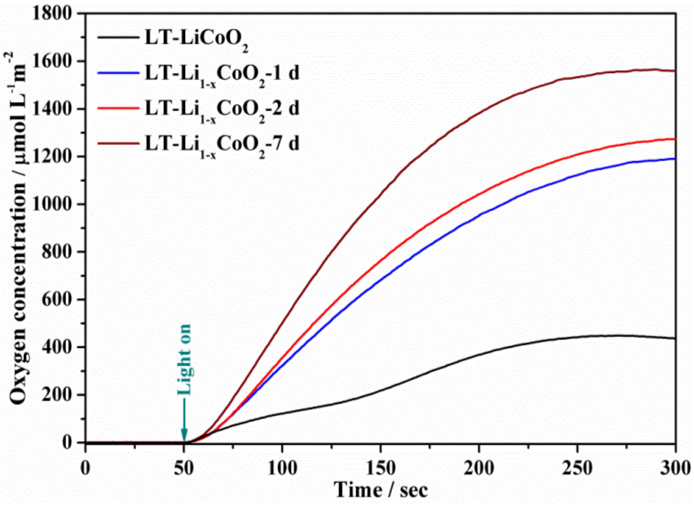

Figure S4.49. Water oxidation activity of LT-$Li_{1-x}CoO_2$ normalized to BET surface.

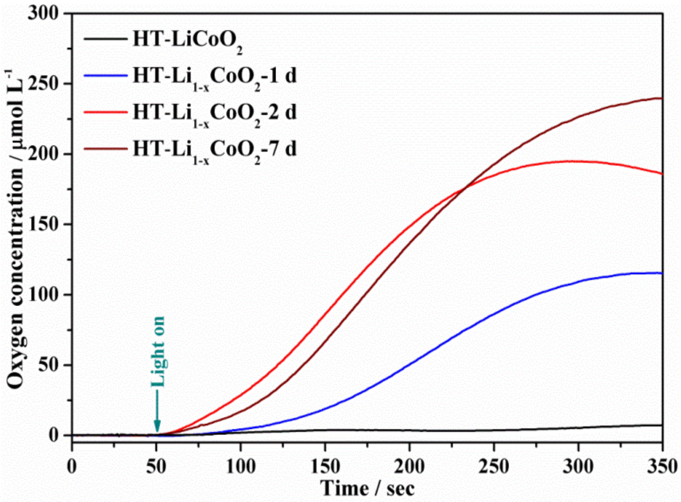

Figure S4.50. Water oxidation activity of HT-$Li_{1-x}CoO_2$ samples obtained after different delithiation times.

Although Li^+ content and BET surface area basically reached their final values for both HT- and LT-forms after 1 d of delithiation (Table S4.6), prolonged 7d treatments afforded the most active WOCs. The (003) peak of the HT-modification initially underwent a shift towards lower angles that was virtually reverted after 7 d (Figure S4.45), indicating that the productive effect of extended delithiation times entails structural reordering after rapid lithium leaching.

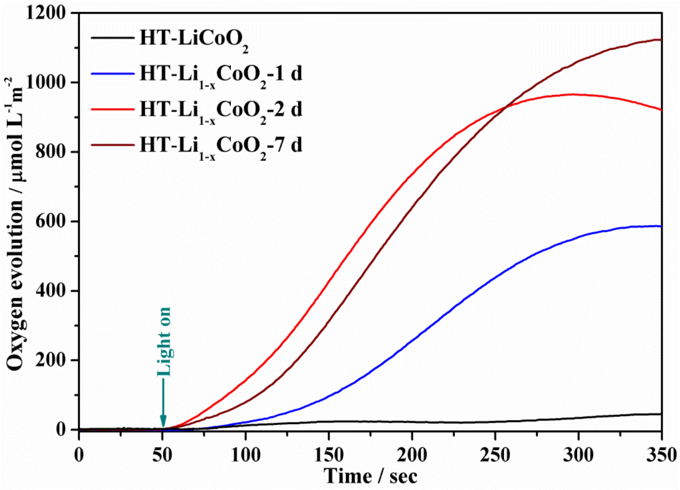

Figure S4.51. Water oxidation activity of HT-$Li_{1-x}CoO_2$ normalized to the total BET surface area.

Table S4.6. Li/Co atomic ratios (ICP-AES) and BET surface area of LT-/HT-$Li_{1-x}CoO_2$ after different delithiation times.

Sample	Time	x	BET(m^2/g)	Sample	Time	x	BET(m^2/g)*
LT-Li_xCoO_2	1d	0.43	33.97	HT-Li_xCoO_2	1d	0.43	19.69
LT-Li_xCoO_2	2d	0.42	33.74	HT-Li_xCoO_2	2 d	0.40	20.19
LT-Li_xCoO_2	7d	0.42	32.25	HT-Li_xCoO_2	7 d	0.42	21.34

*BET surfaces may vary between delithiation runs, cf. Table S4.1

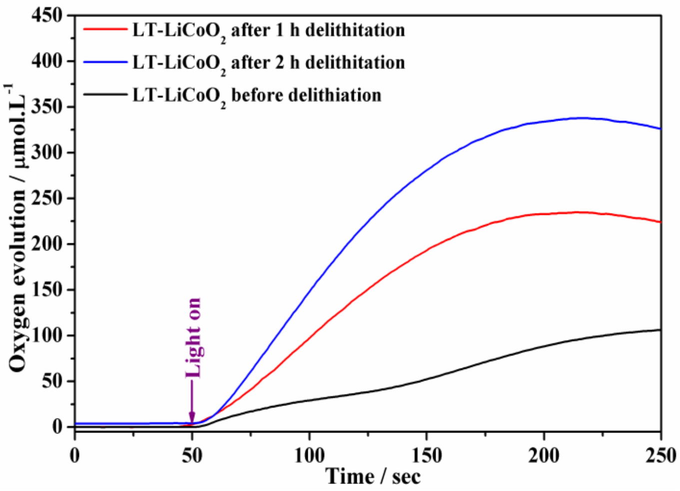

Figure S4.52. Influence of lithium content on the water oxidation activity of LT-LiCoO$_2$. (Clark electrode monitoring in solution; 10 mg WOC, 1.33 mM [Ru(bpy)$_3$]Cl$_2$, 26.25 mM Na$_2$S$_2$O$_8$, 8 mL 0.1 M phosphate buffer (pH 7), 470 nm LED (5000 Lux intensity)).

We further aimed for Li$_x$CoO$_2$ samples with higher lithium contents ($x > 0.4$) by further shortening the delithiation time. Unfortunately, the applied protocol of Br$_2$ assisted lithium extraction generally does not permit complete delithiation of LiCoO$_2$, because the Br$_2$/Br$^-$ oxidation potential of 4.1 V vs. Li$^+$/Li is lower than the required potential of 4.87 V for the formation of CoO$_2$. The WOC test results (Figure R1 below) show that delithiation led to significantly increased activities in the first two hours, whereas the influence of further lithium leaching on the water oxidation activity is less evident (Figure S4.45), in line with the DFT calculations (Figure S4.37). All in all, the samples subjected to shorter delithiation periods of 1-2 h display lower O$_2$ evolution activity than the title compounds (Figure R1). Lithium contents were determined as Li$_{0.84}$CoO$_2$ and Li$_{0.63}$CoO$_2$ by ICP-AES measurements for LiCoO$_2$ after 1 h and 2 h of delithiation, respectively.

^{18}O-labeling experiments

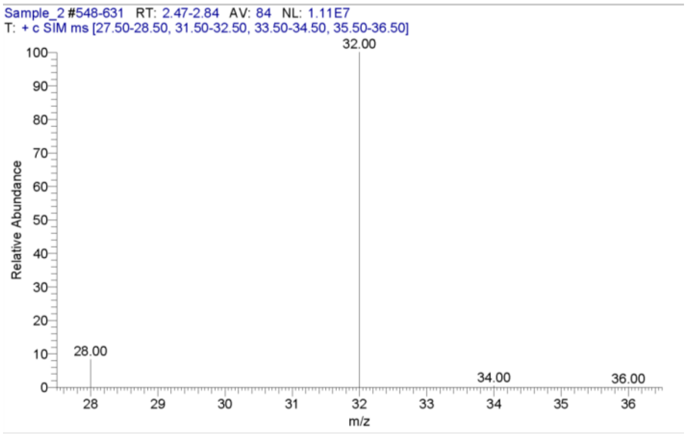

Figure S4.53. MS dedection of headspace composition after water oxidation with LT-$Li_{0.4}CoO_2$ in normal H_2O (irradiation at 465 nm for 30 min).

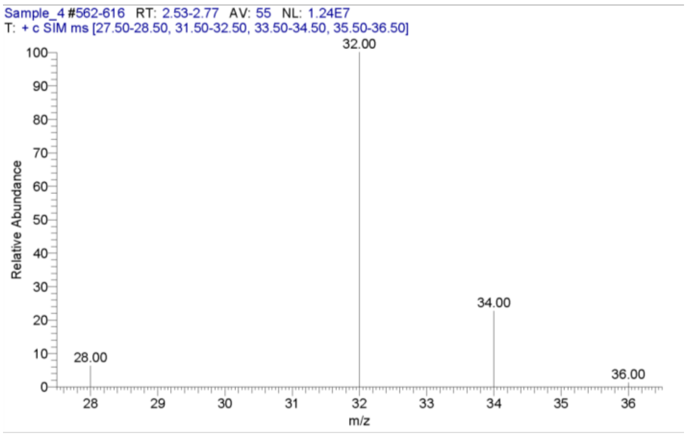

Figure S4.54. MS dedection of headspace composition after water oxidation with LT-$Li_{0.4}CoO_2$ in 10 % ^{18}O containing water (irradiation at 465 nm for 30 min).

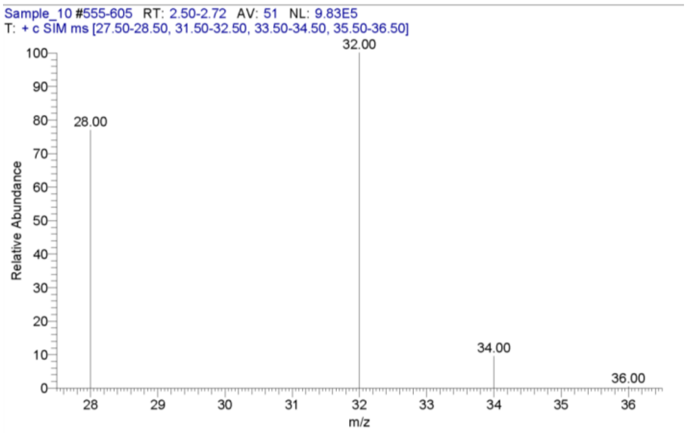

Figure S4.55. MS dedection of headspace composition after water oxidation with LT-$LiCoO_2$ in 10 % ^{18}O containing water (rradiation at 465 nm for 30 min).

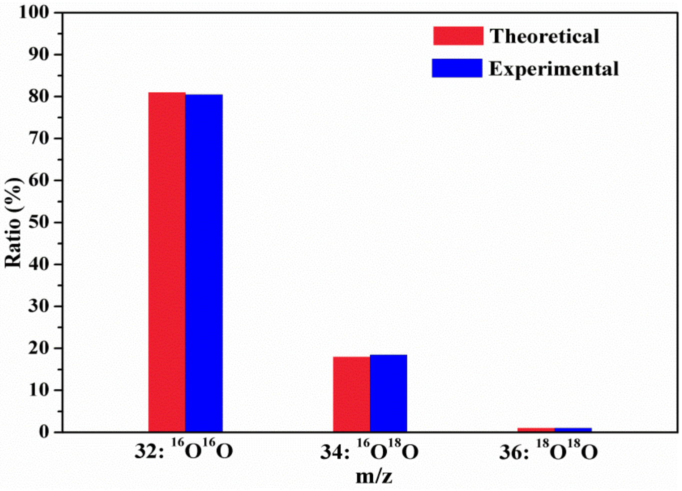

Figure S4.56. Comparison of expected and experimental $^{16}O^{16}O$, $^{16}O^{18}O$ and $^{18}O^{18}O$ ratios after water oxidation with LT- $Li_{0.4}CoO_2$ in 10 % ^{18}O containing water.

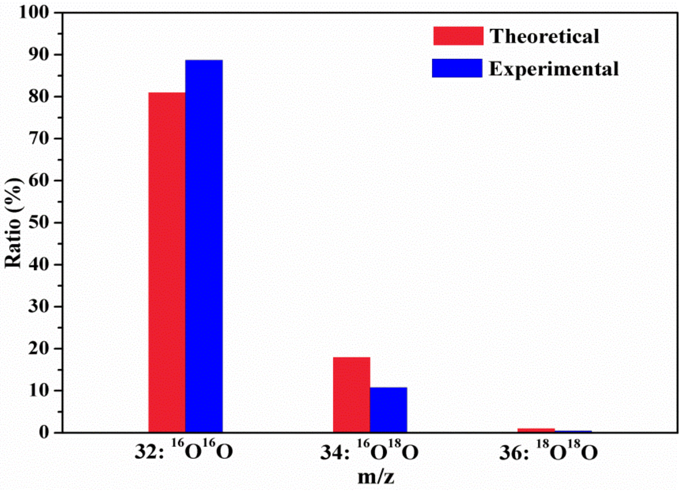

Figure S4.57. Comparison of expected and experimental $^{16}O^{16}O$, $^{16}O^{18}O$ and $^{18}O^{18}O$ ratios after water oxidation with LT- $LiCoO_2$ in 10 % ^{18}O containing water.

Experimental results for LT- $LiCoO_2$ displays a higher deviation from theoretical values compared to LT- $Li_{0.4}CoO_2$, because more $^{16}O^{16}O$ from ambient air diffused into the headspace for LT-$LiCoO_2$, as is evident from the N_2 (m/z = 28) peak the MS data (Figure S4.55).

References

[1] H. Liu, G. R. Patzke. *Chem. Asian J.* **2014**, *9*, 2249-2259.

[2] D. Hong, Y. Yamada, T. Nagatomi, Y. Takai, S. Fukuzumi. *J. Am. Chem. Soc.* **2012**, *134*, 19572-19575.

[3] M Grzelczak, J. Zhang, J. Pfrommer, J. Hartmann, M. Driess, M. Antonietti, X. Wang. *ACS Cat.* **2013**, *3*, 383-388.

[4] M. C. Rao, O. M. Hussain. *Optoelectron. Adv. Mat.*, **2012**, *6*, 245-248.

[5] A. Indra, P. W. Menezes, N. R. Sahraie, A. Bergmann, C. Das, M. Tallarida, D. Schmeiβer, P. Strasser, M. Driess. *J. Am. Chem. Soc.* **2014**, *136*, 17530-17536.

5. Chemical Delithiation Strategies for Water Oxidation Catalyst Design

5.1 Introduction

Even after decades of synthetic and mechanistic studies, the complicated multi-step processes involved in water oxidation are not completely understood, especially in heterogeneous systems. Thus, empirical explorations remain indispensable, and the cuboidal $\{CaMn_4O_5\}$ oxygen evolving center (OEC) of photosystem II has become a key structural and compositional design paradigm[1-5] for molecular,[6-13] oxide,[14-17] and polyoxometalate[18-20] based WOCs. Another general design strategy which applies to most heterogeneous catalysts is to maximize catalytic sites by synthesizing non-agglomerated and high specific surface area WOCs.[21-27] Alternatively, the recent discovery of self-healing amorphous cobalt oxide[28,29] (i.e. Co-Pi) with robust and sustainable electrochemical water oxidation activity under neutral conditions opens up a new direction in exploring amorphous transition metal oxides for both electrochemical[30-34] and photochemical[35-37] water oxidation.

Lithium-containing composite oxides have been known as lithium battery anode materials for more than three decades and were newly introduced as water oxidation catalysts recently.[38-41] *Dismukes* et al. reported on $LiMn_2O_4$ derived λ-MnO_2 and spinel-type $LiCoO_2$ oxide as efficient WOCs and ascribed their activities to the presence of $\{CaMn_4O_5\}$ OEC related $\{M_4O_4\}$ cubane (M = Co and Mn) motifs since layered $LiCoO_2$ oxide without "M_4O_4" cubane units is inactive for water oxidation.[42,43] In addition to the structural design, the mobility of lithium in these materials provides the possibility to tune their electronic properties and therefore the water oxidation activities.[44] Recently, we employed both spinel and layered $LiCoO_2$ oxides for photochemical water oxidation and observed significant improvement of their photocatalytic activities after delithiation regardless of their structural difference.[45] Likewise, two recent parallel studies on $LiCoO_2$ oxides for electrochemical water oxidation also revealed the dramatic impact of delithiation on their catalytic activities even though two opposite conclusions were reached.[46,47] To further explore the influence of delithiation on water oxidation, $LiCoPO_4$ and $LiMn_2O_4$ battery materials were delithiated for photochemical oxygen evolution in the present study. Additionally, pH and buffer dependent water oxidation processes and the influence of these parameters on the interaction between photosensitizer and electron acceptor were studied in detail.

5.2 Experimental

5.2.1 WOC preparation

$LiCoPO_4$ was synthesized via a conventional sol-gel method: LiH_2PO_4 was mixed with Cobalt (II) acetylacetonate in a molar ratio of 1:1 and calcinated at 600 ^oC in argon atmosphere (30 ml/min) for 8 h. The carbon coating was further removed by a following calcination at 350 ^oC in air atmosphere for 5 h to obtain the final product. $LiMn_2O_4$ was preparation by annealing a mixture of MnO_2 nanowires and LiOH at 350 ^oC for 5 h. MnO_2 nanowires were synthesized by hydrothermal treatment of $MnSO_4$ (80 mM) and $(NH_4)_2S_2O_8$ (80 mM) mixed aqueous solution (10 mL) in a 15 mL autoclave at 140 ^oC for 12 hours. Non-stoichiometric $Li_{1-x}CoPO_4$ and $Li_{1-x}Mn_2O_4$ were obtained by chemical lithium extraction of $LiCoPO_4$ and $LiMn_2O_4$, respectively, in a bromine-acetonitrile (4 mL Br_2 in 10 mL CH_3CN) solution for 7 d.

5.2.2 Photocatalytic water oxidation

Water oxidation tests were conducted according to well established $[Ru(bpy)_3]^{2+}/S_2O_8^{2-}$ protocols. First, a suspension was prepared by mixing 10 mg water oxidation catalyst, 8 mg $[Ru(bpy)_3]Cl_2$ photosensitizer and 50 mg NaS_2O_8 in 8 mL phosphate buffer (0.1 M, pH 7) in a 10 mL vial in the dark. Next, the suspension was degassed with helium to remove O_2 in both solution and the headspace. A LED lamp with 460 nm wavelength and 5000 Lux output was used as visible light source. Oxygen produced in solution was online monitored with a calibrated Clarke electrode (Unisense) or by gas chromatography detection of head space (Agilent 7820A packed with a 3 m × 2 mm molecular sieve 13X 80-100 column) as follows: 100 μL samples of gas from the head space were injected into a gas chromatograph using a gastight microliter syringe (Hamilton 1825 RN) during intervals of several minutes. Helium was chosen as carrier gas to increase the detection sensitivity of O_2. Gases were detected with a thermal conductivity detector (Varian) operated at 200 °C. Contamination of the headspace by air was constantly monitored through the N_2 peak on GC chromatograms. Calibration was performed by injection of known quantities of pure oxygen diluted in the vial containing the same volume and concentration of buffered solution as used for the measurements.

5.2.3 Characterizations

Powder X-ray diffraction patterns (PXRD patterns) were recorded on a XPERT-PRO diffractometer (reflection mode, step size: 0.04°/step, 15 s/step) with Cu $K\alpha_1$ radiation. Sample morphologies were examined by scanning electron microscopy (LEO 1530, FEG) and transmission electron microscopy (FEI Tecnai F30, FEG, 300 kV). Brunauer-Emmett-Teller (BET) surface area measurements were conducted on a Quadrasorb SI machine in N_2-adsorption mode. Samples were degassed at 150 °C for 15 h under vacuum prior to the measurements. Raman spectra were recorded on a Renishaw Ramascope spectrometer at 514 nm laser excitation. UV/Vis spectra were recorded on a Lambda 650 S Perkin Elmer UV-visible spectrometer. XPS spectra were measured on an Axis Ultra DLD spectrometer (Kratos, UK) with a 0.1 eV energy resolution. Measurements were performed with a monochromatic Al K_α source without any preceding sputter cleaning or other procedures that might alter the surface of the crystals. The C 1s peak at 284.6 eV was set as reference for the calibration of all XPS peak positions. The composition of lithium cobalt oxides was analyzed with ICP-AES on an Optima 5300DV spectrometer with a 0.008 nm resolution. Samples were completely dissolved in nitric acid and diluted to a certain concentration within the detection range of the spectrometer. Cyclic voltammograms (CV) were recorded with a Metrohm 797 VA computrace, and solutions were purged prior to the measurement with nitrogen. A polished glassy carbon electrode was used as working electrode (Metrohm AG, 3 mm) and Ag/AgCl was used as a reference electrode (Metrohm AG). Lifetimes of excited $[Ru(bpy)_3]^{2+}$ were determined by the luminescence decay dynamics on a LP920 flash laser photolysis instrument from Edinburgh Instruments Ltd.

5.3 Results and discussion

5.3.1 Influence of delithiation on water oxidation of $LiCoPO_4$ and $LiMn_2O_4$

As shown in Figure 5.1a, PXRD patterns of $LiCoPO_4$ before and after delithiation agree well with literature data (JCPDS: 89-6192) and thus confirm the presence of an orthorhombic olivine structure (S.G. *Pnma*). Likewise, the PXRD patterns of $LiMn_2O_4$ before and after delithiation match well with references (JCPDS: 85-341, S. G. Fd-3m), indicating the formation of a spinel structure (Figure 5.1b).

In contrast to Li_xCoO_2[45,48], lithium extraction from $LiCoPO_4$ by treatment with bromine does not lead to an obvious shift of the diffraction peaks. The lattice constants derived from full fitting of PXRD patterns (Jade 5.0) are a=10.202(9), b=5.920(5), c=4.700(4) Å for pristine $LiCoPO_4$ and *a*=10.200(7), *b*=5.920(4), *c*=4.698(3) Å for $LiCoPO_4$ after delithiation respectively, indicating no significant structural changes upon delithiation. The Li/Co atomic ratio for $LiCoPO_4$ after delithiation determined by ICP-AES is 0.86 which is only slightly lower than 1.05 for pristine $LiCoPO_4$, as shown in Table 5.1. The minor lithium leaching is consistent with the much higher potential of $LiCoPO_4$ (4.8 V vs. Li^+/Li for complete delithiation)[49] compared to the oxidation potential of Br_2 (3.7 V vs. Li^+/Li).[50] The insignificant change of lattice constants upon delithiation may imply a partial delithiation on the particle surface instead of the bulk.

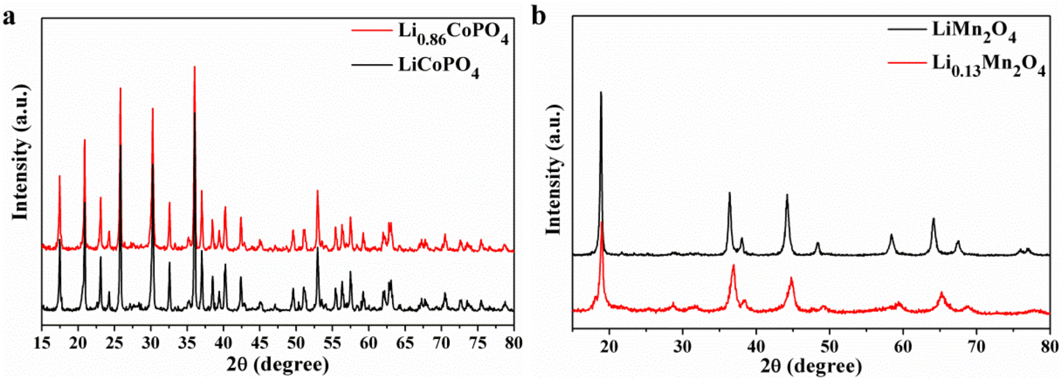

Figure 5.1. PXRD pattern of (a) $LiCoPO_4$ vs. $Li_{0.86}CoPO_4$, and (b) $LiMn_2O_4$ vs. $Li_{0.13}Mn_2O_4$.

In contrast to $LiCoPO_4$, the PXRD pattern of $LiMn_2O_4$ after delithiation underwent a dramatic diffraction peak shift (Figure 5.1b). PXRD full fitting provides the lattice constants of *a*= 8.092 Å for delithiated $LiMn_2O_4$ which are shortened with respect to pristine $LiMn_2O_4$ (*a* = 8.229 Å, Table 5.1), revealing significant lattice contraction in the bulk of $LiMn_2O_4$ nanoparticles during lithium extraction. Elemental analyses confirmed a deep delithiation and the Li/Mn ratios decreased from 0.54 to 0.13, in line with the much lower potential of $LiMn_2O_4$ (4 V vs. Li^+/Li for complete delithiation)[49] compared to $LiCoPO_4$.

Table 5.1. Lattice constants, Li/Co ratio and BET surface of $LiCoPO_4$, Li_xCoPO_4, $LiMn_2O_4$ and $Li_xMn_2O_4$.

WOC	Lattice constants/Å	Li/Co ratio	BET(m^2/g)
$LiCoPO_4$	*a*=10.202(9); *b*=5.920(5); *c*=4.700(4)	1.05	4.41
Li_xCoPO_4	*a*=10.200(7); *b*=5.920(4); *c*=4.698(3)	0.86	2.22
$LiMn_2O_4$	*a*= 8.229(5)	0.54	37.43
$Li_xMn_2O_4$	*a*= 8.092(2)	0.13	38.27

Photochemical water oxidation activity was evaluated according to a well established $[Ru(bpy)_3]^{2+}/S_2O_8^{2-}$ method with a 460 nm LED as light source. The oxygen evolution of

$LiCoPO_4$ and $Li_{0.86}CoPO_4$ was detected by GC in the headspace (Figure 5.2a) and by Clark electrode in solution, respectively (Figure S5.1). Delithiated $Li_{0.86}CoPO_4$ displayed a significantly higher water oxidation activity than $LiCoPO_4$. Compared to the oxygen evolution in solution, the oxygen concentration in headspace increased much more slowly at the first five minutes due to the oxygen diffusion delay from solution to the headspace. While the oxygen concentration in solution was equilibrated after 7 min of irradiation, it took more than 20 minutes to level off in headspace. The total oxygen evolution amount evolved for $Li_{0.86}CoPO_4$ is 6.65 μmol, which is 35 times higher than that of $LiCoPO_4$ according to the GC detection.

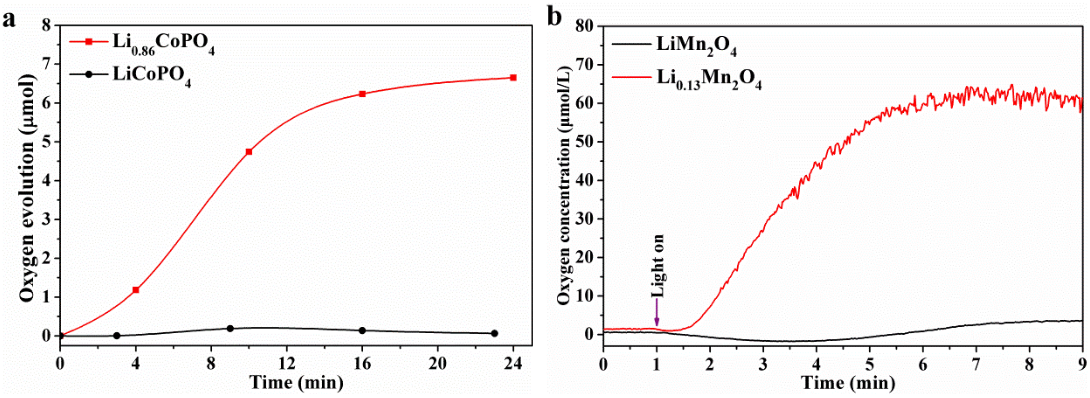

Figure 5.2. Photochemical water oxidation activity of (a) $LiCoPO_4$ and $Li_{0.86}CoPO_4$ detected by GC in headspace, and (b) $LiMn_2O_4$ and $Li_{0.13}$ Mn_2O_4 monitored by Clark electrode.

Similar to $Li_{0.86}CoPO_4$, a significant improvement of water oxidation was observed for $Li_{0.13}Mn_2O_4$ as well compared to $LiMn_2O_4$ (Figure 5.2 b). However, the overall activity of $Li_{0.13}Mn_2O_4$ is much lower than that of $Li_{0.86}CoPO_4$ and cannot be well detected by GC in headspace. Analogous to the superior water oxidation activity of Co_3O_4 and Co_2MnO_4 to $CoMn_2O_4$ and Mn_3O_4,[51,52] this is ascribed to the essentially higher catalytic activities of cobalt-containing WOCs. The consistent impact of delithiation on water oxidation for $LiCoPO_4$, $LiMn_2O_4$ and recently studied $LiCoO_2$[45] may imply a similar working mechanism underlying the performance improvement among these compounds.

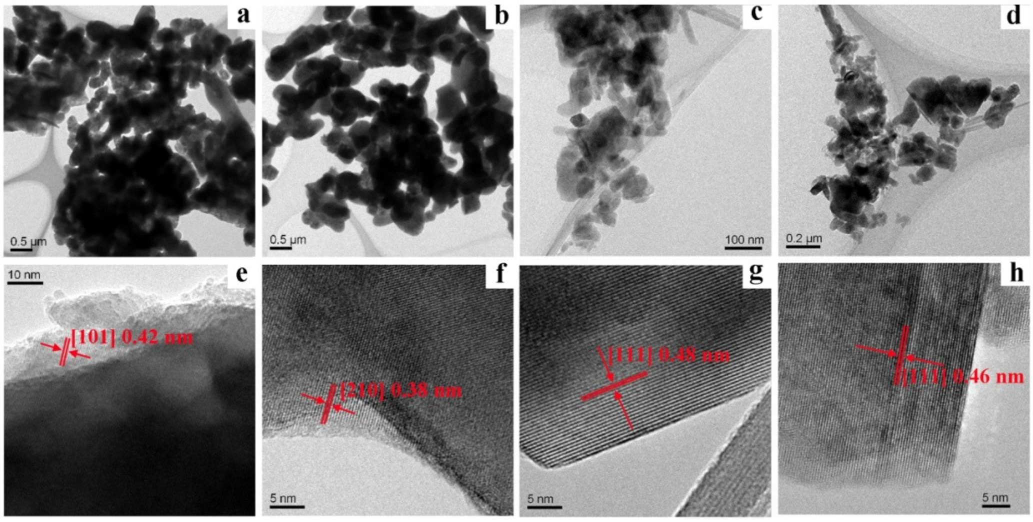

Figure 5.3. TEM pictures of (a) (e) $LiCoPO_4$, (b) (f) $Li_{0.86}CoPO_4$, (c) (g) $LiMn_2O_4$, and (d) (h) $Li_{0.13}Mn_2O_4$.

As the reactions involved in heterogeneous catalysis only proceed on the interface between catalyst and solution, the surface area strongly influences the overall activity for a catalyst with given activity per each catalytic site. Plenty of recent studies indeed revealed that nanostructuring and manufacturing porosity are efficient strategies to improve the performance of heterogeneous WOCs.[21-27] Herein, we investigate the morphology by TEM (Figure 5.3), SEM (Figure S5.2) and Brunauer Emmett Teller (BET) specific area analysis (Table 5.1). In contrast to spinel Li_xCoO_2,[45] SEM and TEM images indicate that $Li_{0.86}CoPO_4$ was not subjected to obvious morphological changes during lithium extraction. Conversely, a possible agglomeration can be observed from TEM pictures which may explain the slightly lower BET surface area (Table 5.1) of $Li_{0.86}CoPO_4$ in comparison to $LiCoPO_4$. Different from $Li_{0.86}CoPO_4$, $LiMn_2O_4$ probably underwent a particle size refinement and agglomeration concluding from the TEM (Figure 5.3) and SEM (Figure S5.3) pictures. However, BET measurements indicate no significant change of surface area, which is probably due to a cancellation of the opposite effects of particle size decrease and agglomerization.

The oxygen evolution was further normalized to BET surface for a standardized comparison (Figure 5.4a). Even after normalization, $Li_{0.86}CoPO_4$ still shows much higher activity than $LiCoPO_4$. The same trend was observed for $LiMn_2O_4$ before and after delithiation (Figure 5.4b). This indicates that the improved water oxidation performance after delithiation is due to enhancement of intrinsic catalytic activities instead of increased catalytic sites accessible to water oxidation reactions.

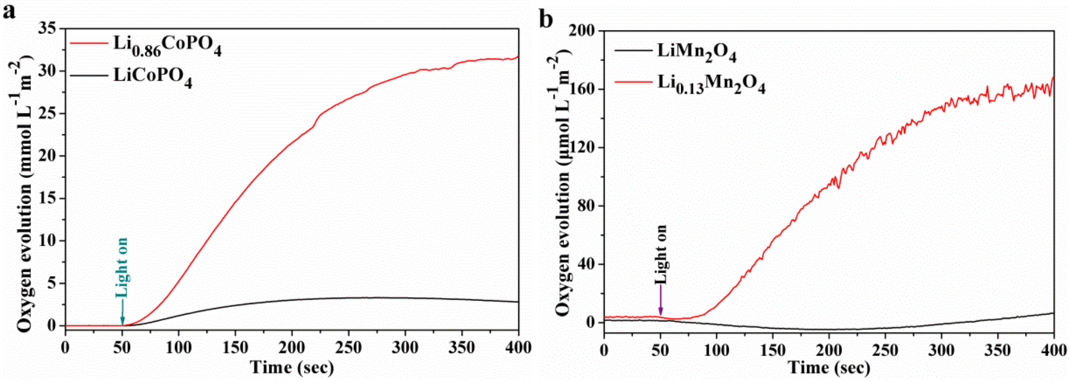

Figure 5.4. Photochemical water oxidation activity of (a) $LiCoPO_4$ and $Li_{0.86}CoPO_4$ and (b) $LiMn_2O_4$ and $Li_{0.13}$ Mn_2O_4 after normalization to the BET surface area (monitored by Clark electrode).

5.3.2 Influence of delithiation on the electronic properties of $LiCoPO_4$

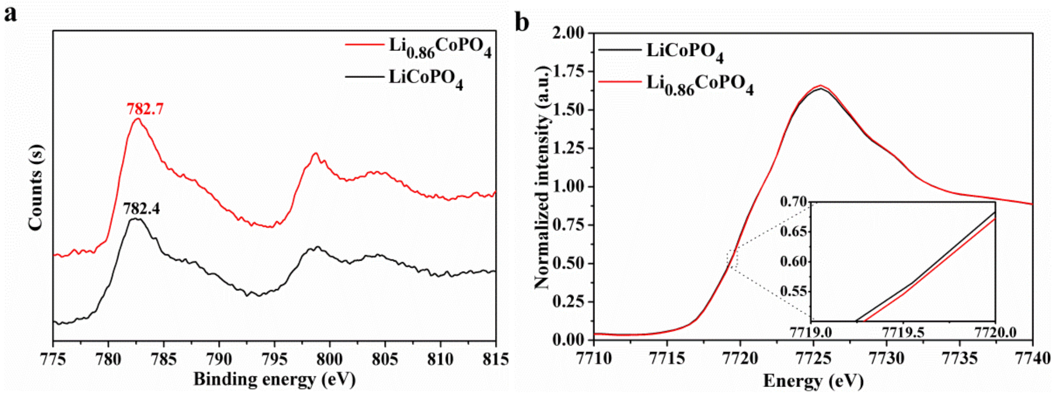

Figure 5.5. (a) Co 2p XPS spectra, (b) *ex-situ* XANES Co K-edge spectra of $LiCoPO_4$ and $Li_{0.86}CoPO_4$.

The influence of delithiation on the electronic structure was studied by XPS and XAS spectroscopy, respectively. Co 2p spectra (Figure 5.5a) are mainly composed of two peaks at 780 eV and 797 eV, which are corresponding to Co $2p_{3/2}$ and Co $2p_{1/2}$ respectively. These two peaks were accompanied by two MLCT-based satellite peaks located at ca. 10 eV higher binding energies. A slight shift of Co $2p_{3/2}$ from 782.4 to 782.7 eV after delithiation indicates partial oxidation of Co^{2+} to Co^{3+} which can be further verified by the broadening of Co 3p peak toward higher binding energy (Figure S5.4). Whereas XPS is surface sensitive, XAS is a more effective way to evaluate the average bulk cobalt valence state. Therefore, we investigated the average valence state of Co by XAS. As shown in Figure 5.5b, Co K edge absorption spectra of $Li_{0.84}CoPO_4$ and $LiCoPO_4$ overlap well with each other except for a neglectable shift toward higher energy for $Li_{0.86}CoPO_{4,}$ which implies no significant change of cobalt valence states in the bulk. This is consistent with the basically unchanged lattice constants after delithiation. These results provide further evidence that lithium leaching is probably only limited to the surface layers.

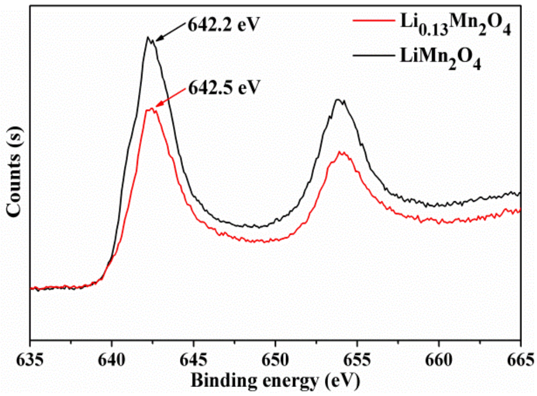

Figure 5.6. Mn 2p spectra of $LiMn_2O_4$ and $Li_{0.13}$ Mn_2O_4.

Mn 2p spectra are known to be rather insensitive to the Mn valence states as well and despite the deep delithiation, only a slight shift from 642.2 to 642.5 eV can be observed. The Mn $2p_{3/2}$ peak of $LiMn_2O_4$ is located at 642.2 eV which is just between MnO_2 (642.6 eV) and Mn_2O_3 (641.2 eV),[53] indicating its mixed valence states of +3 and +4. Noteworthy is that a small shoulder at around 640 eV disappeared after delithiation, which may point to the oxidation of Mn^{3+} to Mn^{4+}. Nevertheless, the significant contraction of lattice constant after delithiation clearly revealed a shorter Mn-O bond length, indicating the presence of higher Mn valence states in the bulk.

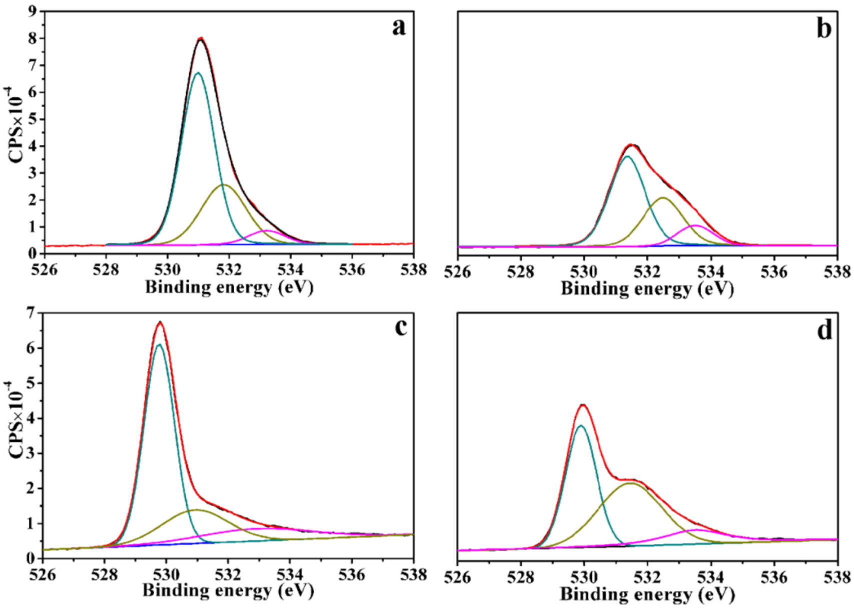

Figure 5.7. O 1s spectra of (a) $LiCoPO_4$, (b) $Li_{0.86}CoPO_4$, (c) $LiMn_2O_4$, and (d) $Li_{0.13}$ Mn_2O_4.

O 1s spectra (Figure 5.7) were well fitted by three peak components at 531, 532 and 533 eV, respectively. While the first component at 531 eV and third component at 533 eV can be undoubtedly ascribed to lattice oxygen and surface absorbed oxygen species, the assignment of the second component at 532 eV remains controversial. It can be ascribed to either surface oxygen species or to lattice oxygen species with stronger covalent bonding character to cobalt compared to the first component. After delithiation of $LiCoPO_4$, the ratio between the different peak components underwent a remarkable change with greatly increased proportions of the second and third fraction (Figure 5.7 a and b). This indicates that delithiation led to enhanced affinity of oxygen to cobalt either by a higher covalent character or by enriched surface oxygen species. Interestingly, similar changes on the O 1s spectra through delithiation were observed for $LiMn_2O_4$ (Figure 5.7 c and d) and $LiCoO_2$ as well. Our recent study on $LiCoO_2$ revealed a semiconductor to metal transition with enhanced hole mobility through delithiation. This is most likely responsible for the significant improvement of water oxidation activity through acceleration of the hole transfer processes involved in water oxidation. The enhanced covalence of Co-O of $Li_{0.86}CoPO_4$ probably facilitates the hole mobility and improves the water oxidation activity following the same mechanism as for Li_xCoO_2. An alternative explanation is the enhanced electrophilicity of surface absorbed oxygen which may facilitate its reaction with OH^- to form –OOH,[54, 55] which has been reported to be the rate-limiting step of oxygen evolution.[56]

5.3.3 Interaction between photosensitizer and persulfate

Photochemical water oxidation with $Li_{0.86}CoPO_4$ was investigated at different pH values (3, 5, 6, 7 and 8 potassium phosphate buffer) for comparison, as shown in Figure 5.8. Maximum performance was reached at pH 7 with an equilibrium oxygen concentration of 700 µmol/L. While higher pH values are supposed to facilitate the proton coupling electron transfer (PCET) and are thus beneficial for water oxidation,[57,58] the oxygen evolution rate reached a maximum at lower pH 7 instead of 8 (Figure S5.19), thereby excluding the PCET process as the rate determining step.

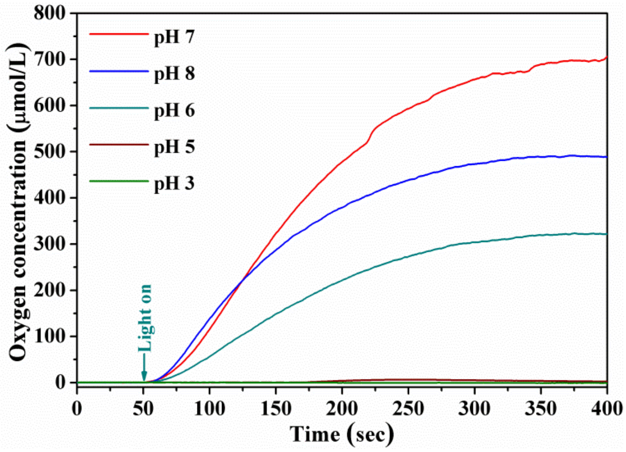

Figure 5.8. pH dependent water oxidation of $Li_{0.86}CoPO_4$.

A previous study[59] predicted the formation of ion pairs between $S_2O_8^{2-}$ and $[Ru(bpy)_3]^{2+}$ in aqueous solution. Here we confirmed this hypothesis by ^{1}H-NMR. As shown in Figure 5.9, ^{1}H spectra of persulfate solution display a single peak at 4.7 ppm corresponding to H_2O, while $[Ru(bpy)_3]^{2+}$ exhibits four peaks at 7.28, 7.74, 7.97 and 8.45 ppm with comparable integral areas which are ascribed to four different H atoms of the bipyridine ring.[60] Mixing persulfate with $[Ru(bpy)_3]^{2+}$ does not result in a combination of their respective spectra but a significant shift and broadening of the ^{1}H spectra of $[Ru(bpy)_3]^{2+}$. This probably implies an electrostatically favored interaction of bipyridine rings and persulfate anions.

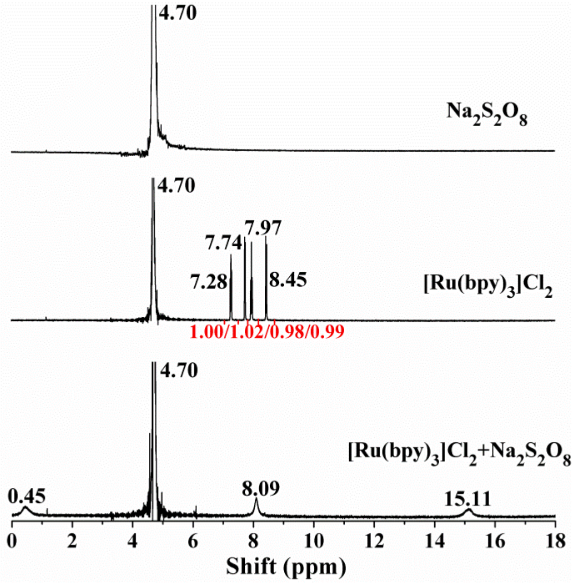

Figure 5.9. ^{1}H-NMR of $Na_2S_2O_8$, $[Ru(bpy)_3]Cl_2$ and of the combination of $Na_2S_2O_8$ and $[Ru(bpy)_3]Cl_2$.

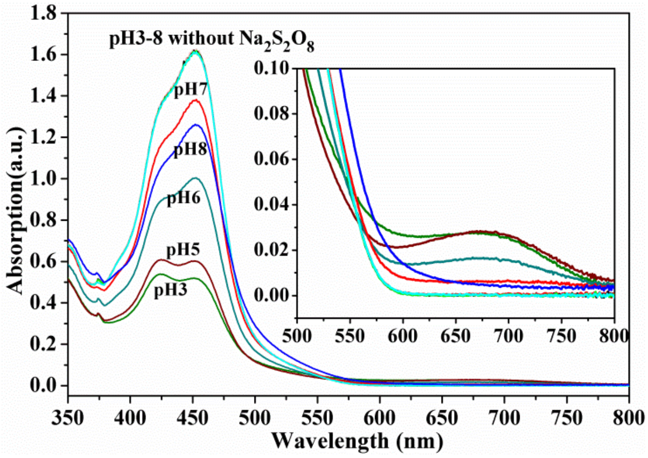

Figure 5.10. pH dependent absorption of $[Ru(bpy)_3]Cl_2$ in the presence and absence of $Na_2S_2O_8$.

To clarify the underlying mechanisms for pH-dependent water oxidation activities, the influence of pH on the interactions between persulfate and $[Ru(bpy)_3]^{2+}$ was investigated. The fluorescence lifetime of photo-excited $[Ru(bpy)_3]^{2+*}$ in the presence and absence of persulfate were investigated by flash laser photolysis. All the lifetime values of $[Ru(bpy)_3]^{2+*}$ were shortened from around 400 ns to 40 ns regardless of the pH (Figure S5.20). Fluorescence measurements of $[Ru(bpy)_3]^{2+*}$ revealed that its fluorescence properties are independent of pH as well (Figure S5.21). In contrast, a clear correlation can be established between water oxidation activity and absorption of $[Ru(bpy)_3]Cl_2$ in the presence of persulfate. The strongest absorption at pH 7 led to the best oxygen evolution performance while the much weaker absorption with increased proportion of the shoulder (425 nm) at pH 3 and 5 basically resulted in inactivity. In the absence of persulfate, the absorption behavior of $[Ru(bpy)_3]^{2+}$ at different pH values remained constant, indicating that pH only influences the interaction between $[Ru(bpy)_3]^{2+}$ and $Na_2S_2O_8$ rather than $[Ru(bpy)_3]^{2+}$ itself.

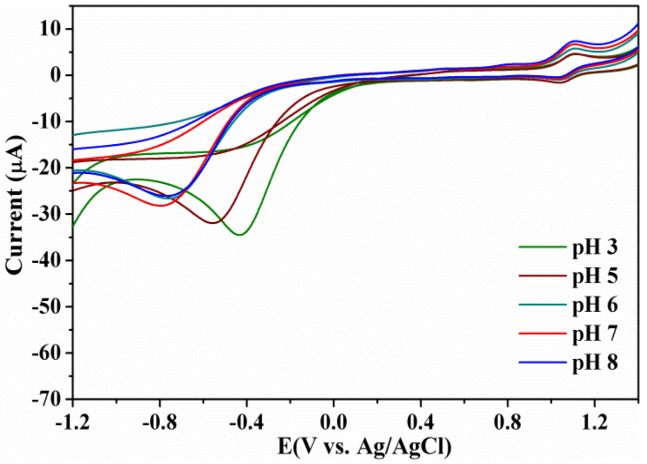

Figure 5.11. Cyclic voltammogram of $Na_2S_2O_8$-$[Ru(bpy)_3]Cl_2$ solution in different pH.

The reduction potential of persulfate and the redox potential of $[Ru(bpy)_3]^{2+}$ were further quantified by cyclic voltammetry. As shown in Figure S5.22, the redox potential of $[Ru(bpy)_3]^{2+}$ remained constant at different pH values with an oxidation wave and a reduction wave situated at 1.12 V and 1.05 V vs. Ag/AgCl, respectively. In contrast, the reduction potential of persulfate changed dramatically with pH both in the presence (Figure 5.11) and absence (Figure S5.23) of $[Ru(bpy)_3]^{2+}$. In line with the trends for water oxidation activity and absorption of $[Ru(bpy)_3]^{2+}$, the reduction wave of persulfate shifted to higher reduction potential when the pH was increased from 3 to 7 and decreased again at pH 8. Previous studies revealed the formation of different oxidation species from persulfate, with $SO_4^{\cdot-}$ radicals prevailing in acidic and $^{\cdot}OH$ radical in alkaline conditions, respectively.[61] This probably explains the pH influence on the reduction potential of persulfate. The absorption observed around 675 nm (inset in Figure 5.10) corresponds to $[Ru(bpy)_3]^{3+}$. While no $[Ru(bpy)_3]^{3+}$ absorption is present in the absence of persulfate, certain amounts of $[Ru(bpy)_3]^{3+}$ are formed after persulfate addition. Moreover, the concentration of $[Ru(bpy)_3]^{3+}$ is inversely proportional to the reduction potential of persulfate over the investigated pH range, indicating that the pH influences the water oxidation activity via transformation of $[Ru(bpy)_3]^{3+}$ to $[Ru(bpy)_3]^{2+}$.

The influence of persulfate concentration on the water oxidation performance was further studied as shown in Figure 5.12. In principle, the oxygen evolution rate should be promoted by higher concentration of electron acceptors as it can accelerate the conversion of photo-excited $[Ru(bpy)_3]^{2+*}$ to $[Ru(bpy)_3]^{3+}$ and therefore facilitate hole injection to the WOC. Unexpectedly, the water oxidation activities decreased with increasing persulfate concentration in the present case. This counterintuitive result implies that other factors than water oxidation kinetics that determine the oxygen evolution rate.

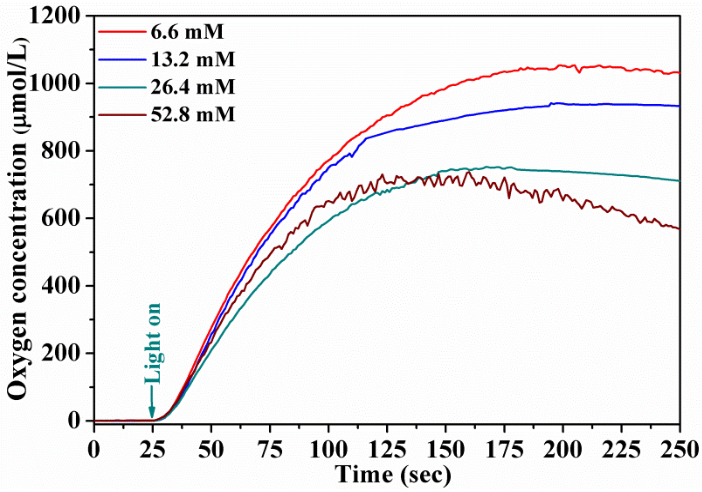

Figure 5.12. Water oxidation of $Li_{0.86}CoPO_4$ as a function of persulfate concentration.

Therefore, the absorption characteristics of $[Ru(bpy)_3]^{2+}$ were recorded in the presence of different persulfate concentrations (Figure 5.13). Analogous to the influence of pH, persulfate concentration significantly changed the absorption concentration of $[Ru(bpy)_3]^{2+}$. This result further confirms that under the present conditions the $[Ru(bpy)_3]^{2+}$ concentration determines the final oxygen evolution amount rather than the water oxidation kinetics. The beneficial influence of $[Ru(bpy)_3]^{2+}$ absorption on water oxidation performance was further verified by concentration-dependent activity tests of $[Ru(bpy)_3]^{2+}$, as presented in Figure S5.25.

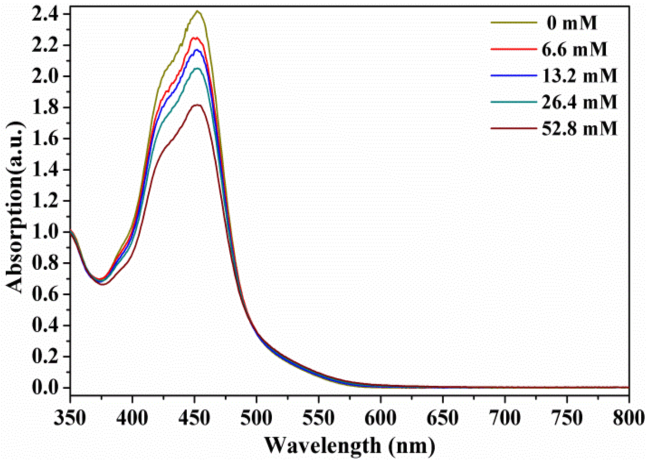

Figure 5.13. Persulfate concentration dependent absorption of $[Ru(bpy)_3]Cl_2$.

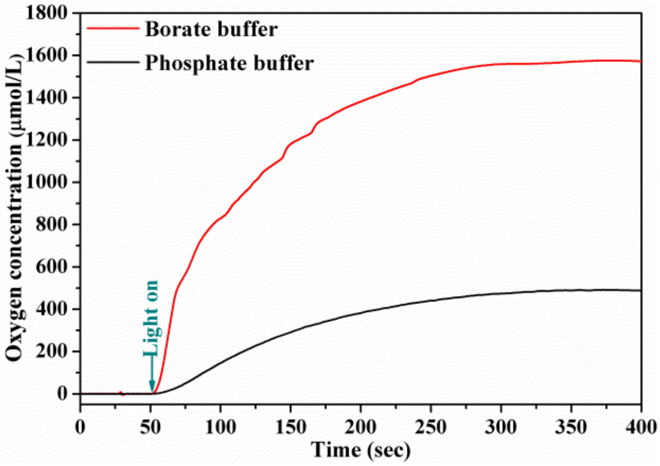

Figure 5.14. Water oxidation of $Li_{0.86}CoPO_4$ as a function of the buffer composition.

Water oxidation activities of $Li_{0.86}CoPO_4$ in both phosphate and borate buffer at pH 8 were further investigated. Interestingly, the oxygen evolution concentration in borate buffer reached a maximum of 1580 μmol/L which is 2.2 times higher than in phosphate buffer (490 μmol/L). Figure 5.15 displays the absorption of $[Ru(bpy)_3]^{2+}$ in borate and phosphate buffers before and after water oxidation. An obvious decrease of the absorption at around 465 nm indicates that $[Ru(bpy)_3]^{2+}$ was decomposed or transformed to $[Ru(bpy)_3]^{3+}$. Noteworthy, the absorption after water oxidation in borate buffer is much stronger than in phosphate buffer even though the pH for borate buffer decreased to an unfavorable value of 3.75 compared to 6.76 for phosphate buffer (Figure 5.15). Moreover, the absorption curve after water oxidation in phosphate buffer had significantly changed compared to pristine $[Ru(bpy)_3]^{2+}$ absorption. The above results strongly suggest a higher extent of degradation for $[Ru(bpy)_3]^{2+}$ in phosphate compared to borate.

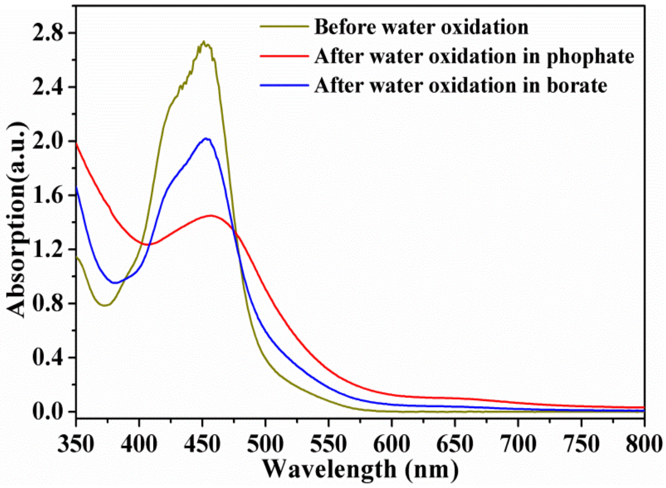

Figure 5.15. Absorption of $[Ru(bpy)_3]Cl_2$ before and after water oxidation in phosphate and borate buffer (pH 8).

Further stability investigations of $[Ru(bpy)_3]^{2+}$ were conducted by aging $[Ru(bpy)_3]^{2+}$ in both borate and phosphate buffers in the presence or absence of persulfate. As seen in Figure 5.16, some absorption decrease of $[Ru(bpy)_3]^{2+}$ sets in after aging for one hour in both borate and phosphate buffer in the presence of persulfate. Phosphate buffer led to a slightly stronger absorption decrease compared to phosphate. 6 d of ageing induced a significant absorption decrease accompanied by an increasing absorption of $[Ru(bpy)_3]^{3+}$ at 675 nm. Furthermore, the absorption at 350 nm in phosphate buffer slightly increased while it remained constant in borate buffer, confirming that $[Ru(bpy)_3]^{2+}$ had undergone more serious decomposition in phosphate. In the absence of persulfate, the absorption of $[Ru(bpy)_3]^{2+}$ remains constant regardless of the ageing time.

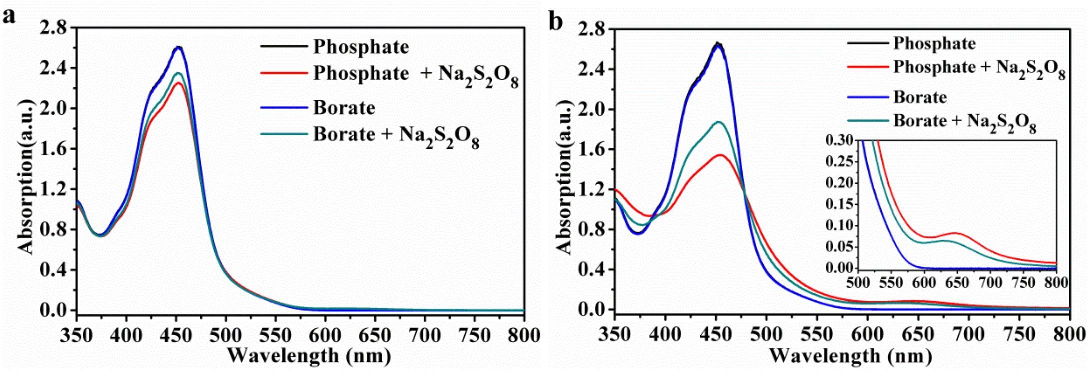

Figure 5.16. Absorption of [Ru(bpy)$_3$]Cl$_2$ after aging in phosphate and borate buffer for 1 h (left) and 7 d (right).

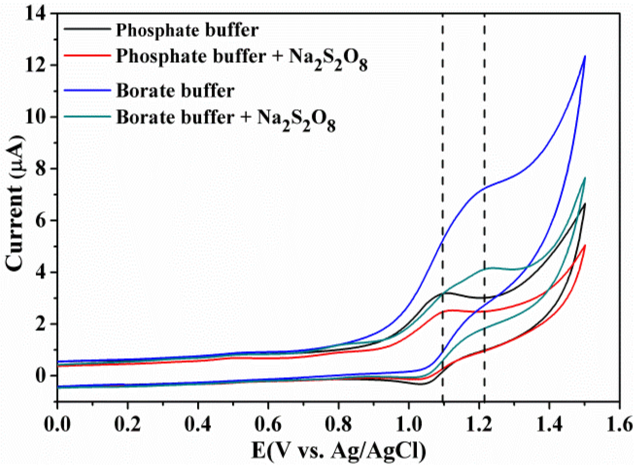

Figure 5.17. Influence of buffer composition on the redox potential of [Ru(bpy)$_3$]$^{2+}$.

While fluorescence spectra indicate no influence of buffer media on the lifetime of [Ru(bpy)$_3$]$^{2+*}$ (Figure S5.26), cyclic voltammogrammetry results displayed a shift of oxidation potential of [Ru(bpy)$_3$]$^{2+}$ from 1.09 V in phosphate to 1.22 V in borate (Figure 5.17). This indicates that [Ru(bpy)$_3$]$^{2+}$ in borate buffer is more stable, especially against oxidation by persulfate, which is consistent with the observation of higher [Ru(bpy)$_3$]$^{2+}$ concentration after aging in borate buffer.

5.4 Conclusions

In summary, LiCoPO$_4$ as a prominent battery material was newly investigated for photochemical water oxidation and a significant improvement of the catalytic activity was achieved by partial chemical delithiation. Lithium mobility is introduced as an efficient concept to tune the electronic structures of lithium-containing ternary oxides for efficient water oxidation. Water oxidation at different pH values revealed a strong interaction between persulfate and $[Ru(bpy)_3]^{2+}$ photosensitizer. Additionally, superior water oxidation activity was observed in borate buffer compared to phosphate buffer. Both pH and buffer composition were found to strongly influence the redox potential of $Na_2S_2O_8$ which in turn affects the interaction between persulfate and $[Ru(bpy)_3]^{2+}$. These trends pave the way to important parameter studies for the optimization of photochemical WOC setups.

References

[1] R. Pokhrel, G. W. Brudvig. *Phys. Chem. Chem. Phys*. **2014**, *16*, 11812-11821.

[2] N. Cox, D. A. Pantazis, F. Neese, W. Lubitz. *Acc. Chem. Res*. **2013**, *46*, 1588-1596.

[3] H. Dau, I. Zaharieva, M. Haumann. *Curr. Opin. Chem. Biol.* **2012**, *16*, 3-10.

[4] A. Sartorel, M. Bonchio, S. Campagna, F. Scandola. *Chem. Soc. Rev.* **2012**, *42*, 2262-2280.

[5] G. C. Dismukes, R. Brimblecombe, G. A. N. Felton, R. S. Pryadun, J. E. Sheats, L. Spiccia, G. F. Swieger. *Acc. Chem. Res.* **2009**, *42*, 1935-1943.

[6] N. S. McCool, D. M. Robinson, J. E. Sheats, G. C. Dismukes. *J. Am. Chem. Soc.* **2011**, *133*, 11446-11449.

[7] B. Zhang, F. Li, F. Yu, X. Wang, X. Zhou, H. Li, Y. Jiang, L. Sun. *ACS Catal.* **2014**, *4*, 804-809.

[8] S. Berardi, G. L. Ganga, M. Natali, I. Bazzan, F. Puntoriero, A. Sartorel, F. Scandola, S. Campagna, M. Bonchio. *J. Am. Chem. Soc.* **2012**, *134,* 11104-11107.

[9] P. F. Smith, C. Kaplan, J. E. Sheats, D. M. Robinson, N. S. McCool, N. Mezle, G. C. Dismukes. *Inorg. Chem.* **2014**, *53*, 2113-2121.

[10] A. E. Kuznetsov, Y. V. Geletii, C. L. Hill, D. G. Musaev. *J. Phys. Chem. A* **2010**, *114*, 11417-11424.

[11] Z. Xu, F. Li, H. Li, B. Zhang, F. Yu, L. Sun. *ChemSusChem* **2014**, *7*, 2453-2456.

[12] G. L. Ganga, V. M. Nardo, M. Cordaro, M. Natali, S. Vitale, A. Licciardello, F. Nastasi, S. Campagna. *Dalton Trans.* **2014**, *43*, 14926-14930.

[13] Y. Gao, R. H. Crabtree, G. W. Brudvig. *Inorg. Chem.* **2012**, *51*, 4043-4050.

[14] M. M. Najafpour, T. Ehrenberg, M. Wiechen, P. Kurz. *Angew. Chem. Int. Ed.* **2010**, *49*, 2233-2237.

[15] M. Wiechen, I. Zaharieva, H. Dau, P. Kurz. *Chem. Sci.* **2012**, *3*, 2330-2339.

[16] V. B. R. Boppana, S. Yusuf, G. S. Hutchings, F. Jiao. *Adv. Funct. Mater.* **2013**, *23*, 878-884.

[17] R. K. Hocking, R. Brimblecombe, L.-Y. Chang, A. Singh, M. H. Cheah, C. Glover, W. H. Casey, L. Spiccia. *Nat. Chem.* **2011**, *3*, 461-466.

[18] X.-B. Han, Z.-M. Zhang, T. Zhang, Y.-G. Li, W. Lin, W. You, Z.-M. Su, E.-B. Wang. *J. Am. Chem. Soc.* **2014**, *136,* 5359-5366.

[19] Q. S. Yin, J. M. Tan, C. Besson, Y. V. Geletii, D. G. Musaev, A. E. Kuznetsov, Z. Luo, K. I. Hardcastle, C. L. Hill. *Science* **2010**, *328*, 342-345.

[20] R. Al-Oweini, A. Sartorel, B. S. Bassil, M. Natali, S. Berardi, F. Scandola, U. Kortz, M. Bonchio. *Angew. Chem. Int. Ed.* **2014**, 53, 1-5.

[21] F. Jiao, H. Frei. *Angew. Chem. Int. Ed.* **2009**, *48*, 1841-1844.

[22] C.-C. Yang, T. M. Eggenhuisen, M. Wolters, A. Agiral, H. Frei, P. E. Jongh, K. P. Jong, G. Mul. *ChemCatChem* **2013**, *5*, 550-556.

[23] J. Rosen, G. S. Hutchings, F. Jiao. *J. Am. Chem. Soc.* **2013**, *135*, 4516-4521.

[24] M. Grzelczak, J. Zhang, J. Pfrommer, J. Hartmann, M. Driess, M. Antonietti, X. Wang. *ACS Catal.* **2013**, *3*, 383-388.

[25] J. D. Blakemore, H. B. Gray, J. R. Winkler, A. M. Müller. *ACS Catal.* **2013**, *3*, 2497-2500.

[26] H. S. Ahn, J. Yano, T. D. Tilley. *Energy Environ. Sci*. **2013**, *6*, 3080-3087.

[27] J. Wei, Y. Liu, Y. Ding, C. Luo, X. Du, J. Lin. *Chem. Commun.* **2014**, *50*, 11938-11941.

[28] M. W. Kanan, D. G. Nocera. *Science* **2008**, *321*, 1072-1075.

[29] D. A. Lutterman, Y. Surendranath, D. G. Nocera. *J. Am. Chem. Soc.* **2009**, *131,* 3838-3839.

[30] R. D. L. Smith, M. S. Prévot, R. D. Fagan, Z. Zhang, P. A. Sedach, M. K. J. Siu, S. Trudel, C. P. Berlinguette. *Science* **2013**, *340*, 60-63.

[31] M. Rish, K. Klingan, F. Rigleb, P. Chernev, I. Zaharieva, A. Ficher, H. Dau. *ChemSusChem* **2012**, *5*, 542-549.

[32] A. Indra, P. Menezes, I. Zaharieva, E. Baktash, J. Pfrommer, M. Schwarze, H. Dau, M. Driess. *Angew. Chem. Int. Ed.* **2013**, *52*, 13206-13210.

[33] L. Kuai, J. Geng, C. Chen, E. Kan, Y. Liu, Q. Wang, B. Geng. *Angew. Chem. Int. Ed.* **2014**, *53*, 7547-7551.

[34] M. Risch, V. Khare, L. Zaharieva, L. Gerencser, H. Dau. *J. Am. Chem. Soc.* **2009**, *131,* 6936-6937.

[35] A. Indra, P. W. Menezes, I. Zaharieva, E. Baktash, J. Pfrommer, M. Schwarze, H. Dau, M. Driess. *Angew. Chem. Int. Ed.* **2013**, *52*, 13206-13210.

[36] A. Iyer, J. Del-Pilar, C. K. King'ondu, E. Kissel, H. F. Garces, H. Huang, A. M. El-Sawy, P. K. Dutta, S. L. Suib. *J. Phys. Chem. C* **2012**, 116, 6474-6483.

[37] A. Indra, P. W. Menezes, N. R. Sahraie, A. Bergmann, C. Das, M. Tallarida, D. Schmeiβer, P. Strasser, M. Driess. *J. Am. Chem. Soc.* **2014**, *136*, 17530-17536.

[38] S. W. Lee, C. Carlton, M. Risch, Y. Surendranath, S. Chen, S. Furutsuki, A. Yamada, D. G. Nocera, Y. Shao-Horn. *J. Am. Chem. Soc.* **2012**, *134*, 16959-16962.

[39] B. Han, D. Qian, M. Risch, H. Chen, M. Chi, Y. S. Meng, Y. Shao-Horn. *J. Phys. Chem. Lett.* **2015**, *6*, 1357-1362.

[40] U. Maitra, B. S. Naidu, A. Govindaraj, C. N. R. Rao. *Proc. Natl. Acad. Sci. USA* **2013**, *110*, 11704-11707.

[41] N. Colligan, V. Augustyn, A. Manthiram. *J. Phys. Chem. C* **2015**, *119*, 2335-2340.

[42] D. M. Robinson, Y. B. Go, M. Greenblatt, G. C. Dismukes. *J. Am. Chem. Soc.* **2010**, *132*, 11467-11469.

[43] G. P. Gardner, Y. B. Go, D. M. Robinson, P. F. Smith, J. Hadermann, A. Abakumov, M. Greenblatt, G. C. Dismukes. *Angew. Chem. Int. Ed.* **2012**, *51*, 1616-1619.

[44] J. Park, H. Kim, K. Jin, B. J. Lee, Y.-S. Park, H. Kim, I. Park, K. D. Yang, H.-Y. Jeong, J. Kim, K. T. Hong, H. W. Jang, K. Kang, K. T. Nam. *J. Am. Chem. Soc.* **2014**, *136*, 4201-4211.

[45] H. Liu, Y. Zhou, R. Moré, R. Müller, T. Fox, G. R. Patzke. *ACS Catal.* **2015**, *5*, 3791-3800.

[46] Z. Lu, H. Wang, D. Kong, K. Yan, P.-C. Hsu, G. Zheng, H. Yao, Z. Liang, X. Sun, Y. Cui. *Nat. Commun.* **2014**, *5*, 4345.

[47] T. Maiyalagan, K. A. Jarvis, T. Soosairaj, P. J. Ferreira, A. Manthiram. *Nat. Commun.* **2014**, *5*, 3949.

[48] F. Nobili, S. Dsoke, M. Minicucci, F. Croce, R. Marassi. *J. Phys. Chem. B* **2006**, *110*, 11310-11313.

[49] R. Robert, C. Villevieille, P. Novak. *J. Mater. Chem. A*, **2014**, *2*, 8589-8598.

[50] P. Yang. The Chemistry of Nanostructured Materials. 2011, Vol. 2, p. 92.

[51] H. Liu, G. R. Patzke. *Ceram. Eng. Sci. Proc.* **2013**, *34*, 75-86.

[52] P. W. Menezes, A. Indra, N. R. Sahraie, A. Bergmann, P. Strasser, M. Driess. *ChemSusChem* **2015**, *8*, 164-171.

[53] M. C. Biesinger, B. P. Payne, A. P. Grosvenor, L. W. M. Lau, A. R. Gerson, R. St. C. Smart, *Appl. Surf. Sci.* **2011**, *257*, 2717-2730.

[54] M. W. Kanan, J. Yano, Y. Surendranath, M. Dincă, V. K. Yachandra, D. G. Nocera. *J. Am. Chem. Soc.* **2010**, *132,* 13692-13701.

[55] J. G. McAlpin, Y. Surendranath, M. Dincă, T. A. Stich, S. A. Stoian, W. H. Casey, D. G. Nocera, R. D. Britt. *J. Am. Chem. Soc.* **2010**, *132,* 6882-6883.

[56] B. S. Yeo, A. T. Bell. *J. Am. Chem. Soc.* **2011**, *133,* 5587-5593.

[57] Z. Chen, J. J. Concepcion, X. Hu, W. Yang, P. G. Hoertz, T. J. Meyer. *Proc. Natl. Acad. Sci. USA*, **2010**, *107*, 7225-7229.

[58] K. Klingan, F. Ringleb, I. Zaharieva, J. Heidkamp, P. Chernev, D. Gonzalez-Flores, M. Rish, A. Fischer, H. Dau. *ChemSusChem*, **2014**, *7*, 1-11.

[59] A. Lewandowska-Andralojc, D. E. Polyansky. *J. Phys. Chem. A* **2013**, 117, 10311-10319.

[60] D. Hong, J. Jung, J. Park, Y. Yamada, T. Suenobu, Y.-M. Lee, W. Nam, S. Fukuzumi. *Energy Environ. Sci.* **2012**, *5*, 7606-7616.

[61] C. Liang, Z.-S. Wang, C. J. Bruell. *Chemosphere* **2007**, 66, 106-113.

Appendix

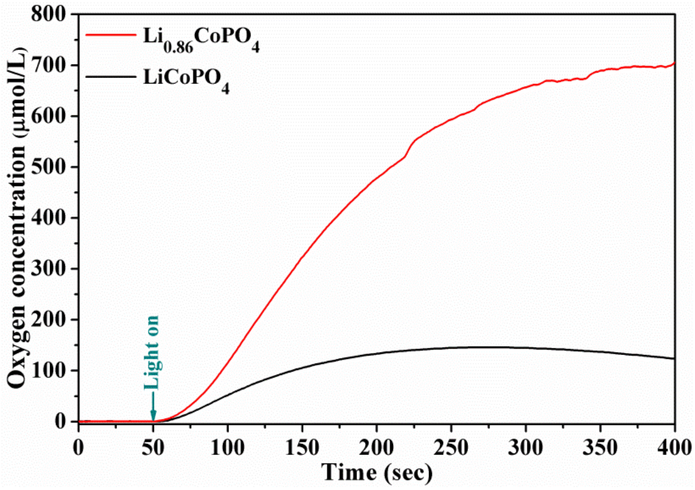

Figure S5.1. Water oxidation activities of $LiCoPO_4$ and $Li_{0.86}CoPO_4$ monitored by Clark electrode in solution.

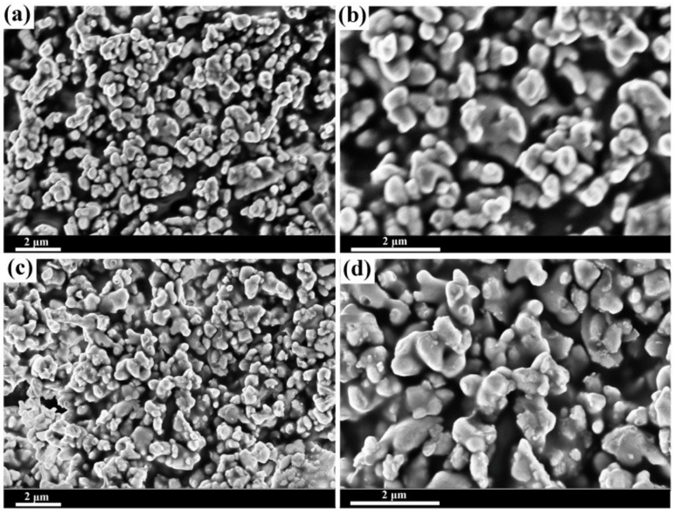

Figure S5.2. SEM pictures of LiCoPO4 (a and b) and $Li_{0.86}CoPO_4$ (c and d).

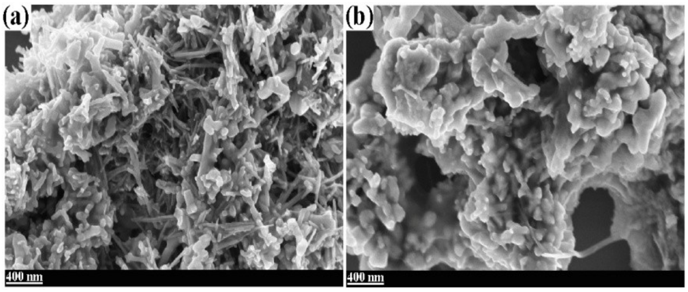

Figure S5.3. SEM pictures of pictures of (a) $LiMn_2O_4$ and (b) $Li_{0.13}Mn_2O_4$.

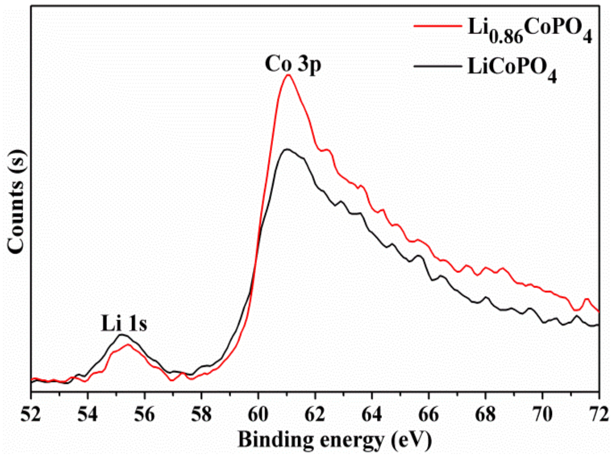

Figure S5.4. Co 3p spectra of $LiCoPO_4$ and $Li_{0.86}CoPO_4$.

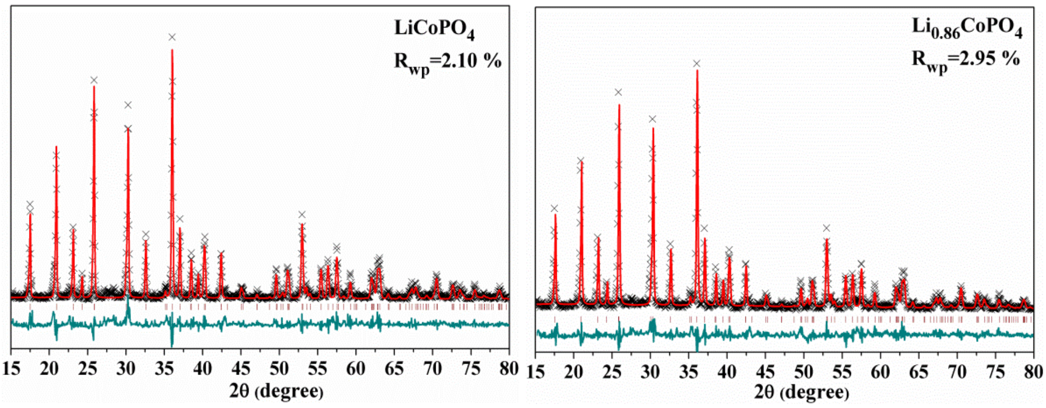

Figure S5.5. Rietveld refinement of $LiCoPO_4$ and $Li_{0.86}CoPO_4$ PXRD patterns.

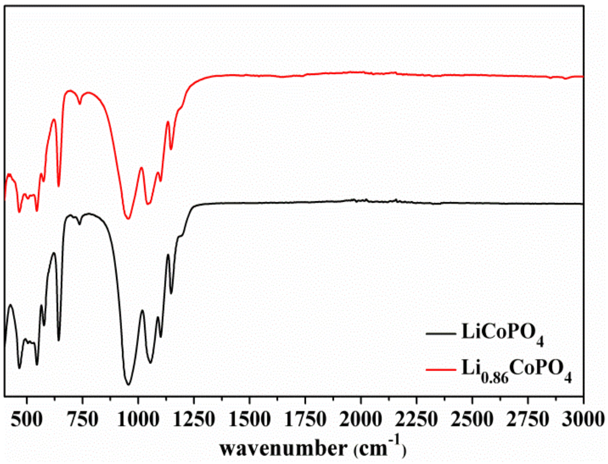

Figure S5.6. FT-IR spectra of $LiCoPO_4$ and $Li_{0.86}CoPO_4$.

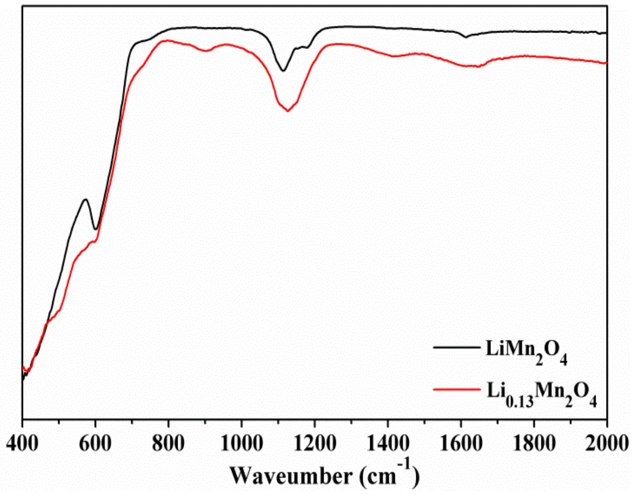

Figure S5.7. FT-IR spectra of LiMn$_2$O$_4$ and Li$_{0.13}$Mn$_2$O$_4$.

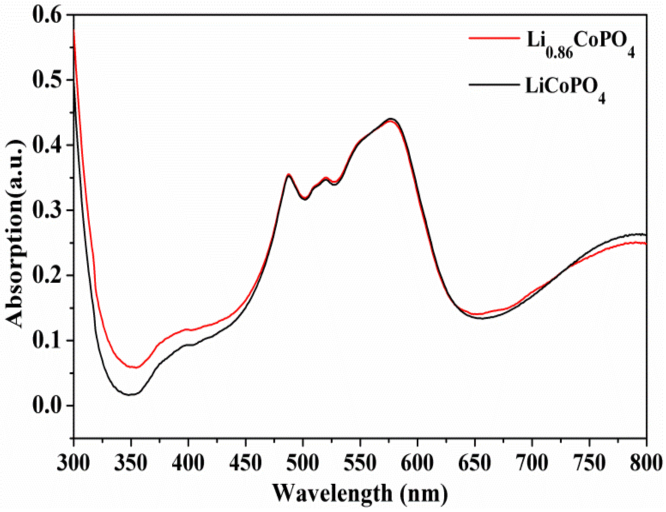

Figure S5.8. UV/Vis spectra of LiCoPO$_4$ and Li$_{0.86}$CoPO$_4$.

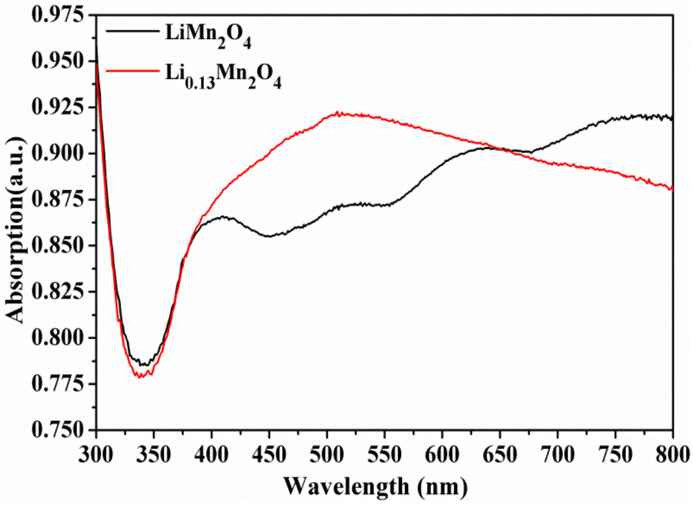

Figure S5.9. UV/Vis spectra of LiMn$_2$O$_4$ and Li$_{0.13}$Mn$_2$O$_4$.

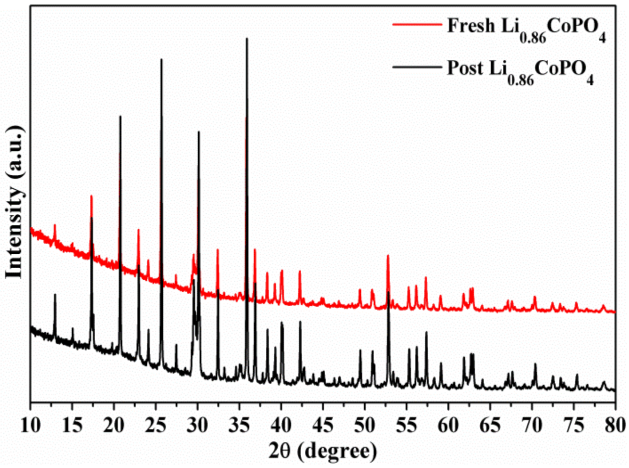

Figure S5.10. PXRD patterns of $Li_{0.86}CoPO_4$ before and after water oxidation.

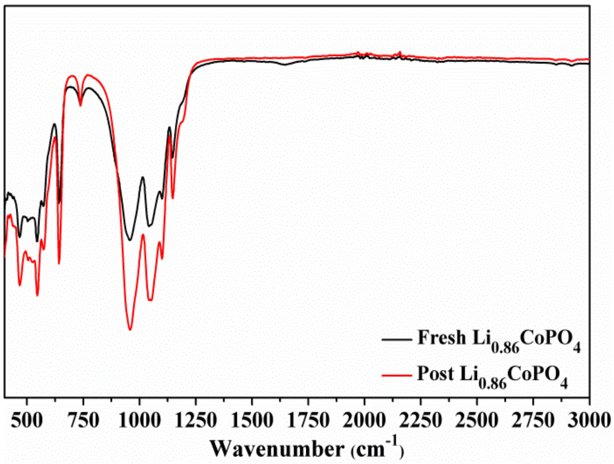

Figure S5.11. FT-IR spectra of $Li_{0.86}CoPO_4$ before and after water oxidation.

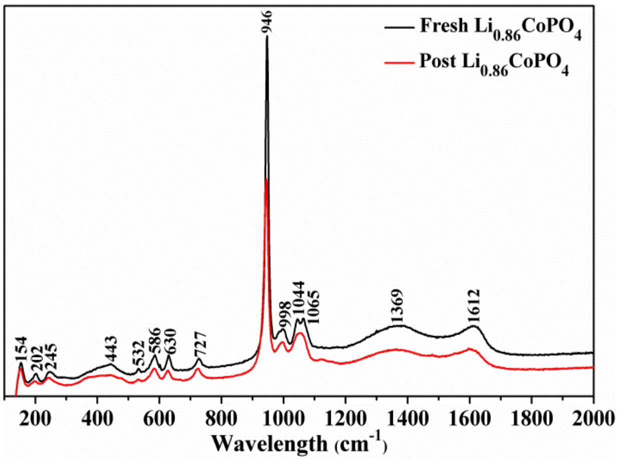

Figure S5.12. Raman spectra of $Li_{0.86}CoPO_4$ after water oxidation cycling.

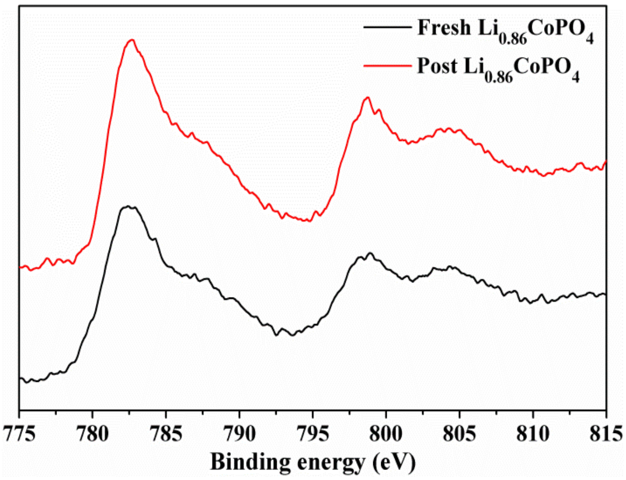

Figure S5.13. Co 2p spectra of $Li_{0.86}CoPO_4$ before and after water oxidation.

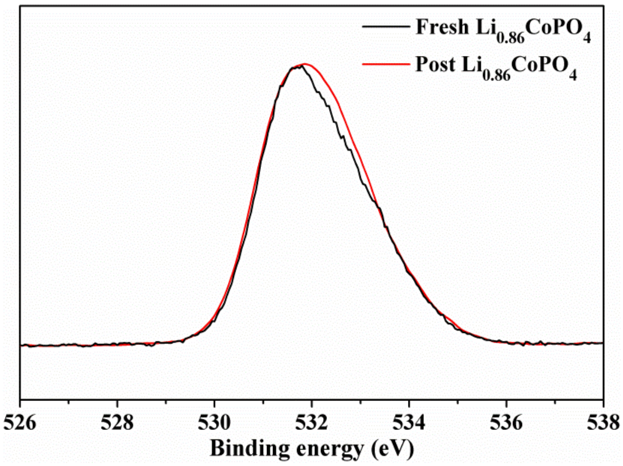

Figure S5.14. O 1s spectra of $Li_{0.86}CoPO_4$ before and after water oxidation.

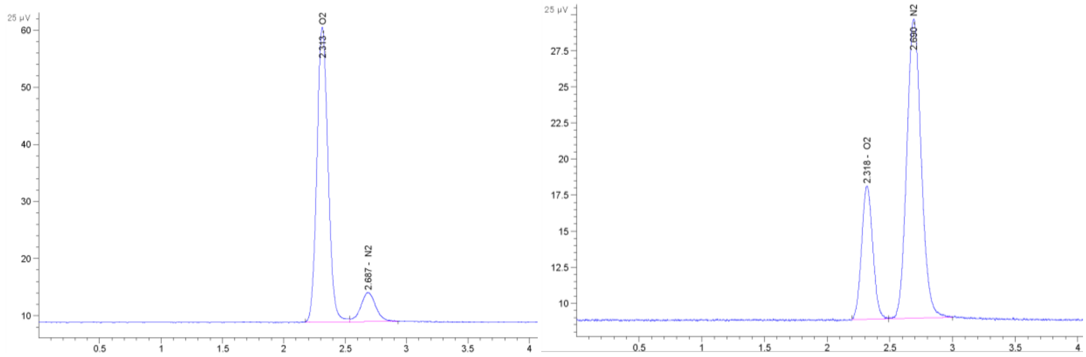

Figure S5.15. GC detection of oxygen after water oxidation with $Li_{0.86}CoPO_4$ after16 min Irridation (left) and with $LiCoPO_4$ after 9 min Irridation (right).

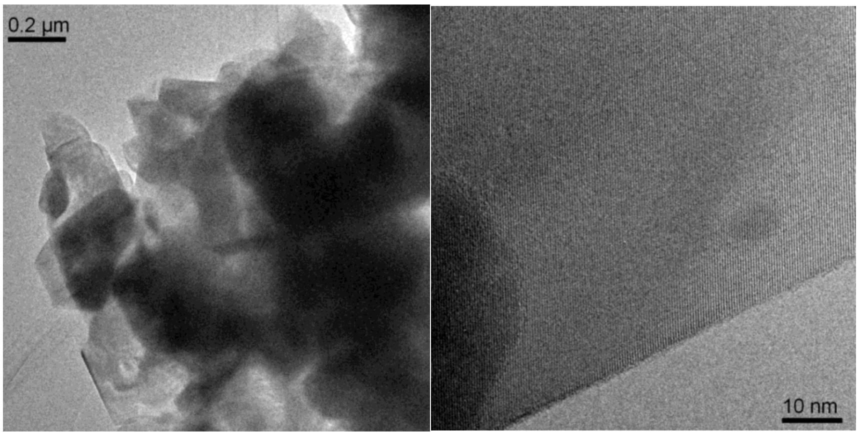

Figure S5.16. TEM pictures of $Li_{0.86}CoPO_4$ after photochemical water oxidation.

In contrast to electrochemical water oxidation,[1, 2] no obvious amorphous layer can be observed after after photochemical water oxidation.

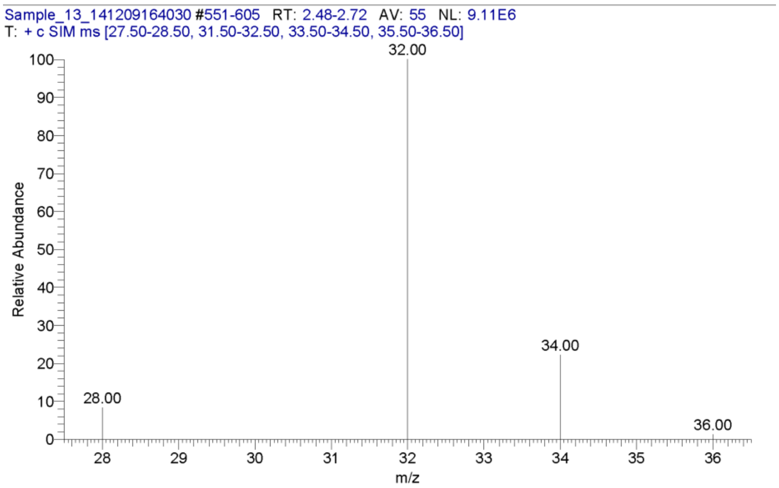

Figure S5.17. MS dedection of headspace composition after water oxidation with $Li_{0.86}CoPO_4$ in 10 % H_2O^{18} / 90 % H_2O^{16}.

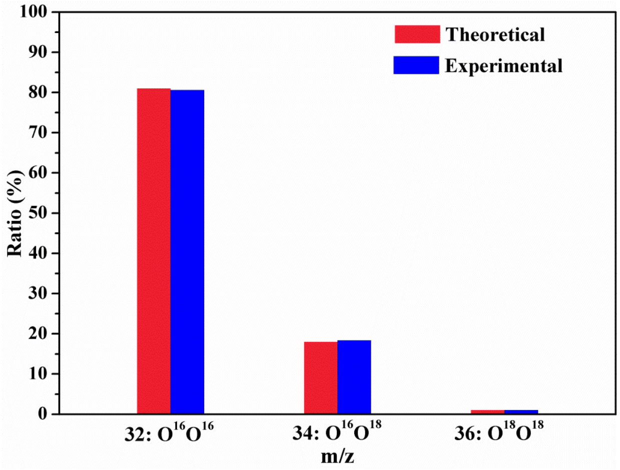

Figure S5.18. Comparison of the ratio of $O^{16}O^{16}$, $O^{16}O^{18}$ and $O^{18}O^{18}$ between theoretical and MS results after water oxidation with with $Li_{0.86}CoPO_4$ in 10 % H_2O^{18} / 90 % H_2O^{16}.

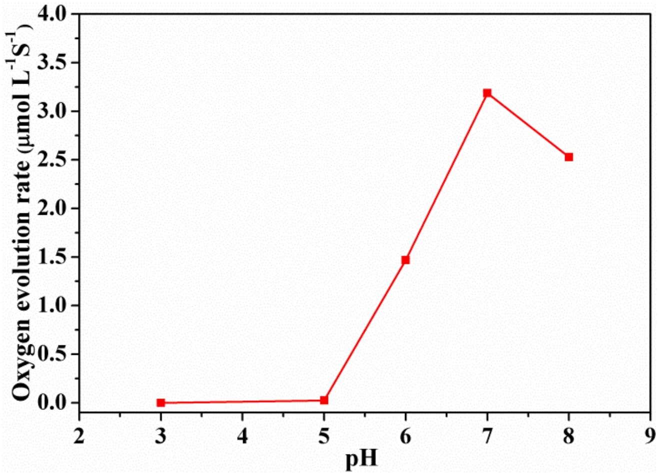

Figure S5.19. Oxygen evolution rates (average value in the first 150 s after irradiation) as a function of pH in phosphate buffer.

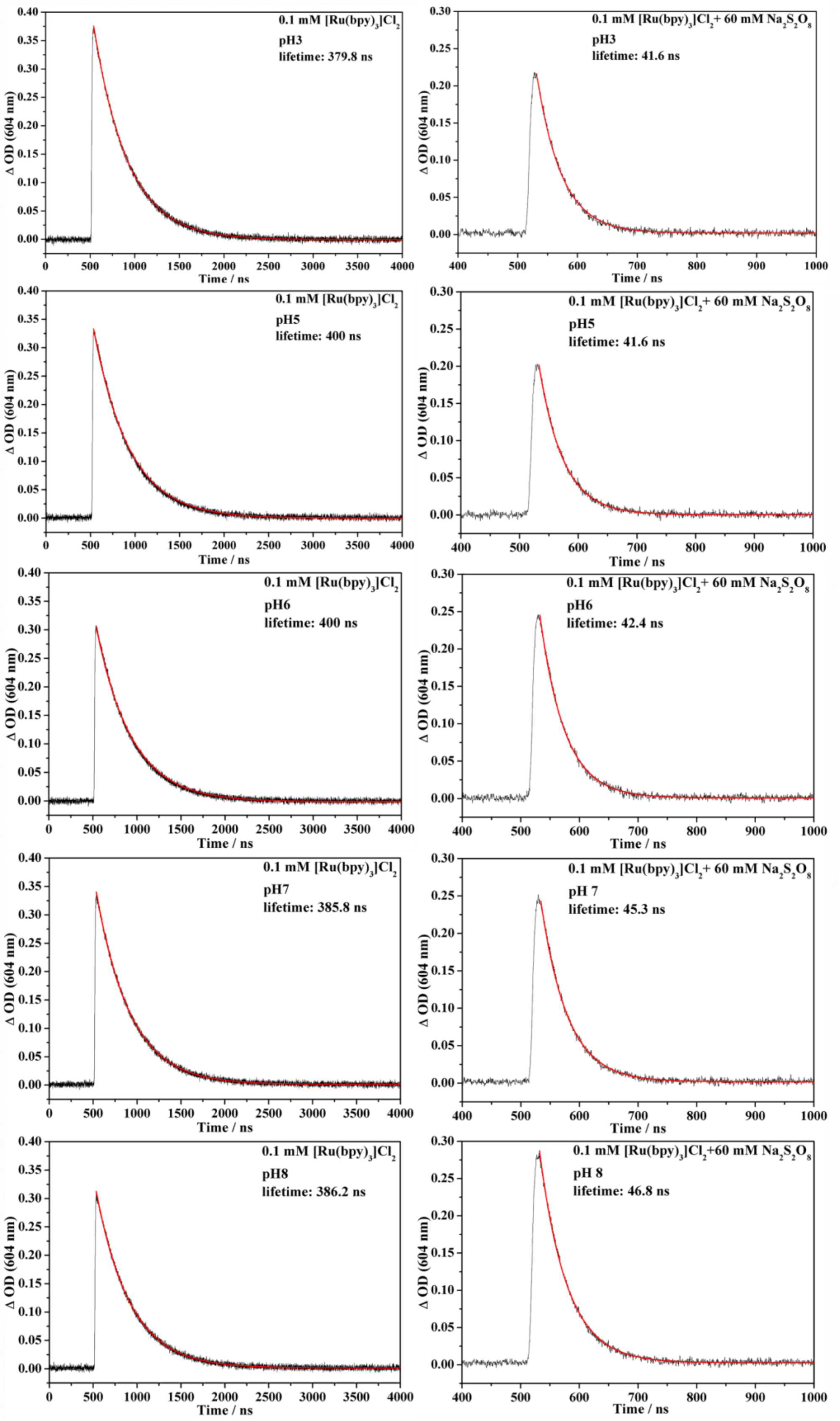

Figure S5.20. Fluorescence lifetimes of [Ru(bpy)$_3$]$^{2+*}$ in the absence and presence of persulfate at different pH.

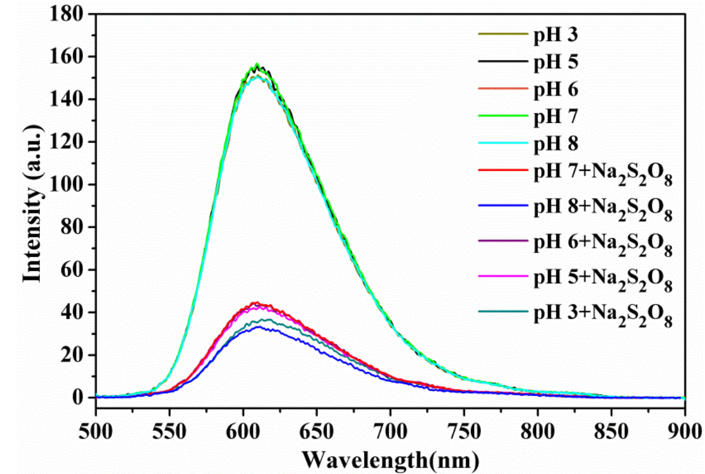

Figure S5.21. Fluorescence intensity of $[Ru(bpy)_3]^{2+*}$ in the absence and presence of persulfate at different pH.

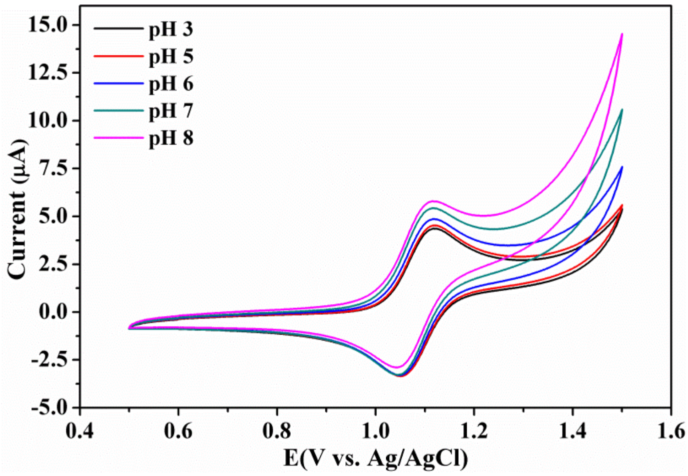

Figure S5.22. Cyclic voltammogram of $[Ru(bpy)_3]Cl_2$ in different pH potassium phosphate buffer.

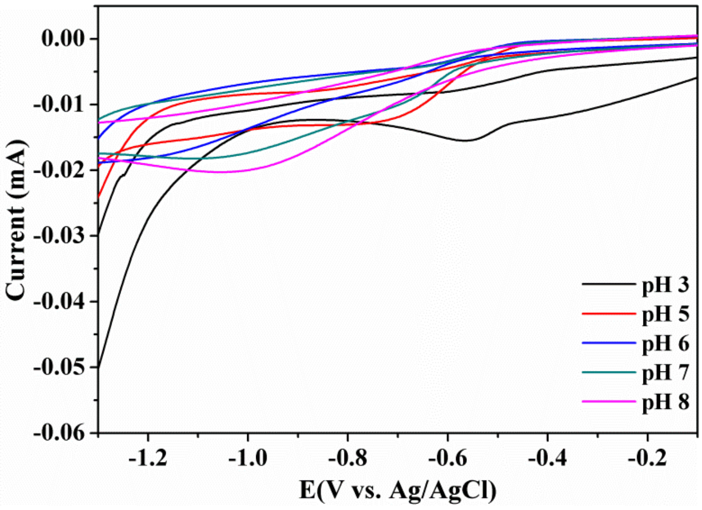

Figure S5.23. Cyclic voltammogram of $Na_2S_2O_8$ in different pH potassium phosphate buffer.

Figure S5.24. Photographs of [Ru(bpy)$_3$]Cl$_2$ solutions in the presence (from left to right: pH 3, 5, 6, 7 and 8) and the absence (rightmost: pH 8) of persulfate.

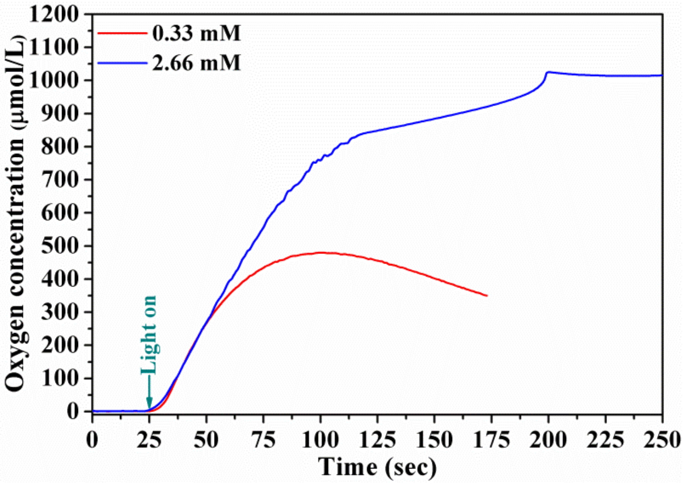

Figure S5.25. [Ru(bpy)$_3$]$^{2+}$ concentration dependent water oxidation.

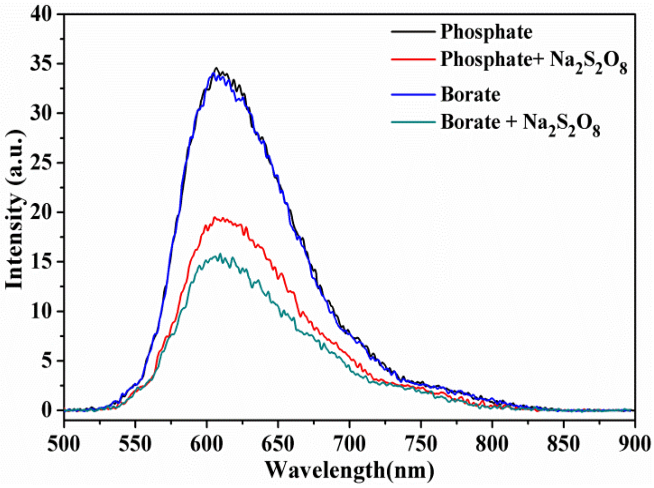

Figure S5.26. Fluorescence intensity of [Ru(bpy)$_3$]$^{2+*}$ in pH 8 borate and phosphate buffers in the absence and presence of persulfate.

References

[1] S. W. Lee, C. Carlton, M. Risch, Y. Surendranath, S. Chen, S. Furutsuki, A. Yamada, D. G. Nocera, Y. Shao-Horn, *J. Am. Chem. Soc.* **2012**, *134*, 16959-16962.

[2] M. Risch, A. Grimaud, K. J. May, K. A. Stoerzinger, T. J. Chen, A. N. Mansour, Y. Shao-Horn, *J. Phys. Chem. C*. **2013**, *117*, 8628-8635.

6. Metallic Band Structure induced Enhancement of Photochemical Water Oxidation in Perovskite-type Oxides

6.1 Introduction

Comprehensive insight into the mechanisms of four-electron-involved water oxidation ($2H_2O \rightarrow O_2 + 4H^+ + 4e^-$) will benefit the targeted design and synthesis of WOC.[1] However, such mechanistic studies remain a forefront challenge. Tuning the electronic structure through such as structural or ligand modifications, element doping, heterojunctions construction, quantum confinement effect targeted nanostructuring, and morphology or crystal facets controlled growth is the general strategy to optimize the catalytic activity of given parent materials.. In search of general principles for the rational design of WOCs, numerous studies aimed to identify the preferable electronic properties for water oxidation as it will provide the directions for electronic structure modification. Along these lines, several electronic properties descriptorsrelated to water oxidation activity were identified, such as the oxidation states of the active metal centers, [2-4] M-OH bond strengths (M = Ni, Co, Fe and Mn),[5] e_g electron configurations,[6] or surface affinity to oxygen species.[7] These studies underscore the significant impact of electronic properties on water oxidation activity. Ideally, catalytically active model systems with well-defined and easily tunable electronic structures are indispensable for studying the correlation between electronic properties and water oxidation activity. The perovskite and layered perovskite-type oxides with transition metal centers (Fe, Co, Mn, Ni) basically meet above criterias. These materials are well known as the so-called strongly correlated electronic systems featured with strong Coulomb repulsion between the 3d electrons which entails orbital ordering, electron localization and so on. Alterations of these 3d electrons' interactions through external factors (e.g. temperature, pressure, magnetic or electrical fields) or internal composition can considerably modify their charge transportation and magnetic properties, resulting in many interesting physical phenomena, such as metal to insulator transitions, high temperature superconductivity and colossal magnetoresistance.[8] Despite the extensive studies in solid state physics, the electronic structures underlying these physic properties were rarely explored for catalysis.

The perovskite-type oxides have a common stoichiometric formula denoted as ABO_3, where "A" is generally composed of divalent alkaline-earth or trivalent lanthanide cations, "B" consists of trivalent or tetravalent transition metals Its basic structure can be described as the close-packing of the cubic ABO_3 units (Figure 6.1a) which allows flexible elemental composition variation through slight structural distortion.. Layered perovskites exhibit a similar structural motif except for the insertion of an additional AO layer between the layers of $\{BO_6\}$ octahedra, giving rise to typical A_2BO_4 stoichiometries (cf. Figure S6.5).

6.2 Experimental

6.2.1 Samples preparation

All the samples were synthesized via a conventional sol-gel method as follows: 6 mmol metal nitrate salts in required stoichiometric ratio, 24 mmol citric acid and 3 ml glycol were dissolved in 200 mL deionized water. The as-prepared solution was stirred and condensed at 90 °C into a gel which was further decomposed at 180 °C over 5 h to form a foam-like precursor. This precursor was subjected to flowing calcinations (650 ^oC, 5 h for $La_{1-x}Sr_xMO_3$ and 900 ^oC, 2 h for $La_{2-x}Sr_xMO_4$) to get the final products.

6.2.2 Photocatalytic tests

Water oxidation tests were conducted according to a well established $[Ru(bpy)_3]^{2+}/S_2O_8^{2-}$ protocol. First, a suspension was prepared by mixing 10 mg water oxidation catalyst, 8 mg $[Ru(bpy)_3]Cl_2$ photosensitizer and 50 mg NaS_2O_8 in 8 mL phosphate buffer (0.1 M, pH 7, 10 mL vial) in dark. Next, the suspension was degassed with helium to remove O_2 in both solution and the head vial. A LED lamp with 460 nm wavelength and 5000 Lux output was used as visible light source. Oxygen produced in solution was monitored with a calibrated Clarke electrode (Unisense) online or by gas chromatography (Agilent 7820A packed with a 3 m × 2 mm molecular sieve 13X 80-100 column) as follows: 100 µL samples of gas from the head vial were injected into a gas chromatograph using a gastight microliter syringe (Hamilton 1825 RN) during intervals of several minutes. Helium was chosen as carrier gas to increase the detection sensitivity of O_2. Gases were detected with a thermal conductivity detector (Varian) operated at 200 °C. Contamination of the headspace by air was constantly monitored through the N_2 peak on GC chromatograms.

6.2.3 Characterizations

Powder X-ray diffraction patterns (PXRD patterns) were recorded on a STOE STADI P diffractometer (reflection mode, step size: 0.3°/step, 60 s/step) with Mo $K_{\alpha 1}$ radiation. Fourier transformed infrared (FT-IR) spectra were collected on a Bruker Opus spectrometer.

Sample morphologies were examined by scanning electron microscopy (LEO 1530, FEG) Bruker energy-dispersive X-ray spectrometer (EDXS) and transmission electron microscopy (FEI Tecnai F30, FEG, 300 kV). Brunauer-Emmett-Teller (BET) surface area measurements were conducted on a Quadrasorb SI machine in N_2-adsorption mode. Samples were degassed at 150 °C for 15 h under vacuum prior to the measurements. XPS spectra were measured on Thermo ESCALAB 250 with a monochromatic Al K_α as x-ray source. The C 1s peak at 284.6 eV was set as a reference for all XPS peak positions. Magnetic susceptibility measurements were conducted on a 7 T Quantum Design MPMS SQUID at a magnetic field of 1.0 T in the temperature range 5-300 K in both zero field and field cooling modes. Fe K-edge X-ray absorption spectroscopy (XAS) was performed at the ESRF Swiss Norwegian Beamline BM01B. $La_{1-x}Sr_xFeO_3$ samples were measured as solid samples dispersed in cellulose in transmission mode. For all experiments an iron metal foil was used as calibration standard. Energy calibration, background removal, linear combination fitting and Fourier transformation of XAS spectra were performed with the Athena software and EXAFS fits were performed with the Artemis software.[9]

^{18}O labeling experiments: 10 mg WOC, 8 mg Ru-PS and 10 mg $Na_2S_2O_8$ were dispersed in 5 mg H_2O with 10 % ^{18}O in ultrasound bath. The pH was adjusted to 7 by adding appropriate amounts of KH_2PO_4 and KH_2PO_4. Photochemical water oxidation was conducted as above described. After 30 min of irradiation, 50 µL gas from headspace was injected into a GC-MS instrument for oxygen separation and detection.

6.3 Results and discussion

The perovskite-type oxides have a common stoichiometric formula denoted as ABO_3, where “A” is generally composed of divalent alkaline-earth or trivalent lanthanide cations, “B” consists of trivalent or tetravalent transition metals Its basic structure can be described as the close-packing of the cubic ABO_3 units (Figure 6.1a) which allows flexible elemental composition variation through slight structural distortion.. Layered perovskites exhibit a similar structural motif except for the insertion of an additional AO layer between the layers of $\{BO_6\}$ octahedra, giving rise to typical A_2BO_4 stoichiometries (cf. Figure S6.5).

In present study, $LaMO_3$ and La_2MO_4 (M= Fe, Co, Mn or Ni) systems with strongly correlated M 3d electrons are selected as the starting materials. Trough replacing trivalent La^{3+} with divalent Sr^{2+}, their electronic structures can be tuned in a wide range. This enables us to monitor the influences of electronic structures evolution on water oxidation activity.

6.3.1 $La_{1-x}Sr_xFeO_3$ for water oxidation

We started with $La_{1-x}Sr_xFeO_3$ (A = La and Sr, B = Fe) as it can accommodate a full range of Sr content from x=0 to 1. Formation of phase pure perovskite sturctures for all the $La_{1-x}Sr_xFeO_3$ (x=0, 0.25, 0.5, 0.75 and 1) were verified by the matching between the powder X-ray diffraction (PXRD) patterns and the stardard $LaFeO_3$ pattern (JCPDS card No. 37-1943, pink red lines in Figure 6.1b). Increasing Sr contents (add lattice constants to SI) leads to gradual structural transition from orthorhombic ($0 \leq x \leq 0.2$) via rhombohedral ($0.4 \leq x \leq 0.7$) to cubic ($0.8 \leq x \leq 1.0$) symmetry.[10] This structural adjustment is evident from a peak shift towards higher angles (cf. (240) reflection in Figure 6.1b), as well as of the gradual disappearance of the (101) reflection and the appearance (111) reflections (Figure S6.1). Shortening of the Fe-O bond length in combination with a precise 180° O-Fe-O bond angle during the formation of cubic structure can inducessignificant changes of the electronic structure, and an insulator to metal transition can be observed.[11]

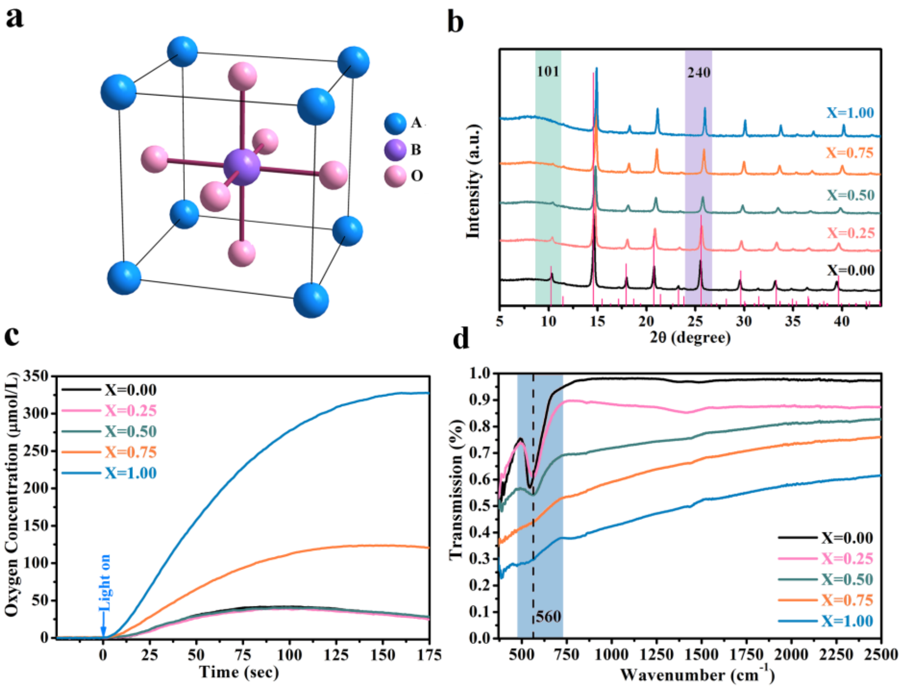

Figure 6.1. Structure and photochemical water oxidation activity of $La_{1-x}Sr_xFeO_3$. (a) Representative structure model of cubic perovskite. (b) PXRD patterns of $La_{1-x}Sr_xFeO_3$. (c) Online monitoring of photochemical oxygen evolution (Clark electrode in solution). (d) FT-IR spectra.

The photochemical water oxidation activity of $La_{1-x}Sr_xFeO_3$ was evaluated according to a standard protocol using $[Ru(bpy)_3]^{2+}$ as photosensitizer and $S_2O_8^{2-}$ as sacrificial electron acceptor. The produced oxygen in solution was online monitored with a Clark electrode

(Figure 6.1c), while the oxygen diffused to the headspace was detected by gas chromatography (GC, Figure S6.3a). Comparably low oxygen amounts (around 40 μmol L^{-1}) evolved for the first three samples with $x \leq 0.5$. Further increase of the Sr content resulted in significant improvement of water oxidation activities, and equilibrium oxygen concentrations of 124 and 327 μmol/L were achieved for $La_{0.25}Sr_{0.75}FeO_3$ and $SrFeO_3$, respectively. The corresponding GC results further confirmed this trend (Figure S6.3). However, negligible oxygen quantities were detected in the headspace by GC for $x \leq 0.5$, indicating that most of the oxygen dissolved in solution instead of diffusing to the headspace.

Noteworthy, the dramatic improvement of water oxidation performance is observed from x=0.75 to 1 where the insulator to metal transition was generally reported. To reveal the possible correlation between them, we used FT-IR (Figure 6.1d) to monitor the electronic structure transition. The disappearance of characteristic Fe-O stretching vibrations at around 560 cm^{-1} for both $La_{0.25}Sr_{0.75}FeO_3$ and $SrFeO_3$ indicates the emergence of metallic properties with strong reflectivity to infrared light.[12] This electronic structure transition trend is in line with the substantial improvement of water oxidation activity for substitution degrees of $x \geq 0.75$.

X-ray absorption near edge spectra (XANES) were recorded at the Fe K-edge to trace the electronic structure changes as a function of the Sr content. A pre-edge absorption peak (green area in Figure 6.2a, enlarged in Figure 6.2b) at 7117 eV is assigned to the quadrupole-allowed 1s to 3d transitions. Its increasing absorption intensity with higher Sr contents indicates an increasing hole concentration in Fe 3d orbits. Furthermore the saturation effect observed at $x \geq 0.75$ is consistent with the disappearance of IR absorption bands at 560 cm^{-1} for $La_{0.25}Sr_{0.75}FeO_3$ and $SrFeO_3$ and points to the presence of less strongly bound charge carriers. [13] The absorption maximum arising from dipole-allowed 1s to 4p transitions continuously decreases with increasing Sr content (cf. difference spectra related to $LaFeO_3$ in Figure 6.2a (bottom)). This trend corresponds to the gradual formation of a metallic band structure with less well-defined energy levels and increasingly covalent Fe-O bonds.[13] In contrast to $La_{0.25}Sr_{0.75}FeO_3$, $SrFeO_3$ exhibits a more significant broadening of 1s→4p peak together with a pronounced ligand-to-metal charge transfer band (around 7123 eV, Figure S6.2a). This provides further evidence for increasingly metallic properties giving rise to superior water oxidation activity than $La_{0.25}Sr_{0.75}FeO_3$.

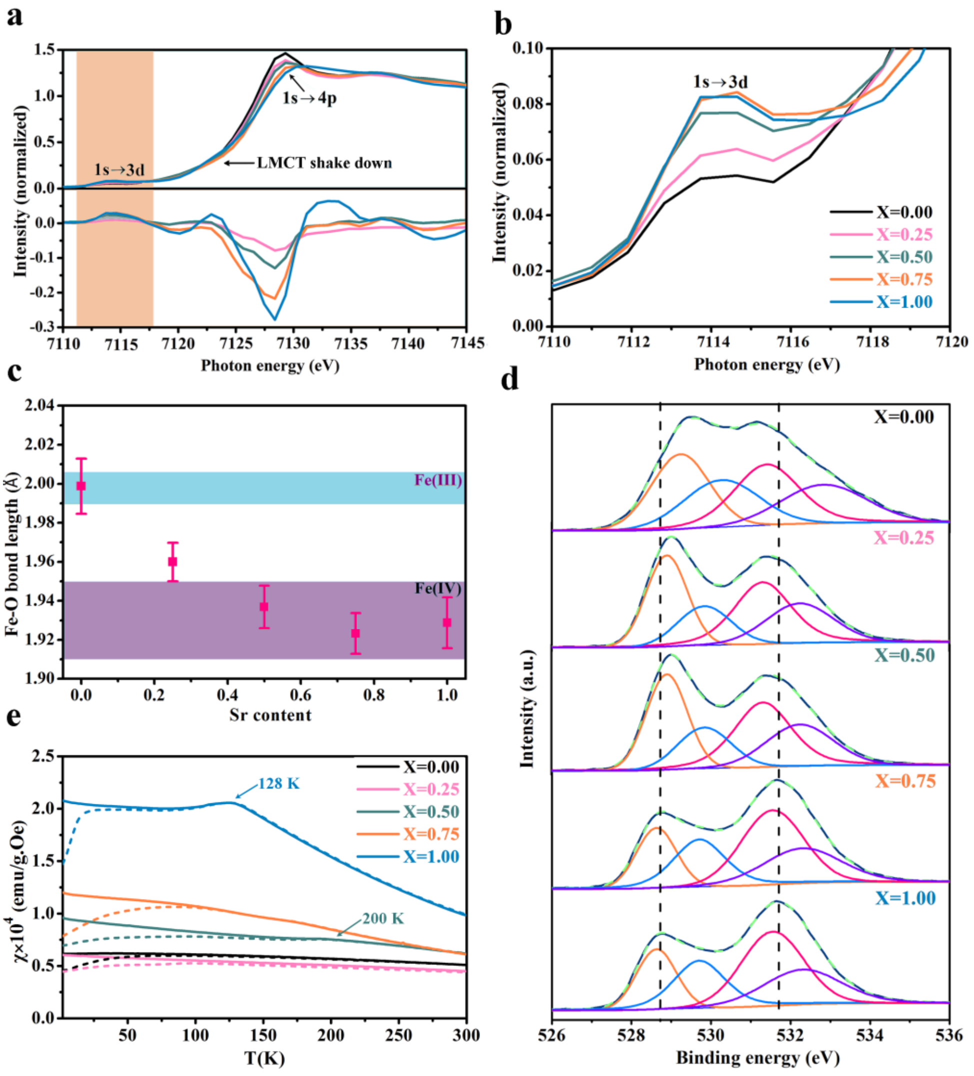

Figure 6.2. Electronic structure evolution of $La_{1-x}Sr_xFeO_3$ as a function of Sr content. (a) XANES spectra. (b) Enlarged pre-edge absorption related to 1s→3d transitions. (c) Average Fe-O bond length as a function of Sr content derived from XAS spectra. (d) O 1s XPS spectra. (e) Temperature-dependent susceptibility (solid line: field cooling; dash line: zero field cooling).

The Fe-O bond lengths (Figure 6.3d) obtained from the fitting of extended X ray absorption fine structure (EXAFS) display a continuous decrease with increased Sr content from x=0 to 0.75, indicating the gradual oxidation of Fe^{3+} to Fe^{4+}. The nearly constant Fe-O bond distance for $x \geq 0.75$ is consistent with the abovementioned saturation effect of 1s to 3d transitions and can be either related to a the rhombohedral to cubic structure transformation symmetry or the formation of oxygen vacancies. While previous works proposed the valence state influence of the active metal centers on water oxidation activity,[2-4] the present results cannot be solely explained with the iron valence state changes: $La_{0.5}Sr_{0.5}FeO_3$ and

$La_{0.25}Sr_{0.75}FeO_3$ with higher Fe valence states than $LaFeO_3$ do not exhibit higher water oxidation activities (Figure 6.1c).

The electronic structure transitions are also evident from a remarkable change of the surface affinity to oxygen species (Figure 6.2b). O 1s spectra for $La_{1-x}Sr_xFeO_3$ are composed of two major peaks corresponding to lattice oxygen (~529.0 eV) and surface absorbed oxygen species (~531.5 eV) respectively. Noteworthy, a significant reverse of the proportions of these two peaks sets in for $x \geq 0.75$. Furthermore, both $La_{0.25}Sr_{0.75}FeO_3$ and $SrFeO_3$ exhibit slight peak shifts compared to $La_{1-x}Sr_xFeO_3$ perovskites with lower Sr contents ($x = 0$, 0.25 and 0.5), namely lattice oxygen peaks at ca. 0.3 eV lower and surface oxygen peaks around 0.2 eV higher binding energies. The enrichment of surface oxygen species after the insulator to metal transition is consistent with the theoretically predicted stabilizing effect of metallic band structures on surface oxygen species.[14]

Temperature-dependent susceptibility measurements indicate that both $LaFeO_3$ and $La_{0.75}Sr_{0.25}FeO_3$ are antiferromagnetic over the 2-300 K range, while $La_{0.5}Sr_{0.5}FeO_3$ experiences a slight ferromagnetic to antiferromagnetic transition around 200 K (Néel temperature). $La_{0.25}Sr_{0.75}FeO_3$ exhibits a more complex magnetic behavior with a broad Néel transition temperature range from 120 to 175 K. This points to electronic phase segregation with some metallic domains with the remaining ones being insulating. Such anelectronic phase segregation agrees well the mixed characters of rhombohedral and cubic structures in PXRD pattern (Figure S6.1). In contrast, $SrFeO_3$ exhibits a sharp ferromagnetic to antiferromagentic transition at 128 K, which reveals a purely metallic phase. The partially metallic domain structure of $La_{0.25}Sr_{0.75}FeO_3$ is in line with its notably lower water oxidation activity compared to purely metallic $SrFeO_3$. Moreover, the slightly higher magnetic moment (2~300 K range) of $La_{0.5}Sr_{0.5}FeO_3$ compared to $LaFeO_3$ and $La_{0.75}Sr_{0.25}FeO_3$ corresponds well with its significantly weaker IR absorption band at 560 cm^{-1}, indicating the onset of the insulator to metal transition.

6.3.2 $La_{1-x}Sr_xCoO_3$ for water oxidation

The $La_{1-x}Sr_xCoO_3$ system exhibits an insulator to metal transition[15] point at x~0.2 and shows similar trends to $La_{1-x}Sr_xFeO_3$ with respect to both water oxidation activities and electronic structure evolution (Figure 6.3). While the insulative $LaCoO_3$ displays two characteristic FT-IR absorption bands (Figure 6.4c) at around 400 cm^{-1} and 500-600 cm^{-1} due to O-Co-O bending and Co-O stretching vibrations,[16] metallic $La_{0.8}Sr_{0.2}CoO_3$ exhibits no absorption at around 400 cm^{-1} and a much weaker absorption in the 500-600 cm^{-1} range. Further incorporation of Sr only results in a slightly stronger background intensity for $La_{0.6}Sr_{0.4}CoO_3$ in the 380-1000 cm^{-1} region, which corresponds well with the minor increase of conductivity beyond x=0.2.[17] The insulator to metal transition at x = 0.2 goes hand in hand with a drastically enhanced oxygen evolution for $La_{0.8}Sr_{0.2}CoO_3$ compared to $LaCoO_3$ (Figure 6.3a). Temperature-dependent magnetic susceptibility measurements indicate that $LaCoO_3$ is slightly paramagnetic (Figure 6.4d) with most Co^{3+} centers adopting low spin states (LS: $t_{2g}^6e_g^0$). The insulator to metal transition at x = 0.2 is clearly reflected by a para- to ferromagnetic transition at around 240 K (cf. inflection points in the upper curves of Figure 6.3d). A further increase of the Sr content to 0.4 results in marginally increased magnetism, which matches well with the trends of both FT-IR spectra and water oxidation performance.

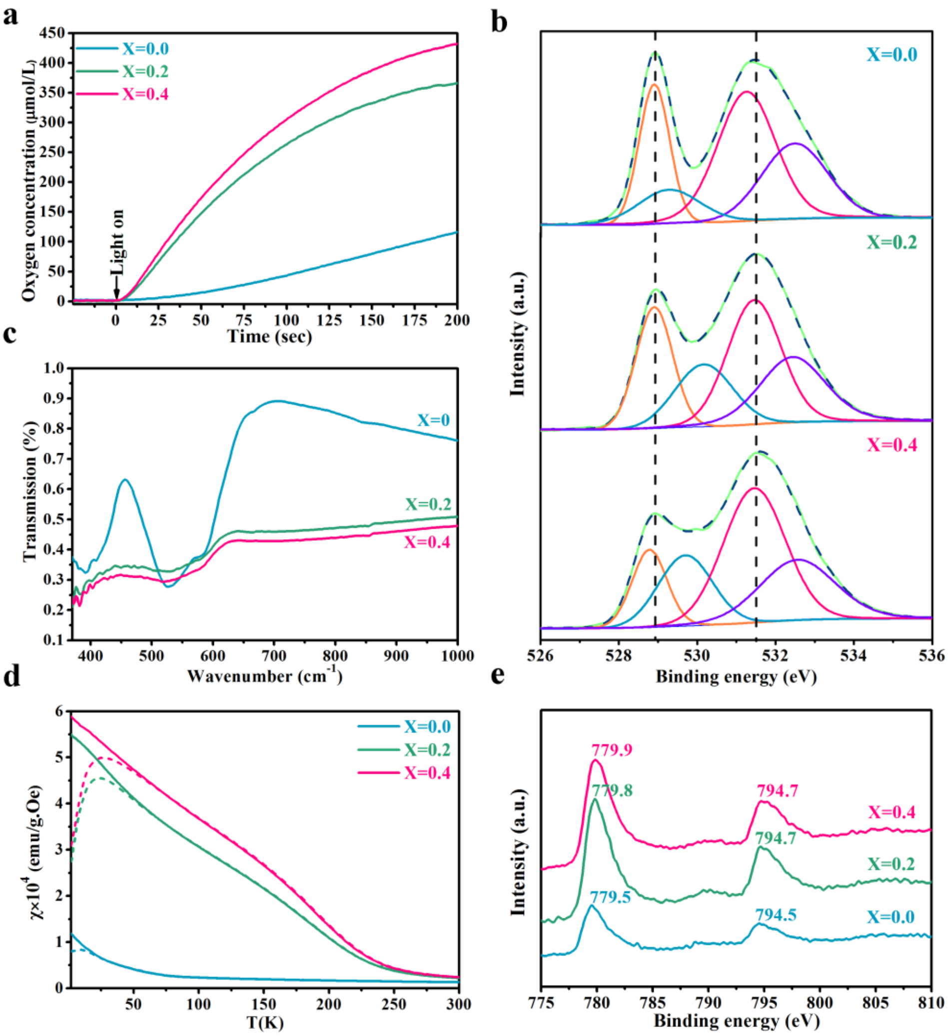

Figure 6.3. $La_{1-x}Sr_xCoO_3$ as photochemical water oxidation catalyst. (a) Photochemical oxygen evolution monitored online with a Clark electrode in solution. (b) O 1s XPS spectra. (c) FT-IR spectra. (d) Temperature-dependent susceptibility (solid line: field cooling; dashed line: zero field cooling). (e) Co 2p XPS spectra.

A slight shift of Co 2p XPS peak toward higher binding energy after Sr doping (Figure 6.4e) indicates the partial oxidation of Co^{3+} to Co^{+4} and the expected hole doping in the Co 3d electronic states. O 1s spectra of $La_{1-x}Sr_xCoO_3$ (Figure 6.4b) display a very similar trend compared to $La_{1-x}Sr_xFeO_3$ in the course of the electronic structure transition. While the lattice oxygen peak (~529 eV) intensity of insulating $LaCoO_3$ is higher compared to adsorbed oxygen species (~531.5 eV), this ratio is completely inverted for the metallic $La_{0.8}Sr_{0.2}CoO_3$ and $La_{0.6}Sr_{0.4}CoO_3$.

6.3.3 $La_{1-x}Sr_xMnO_3$ for water oxidation

$La_{1-x}Sr_xMnO_3$ provides further evidence for the correlation between electronic structure and water oxidation activity. Both water oxidation activity trends (Figure S6.4a) and FT-IR reflectivity values (Figure S6.4c) match well with the transition from paramagnetic insulator ($0 \leq x < 0.2$) to ferromagnetic metal ($0.2 \leq x < 0.5$) temperature) which is reverted into paramagnetic insulator at higher Sr contents ($x \geq 0.5$).[18] The O 1s XPS spectra (Figure S6.4b) of $La_{1-x}Sr_xMnO_3$ display the expected increase of the signal related to surface oxygen species after the insulator to metal transition. However, this effect is far less significant compared to $La_{1-x}Sr_xCoO_3$ and $La_{1-x}Sr_xFeO_3$. This is likely due to the less pronounced metallic character of $La_{0.8}Sr_{0.2}MnO_3$, as it is evident from a strong remnant of FT-IR absorption band at around 563 cm^{-1}.

Layered A_2BO_4 (B= Ni, Co) perovskites were further studied for comparison. Other than ABO_3 perovskites with a 3D $\{BO_6\}$ network, the metallic properties of layered perovskites are dimensionally restricted to the corner-sharing $\{BO_6\}$ layers due to their separation by the AO layers (Figure S6.5). Consequently, the observed improvement of water oxidation activity for $La_{2-x}Sr_xNiO_4$ (Figure S6.5a) and $La_{2-x}Sr_xCoO_4$ (Figure S6.6a) upon Sr doping is less significant compared to $La_{1-x}Sr_xCoO_3$, $La_{1-x}Sr_xFeO_3$ and $La_{1-x}Sr_xMnO_3$.

Generally, the photochemical water oxidation with the standard $[Ru(bpy)_3]^{2+}$-/persulfate assay proceeds through four basic steps (Figure 6.4a): (1) excitation of $[Ru(bpy)_3]^{2+}$ at round 460 nm; (2) the excited $[Ru(bpy)_3]^{2+*}$ is oxidatively quenched by persulfate to form $[Ru(bpy)_3]^{3+}$; (3) hole injection into the WOC by $[Ru(bpy)_3]^{3+}$ and regeneration of $[Ru(bpy)_3]^{2+}$; (4) hole accumulation in the WOC for water oxidation to O_2. Although the detailed steps of water oxidation mechanisms remain under intense investigation, the basic role of WOCs in the process is clearly defined (Figure 6.4): (a) collection and transport of the oxidative equivalents from single-electron transfers via $[Ru(bpy)_3]^{3+}$ to the catalytically active centers; (b) transfer to oxidative equivalents to both molecular and intermediate water species and facilitation of O-O bond formation.

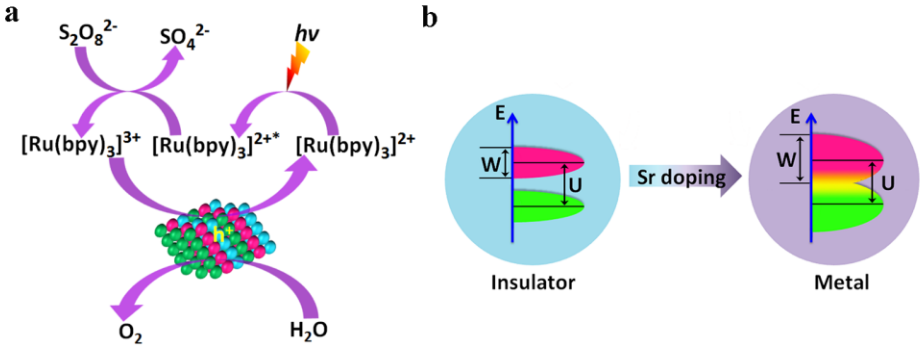

Figure 6.4. Schematic representation: Influence of the insulator to metal transition on the photochemical water oxidation activity of strongly correlated electronic systems. (a) Photochemical water oxidation steps with $[Ru(bpy)_3]^{2+}$ as photosensitizer and persulfate as electron acceptor. (b) Band structure evolution during insulator to metal transition.

In the present study, we provide substantial empirical evidence for a correlation between the insulator to metal transition and the enhanced water oxidation activity of the title compounds. $LaMO_3$ and La_2MO_4 (M= Co, Fe, Mn or Ni) are known as Mott insulators with strong Coulomb repulsion between the 3d electrons of the transition metal centers which results in an energy gap (denoted as U in Figure 6.4b) and renders the 3d electrons strongly localized. In plain terms, hole doping by La^{3+}/Sr^{2+} substitution broadens the bandwidth W of the 3d orbitals (as seen from XAS spectra) up to closing the energy gap U at a critical doping content (denoting the insulator to metal transition point). It is a reasonable assumption that metallic properties thereby enhance the hole accumulation and transfer functions of the WOC. Moreover, the stronger affinity between the metallic compounds and surface oxygen species, as evident from O 1s spectra, is likely to stabilize intermediate oxygen species during water oxidation and to facilitate their interface electron exchange. However, the precise underlying mechanisms remain to be studied in follow-up works.

6.4 Conclusions

In summary, the electronic properties of strongly correlated electronic systems, such as $La_{1-x}Sr_xMO_3$ perovskites and $La_{2-x}Sr_xMO_4$ layer perovskites (M= Fe, Co, Ni or Mn), were tuned via the Sr content and newly correlated with the photochemical water oxidation activity. Gradual substitution of La^{3+} with Sr^{2+} permits a clear correlation between the transition of the electronic properties from insulator to metal and enhanced water oxidation activity. This highlights the introduction of metallic properties as a potential design parameter for WOC construction. The well-investigated and easily accessible set of electronic properties in strongly correlated electron systems, such as localization of 3d electrons or spin polarization, may be turned into a toolbox to selectively tune their interaction with surface adsorbed molecular species. These new perspectives render strongly correlated electron systems promising candidates for systematic exploration of electronic structure-activity relations for heterogeneous catalysis.

References

[1] M. Zhang, M. de Respinis, H. Frei. *Nat. Chem.* **2014**, *6*, 362-367.

[2] Y. Gorlin, B. Lassalle-Kaiser, J. D. Benck, S. Gul, S. M. Webb, V. K. Yachandra, J. Yano, T. F. Jaramillo. *J. Am. Chem. Soc.* **2013**, *135*, 8525-8534.

[3] M. W. Kanan, J. Yano, Y. Surendranath, M. Dincă, V. K. Yachandra, D. G. Nocera. *J. Am. Chem. Soc.* **2010**, *132*, 13692-13701.

[4] M. Risch, F. Ringleb, M. Kohlhoff, P. Bogdanoff, P. Chernev, I. Zaharieva, H. Dau. *Energy Environ. Sci.* **2015**, *8*, 661-674.

[5] R. Subbaraman, D. Tripkovic, K.-C. Chang, D. Strmcnik, P. A. Paulikas, P. Hirunsit, M. Chan, J. Greeley, V. Stamenkovic, N. M. Markovic. *Nat. Mater.* **2012**, *11*, 550-557.

[6] J. Suntivich, K. J. May, H. A. Gasteiger, J. B. Goodenough, Y. Shao-Horn. *Science*, **2011**, *334*, 1383-1385.

[7] J. Rossmeisl, Z. W. Qu, H. Zhu, G. J. Kroes, J. K. Norskov. *J. Electroanal. Chem.* **2007**, *607*, 83-89.

[8] E. Dagotto. *Science* **2005**, *309*, 257-262.

[9] B. Ravel, M. Newville. *J. Synchrotron Rad.* **2005**, *12*, 537-541.

[10] S. E. Dann, D. B. Currie, M. T. Weller, M. F. Thomas, A. D. Al-Rawwas. *J. Solid State Chem.* **1994**, *109*, 134-144.

[11] M. Takano, J. Kawachi, N. Nakanishi, Y. Takeda. *J. Solid State Chem.* **1981**, *39*, 75-84.

[12] S. Tajima, A. Masaki, S. Uchida, T. Matsuura, K. Fueki, S. Sugai. *J. Phys. C : Solid State Phys.* **1987**, *20*, 3469-3484.

[13] O. Haas, U. F. Vogt, C. Soltmann, A. Braun, W.-S. Yoon, X. Q. Yang, T. Graule. *Mater. Res. Bull.* **2009**, *44*, 1397-1404.

[14] S. B. Adler, X. Y. Chen, J. R. Wilson. *J. Catal.* **2007**, *245*, 91-109.

[15] A. Mineshige, M. Inaba, T. Yao, Z. Ogumi. *J. Solid State Chem.* **1996**, *121*, 423-429.

[16] L. Sudheendra, M. M. Seikh, A. R. Raju, C. Narayana. *Chem. Phys. Lett.* **2001**, *340*, 275-281.

[17] H. Kozuka, H. Yamada, T. Hishida, K. Yamagiwa, K. Ohbayashi, K. Koumoto. *J. Mater. Chem. C* **2012**, *22*, 20217-20222.

[18] J. Hemberger, A. Krimmel, T. Kurz, H.-A. Krug von Nidda, V. Yu. Ivanov, A. A. Mukhin, A. M. Balbashov, A. Loidl. *Phys. Rev. B* **2002**, *66*, 094410.

Appendix

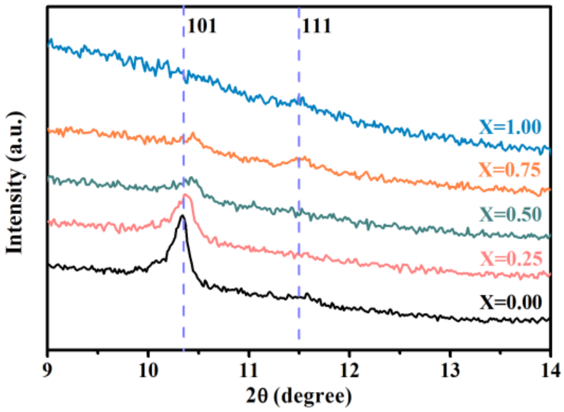

Figure S6.1. PXRD patterns of $La_{1-x}Sr_xFeO_3$.

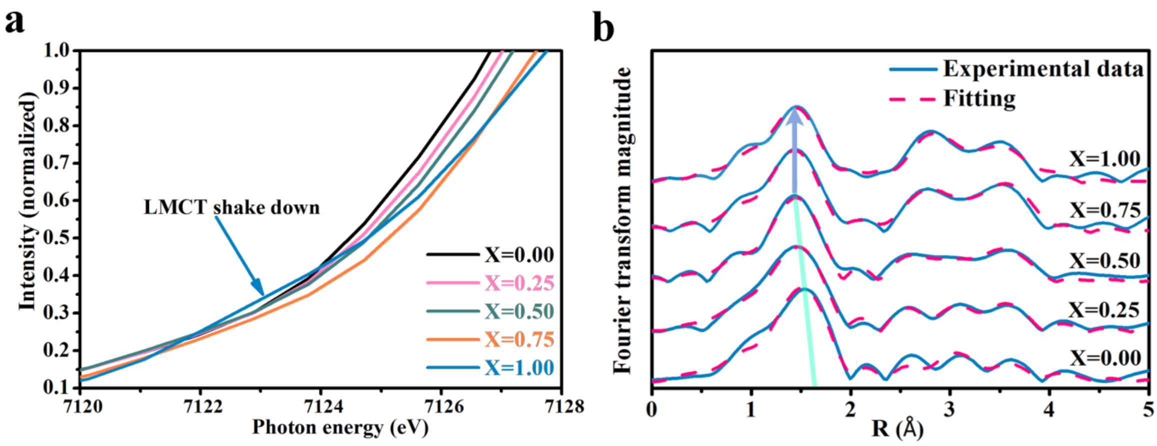

Figure S6.2. X ray absorption spectra of $La_{1-x}Sr_xFeO_3$. (a) the ligand to metal charge transer (LMCT) shake down. (b) experimental EXAFS spectra and the fitting with $La_{1-x}Sr_xFeO_3$ perovskite structure models.

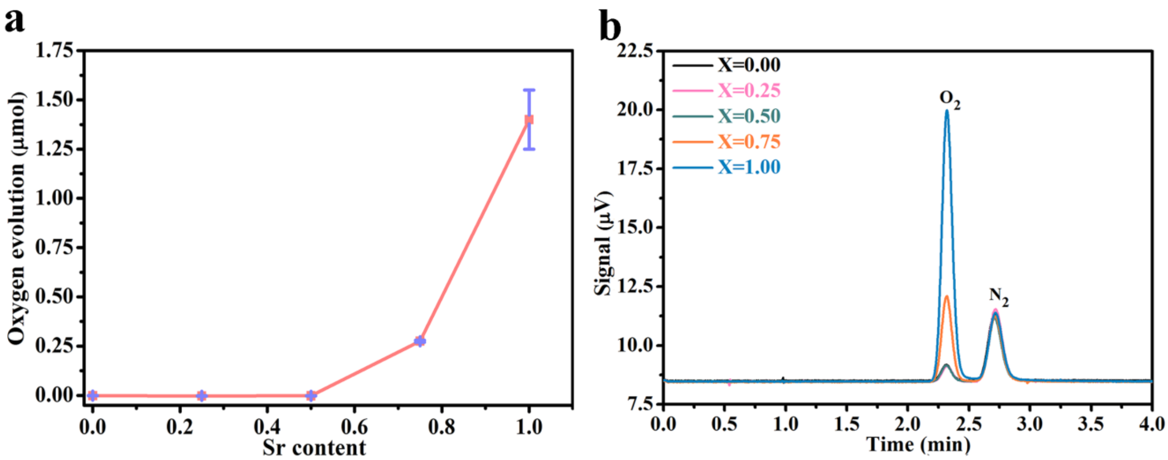

Figure S6.3. GC detection of oxygen diffused to headspace during photochemical water oxidation with $La_{1-x}Sr_xFeO_3$. (a) The oxygen evolution amount as function of Sr content after 10 minutes irradiation (the error bars were estimated from three independent catalytic tests). (b) Respresentive GC detection signals after10 minutes irradiation.

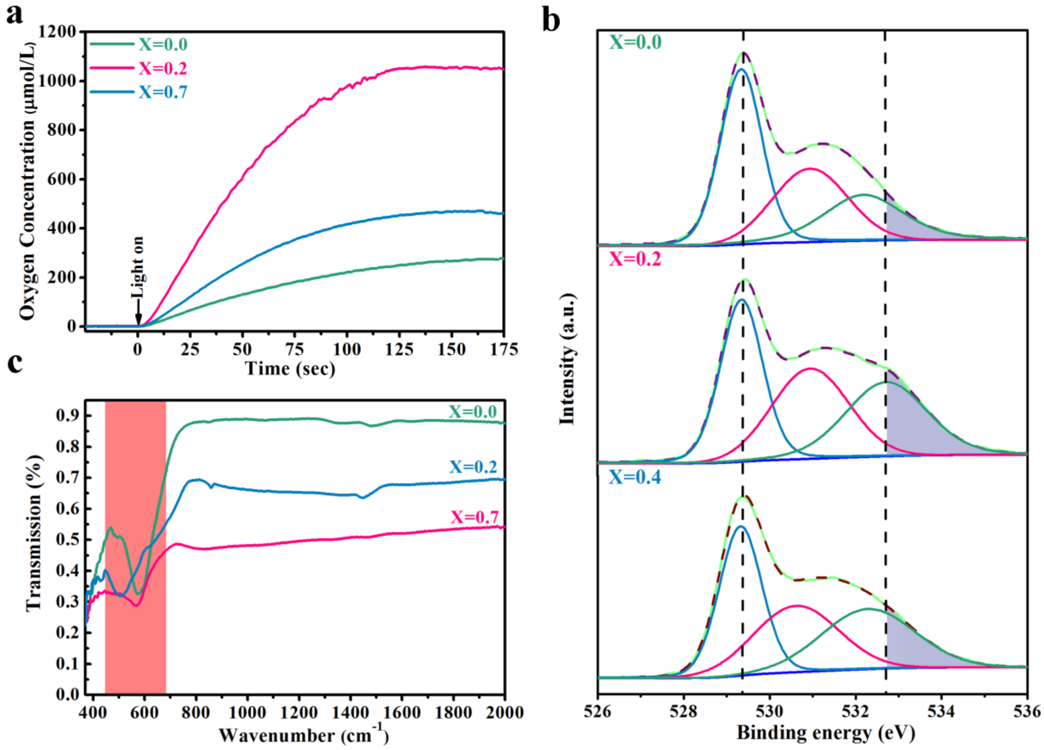

Figure S6.4. La$_{1-x}$Sr$_x$MnO$_3$ as models for photochemical water oxidation. (a) Photochemical oxygen evolution monitored by online Clark electrode in solution. (b) O 1s spectra. (c) FT-IR spectra.

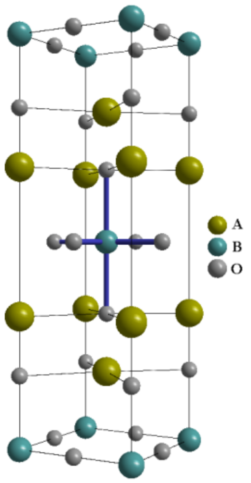

Figure S6.5. Structure model of layered perovskite A$_2$BO$_4$.

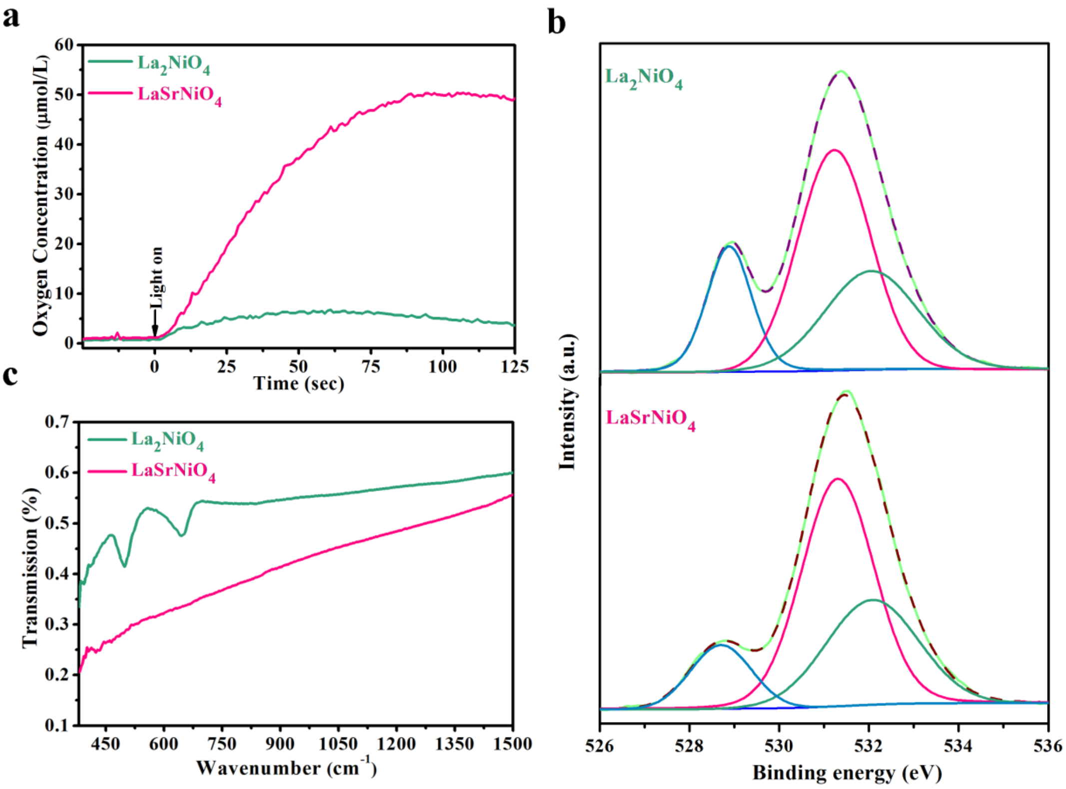

Figure S6.5. $La_{2-x}Sr_xNiO_4$ for photochemical water oxidation. (a) Photochemical oxygen evolution monitored by online Clark electrode in solution. (b) O 1s spectra. (c) FT-IR spectra.

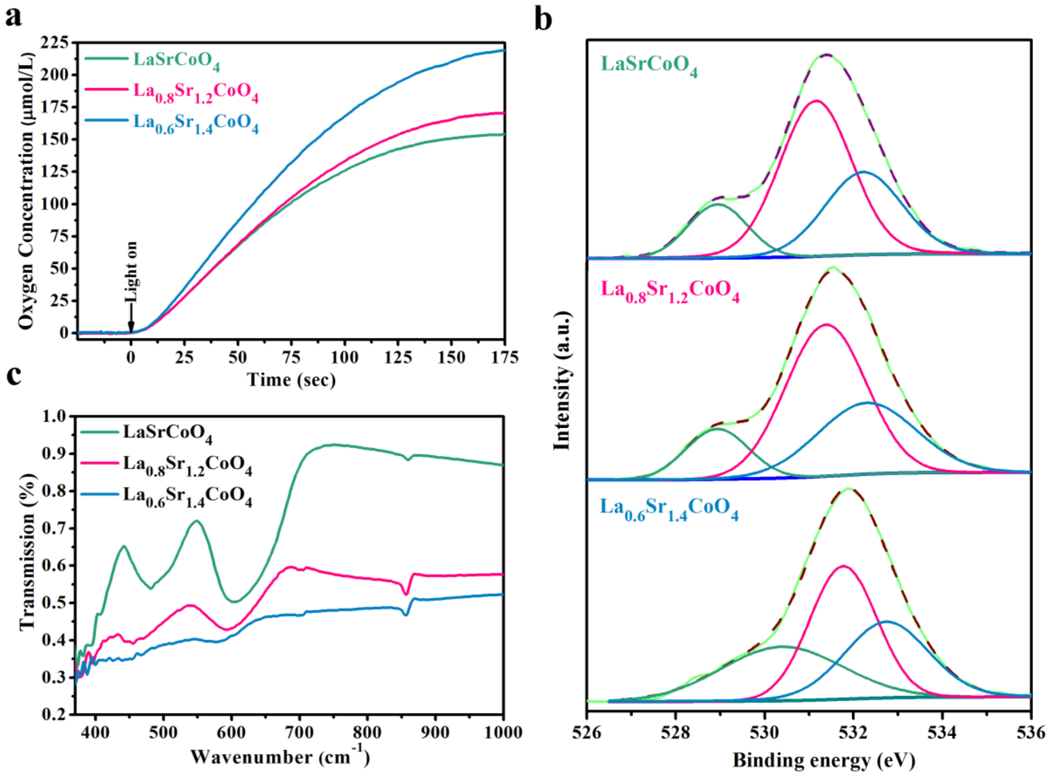

Figure S6.6. $La_{2-x}Sr_xCoO_4$ for photochemical water oxidation. (a) Photochemical oxygen evolution monitored by online Clark electrode in solution. (b) O 1s spectra. (c) FT-IR spectra.

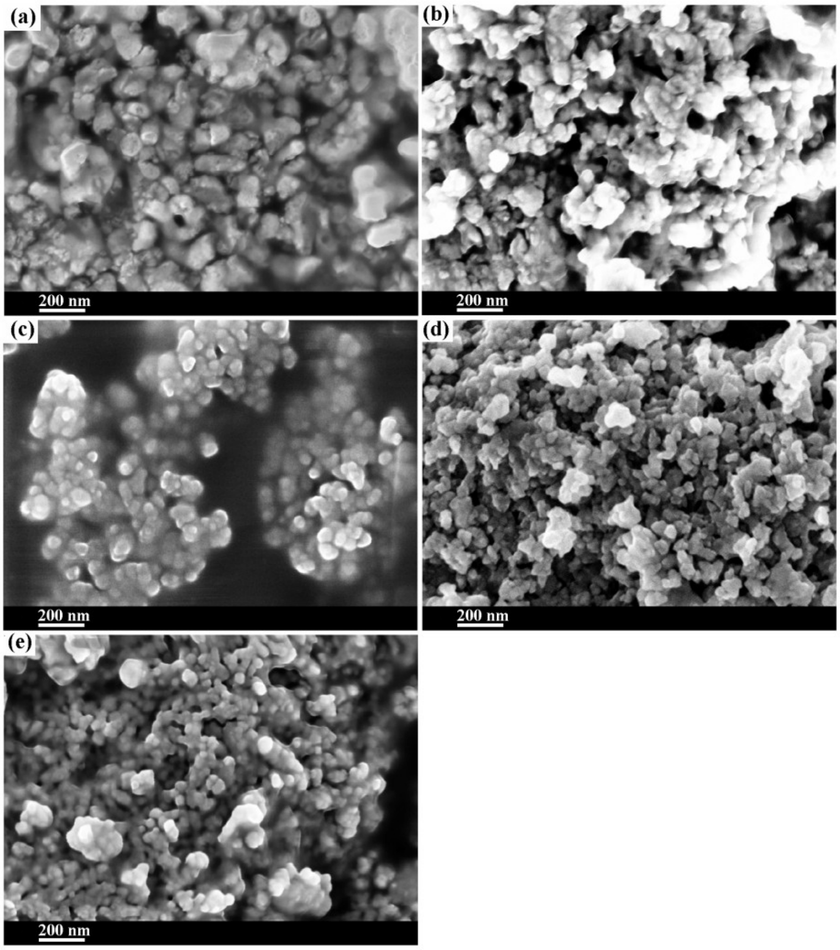

Figure S6.7. SEM picture of $La_{1-x}Sr_xFeO_3$. (a) $LaFeO_3$. (b) $La_{0.75}Sr_{0.25}FeO_3$. (c) $La_{0.5}Sr_{0.5}FeO_3$. (d) $La_{0.25}Sr_{0.75}FeO_3$. (e) $SrFeO_3$.

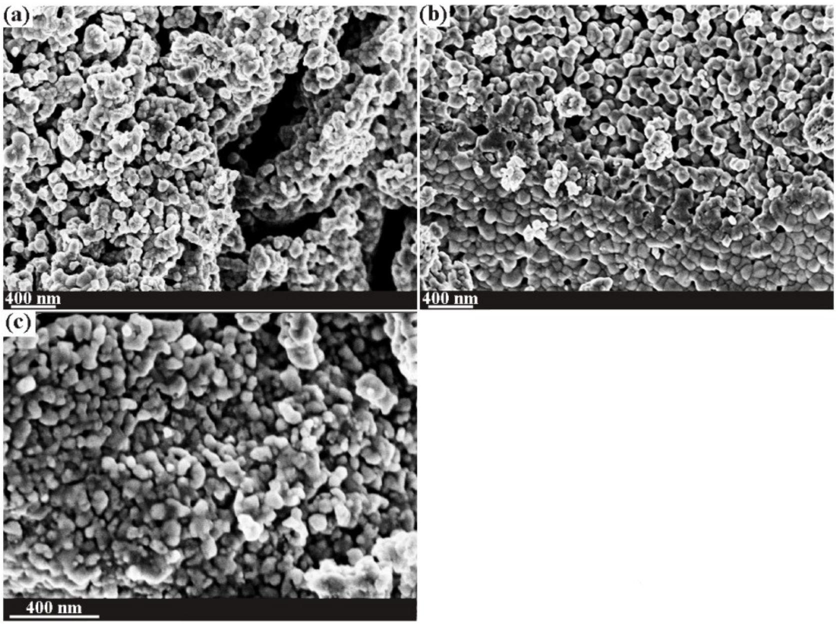

Figure S6.8. SEM picture of $La_{1-x}Sr_xCoO_3$. (a) $LaCoO_3$. (b) $La_{0.8}Sr_{0.2}CoO_3$. (c) $La_{0.6}Sr_{0.4}CoO_3$.

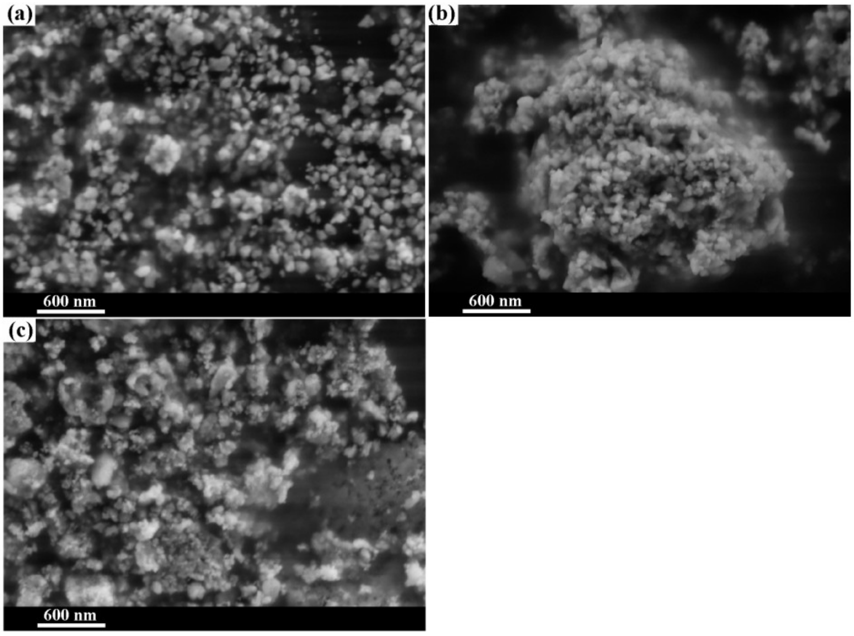

Figure S6.9. SEM picture of $La_{1-x}Sr_xMnO_3$. (a) $LaMnO_3$. (b) $La_{0.8}Sr_{0.2}MnO_3$. (c) $La_{0.3}Sr_{0.7}MnO_3$.

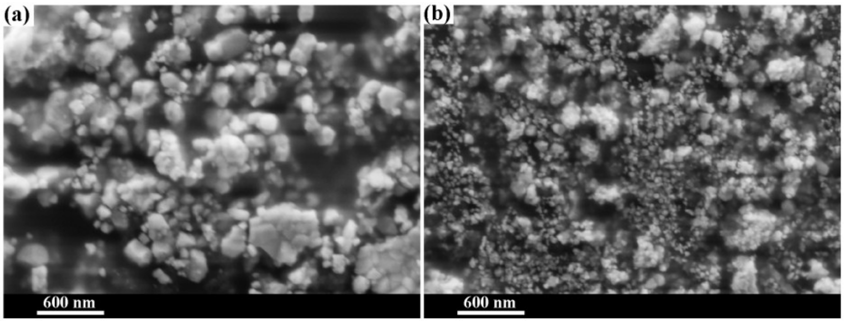

Figure S6.10. SEM picture of $La_{2-x}Sr_xNiO_4$. (a) La_2NiO_4. (b) $LaSrNiO_4$.

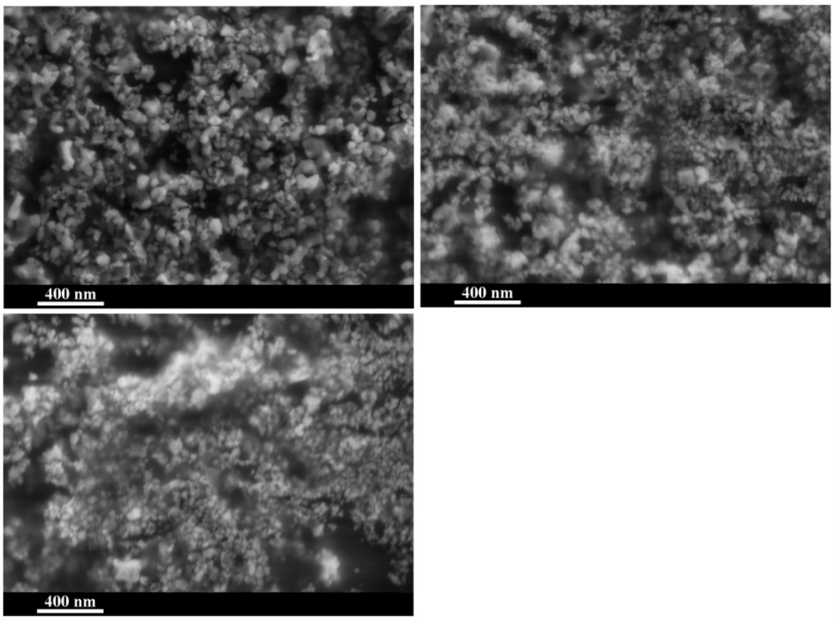

Figure S6.11. SEM picture of $La_{2-x}Sr_xCoO_4$. (a) $LaSrCoO_4$. (b) $La_{0.8}Sr_{1.2}CoO_4$. (c) $La_{0.6}Sr_{1.4}CoO_4$.

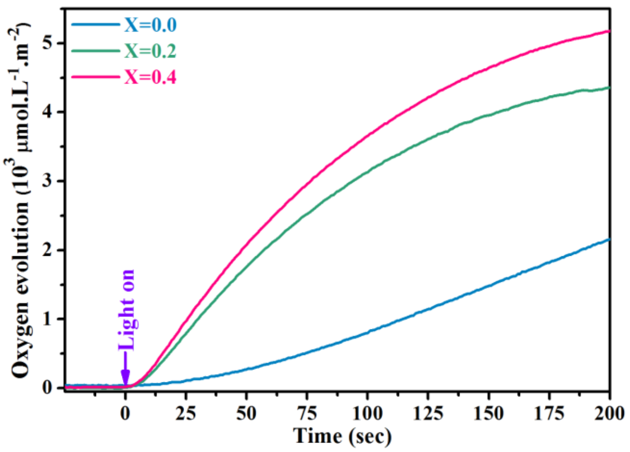

Figure S6.12. Photochemical water oxidation with $La_{1-x}Sr_xCoO_3$ WOCs after normalized to BET surface.

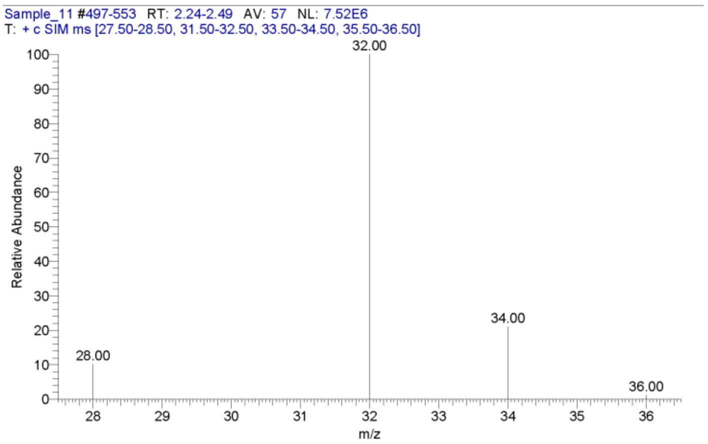

Figure S6.13. MS detection of O_2 during water oxidation labeling experiments with 10% ^{18}O containing H_2O.

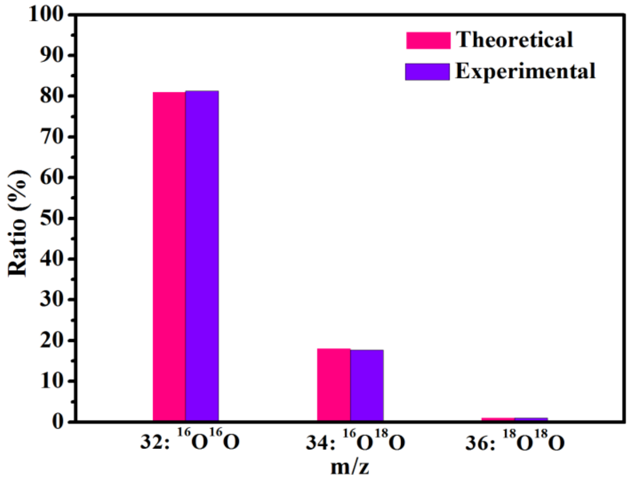

Figure S6.14. Comparison of expected and experimental $^{16}O^{16}O$, $^{16}O^{18}O$ and $^{18}O^{18}O$ ratios after water oxidation with $La_{0.6}Sr_{0.4}CoO_3$ in 10 % ^{18}O containing H_2O.

^{18}O labeling experiment was conducted to identify the oxygen source for oxygen molecule evolution. The experiment was conducted as follow: 10 mg $La_{0.6}Sr_{0.4}CoO_3$, 8 mg Ru-PS and 10 mg $Na_2S_2O_8$ were dispersed in 5 mL H_2O containing 10 % ^{18}O in ultrasound bath. The pH was adjusted to 7 by adding appropriate amounts of KH_2PO_4 and KH_2PO_4. Photochemical water oxidation was conducted as described in the method part. After 30 min of irradiation, 50 µL gas from headspace was injected into a GC-MS instrument for oxygen separation and detection.As shown in Figure S14, the GC-MS detection of the evolved oxygen ratio between $^{16}O^{16}O$, $^{16}O^{18}O$ and $^{18}O^{18}O$ can match well with the theoretical result, indicating the water as the exclusive oxygen source.

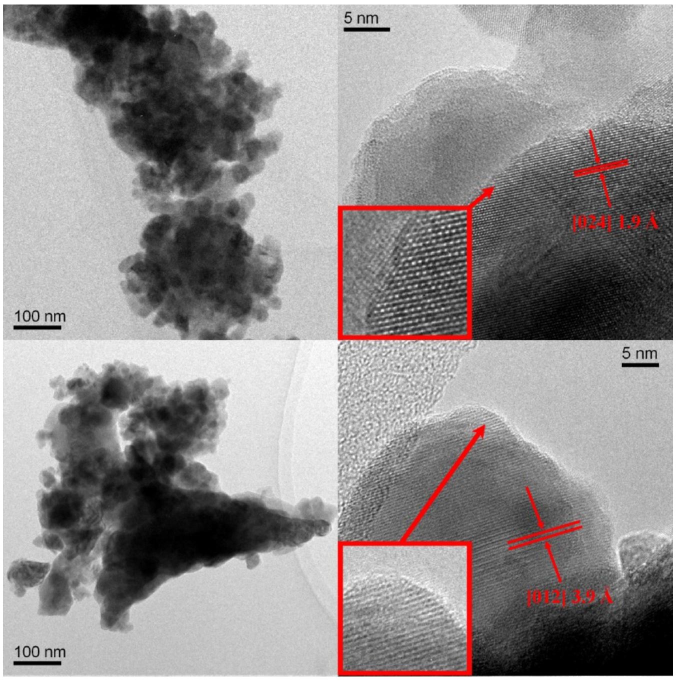

Figure S6.15. TEM pictures of $La_{0.6}Sr_{0.4}CoO_3$ before (above) and after (below) water oxidation.

The stability of WOCs was examined with the $La_{0.6}Sr_{0.4}CoO_3$ as the representative. Both HRTEM (Figure S6.15) and powder x-ray diffraction patterns (Figure S6.16c) indicate no obvious amorphization in either surface or bulk of $La_{0.6}Sr_{0.4}CoO_3$ particles after water oxidation. XPS and FT-IR further verified the electronic properties were retained during water oxidation.

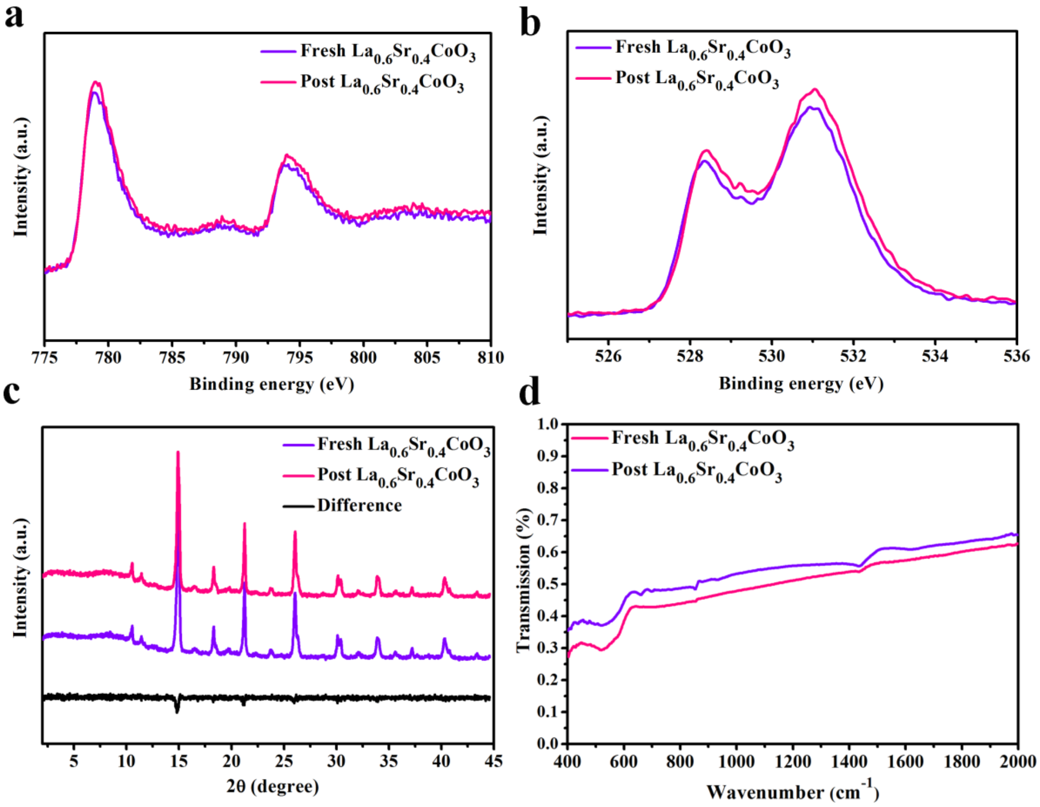

Figure S6.16. Analysis $La_{0.6}Sr_{0.4}CoO_3$ before and after water oxidation. a, Co 2p spectra. b, O 1s spectra. c, PXRD patterns. d, FT-IR spectra.

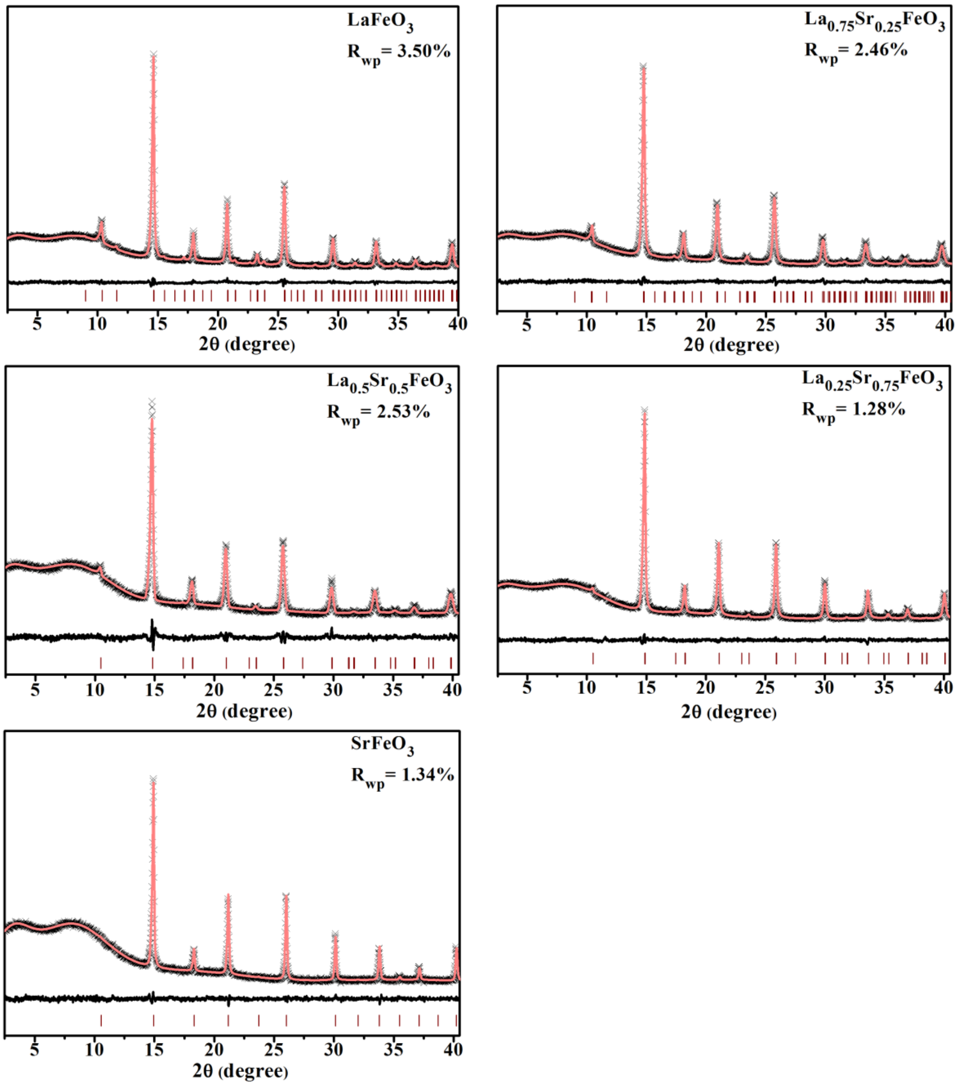

Figure S6.17. Rietveld refinement of $La_{1-x}Sr_xFeO_3$ PXRD patterns.

Table S6.2. Lattice constants of $La_{1-x}Sr_xFeO_3$ derived from Rietveld refinement.

Sample	***a/Å***	***b/Å***	***c/ Å***	***V/ Å³***
$LaFeO_3$	5.553(1)	5.562(1)	7.850(1)	242.45(3)
$La_{0.75}Sr_{0.25}FeO_3$	5.530(1)	5.508(2)	7.834(2)	238.60(4)
$La_{0.5}Sr_{0.5}FeO_3$	5.524(3)	5.524(3)	13.390(2)	353.82(8)
$La_{0.25}Sr_{0.75}FeO_3$	5.476(2)	5.476(2)	13.406(5)	348.14(5)
$SrFeO_3$	3.861(0)	3.861(0)	3.861(0)	57.539(6)

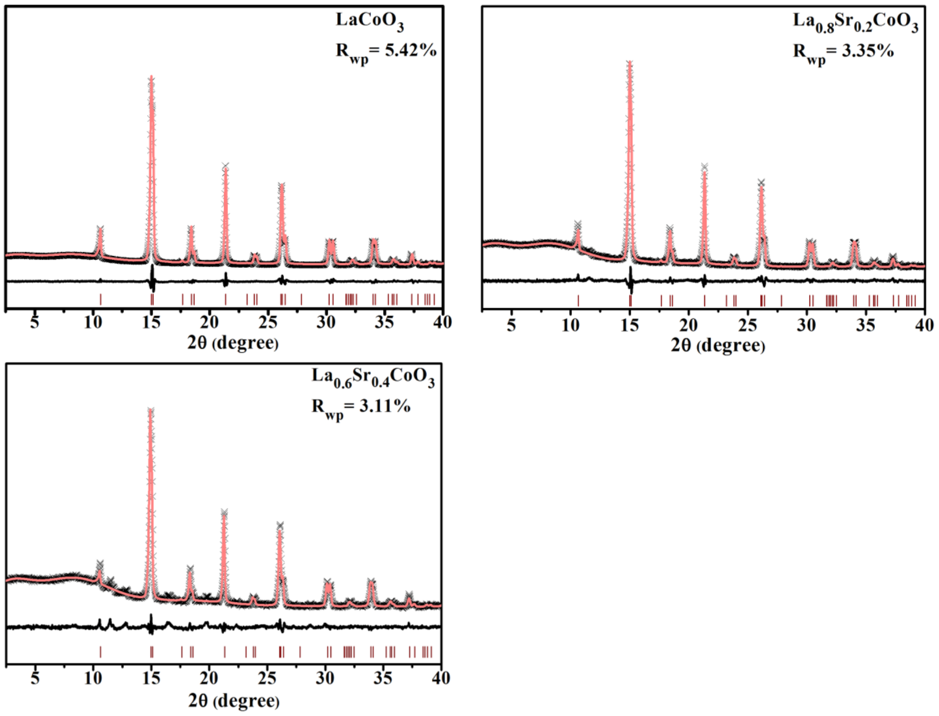

Figure S6.18. Rietveld refinement of La$_{1-x}$Sr$_x$CoO$_3$ PXRD patterns.

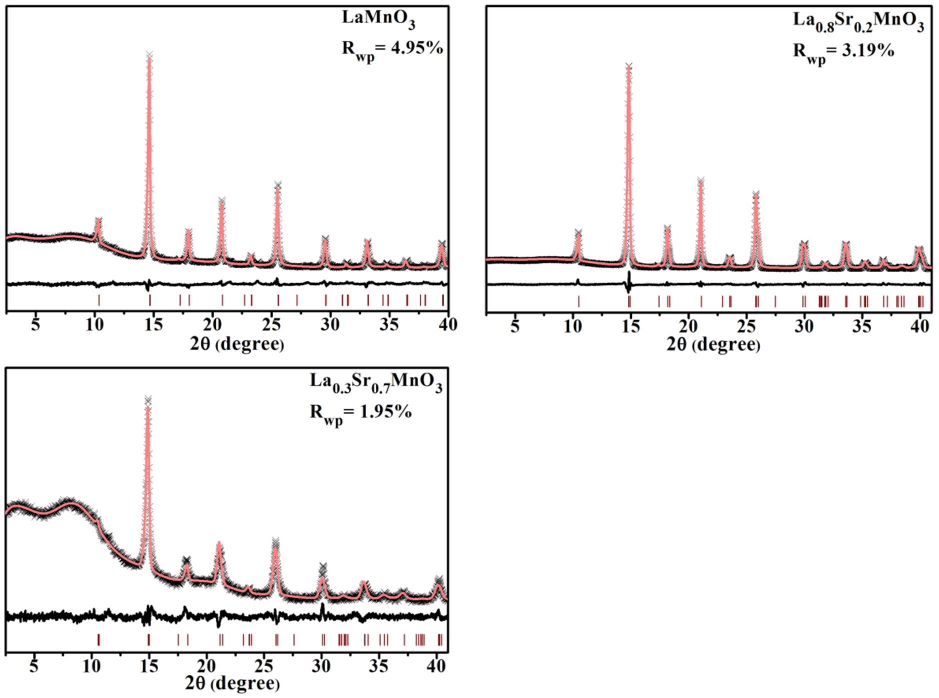

Figure S6.19. Rietveld refinement of La$_{1-x}$Sr$_x$MnO$_3$ PXRD patterns.

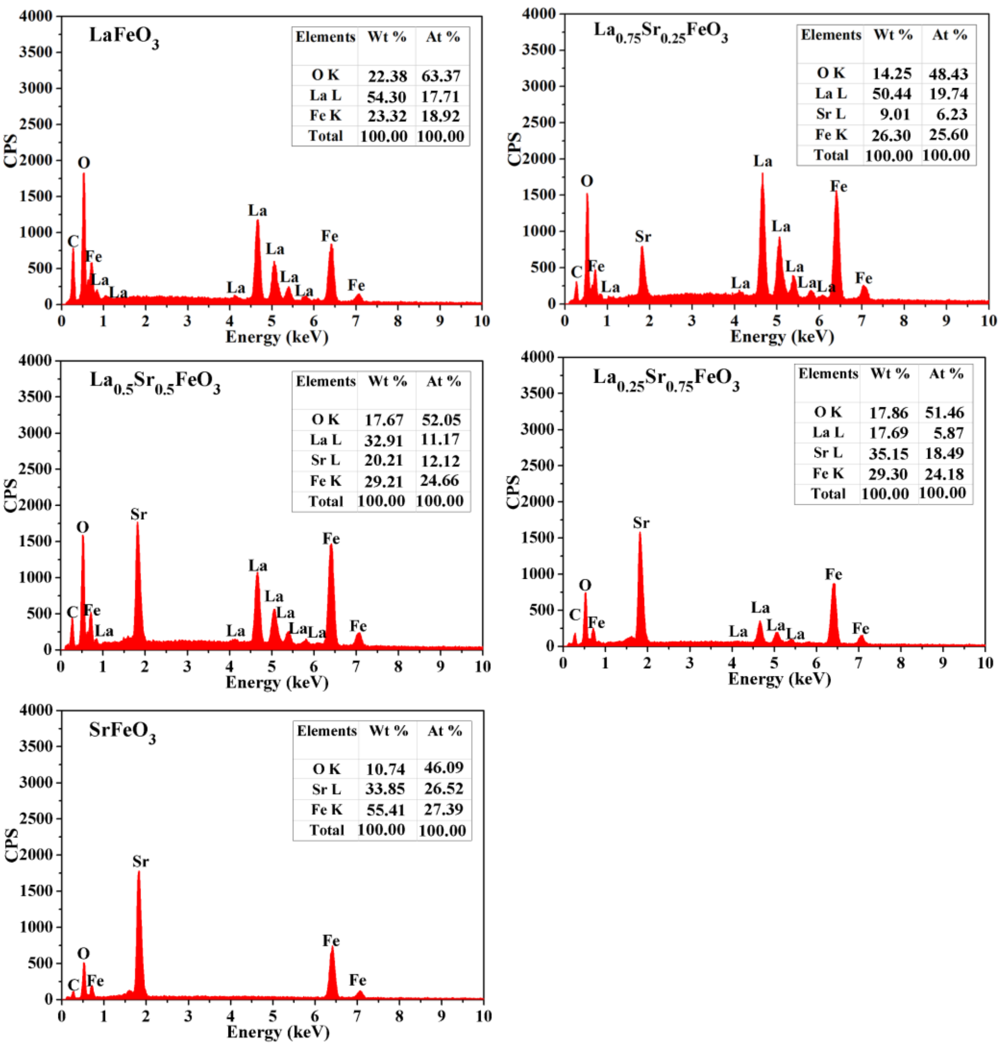

$LaFeO_3$

Elements	Wt %	At %
O K	22.38	63.37
La L	54.30	17.71
Fe K	23.32	18.92
Total	100.00	100.00

$La_{0.75}Sr_{0.25}FeO_3$

Elements	Wt %	At %
O K	14.25	48.43
La L	50.44	19.74
Sr L	9.01	6.23
Fe K	26.30	25.60
Total	100.00	100.00

$La_{0.5}Sr_{0.5}FeO_3$

Elements	Wt %	At %
O K	17.67	52.05
La L	32.91	11.17
Sr L	20.21	12.12
Fe K	29.21	24.66
Total	100.00	100.00

$La_{0.25}Sr_{0.75}FeO_3$

Elements	Wt %	At %
O K	17.86	51.46
La L	17.69	5.87
Sr L	35.15	18.49
Fe K	29.30	24.18
Total	100.00	100.00

$SrFeO_3$

Elements	Wt %	At %
O K	10.74	46.09
Sr L	33.85	26.52
Fe K	55.41	27.39
Total	100.00	100.00

Figure S6.20. Composition analysis of $La_{1-x}Sr_xFeO_3$ by EDXS.

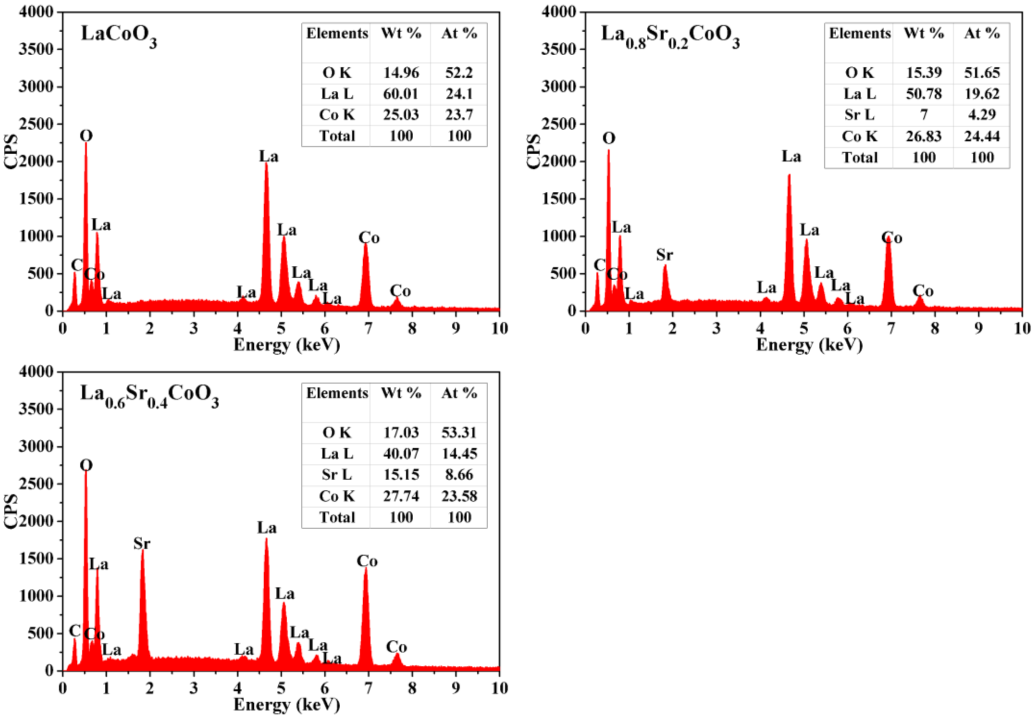

$LaCoO_3$

Elements	Wt %	At %
O K	14.96	52.2
La L	60.01	24.1
Co K	25.03	23.7
Total	100	100

$La_{0.8}Sr_{0.2}CoO_3$

Elements	Wt %	At %
O K	15.39	51.65
La L	50.78	19.62
Sr L	7	4.29
Co K	26.83	24.44
Total	100	100

$La_{0.6}Sr_{0.4}CoO_3$

Elements	Wt %	At %
O K	17.03	53.31
La L	40.07	14.45
Sr L	15.15	8.66
Co K	27.74	23.58
Total	100	100

Figure S6.21. Composition analysis of $La_{1-x}Sr_xCoO_3$ by EDXS.

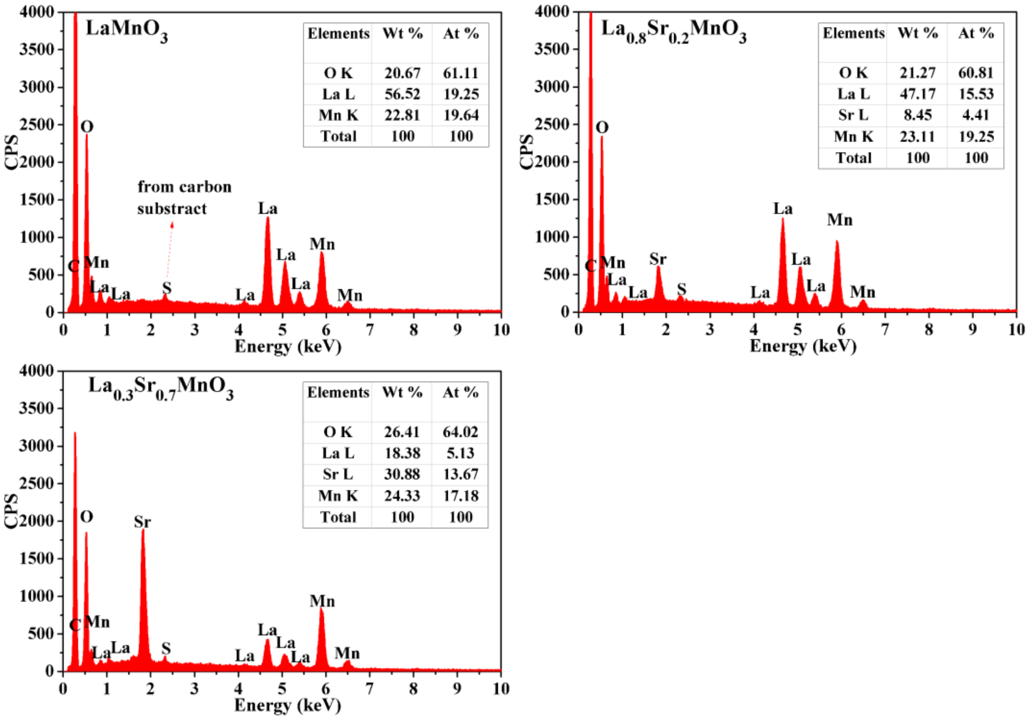

$LaMnO_3$

Elements	Wt %	At %
O K	20.67	61.11
La L	56.52	19.25
Mn K	22.81	19.64
Total	100	100

$La_{0.8}Sr_{0.2}MnO_3$

Elements	Wt %	At %
O K	21.27	60.81
La L	47.17	15.53
Sr L	8.45	4.41
Mn K	23.11	19.25
Total	100	100

$La_{0.3}Sr_{0.7}MnO_3$

Elements	Wt %	At %
O K	26.41	64.02
La L	18.38	5.13
Sr L	30.88	13.67
Mn K	24.33	17.18
Total	100	100

Figure S6.22. Composition analysis of $La_{1-x}Sr_xMnO_3$ by EDXS.

7. Interlayer anions tailored photochemical water oxidation activities of Co-LDHs

7.1 Introduction

A wide range of theoretical and experimental studies indicates that the electronic properties of WOCs, such as the valence states of the transition metals,[1] 3d e_g electron configurations,[2] O p-band position,[3] and surface affinity to oxygen species[4] can significantly influence their water oxidation activity. In the previous chapters, we investigated the influence of the electronic properties on photochemical water oxidation based on $LiCoO_2$, $LiCoPO_4$ and $Li_2Mn_2O_4$ oxides. We observed significant enhancement of water oxidation activity through chemical delithiation of these materials, which went hand in hand with their increased charge carrier mobility as well as a stronger surface affinity to oxygen species. These studies indicate that the generation of mobile cations through extraction or intercalation techniques could be an effective means to tune the electronic properties of a given parent compound.

Cobalt layered double hydroxides (Co-LDHs) are composed of positively charged edge-sharing $\{CoO_6\}$ layers with interlayer counter anions. The stable and flexible layered motif gives rise to various applications, such as drug delivery, catalysis, sewage treatment, battery materials, supercapacitor and so on.[5,6] Recently, a self-healing and highly efficient CoPi WOC was developed by *Nocera*'s group which bears some structural resemblance to Co-LDHs.[7,8] It was proposed that the mixed valence of cobalt (+2 and +3) and removable protons from hydroxyl groups facilitated proton-coupled electron-transfer (PCET) which is probably responsible for efficient water oxidation. Just recently, several studies investigated the electrochemical water oxidation activity of LDHs with mixed metal centers such as Co-Fe, Co-Ni, Co-Mn, Ni-Fe and so on.[9-13] However, the photochemical chemical water oxidation with LDHs has been reported on rather seldom in comparison. Moreover, the possible influence of the interlayer anions on the water oxidation activity remained widely unexplored in these previous studies. In this context, some studies[14-16] already indicated that interlayer anions can significantly affect the charge and the hydrophobic/hydrophilic properties of LDHs which bears the potential to also enhance the water oxidation activity. In the following, we thus studied the influence of interlayer anions on the electronic properties and photochemical water oxidation activity of Co-LDHs.

7.2 Experimental

7.2.1 Synthesis of Co-LDHs with different interlayer anions

Firstly, both α-$Co(OH)_2$ and β-$Co(OH)_2$ were synthesized as precursors for the preparation of Co-LDHs according to previous protocols.[17] Pink β-$Co(OH)_2$ was prepared by hydrolyzing 2.5 mM $CoCl_2$ in the presence of 150 mM hexamethylenetetramine at 75 ^{o}C for 5 h in nitrogen atmosphere. Green α-$Co(OH)_2$ was prepared by hydrolyzing 10 mM $CoCl_2$ in a mixed solution of deionized water and ethanol in 9:1 volume ratio in the presence of 50 mM NaCl and 150 mM hexamethylenetetramine at 75 ^{o}C for 5 h in nitrogen atmosphere as well. Next, one third of Co^{2+} of the as-synthesized cobalt hydroxide was oxidized to Co^{3+} in bromine-acetonitrile solution with accompanied intercatalation of Br^- between the edge-sharing CoO_6 layers of Co-LDHs. Finally, the Br^- intercalated Co-LDHs were subjected to ion exchange reactions with 1 M K_2CO_3 and $KC_6H_7O_2$ for one week to generate Co-LDHs with the corresponding intercalated anions. The final products were obtained by separating the precipitations from solution after anion exchange and three times washing with deionized water.

7.2.2 Characterizations

Powder X-ray diffraction patterns (PXRD patterns) were recorded on a STOE STADI P diffractometer (reflection mode, step size: 0.3°/step, 150 s/step) with Mo $K_{\alpha 1}$ radiation and transformed to Cu $K_{\alpha 1}$ radiation patterns with Jade 5.0. The morphologies and composition were investigated by scanning electron microscopy (LEO 1530, FEG), Bruker energy-dispersive X-ray spectrometer (EDXS) and transmission electron microscopy (FEI Tecnai F30, FEG, 300 kV). Fourier transformed infrared (FT-IR) spectra were recorded on a Bruker Opus spectrometer. UV/Vis diffuse reflectance absorption spectra were recorded on a Lambda 650 S Perkin Elmer UV-visible spectrometer. XPS spectra were measured on Thermo ESCALAB 250 with a monochromatic Al K_{α} as x-ray source. The C 1s peak at 284.6 eV was set as the reference for all XPS peak positions calibration. ^{18}O labeling experiments: 10 mg WOC, 8 mg Ru-PS and 10 mg $Na_2S_2O_8$ were dispersed in 5 mg H_2O with 10 % ^{18}O in ultrasound bath. The pH was adjusted to 7 by adding appropriate amounts of KH_2PO_4 and KH_2PO_4. Photochemical water oxidation was conducted as described below. After 20 min of irradiation, 50 μL gas from headspace was injected into a GC-MS instrument for oxygen detection.

7.2.3 Photocatalytic water oxidation tests

Photochemical water oxidation were conducted according to a standard $[Ru(bpy)_3]^{2+}/S_2O_8^{2-}$ protocol. First, a suspension was prepared by mixing 10 mg water oxidation catalyst, 8 mg $[Ru(bpy)_3]Cl_2$ photosensitizer and 50 mg NaS_2O_8 in 8 mL borate buffer (0.1 M, pH 8, 10 mL vial) in the dark. Next, the vial was degassed with helium to remove O_2 in both solution and headspace. A LED lamp with 460 nm wavelength and 5000 Lux output was used as visible light source. Oxygen produced in solution was online monitored by a calibrated Clarke electrode (Unisense) or the oxygen diffused to headspace was detected by gas chromatography (Agilent 7820A packed with a 3 m × 2 mm molecular sieve 13X 80-100 column) as follows: 100 µL samples of gas from the head vial were injected into a gas chromatograph using a gastight microliter syringe (Hamilton 1825 RN) during intervals of several minutes. Helium was chosen as carrier gas to increase the detection sensitivity of O_2. Gases were detected with a thermal conductivity detector (Varian) operated at 200 °C. Contamination of the headspace by air was constantly monitored through the N_2 peak on GC chromatograms.

7.3 Results and discussion

7.3.1 Synthesis and structure of Co-LDHs

The structure and phase purity of as-synthesized α-$Co(OH)_2$ and β-$Co(OH)_2$ were confirmed by powder X-ray diffraction (PXRD) as shown in Figure 7.1. All the diffraction peaks match well with the reported patterns except for some intensity differences which arise from the preferred orientation of the samples and the transmission data collection mode.[18] β-$Co(OH)_2$ has a stochiometric composition of $Co(OH)_2$ with a brucite-like structure, while α-$Co(OH)_2$ is composed of positively charged $Co(OH)_{2-x}$ layers with interlayer anions for charge balance. α-$Co(OH)_2$ exhibits a larger interlayer distance compared to β-$Co(OH)_2$. This is verified by a lower angle diffraction peak at around 10^o which is absent for β-$Co(OH)_2$. Br^- intercalated compounds (abbreviated in the following as: Co-LDHs-Br^-) obtained from both α-$Co(OH)_2$ and β-$Co(OH)_2$ exhibit very similar diffraction patterns (Figure 7.1), indicating that the influence of the cobalt hydroxide precursor on the structure of the resulting LDHs is not significant.

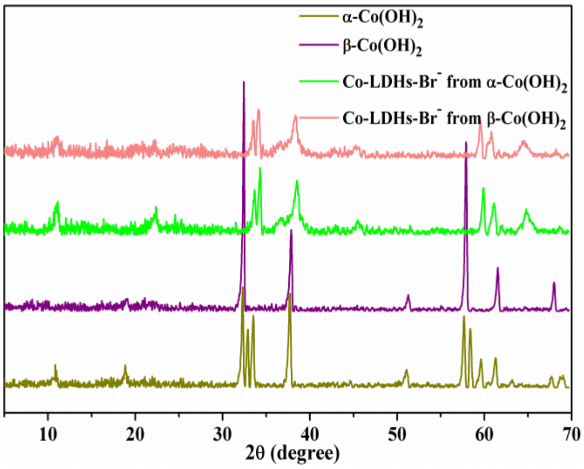

Figure 7.1. PXRD patterns of α-$Co(OH)_2$, β-$Co(OH)_2$ and their Co-LDH-Br^- derivatives.

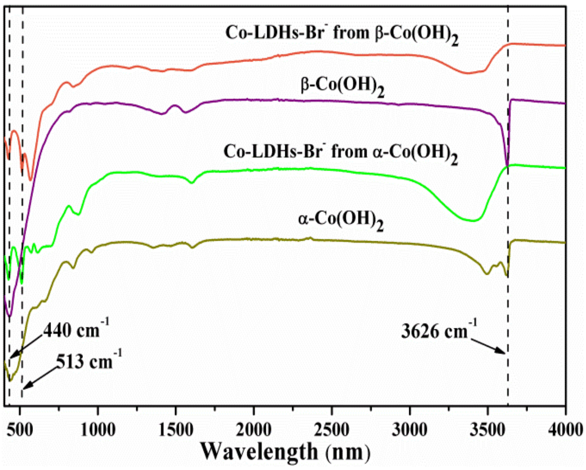

Figure 7.2. FT-IR spectra of α-$Co(OH)_2$, β-$Co(OH)_2$ and their Co-LDH-Br^- derivatives.

The structural and compositional difference between α-$Co(OH)_2$ and β-$Co(OH)_2$ is further evident from their FT-IR spectra (Figure 7.3). A sharp absorption band at 3627 cm^{-1} can be observed for β-$Co(OH)_2$ which originates from the OH stretching vibration In contrast, α-$Co(OH)_2$ displays a very broad absorption around 3400 cm^{-1} which can be further resolved into two stretching vibrations corresponding to the O-H bond of interlayer water molecules and -OH from the $Co(OH)_2$ layers. Several small absorption bands in the range from 500-1000 cm^{-1} indicate the presence of interlayer anions (Cl^-, CO_3^{2-}) for α-$Co(OH)_2$, which is in line with previous studies[19]. However, β-$Co(OH)_2$ displays none of these absorption bands. A strong band at 440 cm^{-1} present in α-$Co(OH)_2$ and β-$Co(OH)_2$ can be assigned to the Co^{2+}-O stretching vibration. Similar absorption bands of the two Co-LDHs-Br^- prepared from α-$Co(OH)_2$ and β-$Co(OH)_2$ again point out that the choice of the cobalt hydroxide precursor is not decisive, consistent with the above conclusions from the PXRD patterns. However, the strong absorption intensity for α-$Co(OH)_2$ derived Co-LDHs-Br^- points to their higher concentration of interlayer species compared to β-$Co(OH)_2$ derived Co-LDHs-Br^-. This could be explained by the superior ion exchange properties of α-$Co(OH)_2$ due to its larger interlayer distance. Compared to α-$Co(OH)_2$ and β-$Co(OH)_2$, an additional absorption band appears at 513 cm^{-1} for Co-LDHs-Br^- which is ascribed to the Co^{3+}-O stretching vibration.

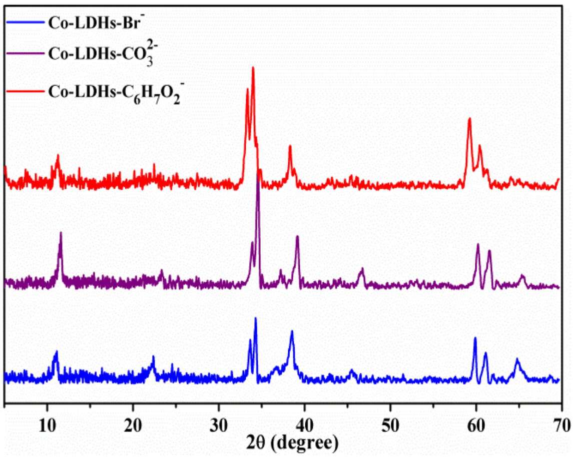

Figure 7.3. PXRD patterns of Co-LDHs with different interlayer anions.

Co-LDHs with different anions (CO_3^{2-} and $C_6H_7O^{2-}$) were obtained through ion exchange of Co-LDHs-Br^- (derived from α-$Co(OH)_2$ as precursor) with the corresponding potassium salts. After anion exchange, the PXRD patterns exhibit a systematic shift according to the anionic radii. Due to the much larger size of $C_6H_7O^{2-}$, the pattern of Co-LDHs-$C_6H_7O^{2-}$ underwent a more significant shift towards lower angles compared to Co-LDHs-Br^- and Co-LDHs- CO_3^{2-} and the peak at 45° even disappears.

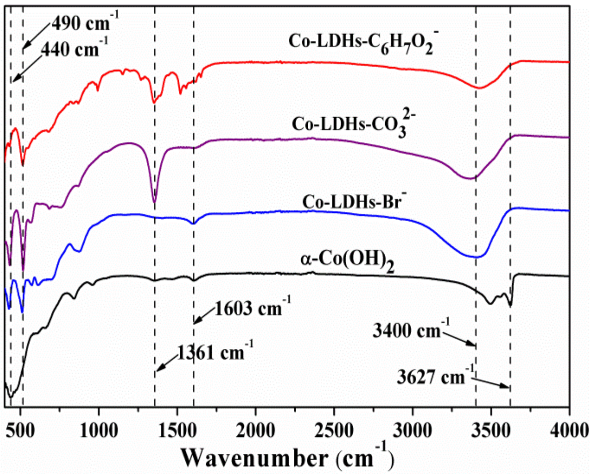

Figure 7.4. FT-IR spectra of Co-LDHs with different interlayer anions.

Ion exchange between Co-LDHs-Br^- and different anions was confirmed with the presence of the characteristic IR absorption bands of the corresponding anions (Figure 7.4). For example, a band at 1361 cm^{-1} related to the symmetric stretching of C=O is clearly present in Co-LDHs-CO_3^{2-}, and Co-LDHs-$C_6H_7O_2^-$, while it is barely observable for Co-LDHs-Br^- due to contamination with environmental CO_2. A further band at 1603 cm^{-1} arising from the asymmetric C=O stretching can be observed, and it is much stronger for Co-LDHs-$C_6H_7O_2^-$ due to their larger guest anion size compared to CO_3^{2-}. The presence of Br^- in Co-LDHs-Br^- is evident from the characteristic Br 3d peak in XPS measurements (Figure S7.6).

7.3.2 Photochemical water oxidation with Co-LDHs

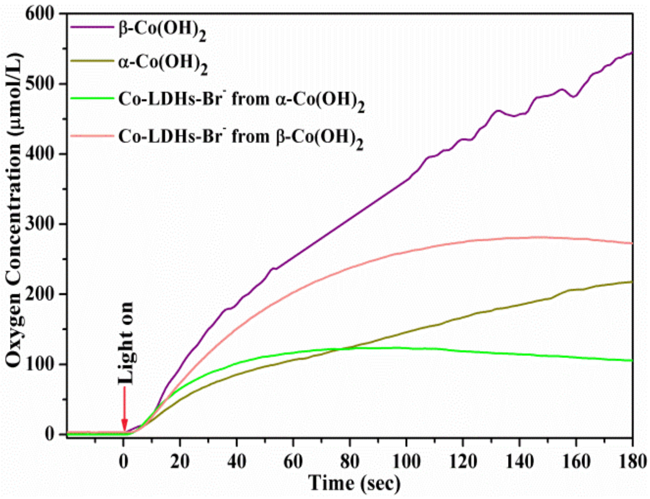

Figure 7.5. Photochemical water oxidation with Co-LDHs containing different interlayer anions.

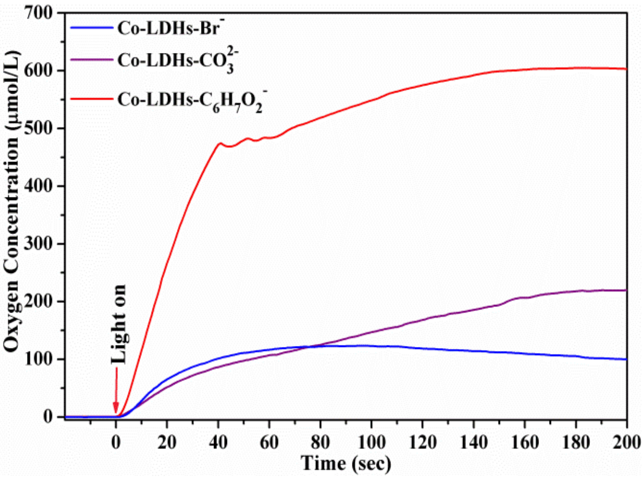

Figure 7.6. Photochemical water oxidation with Co-LDHs with different interlayer anions.

Photochemical water oxidation was conducted according to a standard $[Ru(bpy)_3]^{2+}/S_2O_8^{2-}$ protocol. As shown in Figure 7.5, the interlayer anions exert a significant influence on the water oxidation activities. Replacing Br^- with CO_3^{2-} only slightly increased the water oxidation activity. However, $C_6H_7O_2^-$ intercalation improves the water oxidation activity almost by a factor of 5 compared to Co-LDHs-Br^-. Generally, the morphology and particle size are well known as important factors that affect the water oxidation activity. Therefore, we investigated the Co-LDHs particle size and shape by scanning electron microscopy, as shown in Figure 7.8. All the LDHs maintained the original nanoplate morphology of α-$Co(OH)_2$ (Figure S7.2) with no significant change of the particle size, neither during the transformation of α-$Co(OH)_2$ to Co-LDHs-Br^- nor the following ion exchange. Since all of the LDHs were derived from same batch of α-$Co(OH)_2$, we can safely assume they have basically the same or very close surface areas. Thus, the activity differences between these LDHs cannot be simply interpreted from the perspective of morphology alone.

^{18}O labeling experiments were conducted with 10% ^{18}O containing H_2O as solvent. As shown in Figure 7.8, GC-MS detection revealed a molar ratio of 81.82:17.23:0.95 between $^{16}O^{16}O$, $^{16}O^{18}O$ and $^{18}O^{18}O$ which is very close to the theoretical ratio of 81:18:1 calculated for 10% ^{18}O containing H_2O. This excellent match between the experimental and theoretical results confirms that H_2O is the exclusive oxygen source during water oxidation.

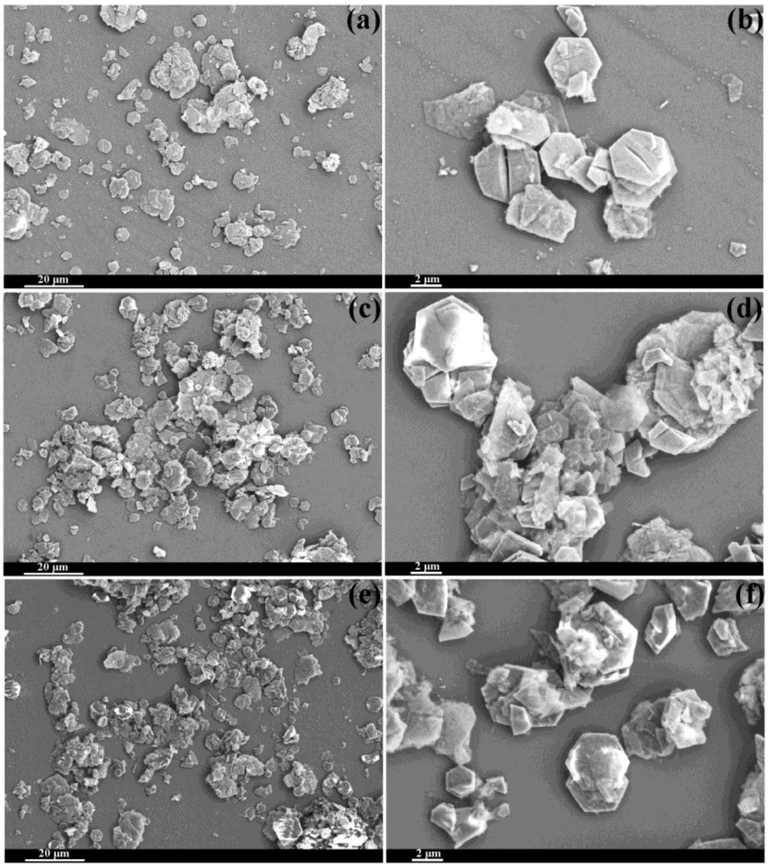

Figure 7.7. Representative SEM images of Co-LDHs with different interlayer anions.

7.3.3 Electronic properties and water oxidation activities

To reveal the possible influence of the anions on the electronic properties of Co-LDHs, the Co-LDHs-Br^-, Co-LDHs-CO_3^{2-} and Co-LDHs-$C_6H_7O_2^-$ were further studied with XPS spectroscopy. As shown in Figure 7.9, the Co 2p XPS spectra are composed of Co $2p_{3/2}$ and Co $2p_{1/2}$ peaks located at around 780 and 796 eV, respectively. Their respective satellites present at around 5.7 eV higher binding energies. This energy gap is just between the value of 10 eV reported for CoOOH and 5.5 eV observed for $Co(OH)_2$,[20] which strongly suggests mixed valence states of +2 and +3. The absence of obvious shift or broadening of the Co $2p_{3/2}$ peaks corresponding to cobalt reduction or oxidation indicates that the cobalt valence states remain unchanged during the anion exchange process. Analogous to Co 2p spectra, O 1s spectra (Figure S7.9) do not exhibit any significant change either, thus pointing to closely related surface affinities to oxygen species for the entire Co-LDHs series.

To correlate the water oxidation activity to the electronic properties, the valence band spectra of Co-LDHs were compared (Figure 7.9). In contrast to the Co 2p spectra, the valence bands display some changes, especially for Co-LDHs-$C_6H_7O_2^-$ where the onset of the valence band was shifted to lower binding energy compared to Co-LDHs-Br^-. Interestingly, this phenomenon goes hand in hand with enhanced water oxidation activity as well as an enlarged layer distance (PXRD), implying a possible interplay between these factors. A recent study revealed the superior electrochemical water oxidation activities of exfoliated LDHs compared to their bulk counterparts.[9] It was found that the improved performance is not only due to the increased particle surface area, but also caused by special electronic properties of the exfoliated $\{MO_6\}$ layers (i.e. higher conductivity). Plenty of studies already confirmed the remarkable alternation of electronic properties (semiconductor to metal transition) of layer materials, such as metal chalcogenides, after exfoliation.[21,22] Thus, the widened interlayer distance of edge-sharing $\{CoO_6\}$ layers of Co-LDHs arising from the larger size of the $C_6H_7O_2^-$ anions may work in the same direction as exfoliation through decreasing electrostatic interaction of the layers with increasing distance between them. The shift of the valence band to lower binding energy furthermore indicates that the valence band moves closer to the Fermi level which may enhance the conductivity. In line with our recent studies,[23,24] the enhanced conductivity may explain the higher water oxidation activity of Co-LDHs-$C_6H_7O_2^-$.

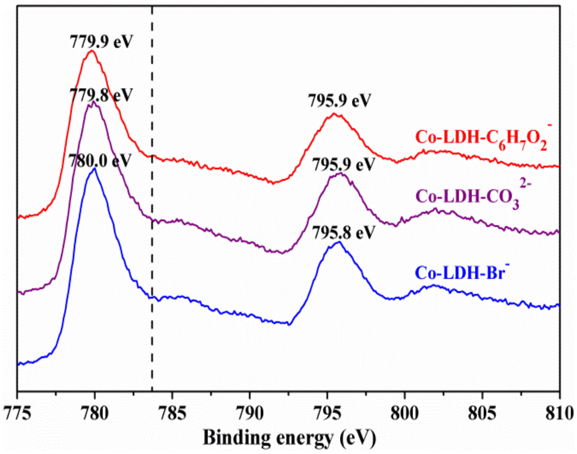

Figure 7.8. Co 2p XPS spectra of Co-LDHs with different interlayer anions.

Compared to α-$Co(OH)_2$, the higher water oxidation activity of β-$Co(OH)_2$ may further reveal the negative influence of electrostatic interactions of positively charged $\{CoO_6\}$ layers on water oxidation, because α-$Co(OH)_2$ is composed of positively charged $Co(OH)_{2-x}$ layers with interlayer anions. This was further confirmed by the decreased activities after transforming α-$Co(OH)_2$ and β-$Co(OH)_2$ to Co-LDHs-Br^- with highly charged $\{CoO_6\}$ layers.

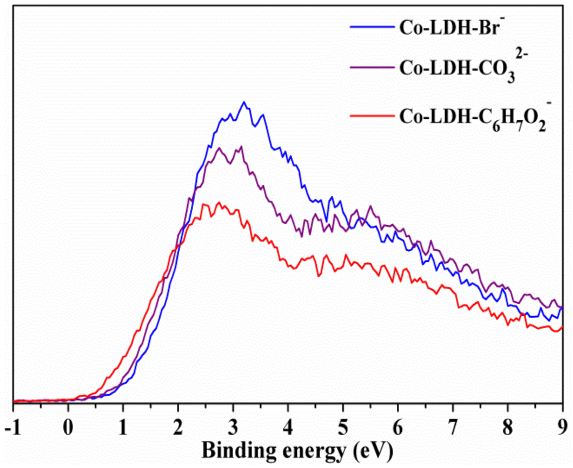

Figure 7.9. Valence band spectra of Co-LDHs with different interlayer anions.

Co-LDHs-$C_6H_7O_2^-$ with the highest water oxidation activity was further studied with respect to post-catalytic structural and morphological changes. As can be seen from TEM images (Figure 7.10), Co-LDHs-$C_6H_7O_2^-$ underwent obvious grain refinement and exfoliation after water oxidation. While fresh Co-LDHs-$C_6H_7O_2^-$ (Figure 7.10a) displays a relatively large particle size and intact morphology, post-catalytic Co-LDHs-$C_6H_7O_2^-$ broke up and most likely afforded a certain amount of exfoliated nanosheets. This can be further verified by their respective electron diffraction patterns. The well separated reflections in Figure 7.10b arise from few well-aligned nanoplates. In contrast, the diffraction pattern of post Co-LDHs-$C_6H_7O_2^-$ is composed of both sharp reflections and diffuse rings, thus suggesting a mixture of several large nanoplates with numerous randomly distributed small nanosheets. The disappearance of the characteristic peaks in the PXRD pattern after water oxidation also supports the exfoliation of Co-LDHs-$C_6H_7O_2^-$ nanoplates into thinner nanosheets.

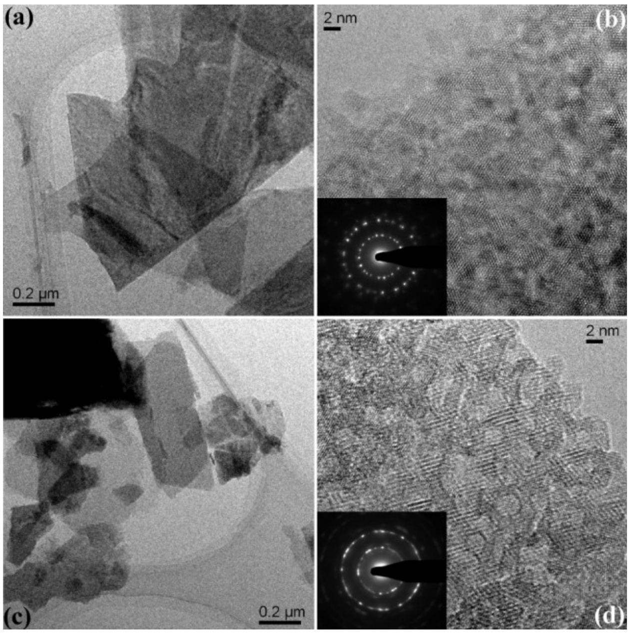

Figure 7.10. TEM picture and SAED pattern of Co-LDHs-$C_6H_7O_2^-$ before (a, b) and after water oxidation (c, d).

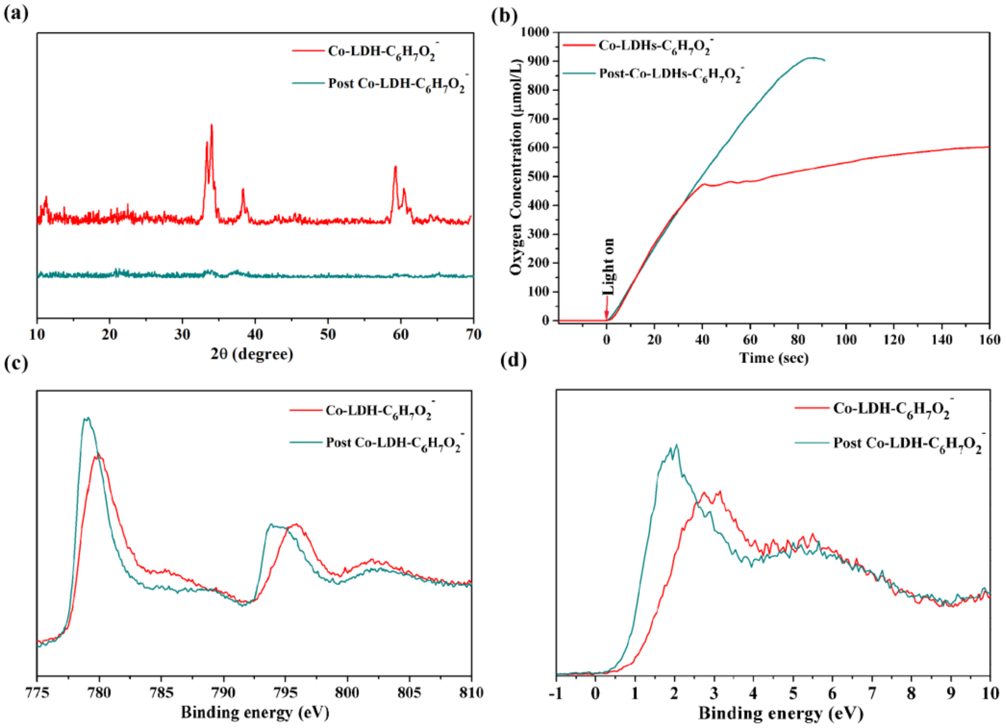

Figure 7.11. (a) Photochemical water oxidation, (b) PXRD patterns, (c) Co 2p XPS spectra and (d) valence band spectra of Co-LDHs-$C_6H_7O_2^-$ before and after water oxidation.

The photochemical water oxidation activity of post Co-LDHs-$C_6H_7O_2^-$ was further examined, as shown in Figure 7.11a. In contrast to other Co-based WOCs such as Co_3O_4 and $LiCoO_2$ which lose some of their activity in the second cycle, post-catalytic Co-LDHs-$C_6H_7O_2^-$ display an even higher water oxidation compared to fresh Co-LDHs-$C_6H_7O_2^-$. Two factors may contribute to the enhanced activity: both the increased surface area and the favorable electronic properties after exfoliation. The further shift of the valence band to lower binding energy (Figure 7.11c) implies a stronger metallic character of exfoliated nanosheets which may facilitate the charge transfer process of water oxidation. Based on the trend of the valence band shift observed for $C_6H_7O_2^-$ guest anions, their intercalation may exert a similar effect as layer exfoliation in the electronic properties tuning of Co-LDHs. In contrast to the constant cobalt valence states in all of the Co-LDHs, the exfoliated Co-LDHs nanosheets underwent an obvious cobalt reduction to maintain the charge neutrality, as it is evident from the shift of Co 2p to lower binding energy.

7.4 Conclusions

The intercalation of different anions intercalated into brucite-related β-$Co(OH)_2$ and double layer α-$Co(OH)_2$ parent cobalt hydroxides was studied with respect to the influence of this structural tuning approach on photochemical water oxidation. The main effect of the interlayer anions is a widening of the $\{CoO_6\}$ interlayer distance which can consequently tune the electronic properties of the $\{CoO_6\}$ layers. While intercatalated Co-LDHs hosting small anions such as Br^- and CO_3^{2-} display a strong electrostatic interaction between the layers which lowers the valence band position, the introduction of the larger $C_6H_7O_2^-$ anion into the interlayer space weakens the interaction and shifts the valence band up. Larger guest anions such as $C_6H_7O_2^-$ exert a similar effect as exfoliation strategies, namely by enhancing the metallic intralayer character of the $\{MO_6\}$ sheets. In line with our preceding studies, this facilitates the charge transfer process of water oxidation, leading to improved water oxidation activities compared to Co-LDHs with stronger interlayer electrostatic interactions.

References

[1] Y. Yamada, K. Kentaro, D. Hong, S. Fukuzumi. *Phys. Chem. Chem. Phys.* **2012**, *14*, 5753-5760

[2] J. Suntivich K. May, H. A. Gasteiger, J. B. Goodenough, Y. Shao-Horn. *Science* **2011**, *334*, 1383-1385.

[3] A. Grimaud, K. J. May, C. E. Carlton, Y.-L. Lee, M. Risch, W. T. Hong, J. Zhou, Y. Shao-Horn. *Nat. Commun.* **2013**, *4*, 2439.

[4] J. Rossmeisl, Z. W. Qu, H. Zhu, G. J. Kroes, J. K. Norskov. *J. Electroanal. Chem.* **2007**, *607*, 83-89.

[5] Q.Wang, D. O'Hare. *Chem. Rev.* **2012**, *112*, 4124-4155.

[6] K.-H. Goh, T.-T. Lim, Z. Dong. *Water Res.* **2008**, *42*, 1343-1368.

[7] C. L. Farrow, D. K. Bediako, Y. Surendranath, D. G. Nocera, S. J. L. Billinge *J. Am. Chem. Soc.* **2013**, *135*, 6403-6406.

[8] J. B. Gerken, J. G. McAlpin, J. Y. C. Chen, M. L. Rigsby, W. H. Casey, R. D. Britt, S. S. Stahl *J. Am. Chem. Soc.* **2011**, *133*, 14431-14442.

[9] F. Song, X. Hu *Nat. Commun.* **2014**, *5*, 4477.

[10] F. Song, X. Hu *J. Am. Chem. Soc.* **2014**, *136*, 16481-16484.

[11] R. Valdez, D. B. Grotjahn, D. K. Smith, J. M. Quintana, A. Olivas *Int. J. Electrochem. Sci*. **2015**, *10*, 909-918.

[12] Y. Zhang, B. Cui, C. Zhao, H. Lin, J. Li *Phys. Chem. Chem. Phys.* **2013**, *15*, 7363-7369.

[13] B. M. Hunter, J. D. Blakemore, M. Deimund, H. B. Gray, J. R. Winkler, M. Müller. *J. Am. Chem. Soc.* **2014**, *136*, 13118-13121.

[14] Z.-A. Hu, Y.-L. Xie, Y.-X. Wang, L.-J. Xie, G.-R. Fu, X.-Q. Jin, Z.-Y. Zhang, Y.-Y. Yang, H.-Y. Wu *J. Phys. Chem. C* **2009**, *113*, 12502-12508.

[15] R. Rojas, F. Bruna, C. P. de Pauli, M. Á. Ulibarri, C. E. Giacomelli *J. Colloid Interface Sci.* **2011**, *359*, 136-141.

[16] V. R. L. Constantino, T. J. Pinnavaia, *Inorg. Chem.* **1995**, *34*, 883-892.

[17] R. Ma, K. Takada, K. Fukuda, N. Iyi, Y. Bando, T. Sasaki, *Angew. Chem. Int. Ed.* **2008**, *47,* 86-89.

[18] H. Cui, Y. Zhao, W. Ren, M. Wang, Y. Liu, *J. Alloys. Compd.* **2013**, *562*, 33-37.

[19] Z. Liu, R. Ma, M. Osada, K. Takada, T. Sasaki *J. Am. Chem. Soc.* **2005**, *127*, 13869-13874.

[20] M. C. Biesinger, B. P. Payne, A. P. Grosvenor, L. W. M. Lau, A. R. Gerson, R. St. C. Smart, *Appl. Surf. Sci.* **2011**, *257*, 2717-2730.

[21] M. A. Lukowski, A. S. Daniel, F. Meng, A. Forticaux, L. Li, S. Jin. *J. Am. Chem. Soc.* **2013**, *135*, 10274-10277.

[22] G. Ozin, K. Liao, V. Hoepfner, B. Mahler. *J. Am. Chem. Soc.* **2014**, *136*, 14121-14127.

[23] H. Liu, Y. Zhou, R. Moré, R. Müller, T. Fox, G. R. Patzke. *ACS Catal.* **2015**, *5*, 3791-3800.

[24] H. Liu, G. R. Patzke. *Chem. Asian J.* **2014**, *9*, 2249-2259.

Appendix

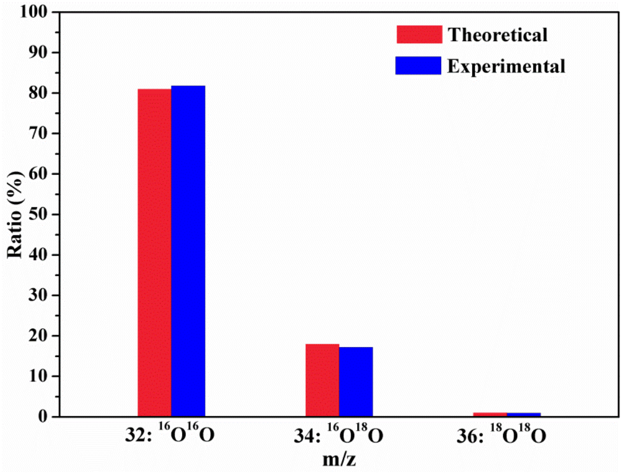

Figure S7.1. Comparison of expected and experimental $^{16}O^{16}O$, $^{16}O^{18}O$ and $^{18}O^{18}O$ ratios after water oxidation with Co-LDHs-$C_6H_7O_2^-$ in 10 % ^{18}O containing H_2O.

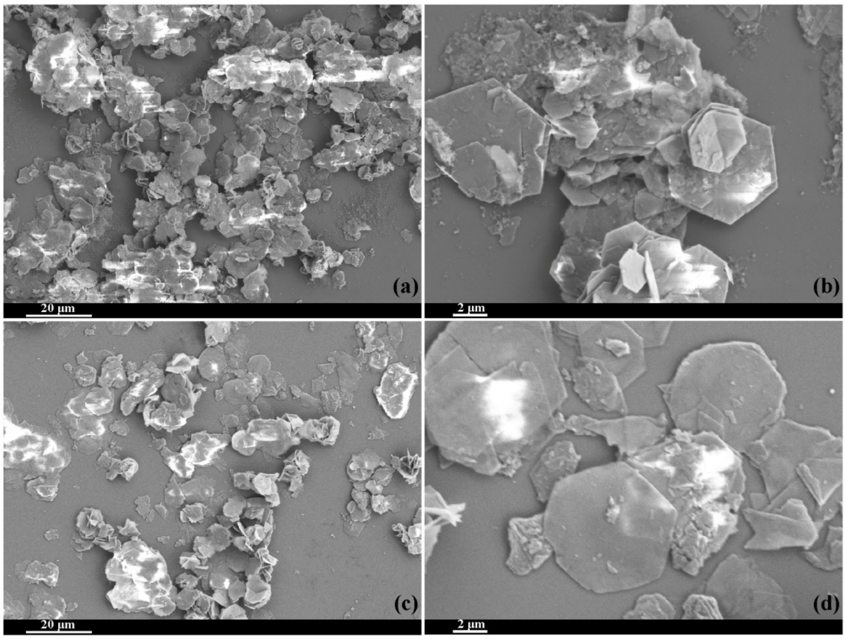

Figure S7.2. SEM pictures of α-$Co(OH)_2$ ((a), (b)) and β-$Co(OH)_2$ ((c), (d)).

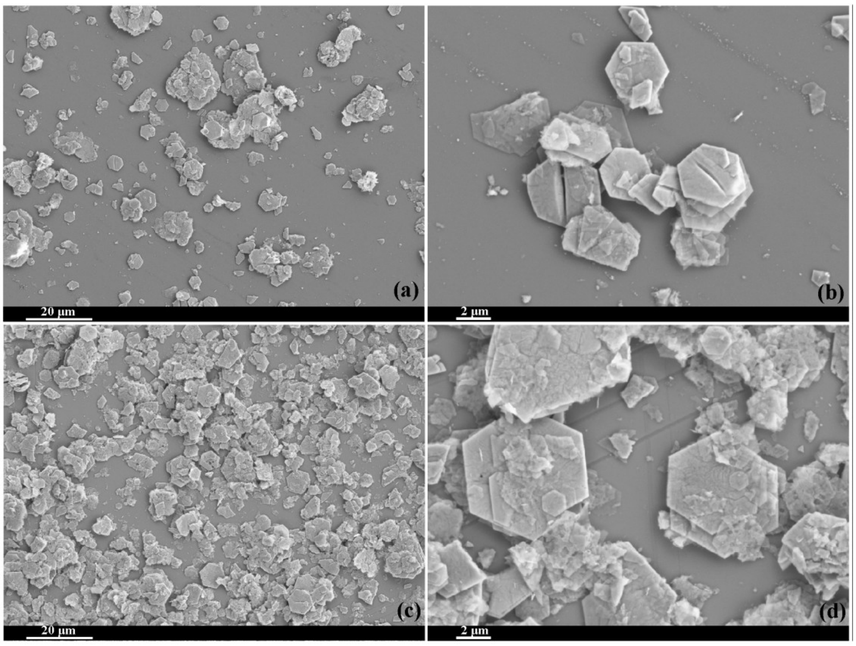

Figure S7.3. SEM pictures of Co-LDHs-Br^- derived from α-$Co(OH)_2$ ((a), (b)) and β-$Co(OH)_2$ ((c), (d)) respectively.

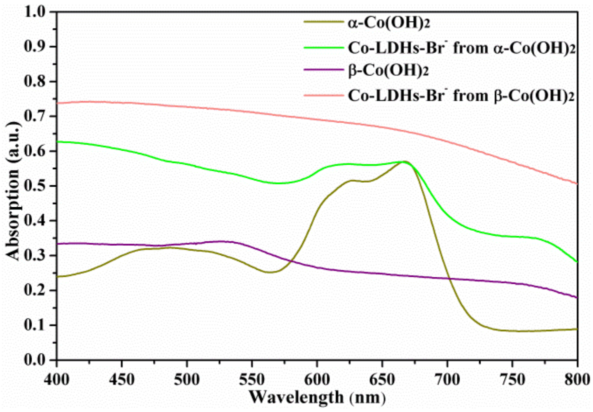

Figure S7.4. UV/Vis spectra of α-$Co(OH)_2$, β-$Co(OH)_2$ and their derived Co-LDHs-Br^-.

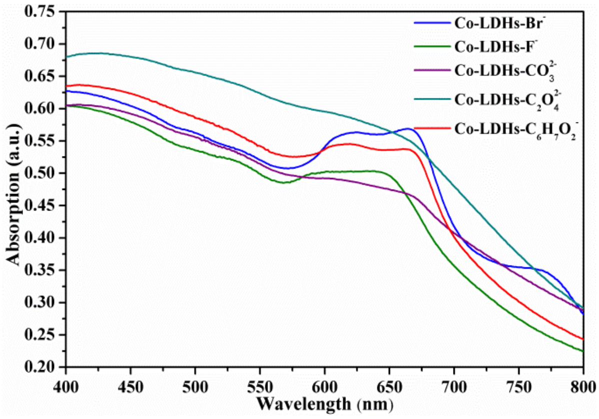

Figure S7.5. UV/Vis spectra of Co-LDHs with different interlayer anions.

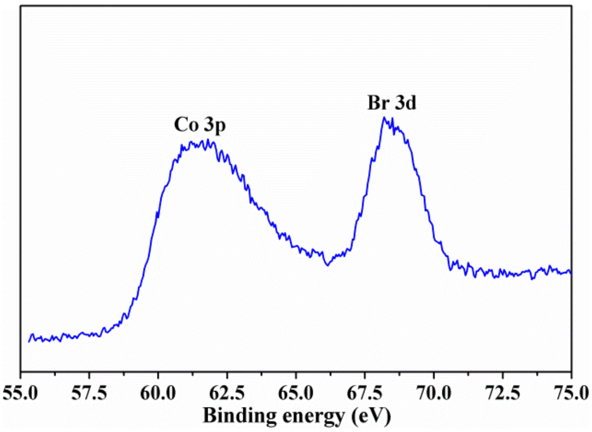

Figure S7.6. Br 3d spectrum of Co-LDHs-Br^- derived from α-$Co(OH)_2$.

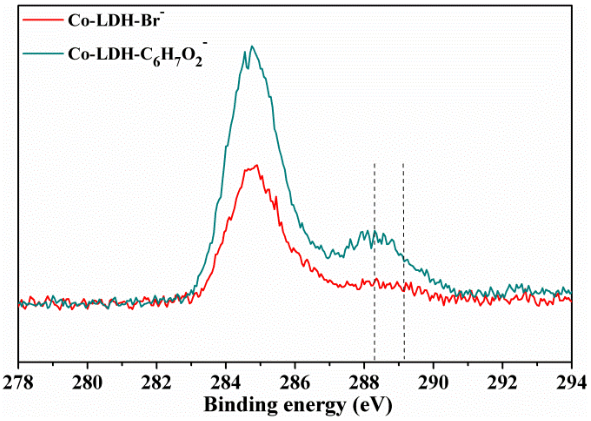

Figure S7.7. C 1s spectra of Co-LDHs-Br^- and Co-LDHs-$C_6H_7O_2^-$.

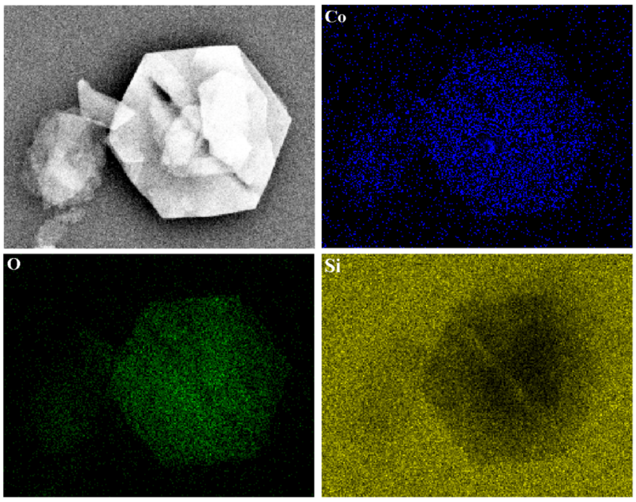

Figure S7.8. EDXS mapping of Co-LDHs-Br^- (No Br was detected due to its low content).

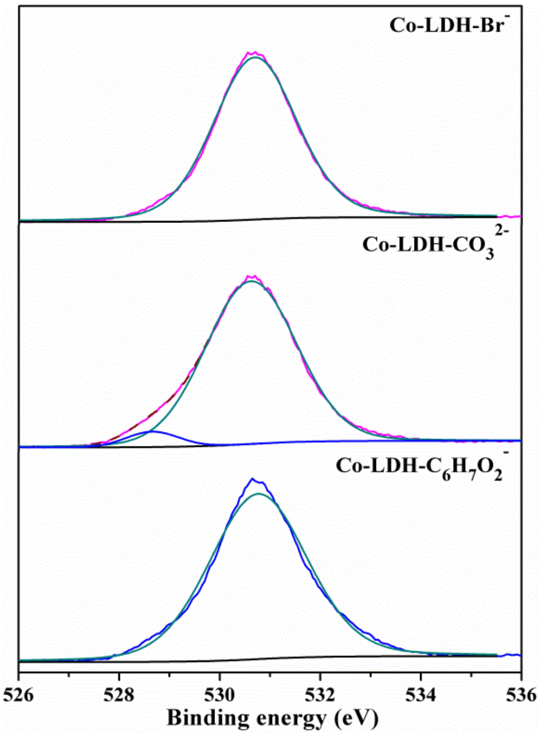

Figure S7.9. O$_{1s}$ spectra of Co-LDHs-Br$^-$, Co-LDHs-CO$_3^{2-}$ and Co-LDHs-C$_6$H$_7$O$_2^-$.

8. Cobalt Chloride as Homogeneous Catalysts for Photochemical Water Oxidation in Acidic Media

8.1 Introduction

Co-WOCs are currently under the focus of water oxidation research due to their competitive performance to noble metal based catalysts, and a wide range of molecular and (nano)crystalline heterogeneous compounds have been reported over the past years.[1-6] In 2008, the introduction of self-healing amorphous CoPi-catalysts via electrodeposition of Co^{2+} in a pH 7 phosphate buffer[7] has awakened broad interest in amorphous Co, Mn, Fe and Ni oxides for both electrochemical[8-17] and photochemical[18-20] water oxidation. In parallel, forefront investigations at the interface between homo- and heterogeneous WOCs indicated that molecular catalysts frequently act as precatalysts, giving rise to oxide precipitation as the true catalysts.[21-27]

Cobalt ions are a central species in this interplay of water oxidation catalysis types, as outlined by the following inspirational trends. (1) The self-repair mechanisms of CoPi were found to depend on the re-deposition of dissolved cobalt ions under electrochemical water oxidation conditions.[28,29] (2) Several molecular Co-WOCs are drawing intense debate concerning their differentiation from active CoO_x catalysts which were formed from leached cobalt ions from molecular catalysts.[30-35] (3) Soluble cobalt salts, such as $Co(NO_3)_2$ have long been used as active standards for newly designed WOCs, whose activities they frequently surpass.[26,32,36-38]

This role of cobalt ions as a key player in homo- and heterogeneous catalyst transformations stands in sharp contrast to the actual mechanistic insight into the Co^{2+} pathways of soluble cobalt salts WOCs. While a few earlier studies proposed Co^{2+} as homogeneous catalysts in neutral media,[39,40] most recent investigations indicates that Co^{2+} is merely precatalysts which form CoO_x, $Co(OH)_2$ or CoPi catalysts in situ under photo- or electrochemical conditions.[41,42] Interestingly, a recent study indicated that Co^{2+} ions may act as homogenous catalysts during electrochemical water oxidation in acidic conditions.[43]

In the following, we explore the options of homogeneous water oxidation with cobalt chloride in acidic conditions (HCl, pH 3) to avoid precipitation. Moreover, the notable influence of buffer/solution media (citrate, glycine, hydrochloric acid) and counter anions (Cl^-, NO_3^-, Br^-, ClO_4^- and SO_4^{2-}) on water oxidation performance was revealed.

8.2 Experimental

8.2.1 Photocatalytic water oxidation tests

Water oxidation tests were performed according to a well established $[Ru(bpy)_3]^{2+}/S_2O_8^{2-}$ protocol. First, a solution was prepared by mixing water oxidation catalyst, $[Ru(bpy)_3]Cl_2$ photosensitizer and NaS_2O_8 in 8 mL buffers (0.1 M, pH 3, 10 mL vial), HCl or HNO_3 solution (pH 3) in dark. Next, the solution was degassed with helium to remove O_2 in both liquid and the head vial. A LED lamp with 470 nm wavelength and 5000 Lux output was used as visible light source. Oxygen produced in solution and head vial was monitored with a calibrated Clarke electrode (Unisense) online and gas chromatography respectively (Agilent 7820A packed with a 3 m × 2 mm molecular sieve 13X 80-100 column) as follows: 100 μL samples of gas from the head vial were injected into a gas chromatograph using a gastight microliter syringe (Hamilton 1825 RN). Helium was chosen as carrier gas to increase the detection sensitivity of O_2 relative to N_2. Gases were detected with a thermal conductivity detector (Varian) operated at 200 °C. Contamination of the headspace by oxygen from environment was subtracted according to the N_2 peak area.

8.2.2 Electrochemical water oxidation tests

An electrochemical cell equipped with Ag/AgCl reference electrode, Pt wire as counter electrode and a FTO glass with round working window of 18 mm in diameter as working electrode. The electrochemical study was performed on a ZAHNER Zennium electrochemical workstation. The sweep rate was set to 0.1 V/s. The cycling was performed with a regular degas of the solution to remove the produced H_2 and O_2. Additionally, the pH was adjusted to 3 at certain interval to avoid the influence of HCl gas evaporation and formation of some less active oxides on the FTO glass.

8.2.3 Analytical techniques

Composition analysis of the FTO electrode after water oxidation were examined on a scanning electron microscopy (LEO 1530 (FEG)) equipped with an EDXS detector. UV/Vis spectra were recorded on a Lambda 650 S Perkin Elmer UV-visible spectrometer. ^{1}H-NMR spectra were recorded on Bruker DRX-500 spectrometer with a 300 MHz frequency. Dynamic light scattering measurements were conducted on a Malvern Zetasizer Nano ZS90 instrument.

8.3 Results and discussion

8.3.1 $CoCl_2$ for photochemical water oxidation

Photochemical water oxidation activity was evaluated according to a standard protocol using $[Ru(bpy)_3]^{2+}$ as photosensitizer and $S_2O_8^{2-}$ as electron acceptor. Oxygen evolution was monitored online by Clark electrode in solution and quantified by gas chromatography (GC) in headspace. Control experiments with either $CoCl_2$, $Na_2S_2O_8$, photosensitizer or combinations thereof demonstrate that oxygen evolution requires the presence of all three components (Figure S8.1), confirming the essential catalytic role of $CoCl_2$.

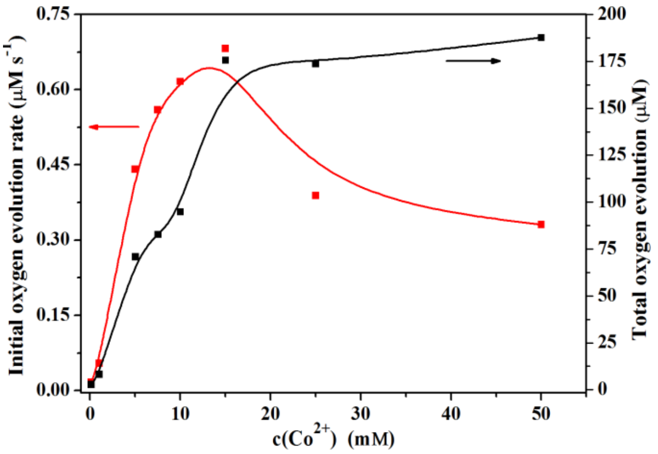

Figure 8.1. Initial oxygen evolution rate with $CoCl_2$ under photochemical water oxidation (10.5 mM $Na_2S_2O_8$; 0.83 mM $[Ru(bpy)_3]Cl_2$; oxygen evolution was online monitored by Clark electrode in solution; visual guidelines have been added).

H_2O was verified as oxygen source with ^{18}O labeling experiments (Figures S8.2-S8.3). The exact superposition of the ^1H-NMR of the solution before and after water oxidation (Figure S8.4) points to a constant concentration of Co^{2+} during water oxidation, i.e. the absence of Co-related precipitates (Co^{2+} concentration can change the peak width of NMR spectra due to its paramagnetism[42b]). Homogeneous water oxidation is further corroborated by the absence of any peaks arising from insoluble particles in dynamic light scattering (DLS) measurements (Figure S8.5). Additionally, the solution remained transparent after water oxidation (Figure S8.6a) without further visual changes even after a storage period of 5 months (Figure S8.6b). Thermodynamical instablity[44] of CoO_x supports our observation here. Formation of secondary molecular cobalt related WOCs through complex formation with 2,2’-bipyridine ligands dissociated from $[Ru(bpy)_3]^{2+}$ (cf. reference spectra in Figure

S8.8) was excluded due to negligible oxygen evolution upon adding 2,2'-bipyridine to the standard reaction protocol (Figure S8.9).

The influence of cobalt concentration on photochemical water oxidation was investigated from the range of 0.1~50 mM (Figure 8.1 and S8.10). In contrast to previous study which revealed high activities for 2 μM Co^{2+} in basic conditions,[38c] no significant activity was observed here when Co^{2+} concentration is below 1 mM. This difference is probably ascribed two different water oxidation pathways and heterogeneous CoO_x must play as major catalyst in basic conditions. While the total oxygen evolution amount keeps increasing with cobalt concentration, the initial oxygen evolution rate reaches a maximum at around 15 mM Co^{2+}.

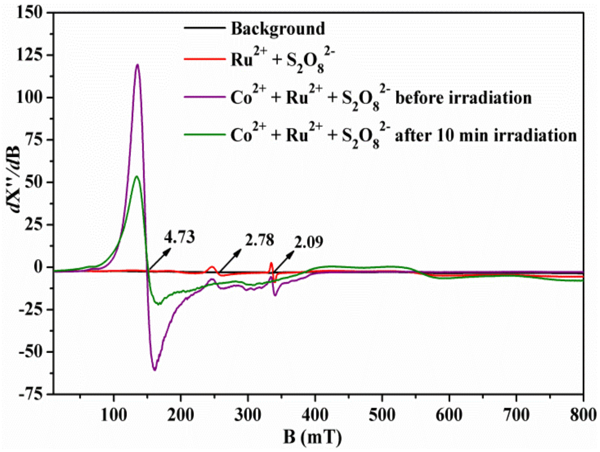

Figure 8.2. EPR spectra (10 K) of $[Ru(bpy)_3]Cl_2$ (10 mM), $Na_2S_2O_8$ (50 mM) and $CoCl_2$(0.83 mM) mixtures (solvent: CH_3CN and pH 3 HCl in 2:1 volume ratio; the solution after 10 min irradiation was frozen in liquid N_2 within less than 5 seconds).

Formation of secondary molecular cobalt related WOCs through complex formation with 2, 2'-dipyridyl ligands dissociated from $[Ru(bpy)_3]^{2+}$ (cf. reference spectra in Figure S8.9) was excluded as negligible oxygen has evolved upon adding 2,2'-dipyridyl to the standard reaction protocol (Figure S8.10).

Electron paramagnetic resonance (EPR) measurements were conducted to investigate the intermediate species during water oxidation (Figure 8.2). A mixed solvent (CH_3CN and pH 3 HCl in 2:1 volume ratio) was used in order to protect the quartz capillary sample holders from freezing damage. Oxygen evolution in this mixed solvent system was confirmed in reference experiments (Figure S8.12). Background measurements with $[Ru(bpy)_3]^{2+}/Na_2S_2O_8$ mixtures displayed two low intensity bands of the $[Ru(bpy)_3]^{3+}$ and $SO_4^{\cdot -}$ radicals at g=2.78 and g=2.09, respectively. Small amounts of $[Ru(bpy)_3]^{3+}$ are formed from auto-oxidation of $[Ru(bpy)_3]^{2+}$ in the presence of $Na_2S_2O_8$ and natural light. Addition of $CoCl_2$ gave rise to a strong absorption band of paramagnetic Co^{2+} with the most intense peak at g = 4.73 and a shoulder extend to g ~ 2.00. Similar spectra were reported for $Co(NO_3)_2$ which can be assigned to high spin Co^{2+}.[12] However, a notable intensity decrease by approx. 50% was observed after 10 min of irradiation at 460 nm, most probably due to the partial oxidation of Co^{2+} to EPR silent Co^{3+} species. This was accompanied by the disappearance of the $[Ru(bpy)_3]^{3+}$ and SO_4^{-} radical bands in the course of the water oxidation. In contrast to recent reports on molecular Co-WOCs,[45] the suggested Co^{4+} intermediate species with a characteristic resonance at g~2.00,[12] probably implying a different water oxidation mechanism in acidic conditions. Spontaneous release of oxygen observed for specific Co^{3+} complexes, such as $[Co(H_2O)_6]^{3+}$, furthermore indicates that Co^{4+} species are not indispensable for oxygen evolution, especially in acidic conditions.[46]

8.3.2 Buffer media on water oxidation performance

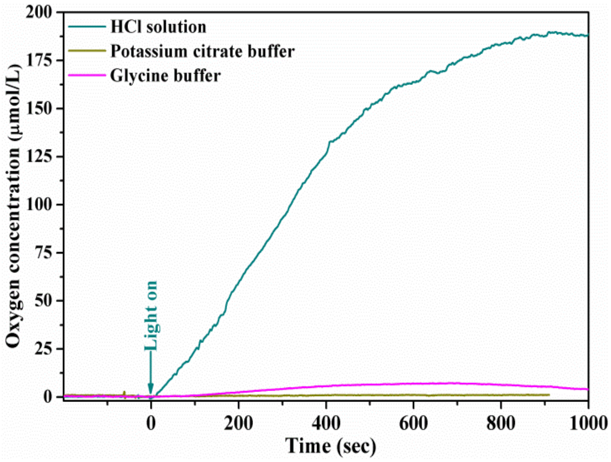

Figure 8.3. Photochemical water oxidation with Co^{2+} in buffered vs. non-buffered conditions (52.6 mM $CoCl_2$, 10.5 mM $Na_2S_2O_8$, 0.83 mM $[Ru(bpy)_3]Cl_2$, 0.1 M pH 3 buffer medium or pH 3 HCl).

Furthermore, the influence of different buffer media on the water oxidation activity of $CoCl_2$ at pH 3 was investigated in detail. The general advantages of buffers in water oxidation systems include the prevention of sharp pH decrease and the facilitation of proton coupled electron transfer processes.[47,48] However, the highest oxygen evolution with $CoCl_2$ WOCs was observed in non-buffered HCl solution, while glycine and potassium citrate buffers had a detrimental effect on the overall activity (Figure 8.3). This trend indicates that the coordination of buffer ions to the Co^{2+} centers significantly influences water oxidation performance. Further information was obtained by density functional theory calculations. Coordination of citrate (Figures S8.35-S8.36) and glycine (Figure S8.37) buffer molecules to $[Co(H_2O)_6]^{2+}$ complexes was investigated in more detail and allowed to identify a range of possible isomers as well as energetically preferred coordination modes. The computed reaction free energies also support a strong binding of the tridentate citrate molecule to the Co^{2+} ion.

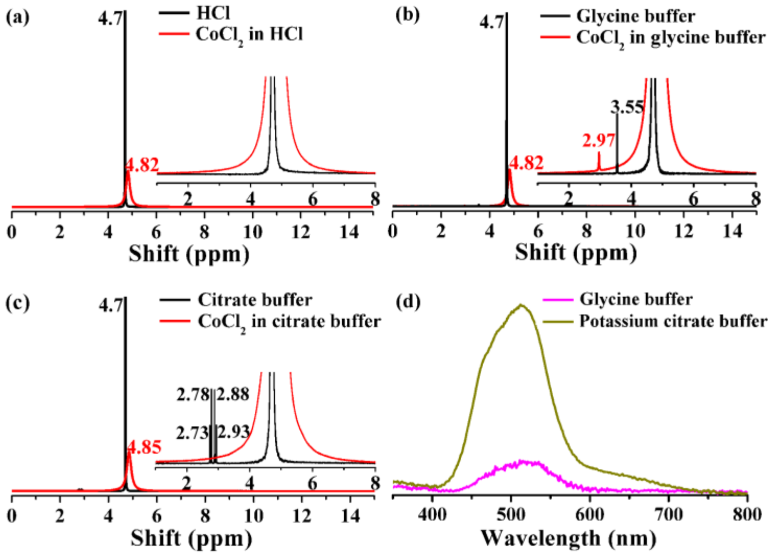

Figure 8.4. ^{1}H-NMR and UV/Vis absorption spectra in buffered or non-buffered conditions. (168.1 mM $CoCl_2$, 0.01 M buffer, solvent: $H_2O/D_2O = 1/9$).

UV/Vis and ^{1}H-NMR spectroscopic characterizations of Co^{2+} species in different buffer media (further verified this hypothesis) point into the same direction (Figure 8.4). The absorption intensity of Co^{2+} at 450 - 550 nm decreased in the following order: potassium citrate buffer > glycine buffer > HCl solution (Figure S8.17, the absorption difference related to HCl solution is shown in Figure 4d). This corresponds well with the water oxidation activity trends: peak performance at pH 3 (HCl), followed by a weak but detectable oxygen evolution in glycine buffer and inactivity in potassium citrate buffer. Comparison of the respective H signals around 4.7 ppm and of the buffer-related peaks in the ^{1}H-NMR spectra illustrates these different complexing properties in a more straightforward manner (Figures 8.4a-c). The presence of paramagnetic Co^{2+} leads to a line broadening and shift to 4.82 ppm for HCl and glycine media, while the stronger coordination of citrate anions to the cobalt centers increases the peak shift to 4.85 ppm. Concerning the buffer peaks, the characteristic signal of glycine at 3.55 ppm is shifted to 2.97 ppm with a notably lower intensity that indicates weaker and non-quantitative coordination to Co^{2+} (Figure 8.4b). Accordingly, the water oxidation activity of $CoCl_2$ is slightly improved in dilute glycine media (Figure S8.18). The stronger and more efficient complexation of the Co^{2+} centers by the citrate buffer is evident from the disappearance of the four peaks corresponding to citrate (2.73, 2.78, 2.88 and 2.93 ppm; Figure 8.4c). These results further underscore the detrimental effect of buffer coordination to Co^{2+} on the oxygen evolution performance.

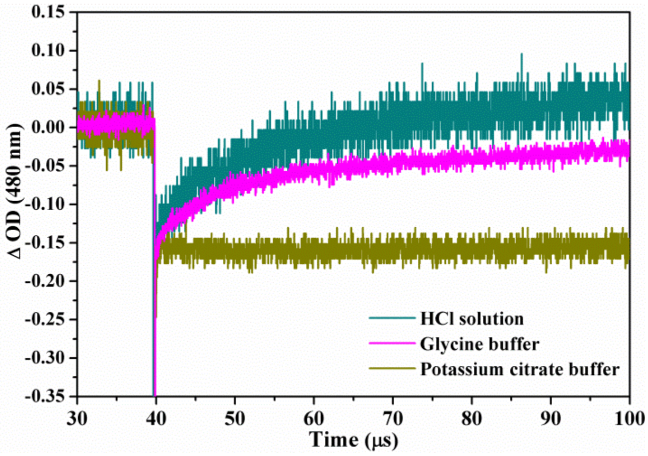

Figure 8.5. Transient absorption of $[Ru(bpy)_3]^{2+}$ at 480 nm after irradiation with a 355 nm laser (10.5 M $CoCl_2$, 2.1 mM $Na_2S_2O_8$, 0.17 mM $[Ru(bpy)_3]Cl_2$, absorption intensities were normalized for comparison).

Electron transfer processes as another crucial parameter for water oxidation efficiency were investigated by laser flash photolysis. Generally, deactivation of the excited $[Ru(bpy)_3]^{2+*}$ photosensitizer follows two main pathways, namely either relaxation to $[Ru(bpy)_3]^{2+}$ via fluorescence or persulfate quenching to $[Ru(bpy)_3]^{3+}$ and subsequent regeneration to $[Ru(bpy)_3]^{2+}$ by hole transfer to the WOC. As the fluorescence lifetime of $[Ru(bpy)_3]^{2+*}$ is in the 200~300 nanosecond range (Figure S8.19), the absorption bleaching of $[Ru(bpy)_3]^{2+}$ after irradiation on the microsecond scale arises from the formation of $[Ru(bpy)_3]^{3+}$. The faster the recovery of the $[Ru(bpy)_3]^{2+}$ absorption, the more efficient the hole injection from $[Ru(bpy)_3]^{3+}$ to WOC. Flash photolysis measurements in citrate buffer display a strong absorption bleaching after irradiation at around 40 μs, followed by immediate recovery to a certain level through fluorescence within 279 ns (Figure S8.19). The absorption level remains constantly low without further increase up to 100 μs (Figure 8.5), thus indicating the absence of hole transfer between $[Ru(bpy)_3]^{3+}$ and WOCs. This agrees well with the observed water oxidation inactivity of Co^{2+} in potassium citrate buffer. In contrast, the absorption bleaching of $[Ru(bpy)_3]^{2+}$ in both glycine buffer and HCl solution displays gradual recovery (Figure 8.5). The notably higher oxygen evolution observed in HCl solution exactly agrees with the faster absorption recovery within no more than 60 μs compared to glycine buffer. The analogous trends of UV/Vis, ^1H-NMR and hole injection rate for different solutions/buffers strongly suggest a significant influence of the coordination between Co^{2+} centers and buffer/solution compositions on catalytic performance.

8.3.3 Co^{2+} for electrochemical water oxidation

The electrochemical water oxidation activity of Co^{2+} centers in buffered (pH 3) and non-buffered conditions was furthermore compared to the photochemical results. The detrimental influence of buffer media on water oxidation is also evident from the electrochemical results (Figure 8.6). All in all, the electro- and photocatalytic activity trends clearly point in the same direction, thus implying a similar water oxidation mechanism.

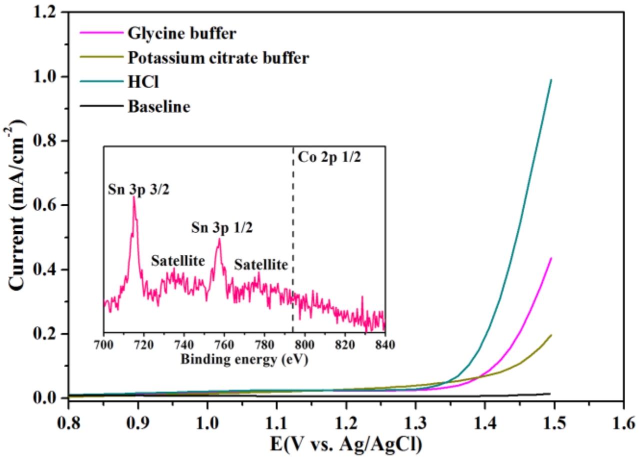

Figure 8.6. Electrochemical water oxidation in buffered vs. non-buffered conditions. (63.0 mM $CoCl_2$, 0.1 M buffer, pH 3. Inset shows the detection of cobalt on FTO electrode by XPS after electrochemcial water oxdiation).

The deposition of secondary heterogeneous Co-electrocatalysts on the electrode surface was excluded with several analytical methods. First, EDS spectra of the FTO electrodes after water oxidation with $CoCl_2$ (Figure S8.20) did not display any cobalt signals. Moreover, electrodes were rinsed with water after $CoCl_2$ assisted water oxidation and tested for water oxidation in freshly prepared HCl (pH 3) solution in the absence of $CoCl_2$. The rinsed FTO electrodes did not display different currents from blank reference FTO electrodes (Figure S8.21), indicating that no WOC active species were deposited on the surface. Moreover, ICP-AES analyses of the Co contents of FTO electrode samples before and after 50 water oxidation cycles afforded values below the detection limit of 0.1 μmol throughout. XPS as a more sensitive technique was used to detect the cobalt on the FTO electrode after water oxidation. As shown in the inset of Figure 8.6, no signal corresponding to Co $2p_{1/2}$ can be observed, indicating the absence of any cobalt precipitation.

In addition to the exploration of the effect of different buffer media, the influence of the counteranion on the water oxidation performance was investigated for $Co(NO_3)_2$ in HNO_3 (pH 3) with respect to photo- and electrochemical water oxidation. Interestingly, the presence of NO_3^- turned out to be detrimental for the photochemical performance of Co^{2+} cations (Figure S8.23). The same trend was observed in electrochemical investigations (Figure S8.24). Further investigation of $CoBr_2$, $Co(ClO_4)_2$ and $CoSO_4$ for photochemical water oxidation indicates $CoBr_2$ is comparably active as $CoCl_2$ while $Co(ClO_4)_2$ displays minor activity and $CoSO_4$ is completely inactive (Figure S8.25). These remarkably different activity trends highlight the complex behavior of this simple cobalt salts oxygen evolving system towards apparently minor parameter changes.

Reference experiments with $NiCl_2$, $MnCl_2$, and $FeCl_3$ for water oxidation were investigated as well (Figures S8.26–S8.31). All of these systems displayed considerably lower water oxidation activities under comparable conditions. $MnCl_2$ was entirely inactive and formed amorphous manganese oxide precipitates during photochemical (photographs: Figure S8.27, PXRD pattern: Figure S8.28) and electrochemical (photographs: Figure S8.32) water oxidation, while $NiCl_2$ and $FeCl_3$ solutions remained homogeneous.

How the counter anions (Cl^- and NO_3^-) and cations (Co^{2+}, Ni^{2+}, Fe^{2+} and Mn^{2+}) influence the water oxidation activity is not very clear. Concerning $CoCl_2$ in pH 3 HCl, Co^{2+} was reported to exist in the form of $Co[(H_2O)_5Cl]^+$.49 This coordination effect may exert certain influence on water oxidation process. A recent study even indicates Cl^- can be more easily oxidized to chlorine after coordination with Ag^+ to form $[AgCl_2]^-$.50 We tried to confirm this possibility for Co^{2+} as well in present study by GC-MS. However, no chlorine was detected. A further mechanism study to clarify the influence of counter cations and anions on water oxidation is underway.

The observed strongly buffer-dependent performance indicates that the role of the buffer includes far more effects than just stabilizing the pH level or facilitating PCET. Adverse buffer effects such as slower electron transfer rates and, most importantly, blocking of active catalyst sites, may even outweigh their benefits.[51] This was recently demonstrated for the notable influence of the electrolyte on heterogeneous electrocatalysts, such as the CoPi OEC.[8,43] The self-healing mechanisms of these WOCs probably imply a partial contribution of homogeneous water oxidation processes mediated by the release of Co^{2+} cations into solution.

8.4 Conclusions

In summary, we have newly investigated simple cobalt salts for water oxidation in a particular parameter window (pH 3) that can prevent the formation of CoO_x. However, this exploration of homogeneous water oxidation with cobalt salts under acidic conditions came at the cost of rather moderate activity. Noteworthy, the presence of different buffer systems dramatically reduced both photo- and electrochemical oxygen evolution. This sheds new light on the crucial role of the buffer media in water oxidation which goes far beyond a proton reservoir. Along this line, the significant influence of counter anions on water oxidation was also revealed. An attempt was made to elucidate intermediates during photochemical water oxidation with $CoCl_2$ by EPR monitoring. At the present stage, no indications of Co(IV) were found. A further investigation on the reaction pathways and role of counteranions during water oxidation is in progress.

Reference

[1] H. Liu, G. R. Patzke. *Chem. Asian J.* **2014**, *9*, 2249-2259.

[2] J. D. Pilar-Albaladejo, P. K. Dutta. *ACS Catal.* **2014**, *4*, 9-15.

[3] H. S. Ahn, J. Yano, T. D. Tilly, *ACS Catal.* **2015**, *5*, 2573-2576.

[4] D. J. Wasylenko, R. D. Palmer, C. P. Berlinguette. *Chem. Commun.* **2013**, *49*, 218-227.

[5] M. Chen, S.-M. Ng, S.-M. Yiu, K.-C. Lau, R. J. Zeng, T.-C. Lau. *Chem. Commun.* **2014**, *50*, 14956-14959.

[6] P. F. Smith, C. Kaplan, J. E. Sheats, D. M. Robinson, N. S. MaCool, N. Mezle, G. C. Dismukes. *Inorg. Chem.* **2014**, *53*, 2113-2121.

[7] M. W. Kanan, D. G. Nocera. *Science* **2008**, *321*, 1072-1075.

[8] Y. Surendranath, M. Dincă, D. G. Nocera. *J. Am. Chem. Soc.* **2009**, *131*, 2615-2620.

[9] J. B. Gerken, J. G. McAlpin, J. Y. C. Chen, M. L. Rigsby, W. H. Casey, R. D. Britt, S. S. Stahl. *J. Am. Chem. Soc.* **2011**, *133*, 14431-14442.

[10] D. K. Bediako, B. Lassalle-Kaiser, Y. Surendranath, J. Yanl, V. K. Yachandra, D. G. Nocera. *J. Am. Chem. Soc.* **2012**, *134*, 6801-6809.

[11] M. Risch, V. Khare, I. Zaharieva, P. Chernev, H. Dau. *J. Am. Chem. Soc.* **2009**, *131*, 6936-6937.

[12] J. G. McAlpin, Y. Surendranath, M. Dincă, T. A. Stich, S. A. Stoian, W. H. Casey, D. G. Nocera, R. D. Britt. *J. Am. Chem. Soc.* **2010**, *132*, 6882-6883.

[13] S. Hu, M. R. Shaner, J. A. Beardslee, M. Lichterman, B. S. Brunschwig, N. S. Lewis. *Science* **2014**, *344*, 1005-1009.

[14] R. D. L. Smith, M. S. Prévot, R. D. Fagan, Z. Zhang, P. A. Sedach, M. K. J. Siu, S. Trudel, C. P. Berlinguette. *Science* **2013**, *340*, 60-63.

[15] M. W. Kanan, J. Yano, Y. Surendranath, M. Dincă, V. K. Yachandra, D. G. Nocera. *J. Am. Chem. Soc.* **2010**, *132*, 13692-13701.

[16] A. Indra, P. W. Menezes, I. Zaharieva, E. Baktash, J. Pfrommer, M. Schwarze, H. Dau, M. Driess. *Angew. Chem. Int. Ed.* **2013**, *52*, 13206-13210.

[17] L. Kuai, J. Geng, C. Chen, E. Kan, Y. Liu, Q. Wang, B. Geng. *Angew. Chem. Int. Ed.* **2014**, *53*, 7547-7551.

[18] A. Indra, P. W. Menezes, I. Zaharieva, E. Baktash, J. Pfrommer, M. Schwarze, H. Dau, M. Driess. *Angew. Chem. Int. Ed.* **2013**, *52*, 13206-13210.

[19] A. Iyer, J. Del-Pilar, C. K. King'ondu, E. Kissel, H. F. Garces, H. Huang, A. M. El-Sawy, P. K. Dutta, S. L. Suib. *J. Phys. Chem. C* **2012**, *116,* 6474-6483.

[20] A. Indra, P. W. Menezes, N. R. Sahraie, A. Bergmann, C. Das, M. Tallarida, D. Schmeiβer, P. Strasser, M. Driess. *J. Am. Chem. Soc.* **2014**, *136*, 17530-17536.

[21] M. M. Najafpour, A. N. Moghaddam, H. Dau, I. Zaharieva. *J. Am. Chem. Soc.* **2014**, *136*, 7245-7248.

[22] R. K. Hocking, R. Brimblecombe, L.-Y. Chang, A. Singh, M. H. Cheah, C. Glover, W.H. Casey, L. Spiccia. *Nat. Chem.* **2011**, *3*, 461-466.

[23] N. D. Schley, J. D. Blakemore, N. K. Subbaiyan, C. D. Incarvito, F. D'Souza, R. H. Crabtree, G. W. Brudvig. *J. Am. Chem. Soc.* **2011**, *133*, 10473-10481.

[24] G. Chen, L. Chen, S.-M. Ng, W.-L. Man, T.-C. Lau. *Angew. Chem. Int. Ed.* **2013**, *52*, 1-4.

[25] S. Fu, Y. Liu, Y. Ding, X. Du, F. Song, R. Xiang, B. Ma. *Chem. Commun.* **2014**, *50*, 2167-2169.

[26] D. Hong, J. Jung, J. Park, Y. Yamada, T. Suenobu, Y. -M. Lee, W. Nam, S. Fukuzumi. Energy Environ. Sci. **2012**, *5*, 7606-7616.

[27] G. Chen, L. Chen, S. -M. Ng, T. -C. Lau. *ChemSusChem*, **2014**, *7*, 127-134.

[28] D. A. Lutterman, Y. Surendranath, D. G. Nocera. *J. Am. Chem. Soc.* **2009**, *131*, 3838-3839.

[29] Y. Surendranath, M. W. Kanan, D. G. Nocera. *J. Am. Chem. Soc.* **2010**, *132*, 16501-16509.

[30] J. J. Stracke, R. G. Finke. *J. Am. Chem. Soc.* **2011**, *133*, 14872-14875.

[31] M. Natali, S. Berardi, A. Sartorel, M. Bonchio, S. Campagna, F. Scandola. *Chem. Commun.* **2012**, *48*, 8808-8810.

[32] J. W. Vickers, H. Lv, J. M. Sumliner, G. Zhu, Z. Luo, D. G. Musaev, Y. V. Geletii, C. L. Hill. *J. Am. Chem. Soc.* **2013**, *135*, 14440-14118.

[33] R. Schiwon, K. Klingan, H. Dau, C. Limberg. *Chem. Commun.* **2014**, *50*, 100-102.

[34] J. J. Stracke, R. G. Finke. *ACS Catal.* **2014**, *4*, 909-933.

[35] J. J. Stracke, R. G. Finke. *ACS Catal.* **2014**, *4*, 79-89.

[36] H.-Y. Wang, E. M. S. Ott, A. Thapper. *Angew. Chem. Int. Ed.* **2014**, *53*, 1-5.

[37] F. Song, Y. Ding, B. Ma, C. Wang, Q. Wang, X. Du, S. Fu, J. Song. *Energy Environ. Sci.* **2013**, *6*, 1170-1184.

[38] H. Lv, J. Song, Y. V. Geletii, J. W. Vickers, J. M. Sumliner, D. G. Musaev, P. KÖgerler, P. F. Zhuk, J. Bacsa, G. Zhu, C. L. Hill. *J Am. Chem. Soc.* **2014**, *136*, 9268-9271.

[39] B. S. Brunschwig, M. H. Chou, C. Creutz, P. Ghosh, N. Sutin. *J. Am. Chem. Soc.* **1983**, *105*, 4832-4833.

[40] V. Y. Shafirovich, N. K. Khannanov, V. V. Strelets. *Nouv. J. Chim.* **1980**, *4*, 81-84.

[41] T. Zidki, L. Zhang, V. Shafirovich, S. V. Lymar. *J. Am. Chem. Soc.* **2012**, *134*, 14275-14278.

[42] A. M. Ullman, Y. Liu, M. Huynh, D. K. Bediako, H. Wang, B. L. Anderson, D. C. Powers, J. J. Breen, H. D. Abruna, D. G. Nocera. *J. Am. Chem. Soc.* **2014**, *136*, 17681-17688.

[43] J. B. Gerken, J. G. McAlpin, J. Y. C. Chen, M. L. Rigsby, W. H. Casey, R. D. Britt, S. S . Stahl. *J. Am. Chem. Soc.* **2011**, *133*, 14431-14442.

[44] A. Minguzzi, F.-R. F. Fan, A. Vertova, S. Rondinini, A. J. Bard. *Chem. Sci.* **2012**, *3*, 217-229.

[45] H.-Y. Wang, E. Mijangos, S. Ott, A. Thapper. *Angew. Chem. Int. Ed.* **2014**, *53*, 1-5.

[46] S. C. Schaffer, C. E. Schaffer. *J. Chem. Educ.* **1996**, *73*, 180-181.

[47] Z. Chen, J. J. Concepcion, X. Hu, W. Yang, P. G. Hoertz, T. J. Meyer. *Proc. Natl. Acad. Sci.* **2010**, *107*, 7225-7229.

[48] K. Klingan, F. Ringleb, I. Zaharieva, J. Heidkamp, P. Chernev, D. Gonzalez-Flores, M. Rish, A. Fischer, H. Dau. *ChemSusChem*, **2014**, *7*, 1-11.

[49] N. Koga, T. Kimizu, M. Sakamoto, Y. Furukawa. *Chem. Educator*, **2009**, *14*, 1-4.

[50] J. Du, Z. Chen, C. Chen, T. J. Meyer. *J. Am. Chem. Soc.* **2015**, *137*, 3193-3196.

[51] D. Strmcnik, K. Kodama, D. van der Vliet, J. Greeley, V. R. Stamenkovic, N. M. Markovic. *Nat. Chem.* **2009**, *1*, 466-472.

Appendix

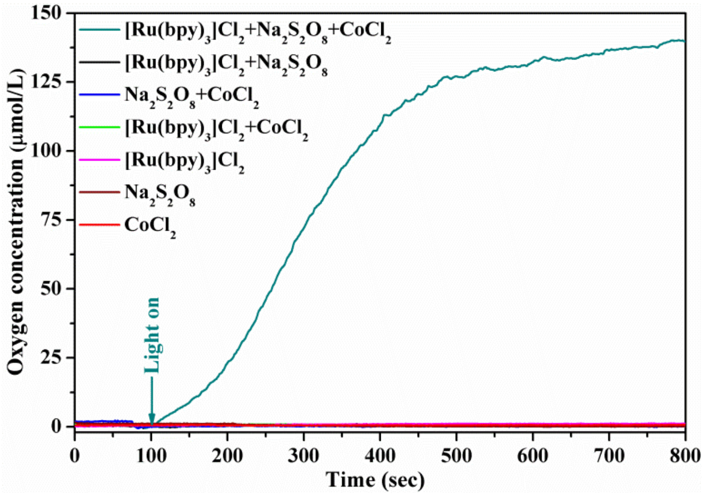

Figure S8.1. Control experiments for photochemical water oxidation with $CoCl_2$ (26.3 mM $CoCl_2$, 10.5 mM $Na_2S_2O_8$, 0.83 mM $[Ru(bpy)_3]Cl_2$, oxygen was online monitored with Clark electrodes in solution).

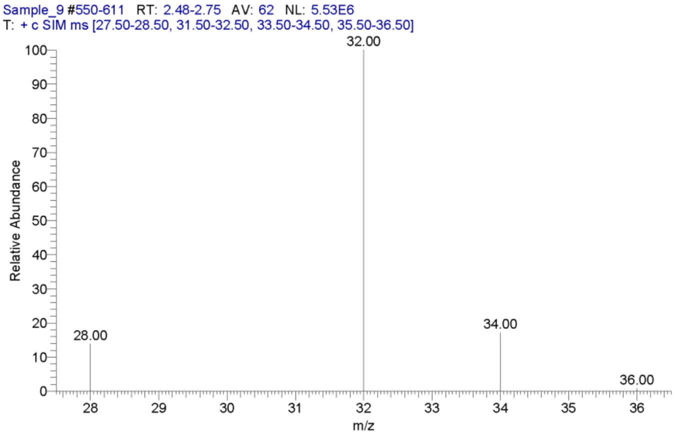

Figure S8.2. MS detection of ^{18}O during labeling experiments (water oxidation with $CoCl_2$ in water containing 10% ^{18}O).

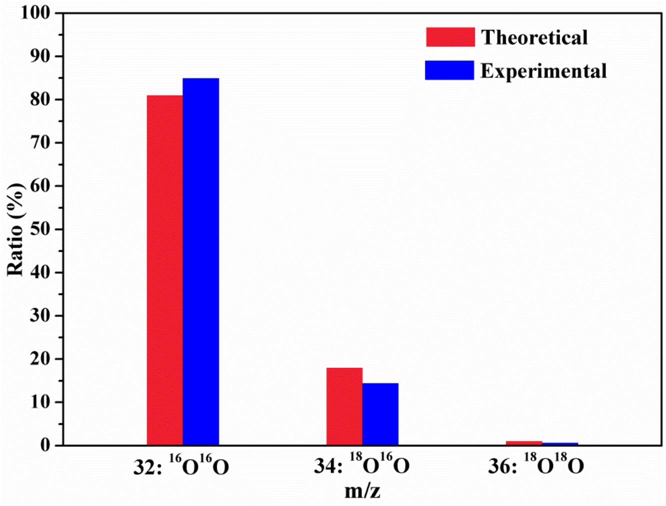

Figure S8.3. Comparison of theoretical vs. experimental $^{16}O^{16}O$, $^{18}O^{16}O$, and $^{18}O^{18}O$ ratios (after water oxidation with $CoCl_2$ in water containing 10% ^{18}O).

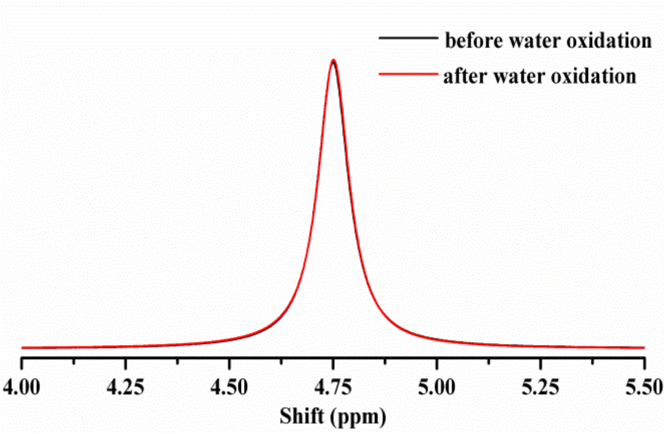

Figure S8.4. ^{1}H-NMR spectra of the solution before and after water oxidation (2.66 mM $[Ru(bpy)_3]Cl_2 \cdot 6H_2O$, 6.3 mM $Na_2S_2O_8$, 63.12 mM $CoCl_2$, solvent: 90% D_2O+ 10% H_2O).

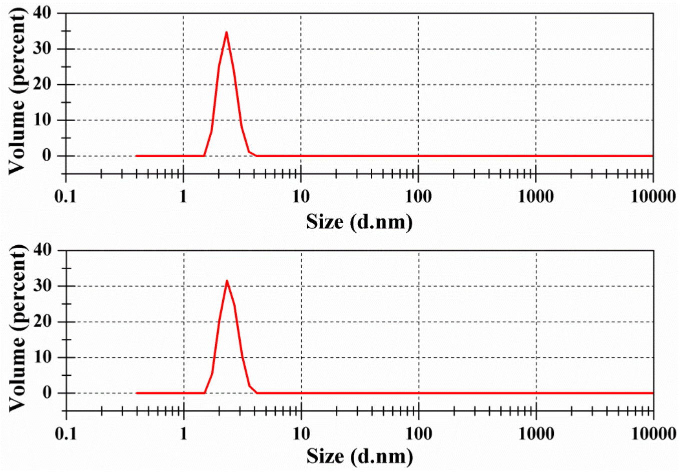

Figure S8.5. DLS analysis of solution (bottom) after water oxidation (vs. distilled water as a reference (top)).

The peak around 1~3 nm is ascribed to background effects (gas bubbles or particles from the environment) as it is present for distilled water as well.

(a) (b)

Figure S8.6. Photographs of the solutions: (a) immediately after photochemical water oxidation in pH 3 HCl solution, (b) after 5 months of ageing.

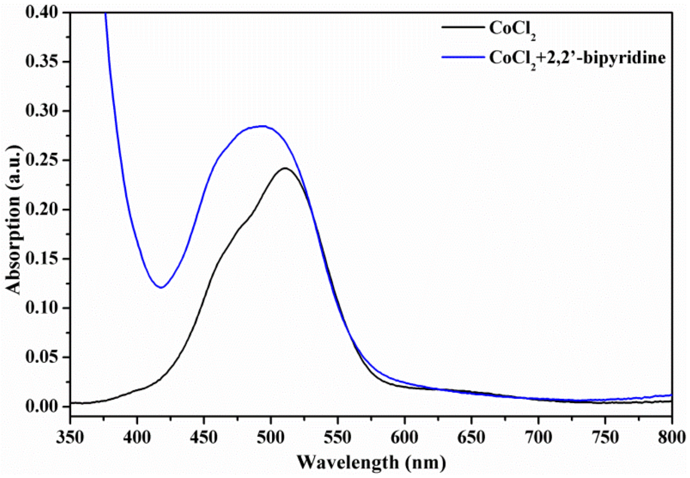

Figure S8.7. UV/Vis absorption spectra of $CoCl_2$ solution in the presence or absence of 2,2’-bipyridine.

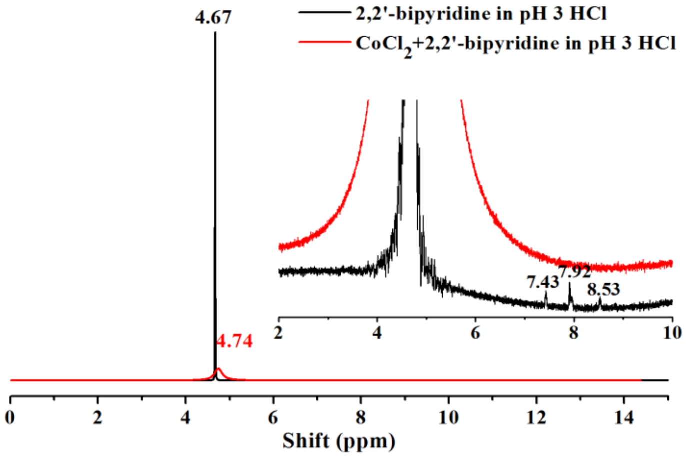

Figure S8.8. ^{1}H-NMR of $CoCl_2$ in pH3 HCl solution in the presence or absence of 2,2'-bipyridine (168.1 mM $Co(NO_3)_2$, 0.01 M buffer, solvent: 90% D_2O+ 10% H_2O, 400 MHz).

The coordination of 2,2'-bipyridine to Co^{2+} is verified by the disappearance of three characteristic peaks of 2,2'-bipyridine at 8.53, 7.92 and 7.43 ppm.

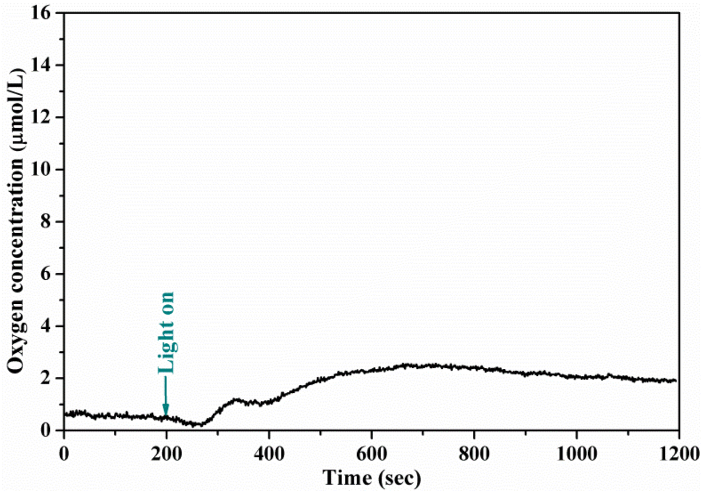

Figure S8.9. Photochemical water oxidation of $CoCl_2$ in pH 3 HCl in the presence of 2,2'-bipyridine (52.6 mM $CoCl_2$, 10.5 mM $Na_2S_2O_8$, 0.83 mM $[Ru(bpy)_3]Cl_2$, 24 mM 2,2'-bipyridine).

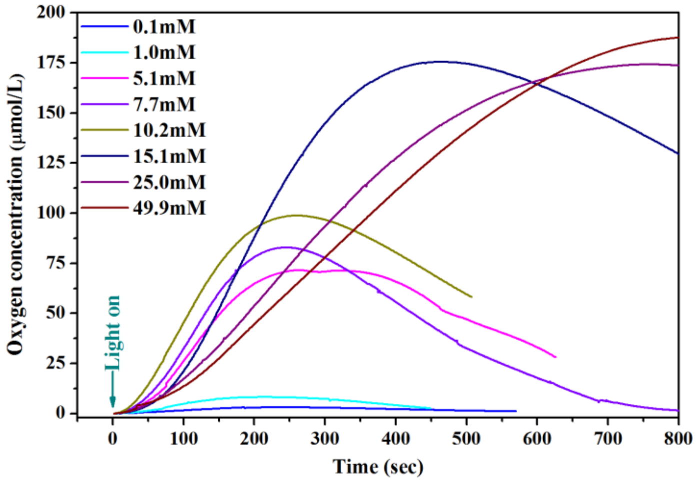

Figure S8.10. $CoCl_2$ concentration dependent photochemical water oxidation (10.5 mM $Na_2S_2O_8$, 0.83 mM $[Ru(bpy)_3]Cl_2$, oxygen evolution was online monitored by Clark electrode in solution).

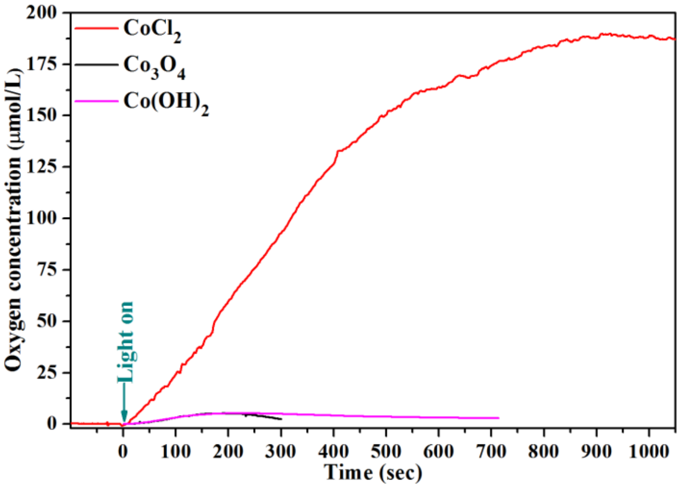

Figure S8.11. Photochemical water oxidation of $CoCl_2$, $Co(OH)_2$, and Co_3O_4 in pH 3 HCl solution. (WOC: 52.6 mM $CoCl_2$, 55.3 mM $Co(OH)_2$, 17.2 mM Co_3O_4, respectively; 10.5 mM $Na_2S_2O_8$; 0.83 mM $[Ru(bpy)_3]Cl_2$; oxygen evolution was online monitored by Clark electrode in solution).

Cobalt hydroxide precipitated from Co^{2+} in KOH solution (cf. PXRD pattern in Figure S8.12) was tested for water oxidation as a reference. Whereas no oxygen was produced at pH 3 (Figure 8.1), rapid oxygen evolution was observed at pH 11 (Figure S8.13). Likewise, representative nanoscale Co_3O_4 WOCs (10~30 nm, hydrothermally synthesized) did not exhibit significant oxygen evolution at pH 3 HCl (Figure 1), but considerable activity in pH 7 phosphate buffer (Figure S8.14). The water oxidation inactivity of both Co_3O_4 and $Co(OH)_2$ in acidic media provides further evidence for the absence of cobalt related oxide

WOCs in the Co^{2+}/pH 3 system as they obviously follow different water oxidation kinetics. It should be mentioned that both $Co(OH)_2$ and Co_3O_4 can release Co^{2+} into solution thermodynamically. However, the Co^{2+} dissolved in the solution during the catalytic tests period would not provide significant activity. The PXRD pattern of $Co(OH)_2$ after water oxidation in pH 3 HCl indicates the loss of crystallinity but the basic structure framework were maintained (Figure S8.12).

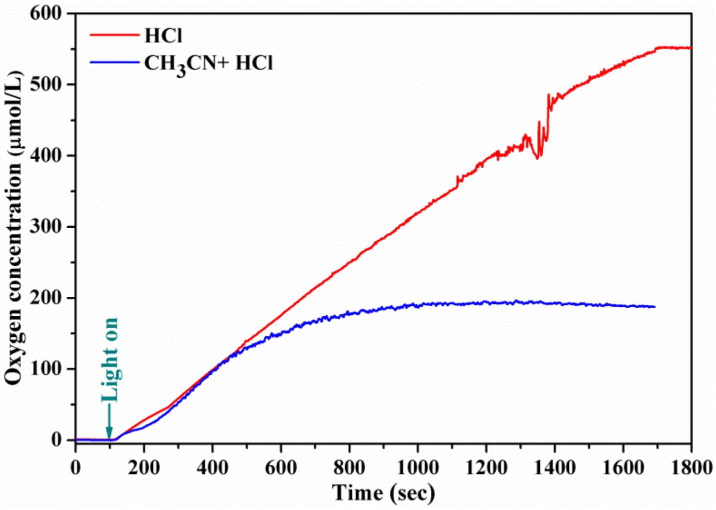

Figure S8.12. Photochemical water oxidation with $CoCl_2$ in HCl (pH 3) or CH_3CN-HCl mixed solvent (67 vol.% pH 3 HCl + 33 vol.% CH_3CN; blue); (13.15 mM $CoCl_2$, 52.5 mM $Na_2S_2O_8$, 0.83 mM $[Ru(bpy)_3]Cl_2$, pH 3 HCl solution).

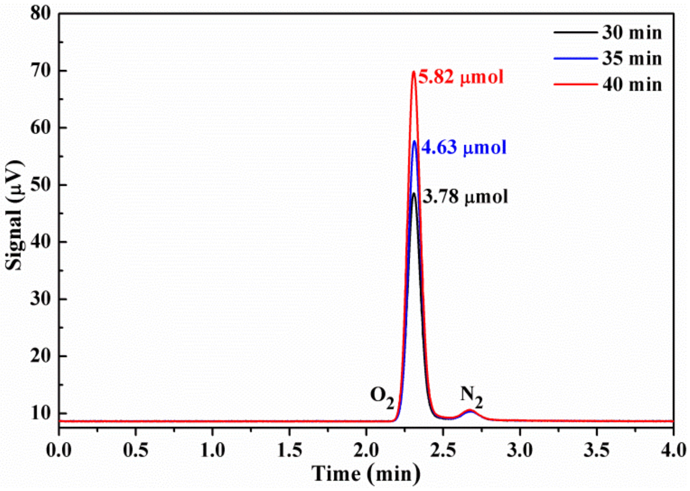

Figure S8.13. Photochemical water oxidation with $CoCl_2$ in pH 3 HCl monitored by GC (13.15 mM $CoCl_2$, 52.5 mM $Na_2S_2O_8$, 0.83 mM $[Ru(bpy)_3]Cl_2$, pH 3 HCl solution).

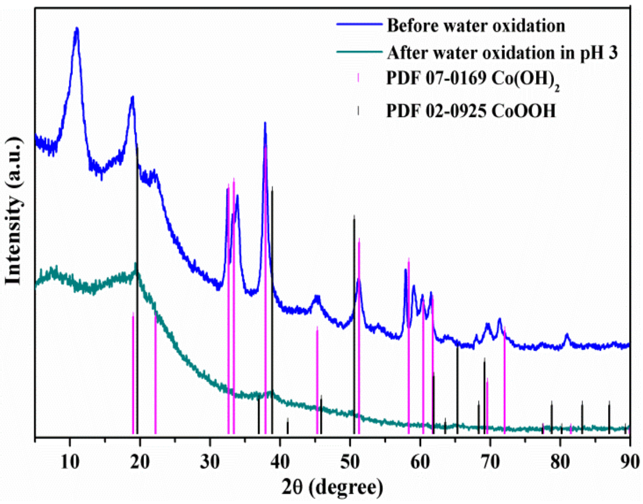

Figure S8.14. PXRD patterns of $Co(OH)_2$ (precipitated by adding 1 M KOH into 52.6 mM $CoCl_2$ under strong stirring) before and after water oxidation in pH 3 HCl solution.

The precipitate is mainly composed of $Co(OH)_2$ with minor amounts of double layered cobalt hydroxide (Co-LDH, evident from the peak at around 10 deg) arising from auto-oxidation of $Co(OH)_2$ by O_2.

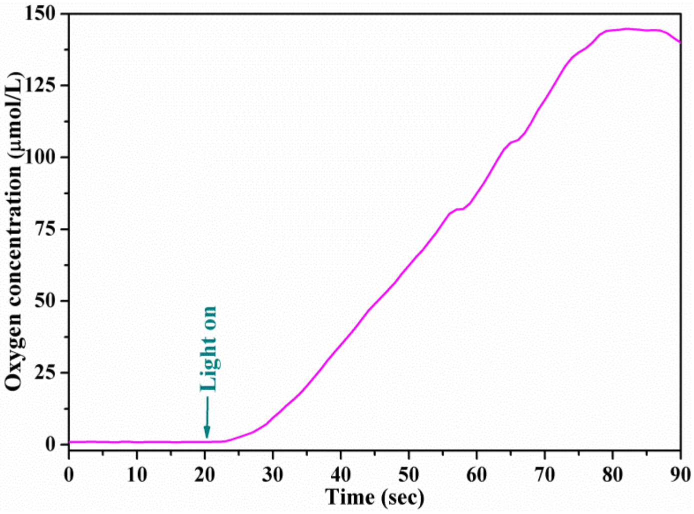

Figure S8.15. Photochemical water oxidation with $Co(OH)_2$ in pH 11 KOH solution (10 mg $Co(OH)_2$, 10.5 mM $Na_2S_2O_8$, 0.83 mM $[Ru(bpy)_3]Cl_2$).

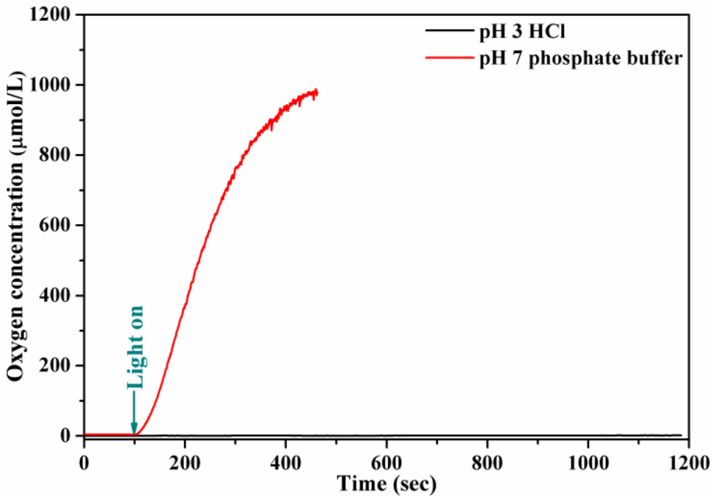

Figure S8.16. Photochemical water oxidation with Co_3O_4 nanocrystals in pH 3 HCl solution and pH 7 potassium phosphate buffer (10 mg Co_3O_4, 10.5 mM $Na_2S_2O_8$, 0.83 mM $[Ru(bpy)_3]Cl_2$).

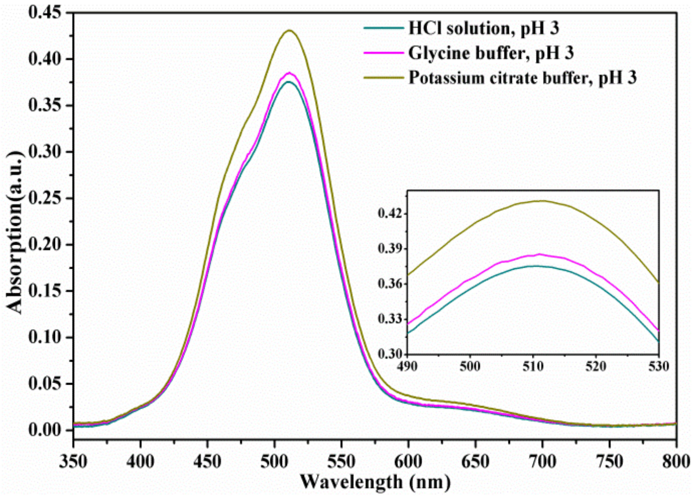

Figure S8.17. UV/Vis spectra of $CoCl_2$ in buffered vs. non-buffered solutions (84.2 mM $CoCl_2$, 0.1 M buffer).

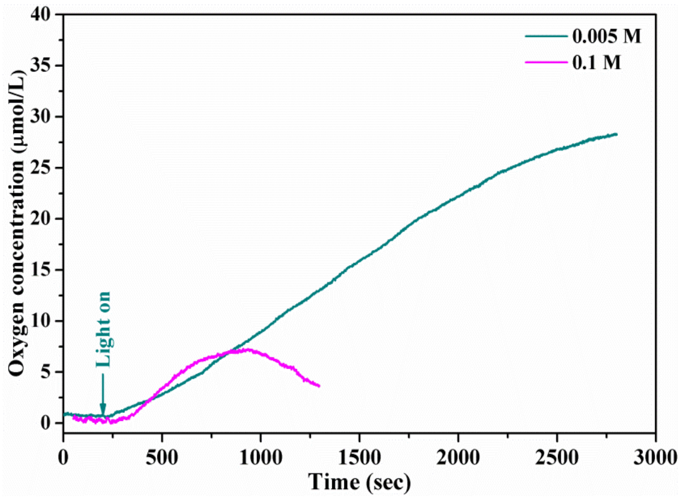

Figure S8.18. Photochemical water oxidation with $CoCl_2$ in different concentrations of pH 3 glycine buffer.

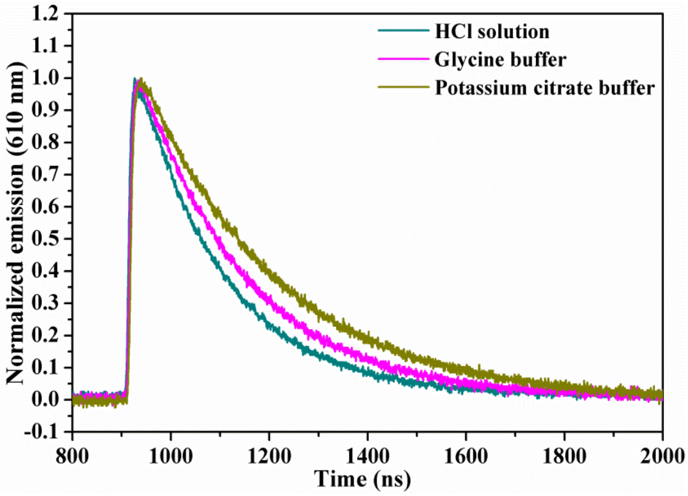

Figure S8.19. Emission spectra of $[Ru(bpy)_3]^{2+}$ after irradiation with a 355 nm laser (8.4 mM $CoCl_2$, 1.68 mM $Na_2S_2O_8$, 0.13 mM $[Ru(bpy)_3]Cl_2$).

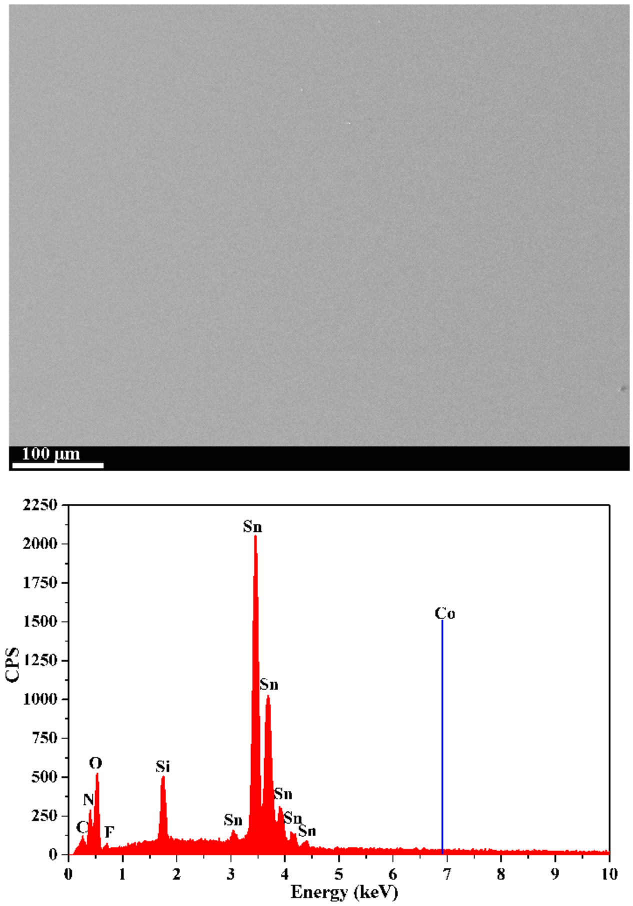

Figure S8.20. Representative SEM picture and EDXS of FTO electrode after water oxidation with $CoCl_2$.

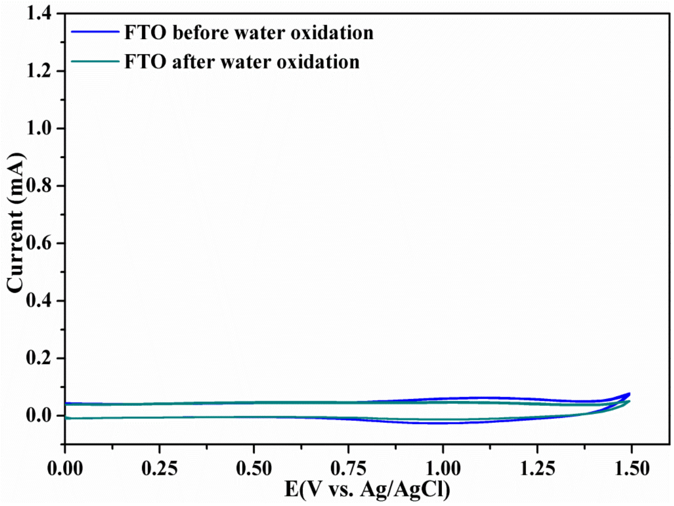

Figure S8.21. Electrochemical water oxidation with FTO electrodes in pH 3 HCl solution (FTO before water oxidation: fresh FTO； FTO after water oxidation: the FTO electrode after water oxidation with $CoCl_2$ in pH 3 HCl solution was rinsed with distilled water to remove the adsorbed Co^{2+}).

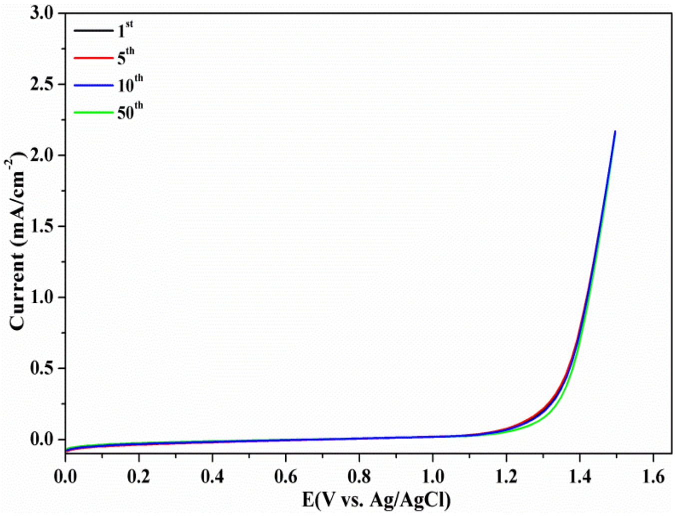

Figure S8.22. Electrochemical water oxidation with $CoCl_2$ in pH 3 HCl for 50 cycles ($CoCl_2$: 126.0 mM).

Here, we examined the stability of $CoCl_2$-assisted water oxidation by cycling. As shown in Figure S8.20, the current density remained at a constant level without significant decrease after 50 cycles.

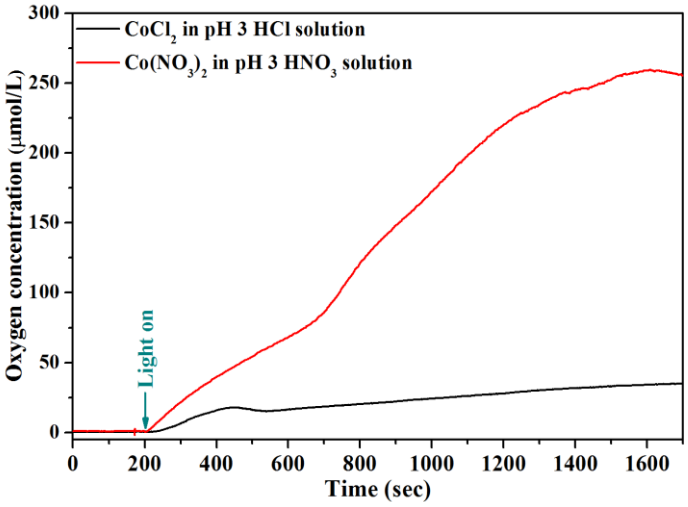

Figure S8.23. Comparison of photochemical water oxidation between $CoCl_2$ in pH 3 HCl and $Co(NO_3)_2$ in pH 3 HNO_3 (52.6 mM $CoCl_2$, 52.6 mM $Co(NO_3)_2$, 21 mM $Na_2S_2O_8$, 0.83 mM $[Ru(bpy)_3]Cl_2$, pH 3 HCl solution).

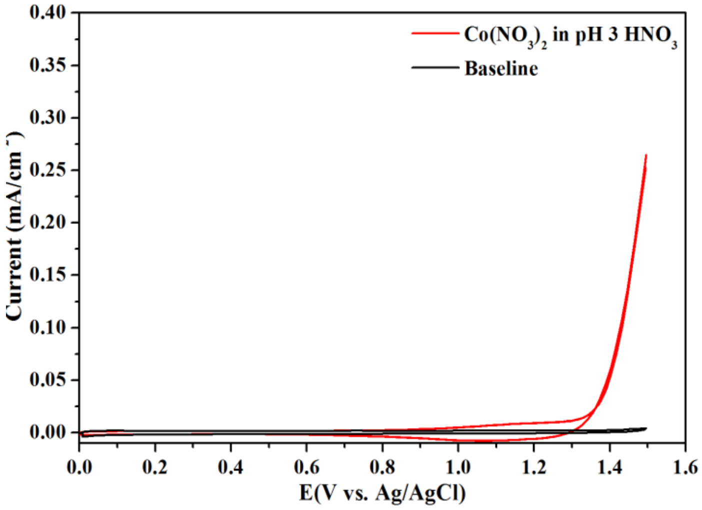

Figure S8.24. Electrochemical water oxidation with $Co(NO_3)_2$ in pH 3 HNO_3 (42 mM $Co(NO_3)_2$).

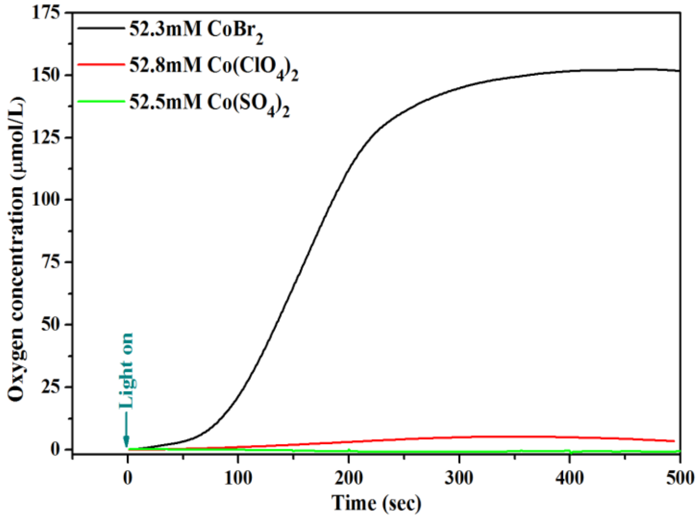

Figure S8.25. Photochemical water oxidation with Co(Br)$_2$, Co(ClO$_4$)$_2$ and CoSO$_4$ (10.5 mM $Na_2S_2O_8$, 0.83 mM [Ru(bpy)$_3$]Cl$_2$, oxygen was online monitored with Clark electrodes in solution).

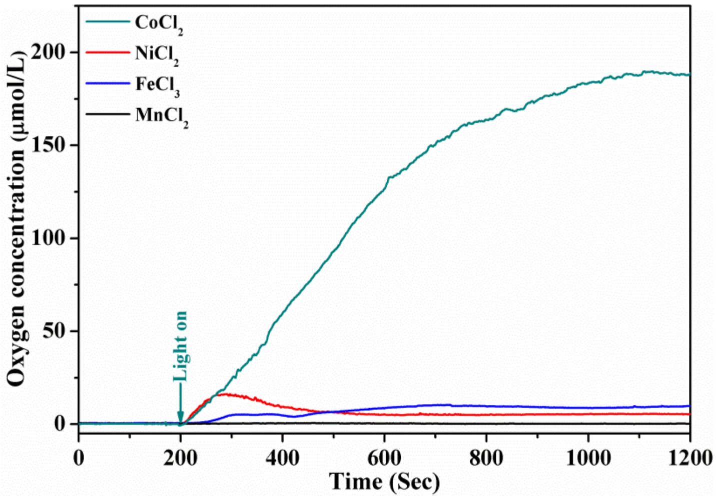

Figure S8.26. Photochemical water oxidation of NiCl$_2$, FeCl$_3$, and MnCl$_2$ in pH 3 HCl (52.6 mM NiCl$_2$, 52.6 mM FeCl$_3$, 52.6 mM MnCl$_2$, 10.5 mM $Na_2S_2O_8$, 0.83 mM [Ru(bpy)$_3$]Cl$_2$).

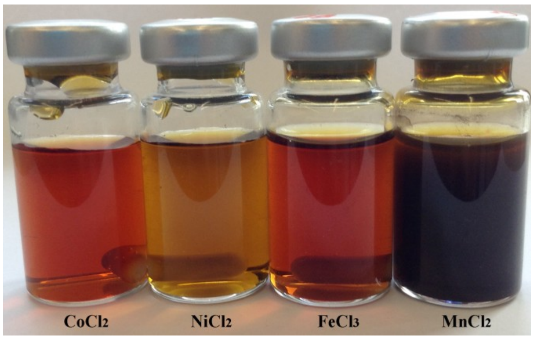

Figure S8.27. Photographs of the solutions after photochemical water oxidation at pH 3 in HCl (precipitations are observed for $MnCl_2$ after water oxidation even in strongly acidic conditions).

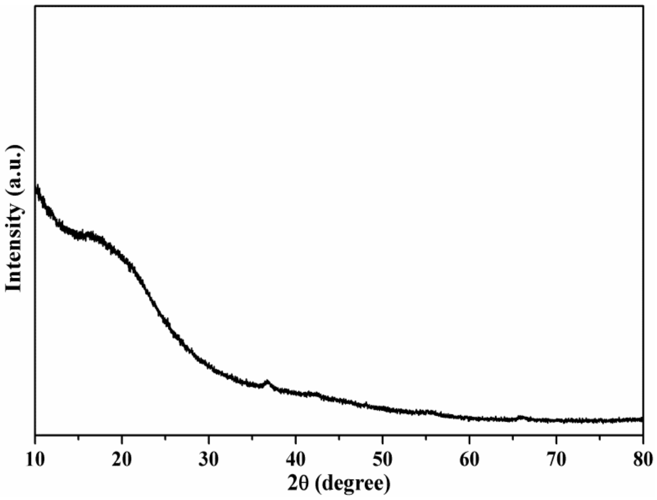

Figure S8.28. PXRD pattern of the precipitation formed from $MnCl_2$ solution after photochemical water oxidation in pH 3 HCl.

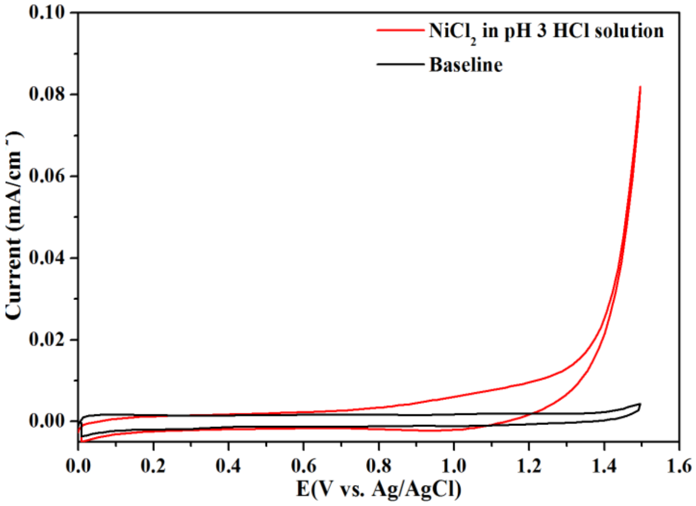

Figure S8.29. Electrochemical water oxidation with $NiCl_2$ in pH 3 HCl (42 mM $NiCl_2$).

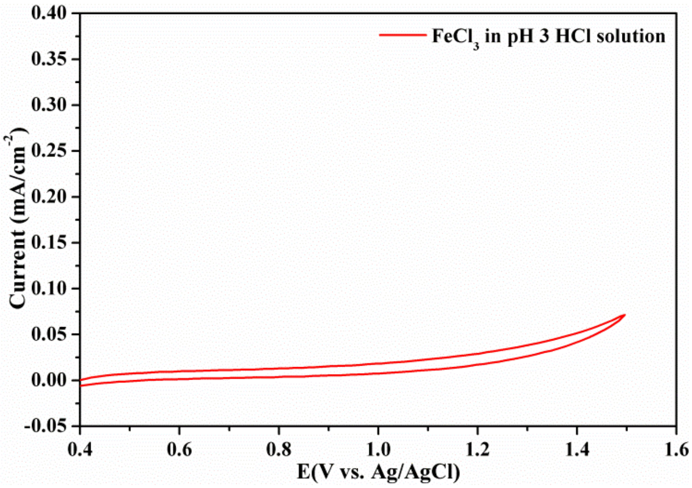

Figure S8.30. Electrochemical water oxidation with $FeCl_3$ in pH 3 HCl (42 mM $FeCl_3$).

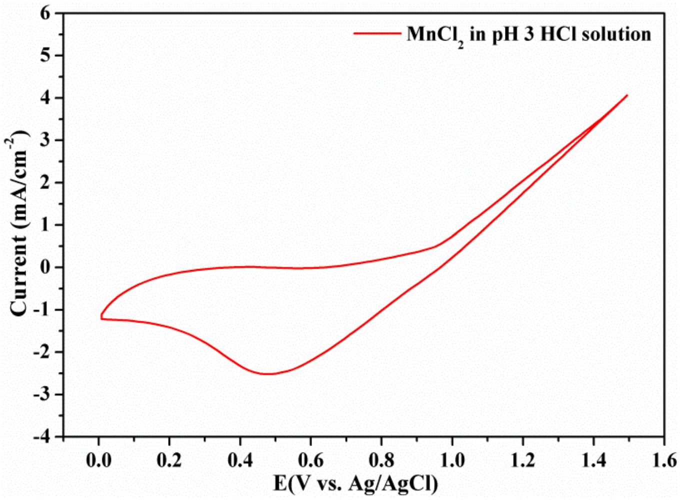

Figure S8.31. Electrochemical water oxidation with $MnCl_2$ in pH 3 HCl (42 mM $MnCl_2$).

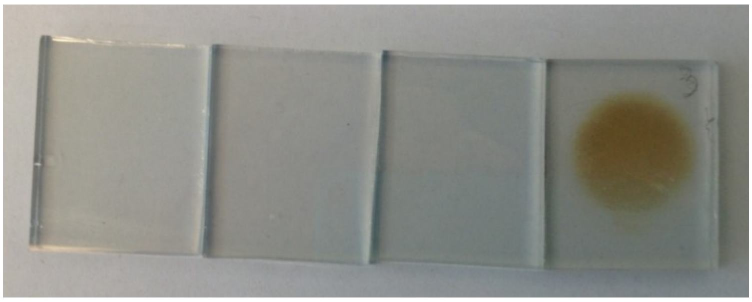

Figure S8.32. Photographs of FTO electrodes after electrochemical water oxidation (left to right: $CoCl_2$-$NiCl_2$-$FeCl_3$-$MnCl_2$).

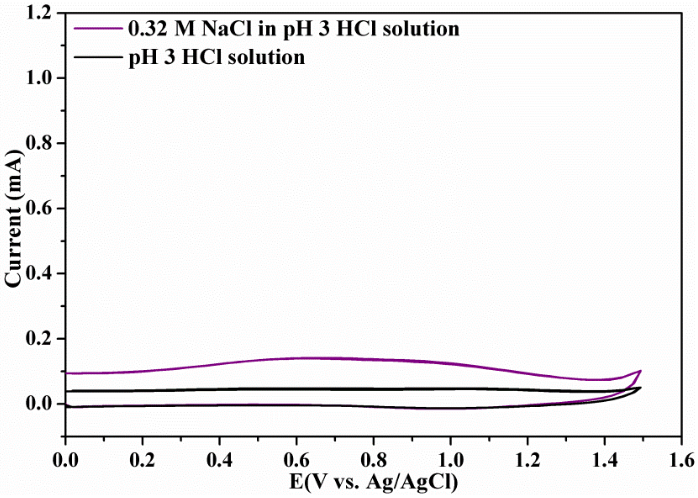

Figure S8.33. Water oxidation with pristine FTO electrode in pH 3 HCl solution with and without NaCl.

As blank FTO glass displayed some background water oxidation activity, this contribution might be influenced by the conductivity of the electrolyte. Thus, conductivity differences between buffer types might be a possible explanation for the remarkably different water oxidation performance observed in various buffers. Consequently, tuning the conductivity of the electrolyte to investigate its influence on water oxidation is of interest. As shown in Figure S8.30, adding NaCl as an additional conductive medium to pH 3 HCl does not result in improved water oxidation performance except for a higher capacity arising from the concentrated electrolyte.

Computational modeling

Molecular structures were optimized employing the program package TURBOMOLE,[1] version 6.4, by means of Kohn-Sham density functional theory (DFT). The BP86 exchange-correlation density functional[2] Ahlrichs' def2-TZVP basis set,[3] the resolution of identity (RI) approach[4] and the corresponding auxiliary basis sets[5] were used for all calculations.[6] We employed the solvent continuum model COSMO[7] with the standard settings as implemented in TURBOMOLE to account for solvation effects. For the optimized structures, vibrational analyses were performed using the NUMFORCE script using default settings. The absence of imaginary vibrational frequencies for all structures was used as a proof that the structures correspond to minima on the potential energy surface. We also calculated the thermochemical contributions to the Gibbs energies using the FREEH script. These values were obtained approximating the translational, rotational, and vibrational degrees of freedom by the ideal gas, rigid rotor, and harmonic oscillator models. All values were calculated at 298.15 K and 0.1 MPa. Our results were further investigated using the B3LYP density functional.[8] The relative stabilities of the isomers were the same for both employed functionals. Pictures of molecular structures were prepared with VMD 1.9.1.[9]

Binding mode – nomenclature

A citrate contains two terminal carboxyl groups (T), one central carboxyl group (C), and one hydroxyl group (O)(Figure S8.31). Usually, three of them coordinate to the metal center, this leads to a total of three (TTO, TCO, and TTC) binding modes. If bound to the metal center, the pK_a of carboxyl and hydroxyl group changes, therefore all possible protonation sites were considered to identify the minimum electronic energy structures. All structures with a relative free energy (ΔG) < 10 kcal/mol are shown (Figures S32 and S33). Reported free energies are relative to the most stable isomer indicated by $\Delta G = 0$ kcal/mol.

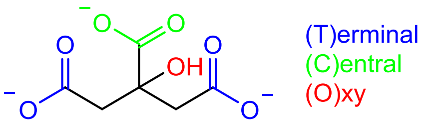

Figure S8.31. Visualization of the nomenclature used to describe the different coordination modes.[10]

The precise structural speciation emerging from the coordination of buffer molecules to Co^{2+} ions was modeled with density functional theory (DFT) calculations. Based on previous results on the speciation of Co^{2+} in the presence of citrate[11]we assumed that the relevant species present in solution were $[Co(H_2O)_3(citrate)]^{1-}$ and $[Co(H_2O)_3(citrateH)]$ ($Citrate^{3-} = C_6H_5O_7^{3-}$). An extensive DFT study of different coordination isomers and their protonation site was performed. Our approach was found to be consistent with previous studies performed for Al^{3+} ions.[10] An analogous study was carried out for the glycine buffer/Co^{2+} system and the results are in good agreement with preceding work.[12]

$[Co(H_2O)_3(citrate)]^{1-}$

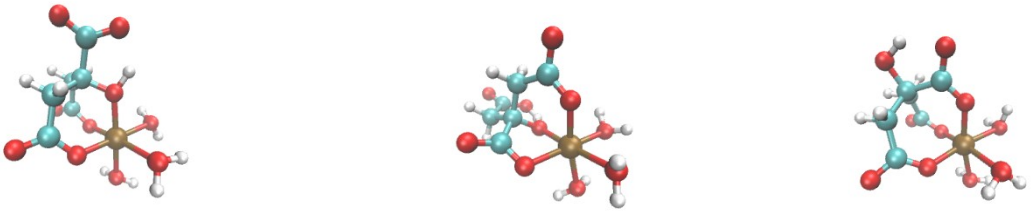

TTO
$\Delta G = 6.85$ kcal/mol

TCO
$\Delta G = 0.00$ kcal/mol

TTC
$\Delta G = 8.89$ kcal/mol

Figure S8.34. Modeling of the structure of citrate coordinated Co^{2+}.

TCO is the most stable binding mode for the deprotonated form of citrate, probably due to the fact that a six-membered ring can be formed by an internal hydrogen bond. This internal hydrogen bond can be established by the free terminal carboxylate (T) and coordinating hydroxyl group (O). The two other conformers are considerably less stable by 6.85 kcal/mol (TTO) and 8.89 kcal/mol (TTC). For all three conformers, protonation of the hydroxyl group (O) is preferred.

[Co(H_2O)$_3$(citrateH)]

TTO **TCO** **TTC**

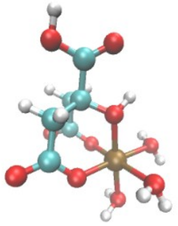

ΔG = 3.69 kcal/mol

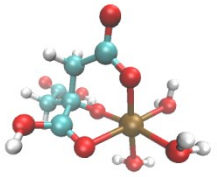

ΔG = 1.03 kcal/mol

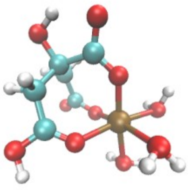

ΔG = 5.58 kcal/mol

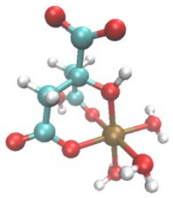

ΔG = 2.88 kcal/mol

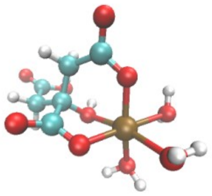

ΔG = 0.00 kcal/mol

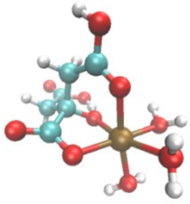

ΔG = 0.99 kcal/mol

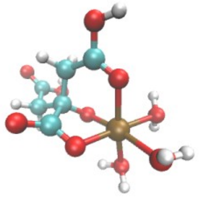

ΔG = 8.18 kcal/mol

Figure S8.35. Modeling of the structure of protonated citrate coordinated Co^{2+}.

For the protonated form of the citrate ligand, the TCO binding mode is also the most stable one (Figure S8.33). As for the deprotonated form, a six membered ring formed by an internal hydrogen bond might be the reason for the stability of this binding mode. The second protonation site appears not to have a great influence on the overall stability of the conformer.

$[Co(H_2O)_5Gly]^{2+}$/ $[Co(H_2O)_4(Gly)]^{2+}$

$[Co(H_2O)_5Gly]^{2+}$ $[Co(H_2O)_4(Gly)]^{2+}$

ΔG =1.60 kcal/mol ΔG = 0.00 kcal/mol

Figure S8.36. Modeling of the structure of glycine coordinated Co^{2+}.

The calculations indicate that there is no large energetic difference between mono and bidentate coordination of glycine to the cobalt center. The relative free energy between the two coordination modes was calculated according to reaction equation (1). In principle one could also consider coordination of the nitrogen atom,[13] but earlier studies showed that the zwitterionic isomer is the dominant one,[14] especially under the applied experimental conditions (pH = 3).

$$[Co(H_2O)_5Gly]^{2+} = [Co(H_2O)_4(Gly)]^{2+} + H_2O \quad (1)$$

$$[Co(H_2O)_6]^{2+} + Gly = [Co(H_2O)_4(Gly)]^{2+} + 2\ H_2O \quad (2)$$

ΔG_{rxn} = -15.90 kcal/mol

$$[Co(H_2O)_6]^{2+} + citrate^{3-} = [Co(H_2O)_3(citrate)]^{1-} + 3\ H_2O \quad (3)$$

ΔG_{rxn} = -50.59 kcal/mol

$$[Co(H_2O)_6]^{2+} + citrateH^{2-} = [Co(H_2O)_3(citrateH)] + 3\ H_2O \quad (4)$$

ΔG_{rxn} = -38.67 kcal/mol

Comparison of the reaction free energies (ΔG_{rxn}) clearly indicates a strong binding of the tridentate citrate molecule to the cobalt ion. This finding supports our experimental results, which show a complete inhibition of the oxygen evolution in citrate buffer but still weak activity in glycine buffer.

References

[1] R. Ahlrichs, M. Bär, M. Häser, H. Horn, C. Kölmel. *Chem. Phys. Lett.* **1989**, *162*,165-169

[2] A. D. Becke. *Phys. Rev. A* **1988**, *38*, 3098-3100; (b) J. P. Perdew. *Phys. Rev. B* **1986**, *33*, 8822-8825.

[3] (a) A. Schäfer, C. Huber, R. Ahlrichs. *J. Chem. Phys.***1994**, *100*, 5829-5835; (b) F. Weigend, R. Ahlrichs. *Phys. Chem. Chem. Phys.* **2005**, *7*, 3297-3305.

[4] K. Eichkorn, O. Treutler, H. Öhm, M. Häser, R. Ahlrichs. *Chem. Phys. Lett.* **1995**, *240*, 283-290.

[5] F. Weigend. *Phys. Chem. Chem. Phys.* **2002**, *4*, 4285-4291.

[6] (a) C. Hättig. *J. Chem. Phys.* **2003**, *118*, 7751-7761; (b) F. Weigend, M. Häaser, H.Patzelt, R. Ahlrichs. *Chem. Phys. Lett.***1998**, *294*, 143-152.

[7] A. Klamt, G. Schüürmann. *J. Chem. Soc. Perkin Trans. 2* **1993**, *5*, 799-805.

[8] (a) A. D. Becke. *J. Chem. Phys*.**1993**, *98*, 5648-5652; (b) C. Lee, W. Yang, R. G. Parr, *Phys. Rev. B* **1988**, *37*, 785-789.

[9] W. Humphrey, A. Dalke, K. Schulten. *J. Molec. Graphics* **1996**, *14*, 33-38.

[10] (a) J. I. Mujika, J. M. Ugalde, X. Lopez. *Phys. Chem. Phys.* **2012**, *14*, 12465-12475; (b) A. L. Oliveira de Noronha, L. Guimarães, H. A. Duarte, *J. Chem. Theory Comput.* **2007**, *3*, 930-937.

[11] N. Kotsakis, C. P., Raptopoulou, V. Tangoulis, A. Terzis, J. Giapintzakis, T. Jakusch, T. Kiss, A. Salifoglou. *Inorg. Chem.* **2003**, *42*, 22-31.

[12] T. Marino, M. Toscano, N. Russo, A. Grand. *J. Phys. Chem. B* **2006**, *110*, 24666-24673.

[13] E. Constantino, L. Rodriguez-Santiago, M. Sodupe, J. Tortajada. *J. Phys. Chem. A* **2005**, *109*, 224-230.

[14] M. H. Khodabandeh, M. D. Davari, M. Zahedi, G. Ohanessian. Int. *J. Mass Spec.* **2010**, *291*, 73-83.

Summary

The development of water oxidation catalysts based on earth-abundant metals is a crucial step toward solar water splitting for future clean and sustainable energy resources. In this thesis, different oxide types based on Co, Mn, Ni and Fe were investigated and tuned with respect to photochemical water oxidation activity. A wide range of analytical techniques (including ICP-AES, EDXS, SEM, TEM, BET, PXRD, XPS, XAS, UV/Vis, FT-IR, Raman, EPR and SQUID measurements) were applied to characterize the composition, morphology, structure and electronic properties of the targeted water oxidation catalysts. The water oxidation activity was mainly evaluated by with a well-established photochemical assay based on the $[Ru(bpy)_3]^{2+}/S_2O_8^{2-}$ system, which was complemented by electrochemical methods. The influence of various parameters, such as composition, structure and electronic properties, on the water oxidation activity was explored and the underlying mechanisms were discussed. In the following, the main results are summarized along the lines of our strategic investigations of WOC tuning parameters.

In chapter 2, nanostructured $Co_xMn_{3-x}O_4$ ($x = 0, 1, 2, 3$) spinel oxides were investigated for photochemical water oxidation which combine two of currently most promising active metal centers. The observed water oxidation activity trend ($Co_3O_4 > Co_2MnO_4 > CoMn_2O_4 > Mn_3O_4$) can be explained with at least three hypotheses. First, the hydrothermally obtained Co-rich spinel oxides exhibit the smallest particle sizes which provide a higher number of catalytically active sites for water oxidation. Second, structural differences may contribute to the oxygen evolution efficiency: the cubic spinel compounds Co_2MnO_4 and Co_3O_4 showed higher WOC activity than the tetragonally distorted Mn-rich spinels $CoMn_2O_4$ and Mn_3O_4. Cubane motifs in Co_2MnO_4 and Co_3O_4 are mostly composed of $\{Co_4O_4\}$ while $CoMn_2O_4$ and Mn_3O_4 they primarily contain $\{Mn_4O_4\}$ moieties. These compositional differences may also affect the efficiency of the cubane-related structural motif, which is widely accepted as a paradigm for constructing catalytic centers along the lines of the $\{CaMn_4O_5\}$ OEC of PSII. Finally, higher Co contents promote the interaction of the spinel surface with H_2O molecules, which might accelerate the reaction kinetics.

Proceeding with Co_3O_4 as a target compound in chapter 3, the influence of the preparative parameters on the photochemical water oxidation activity of hydrothermally synthesized Co_3O_4 nanoparticles was investigated. The complex interplay of morphology/surface area, crystallinity and cobalt valence states was analyzed with a wide range of analytical methods (including PXRD, Raman, UV/Vis, XPS and EPR techniques) and the results were further correlated to the water oxidation performance. A counterintuitive trend for WOC activity vs. BET surface area was established: interestingly, the most active WOCs displayed reduced surface areas. Crystallinity and oxidation states were identified as more influential parameters than surface area maximization in the performance optimization of Co_3O_4-WOCs.

In chapter 4, we set out to further investigate the structural tuning options for Co-based WOCs with special emphasis on their electronic properties. Spinel-type $LiCoO_2$ featuring 3D bio-mimetic $\{Co_4O_4\}$ cubane motifs and the layered $LiCoO_2$ modification without such $\{Co_4O_4\}$ units were selected as model systems to study the correlation between structure, electronic properties and dye-sensitized photocatalytic water oxidation. Chemical delithiation of both forms led to dramatically improved water oxidation activity compared to the fully lithiated parent compounds. This performance enhancement goes hand in hand with a semiconductor to metal transition upon delithiation. Characterization of the electronic structure with a wide spectrum of analytical techniques indicates that increased hole mobility is most likely to be the major driving force behind the enhanced water oxidation activity. Cuboidal $\{Co_4O_4\}$ motifs were identified as the basic building blocks of 3D Co-O-Co charge transport networks for enhanced hole transfer efficiency. Their networking role is further reinforced through stronger covalent character of the Co-O bonds after delithiation. These results pave the way to new optimization strategies for water oxidation catalysts through combined control over structural and electronic properties.

In chapter 5, these concepts were further confirmed for the prominent battery material $LiCoPO_4$ and $LiMn_2O_4$ as targets. A significant improvement of photocatalytic water oxidation activity was achieved through partial delithiation of these materials. Enhanced mobility of lithium ions was further confirmed as a useful tuning strategy for to optimize the electronic structures of lithium-containing ternary and higher oxides for efficient water oxidation. Furthermore, detailed water oxidation parameter screening (in the presence of $LiCoPO_4$-based WOC) at different pH values revealed a strong interaction between persulfate and $[Ru(bpy)_3]^{2+}$ photosensitizer. Additionally, superior water oxidation activity was observed in borate buffer compared to phosphate buffer. Both pH and buffer composition were found to strongly influence the redox potential of $Na_2S_2O_8$ and therefore the interaction between persulfate and $[Ru(bpy)_3]^{2+}$. These results shed new light on the underlying factors of the photochemical assay.

Chapter 6 continues the tuning strategies of the photochemical activity via the electronic properties with an investigation of strongly correlated electron systems, namely $La_{1-x}Sr_xMO_3$ perovskites and $La_{2-x}Sr_xMO_4$ layer perovskites (M= Fe, Co, Ni or Mn). Their electronic properties are well tunable through Sr doping, and their influence on the water oxidation performance was systematically studies. A clear correlation between the transition of the electronic properties from semiconductor to metal and the improved water oxidation activity was established, which highlights the metallic properties as an alternative strategy for efficient WOC construction. Strongly correlated electrons systems were introduced as effective electronic structure models for assigning favorable electronic properties for photochemical water oxidation. Their versatile, well studied and easily tunable electronic properties, such as localization of 3d electrons, orbital ordering and spin polarization, are furthermore likely to significantly improve their surface interaction with absorbed catalytic reactants. This renders the target perovskites and related compounds excellent electronic structure models for exploring other heterogeneous catalysis processes.

Chapter 7 further pursues structure-activity relationships of Co-based WOCs:, double layer cobalt hydroxides derived from brucite-related β-$Co(OH)_2$ and double layer α-$Co(OH)_2$ parent cobalt hydroxides were intercalated with different anions and studied as photochemical water oxidation catalysts. The main role of the guest anions is an alteration of the $\{MO_6\}$ interlayer distance, which has promising potential to tune the electronic properties of the layers. While Co-LDHs intercalated with small anions such as Br^- and CO_3^{2-} display a rather strong electrostatic interaction between the layers, which lowers the valence band position, the introduction of larger $C_6H_7O_2^-$ anions in the interlayer region weakens the electrostatic interaction and shifts the valence band position up. Larger anions such as $C_6H_7O_2^-$ can exert a similar effect as exfoliation strategies by strengthening the metallic character of the $\{MO_6\}$ layers and facilitating the charge transfer process involved in water oxidation. This results in improved water oxidation activities compared to Co-LDHs with stronger electrostatic interlayer interactions.

Finally,, Co^{2+} was investigated for water oxidation in a parameter window (pH 3, HCl) that ensures homogeneous water oxidation conditions. Representative CoO_x WOCs are inactive under these conditions, and their presence was furthermore excluded with a variety of other analytical methods. This exploration of molecular Co^{2+}-WOCs, however, came at the cost of their rather moderate activity under acidic conditions. Interestingly, the presence of different buffer systems notably reduced both photo- and electrochemical water oxidation activity of Co^{2+}, most likely due to coordinative blocking of active sites. This sheds new light on the crucial role of the electrolyte in water oxidation catalysis which goes far beyond a spectator-type proton reservoir.

All in all, the present work opens up new design strategies for Co-based and other transition metal-containing WOCs by addressing well-defined structural and electronic properties. Furthermore, the results open up interesting perspectives to study the underlying parameters of photochemical assays with respect to optimal WOC assessment conditions.

The emerging trends can be used as clear guidelines in screening and optimization processes of new WOCs on the way to future technological implementations.

Zusammenfassung

Die Erforschung von Wasseroxidationskatalysatoren (water oxidation catalysts; im folgenden: WOCs), welche auf häufig vorkommenden Übergangsmetallen basieren, ist ein wichtiger Schritt zur Gewinnung solarer Brennstoffe mittels photokatalytischer Wasserspaltung. In dieser Arbeit wurden verschiedene Übergangsmetalloxid-Typen, basierend auf Co, Mn, Ni und Fe, auf ihre photochemische WOC-Aktivität untersucht. Ein breites Spektrum analytischer Techniken (ICP-AES, EDXS, SEM, TEM, BET, PXRD, XPS, XAS, UV/Vis, FT-IR, Raman, EPR und SQUID-Messungen) wurde verwendet, um die Zusammensetzung, Morphologie, Struktur und die elektronischen Eigenschaften der WOCs zu charakterisieren. Die WOC-Aktivität wurde hauptsächlich mittels eines etablierten photochemischen Testverfahrens, welches auf dem $[Ru(bpy)_3]^{2+}/S_2O_8^{2-}$-System beruht, ermittelt. Elektrochemische Methoden wurden zur Ergänzung herangezogen. Der Einfluss verschiedener Parameter (z.B. Zusammensetzung, Struktur und elektronische Eigenschaften) auf die katalytische Aktivität und die zugrundeliegenden Mechanismen wurde erforscht. Die wichtigsten Resultate aus der systematischen Untersuchung von WOC-Optimierungsparametern sind im folgenden zusammengefasst.

In Kapitel 2 wurden nanostrukturierte $Co_xMn_{3-x}O_4$ ($x = 0, 1, 2, 3$) Spinell-Oxide als photochemische WOCs untersucht, da sie die nach heutigem Wissensstand vielversprechendsten Übergangsmetallzentren enthalten. Für den beobachteten Zusammenhang zwischen Co/Mn-Verhältnis und katalytischer Aktivität ($Co_3O_4 > Co_2MnO_4 > CoMn_2O_4 > Mn_3O_4$) wurden drei verschiedene Hypothesen erstellt. Zum einen wurden die Co-reichen Spinell-Oxide mittels hydrothermaler Synthese generell in einer kleineren Partikelgrösse erhalten, was eine höhere Anzahl katalytisch reaktiver Zentren für die Wasseroxidation zur Folge hat. Zweitens könnten strukturelle Unterschiede die Sauerstoffproduktionseffizienz beeinflussen: die kubischen Spinelle Co_2MnO_4 und Co_3O_4 wiesen höhere Aktivitäten als die tetragonal-verzerrten Mn-reichen Spinelle $CoMn_2O_4$ und Mn_3O_4 auf. Die charakteristischen Cuban-Motive in Co_2MnO_4 und Co_3O_4 bestehen hauptsächlich aus $\{Co_4O_4\}$, während $CoMn_2O_4$ und Mn_3O_4 primär $\{Mn_4O_4\}$-Einheiten enthalten. Diese Unterschiede in der Zusammensetzung beeinflussen wahrscheinlich auch die katalytische Effizienz des Cuban-ähnlichen Strukturmotivs, welches eine führende Position als Design-Element für WOCs in Analogie zum sauerstoffproduzierenden $\{CaMn_4O_5\}$ Komplex im Photosystem II einnimmt. Im Rahmen einer dritten Hypothese kann der erhöhte Co-Gehalt die Wechselwirkungen zwischen der Spinell-Oberfläche und

Wasser-Molekülen verbessern, was eine Erhöhung der Reaktionskinetik zur Folge haben könnte.

Kapitel 3 beschäftigt sich mit dem Einfluss der präparativen Parameter zur hydrothermalen Synthese von Co_3O_4-Nanopartikeln auf deren WOC Aktivität. Das komplizierte Zusammenspiel zwischen Morphologie/Oberfläche, Kristallinität und Co-Valenz wurde mithilfe verschiedener Methoden (u.a. PXRD, Raman, UV/VIS, XPS und EPR-Methoden) untersucht. Die Ergebnisse dieser Messungen wurden mit der WOC Aktivität korreliert, wobei ein kontraintuitiver Zusammenhang zwischen Aktivität und BET-Oberfläche beobachtet wurde: die WOCs mit den höchsten Aktivitäten hatten im Zuge einer post-synthetischem Behandlung relativ geringe BET-Oberflächen. Kristallinität und Oxidationszustand wurden als erste entscheidende Parameter für die Aktivitäts-Optimierung der Co_3O_4-Katalysatoren identifiziert.

In Kapitel 4 wurden diese Untersuchungen heterogener Co-haltiger WOCs vertieft, wobei besonderes Augenmerk auf die elektronischen Eigenschaften gelegt wurde. $LiCoO_2$ vom Spinell-Typ, welches biomimetische $\{Co_4O_4\}$-Cuban-Motive enthält, und die entprechende Hochtemperatur-$LiCoO_2$-Modifikation mit einer Schichtstruktur ohne solche $\{Co_4O_4\}$-Einheiten wurden als Modellsysteme zur Untersuchung des Zusammenhangs zwischen Struktur, elektronischen Eigenschaften und photokatalytischer Wasseroxidation herangezogen. Mittels chemischer Delithiierung gelang es, die WOC-Aktivität im Vergleich zu den vollständig lithiierten Proben drastisch zu erhöhen. Diese Optimierung der katalytischen Aktivität wurde mit dem einhergehenden Übergang der elektronischen Struktur von halbleitenden zu metallischen Eigenschaften korreliert. Eine genaue Charakterisierung der elektronischen Struktur der Materialien mit einem breiten Methodenspektrum weist darauf hin, dass ein wichtiger Grund für die beobachtete erhöhte Aktivität die grössere Mobilität der Ladungsträger im WOC sein könnte. Cuban-ähnliche $\{Co_4O_4\}$-Motive wurden als wichtige Bausteine zur Bildung von dreidimensionalen Co-O-Co-basierten Transportnetzwerken identifiziert, welche den Loch-Transfer bei der Wasseroxidation deutlich effizienter machen können. Dieser Effekt wird durch den höheren kovalenten Charakter der Co-O-Bindung nach der Delithiierung verstärkt. Die Ergebnisse ebnen den Weg für zukünftige WOC-Optimierungsstrategien durch kombinierte Kontrolle der strukturellen und elektronischen Eigenschaften.

In Kapitel 5 wurden die bisher entwickelten Konzepte anhand der bekannten Batterie-Materialien $LiCoPO_4$ und $LiMn_2O_4$ bestätigt. Eine deutliche Verbessung der photokatalytischen Aktivität wurde durch partielle Delithiierung dieser Materialien erhalten. Die Erhöhung der Mobilität der Lithium-Ionen wurde als weitreichende Tuning-Strategie für effiziente Wasseroxidation mit Lithium-haltigen ternären und höheren Oxide identifiziert. Ausserdem wiesen weitere Parameter-Screening-Tests bei verschiedenen pH-Werten auf eine starke Wechselwirkung zwischen Persulfat als Elektronenakzeptor und $[Ru(bpy)_3]^{2+}$-Photosensitizer hin. Zusätzlich wurde eine höhere WOC Aktivität in Borat- im Vergleich zu Phosphat-Pufferlösungen erhalten. Es wurde festgestellt, dass sowohl der pH-Wert als auch die Wahl des Puffers starken Einfluss auf das Redoxpotential von $Na_2S_2O_8$ und damit auf die Interaktionen zwischen Persulfat und $[Ru(bpy)_3]^{2+}$ haben kann. Diese Ergebnisse werfen neues Licht auf die zugrundeliegenden Faktoren des photochemischen Testverfahrens.

In Kapitel 6 wird die Tuning-Strategie zur Erhöhung der photochemischen Aktivität durch Änderung der elektronischen Eigenschaften weiterentwickelt. Als neue Modellverbindungen wurden die repräsentativen stark korrelierten Elektronensysteme $La_{1-x}Sr_xMO_3$ und $La_{2-x}Sr_xMO_4$ (M = Fe, Co, Ni oder Mn) mit Perovskit- bzw. geschichteter Perowskitstruktur ausgewählt. Die elektronischen Eigenschaften dieser Systeme lassen sich leicht durch die Sr-Dotierung feinabstimmen, was eine genaue Korrelation mit der WOC-Aktivität ermöglicht. Es wurde ein klarer Zusammenhang zwischen dem Übergang vom Halbleiter zum Metall und erhöhter Wasseroxidations-Aktivität gefunden, was auf metallische Eigenschaften als alternative Optimierungsstrategie für effiziente WOCs hinweist. Stark korrelierte Elektronensysteme wurden als aussagekräftige Elektronenstrukturmodelle identifiziert, um optimale elektronische Eigenschaften für die photochemische Wasseroxidation systematisch zu ermitteln. Die vielseitigen, gut untersuchten und einfach zu tunenden elektronischen Eigenschaften dieser Systeme, wie z.B. die Lokalisierung der 3d-Elektronen oder Spin-Polarisation, verbessern wahrscheinlich ausserdem die Oberflächeninteraktion mit absorbierten katalytischen Species. Die untersuchten Perowskite und verwandte Materialien eignen sich somit ausgezeichnet als generelle elektronische Strukturmodelle zur Untersuchung heterogener katalytischer Prozesse.

Kapitel 7 untersucht die Struktur/Aktivitäts-Beziehungen Co-haltiger LDHs (layered double hydroxides) als WOCs. In β-$Co(OH)_2$ vom Brucit-Typ und in doppelschichtiges α-$Co(OH)_2$ wurden verschiedene Anionen eingelagert, um die resultierende photochemische Wasseroxidationsaktivität zu untersuchen. Die Hauptrolle der Gastanionen ist die Veränderung des $\{MO_6\}$-Schichtabstands, die mit einer Änderung der elektronischen Eigenschaften in den Schichten einhergehen kann. Während in Co-LDHs mit kleineren Anionen wie Br^- oder CO_3^{2-} starke elektrostatische Anziehungskräfte zwischen den

Schichten herrschen, hat die Einführung des grösseren $C_6H_7O_2^-$-Anions eine Abnahme der elektrostatischen Interaktionen und eine Erhöhung der Valenzbandposition zur Folge. Grössere Anionen wie $C_6H_7O_2^-$ können einen ähnlichen Effekt wie das Exfoliieren von LDHs in Einzelschichten durch Verstärkung des metallischen Charakters der $\{MO_6\}$-Schichten bewirken. Dies kann den Ladungstransport bei der Wasseroxidation verbessern und führt zu erhöhter Aktivität im Vergleich zu Co-LDHs mit starken elektrostatischen Zwischenschichtkräften.

Schliesslich wurden Co^{2+}-haltige Oxide in einem klar definierten Parameterbereich ($CoCl_2$, pH 3, HCl) untersucht, der homogene Wasseroxidation ermöglicht. Diese Untersuchung molekularer Co^{2+}-WOCs schloss die Anwesenheit von CoO_x-WOCs, die bei höheren pH Werten sehr aktiv sind, aus. Die Abwesenheit nanoskaliger CoO_x-WOCs wurde zudem mit verschiedenen analytischen Methoden belegt. Gesamthaft wurde eine deutlich geringere photochemische WOC-Aktivität der homogenen Systeme im Vergleich zu CoO_x-WOCs festgestellt. Interessanterweise reduzierten verschiedener typische Puffersysteme sowohl photo- wie auch elektrochemische Wasseroxidationsaktivität. Diese Ergebnisse werfen neues Licht auf die unerwartet entscheidende Rolle der Elektrolyte für die Wasseroxidationskatalyse, welche über Hintergrundeffekte weit hinausgeht.

Insgesamt öffnet diese Arbeit neue Designstrategien für Co-haltige und andere Übergangsmetalloxid-WOCs durch systematische Optimierung der strukturellen und elektronischen Eigenschaften. Darüber hinaus wurden neue Ansätze zur genaueren Parameteruntersuchung photochemischer Testverfahren für die Entwicklung optimaler Wasseroxidationsbedingungen aufgezeigt.

Curriculum Vitae

First name: Hongfei **Last name:** Liu

Birthday: 20.08.1986 **Nationality:** China

Email: Liu.hfscut@gmail.com or hongfei.liu@chem.uzh.ch

Education

10/2011-Present PhD study major in inorganic chemistry, Department of Chemistry, University of Zurich, Switzerland.
Advisor: Prof. Dr. Greta R. Patzke
PhD Thesis: Earth-Abundant Transition Metals Based Oxides for Water Oxidation.

09/2008-06/2011 M.S. major in Chemical Engineering in South China University of Technology, Guangzhou, China.
Advisor: Prof. Dr. Haihui Wang
Master thesis: Oxygen Permeability of Chlorine Doped $Ba_{0.5}Sr_{0.5}Co_{0.8}Fe_{0.2}O_{3-\delta}$ and Their Applications in Low Carbons Alkanes Conversion.

09/2004-06/2008 B.S. major in Chemical Engineering and Technology in Wuhan University of Science and Technology, Wuhan, China
Supervisor: Prof. Dr. Jun Han
Bachelor thesis: Design of fluid bed reactor for combustion electricity generation.

Publications

1. **H. Liu,** M. Schilling, M. Yulikov, S. Luber, G. R. Patzke. Homogeneous photochemical water oxidation with cobalt chloride in acidic media. *ACS Catal.* **2015**, *5*, 4994-4999.

2. **H. Liu**, Y. Zhou, R. Moré, R. Müller, T. Fox, G. R. Patzke. Correlations between Structure, Electronic Properties and Photochemical Water Oxidation: A Case Study on Lithium Cobalt Oxides. *ACS Catal.* **2015**, *5*, 3791-3800.

3. H. Liu, G. R. Patzke. Visible-light-driven water oxidation with nanoscale Co_3O_4: New optimization strategies. *Chem. Asian J.* **2014**, *9*, 2249-2259. (Invited paper in special Issue: Sino-German Frontiers of Chemistry)

4. H. Liu, G. R. Patzke. Cobalt-Manganese Spinel Oxides as Visible-Light-Driven Water Oxidation Catalysts. *Ceram. Eng. Sci. Proc.* **2013**, *34*, 75-86.

5. H. Liu, Y. Wei, H. Wang, J. Caro. Oxidative Coupling of Methane with High C_2 Yield by Using Packed Bed of Chlorinated Perovskite $Ba_{0.5}Sr_{0.5}Fe_{0.2}Co_{0.8}O_{3-\delta}$ as Catalyst and N_2O as Oxidant. *ChemCatChem* **2010**, *2*, 1539-1542.

6. H. Liu, Y. Wei, J. Caro, H. Wang. Chlorine-Doped $Ba_{0.5}Sr_{0.5}Fe_{0.2}Co_{0.8}O_{3-\delta}$ as an Oxygen-Permeable Membrane at Intermediate Temperature. *Functional Materials Letters*, **2011**, *4*, 1-4.

7. Y. Zhou, H. Wang, M. Sheng, Q. Zhang, Z. Zhao, Y. Lin, **H. Liu**, G. R. Patzke. Environmentally friendly room temperature synthesis and humidity sensing applications of nanostructured $Bi_2O_2CO_3$. *Sensors and Actuators B.* **2013**, *188*, 1312-1318.

8. Y. Wei, **H. Liu**, J. Xue, Z. Li, H. Wang. Preparation and oxygen permeation of U-shaped perovskite hollow-fiber membranes. *AIChE Journal* **2010**, *57*, 975-984.

9. X. Chen, **H. Liu**, Y. Wei, J. Caro, H. Wang. A novel zincum-doped perovskite-type ceramic membrane for oxygen separation. *Journal of Alloys and Compounds* **2009**, *484*, 386-389.

Workshop and Trainings

1. 04/2015 Workshop, New Possibilities in high-end TEM Instrumentation and In Situ Analysis in Gas and Liquid Environments, ETH, Switzerland.

2. 09/2014 Summer school for solar fuels, Eurotel Victoria, Les Diablerets, Switzerland.

3. 11/2012 Power Diffraction School for Rietveld refinements, Paul Scherer Institute (PSI), Switzerland.

4. 10/2012 Workshop for OringinPro 9.0, ADDITVE GmbH, University of Zurich, Switzerland.

Honors and awards

12/2013 Excellent Award of 6th "Chunhuibei" Innovative and Entrepreneurial Contest, Guangzhou, China

2008-2011: Honor of "Excellent Graduate", South China University of Technology

2008-2011: First Class Scholarship each year, South China University of Technology

2010-2011: Honor of "Excellent Postgraduate", South China University of Technology

2008-2009: Outstanding Director in Academic Exchange Association, South China University of Technology

06/2006: The Second Prize in Chemistry and Chemical Experiment Skills Competition for Colleges in Hubei province